Quantitative evaluation of structural compartmentalization in the Heidrun field using time-lapse seismic data

Amran Benguigui

A thesis Submitted for the Degree of Doctor of Philosophy

Heriot-Watt Institute of Petroleum Engineering,

Heriot-Watt University, Edinburgh, Scotland.

February, 2010

Abstract

In reservoir settings with structural compartmentalization, fault properties can constrain the fluid flow and pressure development, thus affecting decisions associated with the selection of the drainage strategy within reservoir management activities. Historically, we have relied on geological analysis to evaluate the fault seal, however this can be restricted by available well coverage which can introduce considerable uncertainty. More recently, time-lapse seismic has become useful in the assessment of the dynamic connectivity. Indeed, seismic changes are in general a combination of pressure and saturation changes which, for compartmentalized reservoirs, seem to be associated with the sealing behaviour of faults. Based on this observation, this thesis presents a new effort in which the spatial coverage of the time-lapse seismic data is used as an advantage to more fully resolve properties of the fault seal, particularly in areas with poor data control. To achieve this task, statistics of amplitude contrast and the spatial variability of the 4D seismic signatures are considered. Tests performed on modelled data have revealed that the proposed 4D seismic measurements can be calibrated at the wells in a sector with known geological characteristics via a quadratic polynomial expression that allows fault permeability to be derived. Uncertainties in the 4D seismic estimation have also been considered in a Bayesian framework, leading to the identification of error bounds for the estimates. Results on synthetic data are encouraging enough to investigate its applicability on the Heidrun field. In this real example, the Jurassic reservoirs are compartmentalized due to the presence of a set of faults for which their flow capacity strongly affects field depletion. Here, previous studies have attempted to characterize the fault seals, yet the sparse nature of well data has limited their evaluation, leaving uncertainties when adjusting fault properties in the reservoir simulation model. In this case, application of our approach has proven useful, as it has allowed the detailed characterization of major faults in this field. Predictions obtained with the 4D seismic appear consistent when compared to previous core observations made from fault-rocks studies. Also, the results have been used to update

the flow simulation model by adjusting transmissibility factors between compartments, leading to a decrease of the mismatch between the simulated forecast and historical production data. Furthermore, uncertainty in the 4D seismic prediction has been considered when implementing an automatic history match workflow allowing further improvements.

New insights into the implications of the dynamic fault behaviour in the time-lapse seismic response are also provided in this thesis. We make use of synthetic models in which faults represent the main constraint for fluid flow, to show that an adjustment of the relation between the reservoir capillary pressure and the capillary threshold pressure of the fault-rock can alter the variance of the time-lapse seismic signature. However, a similar behaviour can be obtained when strong variations in the transmissibility of the fault are present. As a consequence, we propose that this statistic might help to identify fault seal dependent controls on individual fluid phases when the transmissibilities are fairly similar along the fault segment. This is particularly useful in the Heidrun field where we have found it difficult to explain the water encroachment by only using the single-phase approximation offered by the fault transmissibility multipliers. Here, the variance of the 4D seismic signature is employed together with the fault permeability values to suggest that in some compartments, waterflooding might be affected by the presence of a specific fault with sealing capacity strongly dependent on the individual fluid phases. This helps to explain the observed fluid uncertainties. It is also recognized that more data might be required to gain greater insight into this issue; hence alternative hypotheses are not discarded.

This thesis is dedicated to the loving memory of my grandfather,

Shemaya Benguigui (1924-2008)

and my grandfather-in-law,

Carlos Alberto Paez (1914-2007)

Both remain shining beacons that illuminate the paths of their families.

Acknowledgements

This research experience has been an amazing journey packed with excitement and difficulties, both in equal measure. Many have participated in this huge effort and I would like to acknowledge them for helping me in various ways to make this possible.

First of all, I am very grateful to my supervisor Prof. Colin MacBeth for giving me the opportunity to perform this research, as well for all of his guidance, encouragement and patience during this project. Also, I want to express my gratitude to the Statoil Heidrun asset, Statoil research teams and Heidrun field partners (Petoro, ConocoPhillips Skandinavia and Eni Norge) for providing the data I used, for their co-operation and their permission to publish results. A special note of appreciation to Helene Hafslund Veire and Svend Østmo for their support in the early stages of this study, and for their help with my visits to Statoil in Trondheim. I would like to thank Dr. Rossmary Villegas for her assistance in the history matching workflow. I am also indebted to my examiners Dr. Asghar Shams and Prof. Fernando Moraes for the time invested in the reviewing of this thesis. I acknowledge the sponsors of the Edinburgh Time Lapse (ETLP) Project, Phase III (BG, BP, ChevronTexaco, ConocoPhillips, EnCana, Eni, ExxonMobil, Hess, Ikon Science, Landmark, Maersk, Marathon, Norsar, Ohm, Petrobras, Shell, StatoilHydro, Total and Woodside) for providing the funding of this research. Additionally, as a recipient of the Dorothy Hodgkin Postgraduate Awards (DHPA) I want to thank the university for the financial support granted by this UK scheme. My gratefulness goes as well to the Society of Exploration Geophysicists (SEG) Foundation for awarding me with the Leon Thompson/BP UK scholarship, which indeed represents a source of encouragement in my career.

Also, as part of the Reservoir Geophysics group, I had the opportunity to meet wonderful people and I am thankful to all its members: Hamed Amini, Margarita Corzo, Fabian Domes, Reza Falahat, Alejandro Garcia, Hansel Gonzalez, Yesser HajNasser,

Neil Hodgson, Weisheng He, Yi Huang, Nader Kooli, Otelindo Medina, Jesus Nuñez, Mehdi Paydayesh, Ludovic Ricard, Rahul Tiwari, Rui Cesar Sansonowski, Asghar Shams and Karl Stephen. I would like to give you my appreciation for providing an excellent atmosphere and many insightful discussions.

I also want to express my sincere and endless gratitude to my wife Aisha Paez for her patience whilst I have spent hundreds of hours working on this project as well as in the preparation of this thesis. Her love, massive help and encouragement in difficult times have considerably helped towards the completion of this work. Also, deepest thanks to our families for their affection and support throughout these years.

Last, but certainly not least, I would like to thank God, for everything that has been given me in this life.

ACADEMIC REGISTRY
Research Thesis Submission

Name*:*	Amran Benguigui		
School/PGI:	Institute of Petroleum Engineering		
Version: *(i.e. First, Resubmission, Final)*	Final	Degree Sought (Award **and** Subject area)	Ph.D. in Petroleum Engineering

Declaration

In accordance with the appropriate regulations I hereby submit my thesis and I declare that:

1) the thesis embodies the results of my own work and has been composed by myself
2) where appropriate, I have made acknowledgement of the work of others and have made reference to work carried out in collaboration with other persons
3) the thesis is the correct version of the thesis for submission and is the same version as any electronic versions submitted*.
4) my thesis for the award referred to, deposited in the Heriot-Watt University Library, should be made available for loan or photocopying and be available via the Institutional Repository, subject to such conditions as the Librarian may require
5) I understand that as a student of the University I am required to abide by the Regulations of the University and to conform to its discipline.

* *Please note that it is the responsibility of the candidate to ensure that the correct version of the thesis is submitted.*

Signature of Candidate*:*		Date:	23/02/10

Submission

Submitted By *(name in capitals):*	AMRAN BENGUIGUI
Signature of Individual Submitting:	
Date Submitted:	23/02/10

For Completion in Academic Registry

Received in the Academic Registry by *(name in capitals):*			
Method of Submission *(Handed in to Academic Registry; posted through internal/external mail):*			
*E-thesis Submitted (**mandatory for final theses from January 2009)***			
Signature:		Date:	

Please note this form should bound into the submitted thesis.

Updated February 2008, November 2008, February 2009

Publications

Part of this work is presented in the following publications:

- Benguigui A. and MacBeth C. (2008). Quantitative Evaluation of Reservoir Fault Communication using 4D Seismic: An Application to the Heidrun Field. 70th Meeting of the European Association of Geoscientist and Engineers. Expanded Abstracts.

- Benguigui A. and MacBeth C. (2009). Updating the Simulation Model using 4D-derived fault transmissibility multipliers: An Application to the Heidrun Field. 71st Meeting of the European Association of Geoscientist and Engineers. Expanded Abstracts.

- Villegas, R., MacBeth, C. and Benguigui, A. (2009). History matching of reservoirs by modifying fault properties using 4D seismic results: a synthetic study. Conference on Faults and Top Seals of the European Association of Geoscientists and Engineers. Montpellier, France. Expanded Abstract.

Contents

List of Figures

List of Tables

List of Symbols

a_i	i coefficient of the polynomial expression
ΔA	change in seismic attribute
c	constant
C_P	coefficient related to the change in pressure for an water-oil system
C_S	coefficient related to the change in oil saturation for an water-oil system
D	fault displacement
h	distance
ΔIp	P-wave impedance change
J	cost function
k	cell permeability
k_e	equivalent permeability
k_f	fault-rock permeability
kh	horizontal permeability
k_{ro}	oil relative permeability
k_{rw}	water relative permeability
kv	vertical permeability
L	cell length
p(m|d)	likelihood function
m	model
N_h	number of pairs within the lag interval h
P10	10% probability
P50	50% probability
P90	90% probability
Pc	capillary pressure
P_K	bulk constant for pressure dependency
P_μ	shear constant for pressure dependency
ΔP	average pore pressure change

Q_w	estimated water rate in the producer well
Q_{Wobs}	observed water rate in the producer well
S_e	effective water phase saturation
S_{gr}	residual gas saturation
S_o	oil saturation
S_{or}	residual oil saturation
S_w	water saturation fraction
S_{wc}	connate water saturation
S_K	maximum possible change in the bulk moduli
S_μ	maximum possible change in the shear moduli
ΔS_o	average oil saturation
ΔS_w	average water saturation
T	transmissibility multiplier
t_f	fault thickness
$Trans_{ij}$	transmissibility between grid-blocks i and j
Vshale	shale content
x	inter-compartment difference
y	spatial variability
Z_{max}	maximum burial depth
z_f	depth at time of deformation
Δz	thickness

Greek Letters

φ	porosity
φ_f	fault-rock porosity
γ_h	variogram value for a distance h
K_d	dry rock modulus
K_f	bulk modulus of the fluid mixture
K_{gr}	grain bulk modulus
K_{inf}	bulk modulus asymptote at high pressure
K_s	saturated-rock modulus
σ	standard deviation

σ^2	variance
μ_{inf}	shear modulus asymptote at high pressure

Abbreviations

4D	multiple 3D surveys at different times, the fourth dimension is time
AI	acoustic impedance
AVO	amplitude versus offset
CSP	clay smear potential
ETLP	Edinburgh time lapse project
Fm	Formation
FVF	formation volume factor
FW	foot-wall
FWL	free water level
GOR	gas oil ratio
Gp	Group
GR	gamma-ray
HW	hanging-wall
N/G	net-to-gross
NRMS	normalized root-mean square
OGOC	original gas oil contact
OOWC	original oil water contact
pdf	probability density function
PGOC	gas oil contact after production
POWC	oil water contact after production
RC	reflection coefficient
S/N	signal-to-noise
SF	smear factor
SGR	shale gouge ratio
SSF	shale smear factor

Chapter 1

Introduction

This chapter provides a review of the fault-seal phenomena that lead to reservoir compartmentalization. It describes several techniques that have been used to predict the fault sealing capacity and its application to full field flow simulation modelling. An overview on the use of time-lapse seismic as a tool to characterize the dynamic effects of fault properties is also shown. Some advantages and disadvantages of these studies are discussed. In this thesis, 4D seismic is postulated as a tool to help the aerial resolution of fault seal determination beyond that obtained by well-based estimation. Finally, the main challenges and contribution of this thesis are discussed.

1.1 Preamble

Success in dynamic reservoir management is strongly linked to the understanding of the impact of faults as fluid flow transmitters or barriers. Their spatial occurrence in the reservoir controls the degree of connectivity of the hydrocarbon accumulation defined by compartments which store the reserves in similar or different reservoir conditions. The compartmentalisation phenomenon considerably affects the fluid flow behaviour; hence, fault characterization will influence decision on well numbers, well location and ultimate success or failure in the drainage strategy. Developments in faulted siliciclastic units have focused on two separate but inter-related aspects of faulting: fault architecture and fault-rock properties (Ceverny et al. 2005). The fault architecture refers to the fault shape, size, orientation and interconnectivity, however, the fault-rock properties explain the interaction of local facies, reservoir-fluid types, pressure differentials across faults, burial history and lithological juxtaposition, related to the fault ability to seal. In particular, the analysis of the sealing capacity of the fault is a major topic in reservoir characterization studies and it represents the subject of this thesis.

In a first attempt to understand the effects of faults on fluid flow behaviour within hydrocarbon provinces, early work (Bouvier et al. 1989, Jev et al. 1993, Møller-Pederson & Koestler 1997) provided fundamental insights which introduce the importance of the faults in reservoir management prediction. Since then, different approaches have been proposed to evaluate the impact of faults in hydrocarbon flow (Berg 1975, Schowalter 1979, Knipe 1992, Knott 1993, Knipe et al 1997). More recent papers indicate how the flow-patterns are affected by the fault control (e.g., Antonelli and Aydin, 1994; Fowles and Burley, 1994; Childs et al., 1997; Gibson, 1998; Knai and Knipe, 1998, Hesthammer and Fossen, 2000). However, although most of the proposed workflows are beyond their actual applicability in common fluid flow simulators, they allow the characterisation of the fault behaviour reducing uncertainties and improving predictions.

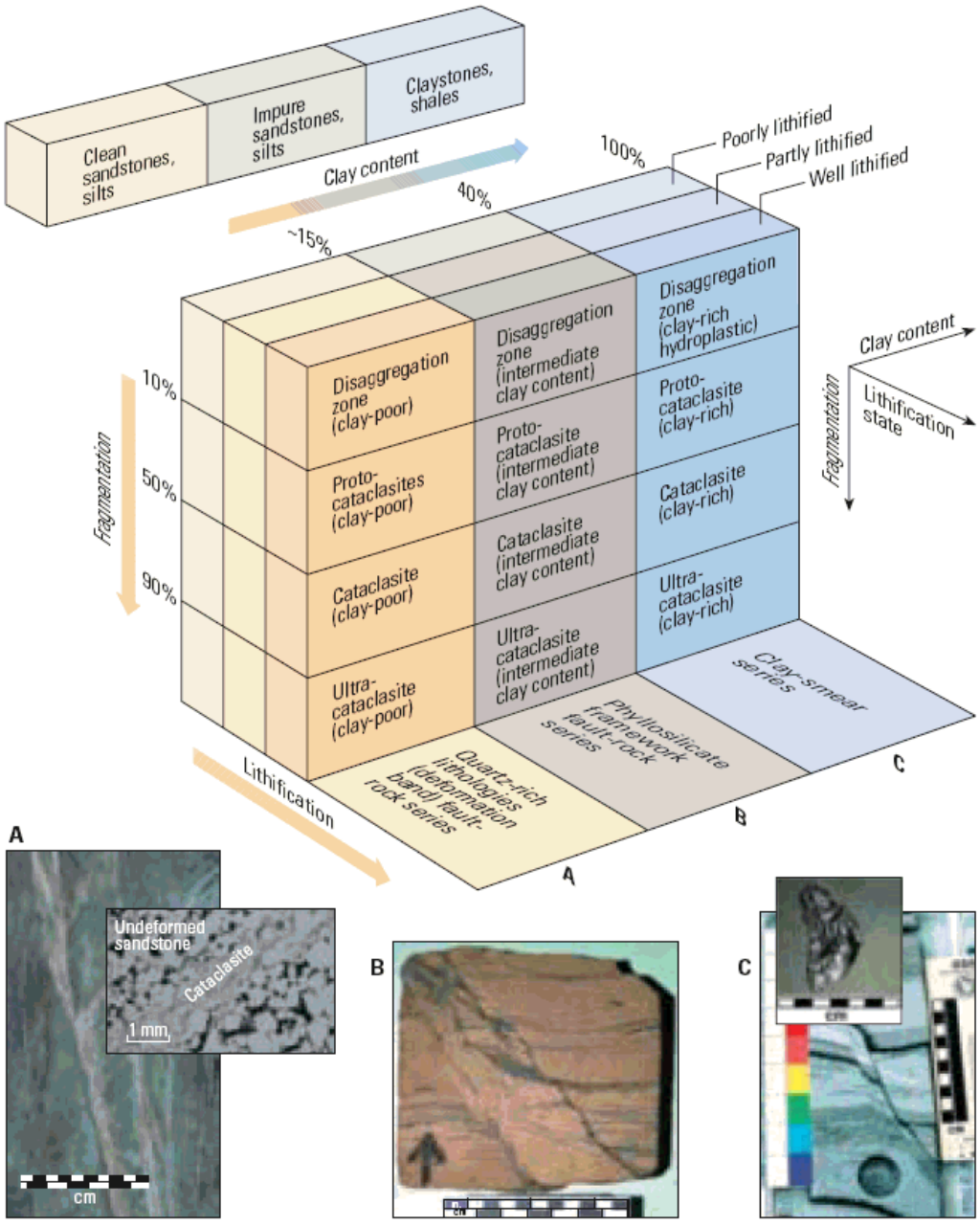

Figure 1.1. *Fault-rock classification relating clay content, fragmentation and lithification. The original host rocks include clean sandstones with less than 15% clay, impure sandstones with 15% to 40% clay, and claystones and shales with greater than 40% clay. Fragmentation and lithification progress throughout the fault history producing one of three types of fault rocks from each host as shown in the lower portion of the diagram. Photographs at the bottom illustrate different forms of fault-rocks, including (A) disaggregated and cement (left), (B) phyllosilicate-smear framework (center) and (C) clay-smear fault rocks (After Cerveny et al. 2005).*

Acquired insights reveal that deformation processes involved in the evolution of rock faulting reduce permeabilities inside the fault and increase the entry pressure for the non-wetting phase (Onyeagoro et al. 2006). The development of the permeability barrier has been reviewed in detail by Mitra (1988), Knipe (1989, 1992, 1993) and Knipe et al. (1998) and it comprises: deformation-induced porosity collapse by disaggregation and mixing, pressure solution, cataclasis, cementation and clay/phyllosilicate smearing (Figure 1.1). These processes define the communication capacity of the fault-rocks which in turn affects the fluid flow in structurally compartmentalized reservoirs.

Despite this understanding, very few faults have been characterized in a degree which categorically allows identification of the sealing mechanism (Knipe et al. 1998). Construction and further development of fault seal evaluation should be addressed to allow a clearer comprehension and quantification and therefore predictability of the factors involved.

1.2 Fault characterization through clay smear prediction algorithms

Following the previous studies, an effort has been made to derive empirical approaches to enhance prediction of the fault seal capacity from simple geological criteria. To assess the fault properties, several quantitative techniques have been proposed (Figure 1.2). Derived from the static data domain, the different methods are purely based on the following information:

- The fault geometry (fault throw).
- The thickness of the damage zone.
- The host rock properties (shale or clay fraction).

These approaches are generally based on the seal effectiveness of the clay smear within the fault rock (to fluids) which depends primarily on the cumulative thickness of shale source beds that are contributing. Here, the vertical load on the shale beds is assumed greater than normal stress across the fault surface. Hence, if shale is fluid enough (in geological time scales), it can be squeezed from the original bedding position into the fault zone as the fault is developed.

Bouvier et al. (1989) described the clay smear potential (*CSP*) as a means of estimating the likelihood of clay smearing in areas of sand/sand juxtaposition on faults related to the Nun River field in the Niger Delta. The clay smear potential is stated to represent the relative amount of clay that has smeared from individual shale source beds at a certain point along the fault plane.

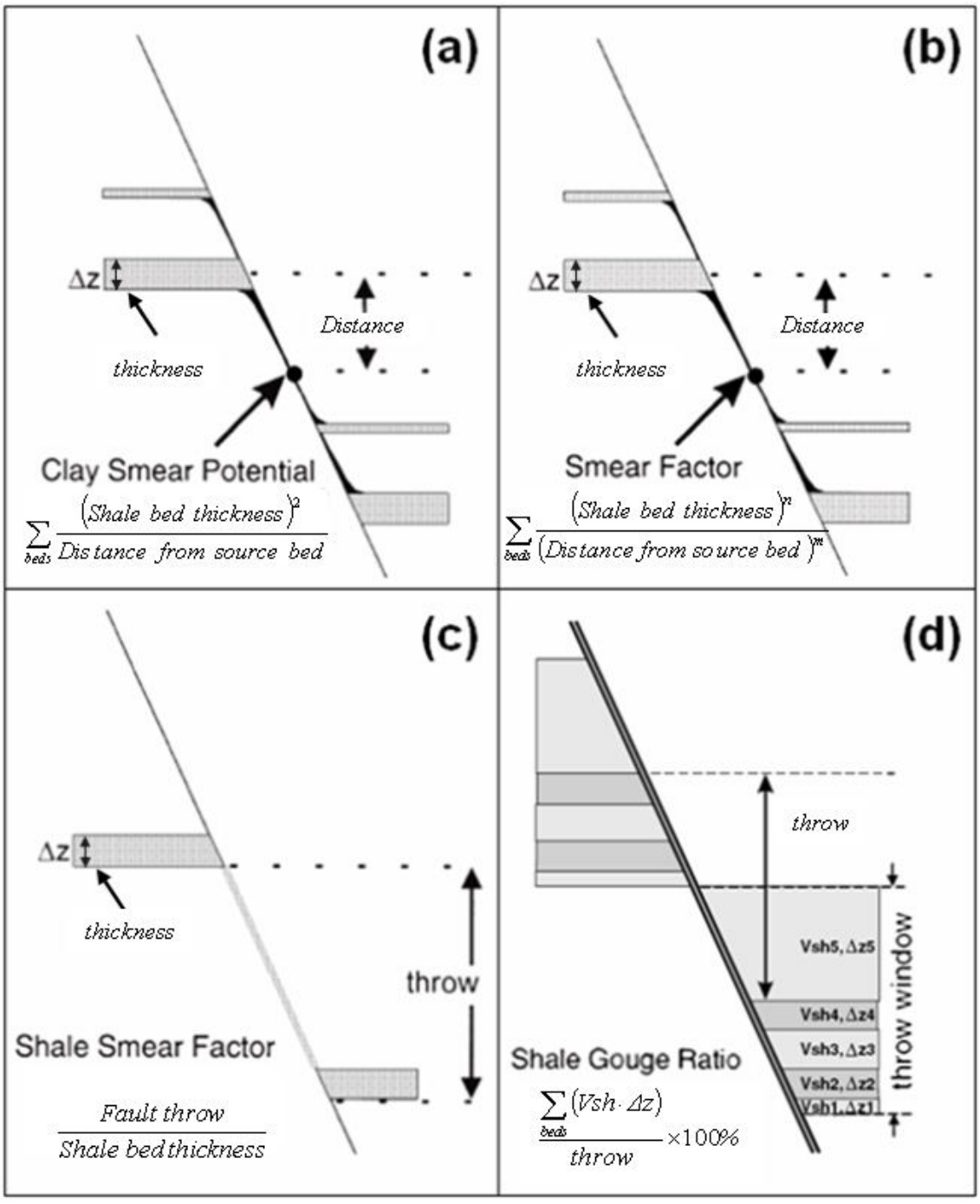

Figure 1.2. *Smear factor algorithms for estimating likelihood of clay smear on a fault plane. (a) Clay smear potential (CSP) linked to the point P at a defined distance from the upthrown shaly source bed (Bouvier et al., 1989; Fulljames et al., 1996); (b) generalized smear factor (SF); (c) shale smear factor (SSF) (Lindsay et al. 1993); (d) shale gouge ratio (SGR) (Yielding et al., 1998). Vsh and Δz represent clay/shale content and thickness of the source shale bed respectively (After Yielding et al., 1998).*

The *CSP* increases with shale source bed thickness and with the number of source beds displaced past a particular point along a fault plane. A decrease will be observed with increased fault throw or fault displacement. These relationships have been expressed by Fulljames et al. (1996) as,

$$CSP = \sum_{beds} \frac{\left(Shale\ bed\ thickness\right)^2}{Distance\ \ from\ source\ bed} \tag{1.1}$$

for distances less than the fault offset. For a point lying within the offset between hangingwall and footwall, the distance to the nearest shale bed (upthrown or downthrown termination according to the point position) is measured as well as it thickness. As the distance is calculated from the nearest termination of the bed, the smear profile is assumed to be symmetric. If more than one shale layer is present, *CSP* calculations are summed according to the previous equation. Generally speaking, *CSP* calculation defines the length of a continuous shale tail smeared out in the fault zone (Naruk et al. 2002).

Outcrop studies are often employed as a way to determine *CSP* values classifying them for continuous and discontinuous clay smears. Bouvier et al. (1989) calibrated known sealing and non-sealing faults against their respective *CSP* calculation allowing the division of the observations into high, medium and low *CSP* for low representing little chance for hydrocarbon entrapment. Jev et al. (1993) applied the technique on the Akaso field in the Niger Delta concluding that a *CSP* less than 15 length units represents non-sealing as *CSP* greater than 30 is associated to sealing faults. Bentley and Barry (1991) used *CSP* values to constrain a reservoir simulation of Cormorant Block IV in the Brent province of northern North Sea, finding that on a production time scale a *CSP* of 5 marked the general threshold for fault sealing. Even though the shale bed thickness is raised to the power of two as stated by fluid dynamics arguments (Lehner and Pilaar, 1996), Yielding et al. (1997) suggest that *CSP* can be considered as one example of a generalized smear factor (*SF*) given by:

$$SF = \sum_{beds} \frac{\left(Shale\ bed\ thickness\right)^n}{\left(Distance\ from\ source\ bed\right)^m} \tag{1.2}$$

where the exponents *m* and *n* can be regarded as additional variables whose values may be justified by experimental or observational studies. Both *CSP* and the *SF* are essentially measuring the degree of continuity of the clay smear along the fault plane.

Based on observations of abrasion smears in a carboniferous deltaic sequence from northern England, Lindsay et al. (1993) proposed another shale smear factor to constrain the likelihood of shale smear continuity. They define the shale smear factor (*SSF*) as:

$$SSF = \frac{Fault\ throw}{Shale\ bed\ thickness} \tag{1.3}$$

The factor remains constant between the offset terminations as it does not depend on the smear distance. According to their study on 80 faults, Lindsay et al. (1993) concluded that shale smear may become continuous for *SSF* values less than 7 and therefore a sealing layer on the fault surface is formed. *SSF* values are not added for compound smears as thin shales result in a higher *SSF* dominating the summation. In such cases, *SSF* should be taken as the minimum obtained value (most sealing) given by the relevant shale beds affected by the fault.

However, the *CSP*, *SF* and *SSF* methods depend upon thickness and offset (defined as the vertical distance from a shale unit to a particular point in the fault plane) of individual shale beds. As a consequence, such approaches may be difficult to apply directly in thick heterogeneous sequences as individual shale units are not necessarily feasible to map. Furthermore, they only provide information on the continuity of clay smears and do not take into account an estimate of the clay content along the fault plane. In those cases, Yielding et al. (1999) suggest a simpler approach which considers the bulk properties of the sequence at the scale of reservoir mapping. The proposed

attribute defined as the shale gouge ratio (*SGR*), measures the percentage of shale or clay in the slipped interval:

$$SGR = \frac{\sum_{beds}(Shale\ bed\ thickness)}{Fault\ throw} \times 100\% \tag{1.4}$$

The shale thickness is measured in a window with a width equal to the throw representing the column of rock that has slipped on the fault. The concept can be extended for cases with a stratigraphic reservoir zone definition, where the net contribution of fine-grained material from each reservoir zone can be related to the clay content and thickness of the zone. Subsequently, the smearing of fine-grained layers (such as shales) incorporated along the fault plane is estimated by:

$$SGR = \frac{\sum_{beds}[(Zone\ thickness)\times(Zone\ clay\ fraction)]}{Fault\ throw} \times 100\% \tag{1.5}$$

The *SGR* represents the proportion of shale or clay that might be entrained in the fault zone by a variety of mechanisms. The more shaly the wall rocks, the greater the proportion of shale in the fault zone. Although this is an oversimplification of the detailed processes occurring in the fault zone (discussed previously) it represents a tractable upscaling of the lithological diversity. Comparisons of the observed fault composition at the Moab fault zone (Yielding, 2002) show correlation with the calculated shale gouge ratio derived from the outcrop (Figure 1.3) although the predicted composition might be upscaled by the algorithm covering up local variations. Calibrating *SGR* values with pore pressure profiles across fault surfaces in a variety of datasets (Nun River field – Niger delta, Oseberg Syd – Northern North Sea, Columbus Basin – Offshore Trinidad), Yielding et al. (1999) highlight that threshold values for the *SGR* are about 15-20%. Below this limit no fault-sealed hydrocarbons are observed as pressure difference cannot be supported by the fault. Corresponding maps of *SGR* distribution on faults can clearly show where the inter-compartment communication is enhanced as indicated by low values of *SGR* (Figure 1.4). Implementing dynamic data

such as pressure (Figure 1.5), fault seals calculations are commonly calibrated from the juxtaposed units (e.g., Bretan et al. 2003, Sverdrup et al. 2003) by evaluating the minimum *SGR* values in which the pressure contrast between compartments is developed. Naruk et al. (2002) show that in most reservoirs with a sand/shale stratigraphic section less than 80%, fault seal capacity is mainly controlled by the fault zone composition regardless of the in situ stress, burial depth, burial history and clay type. Therefore the advantage of the *SGR* method is in the prediction of a physically measurable parameter (composition) (Yielding et al. 2002). Comparison between *SGR* and *CSP* estimators has been made via cross plots (Yielding et al. 1999, Naruk et al. 2002). As shown in Figure 1.6 *CSP* cannot fully resolve the fault sealing behaviour as it has multiple corresponding values of *SGR*. Furthermore, as illustrated in several studies (Figure 1.7), the *SGR* algorithm can be used to predict other compositionally-controlled properties such as the fault-zone permeability and a *SGR*-dependent transmissibility multiplier which may easily be incorporated into the reservoir model (Manzocchi et al., 1999). This is ultimately useful, as the final purpose of this thesis is related to the derivation of a geologically and numerically meaningful strategy to include the petrophysical properties of the faults in production simulation models.

1.3 Fault transmissibility multiplier

Conventionally, in production flow models, faults are represented by a multiplier factor *T* defined in between pairs of grid-blocks. To explain its application, consider two contiguous grid-blocks *i* and *j* with cell length *L* and permeability *k* with an associated subscript for each discrete block (Figure 1.8). For the illustrated pair of blocks, transmissibility between cells *i* and *j* ($Trans_{ij}$) is obtained with the following equation:

$$Trans_{ij} = \frac{2T}{\left(\frac{L_i}{k_i} + \frac{L_j}{k_j}\right)} \tag{1.6}$$

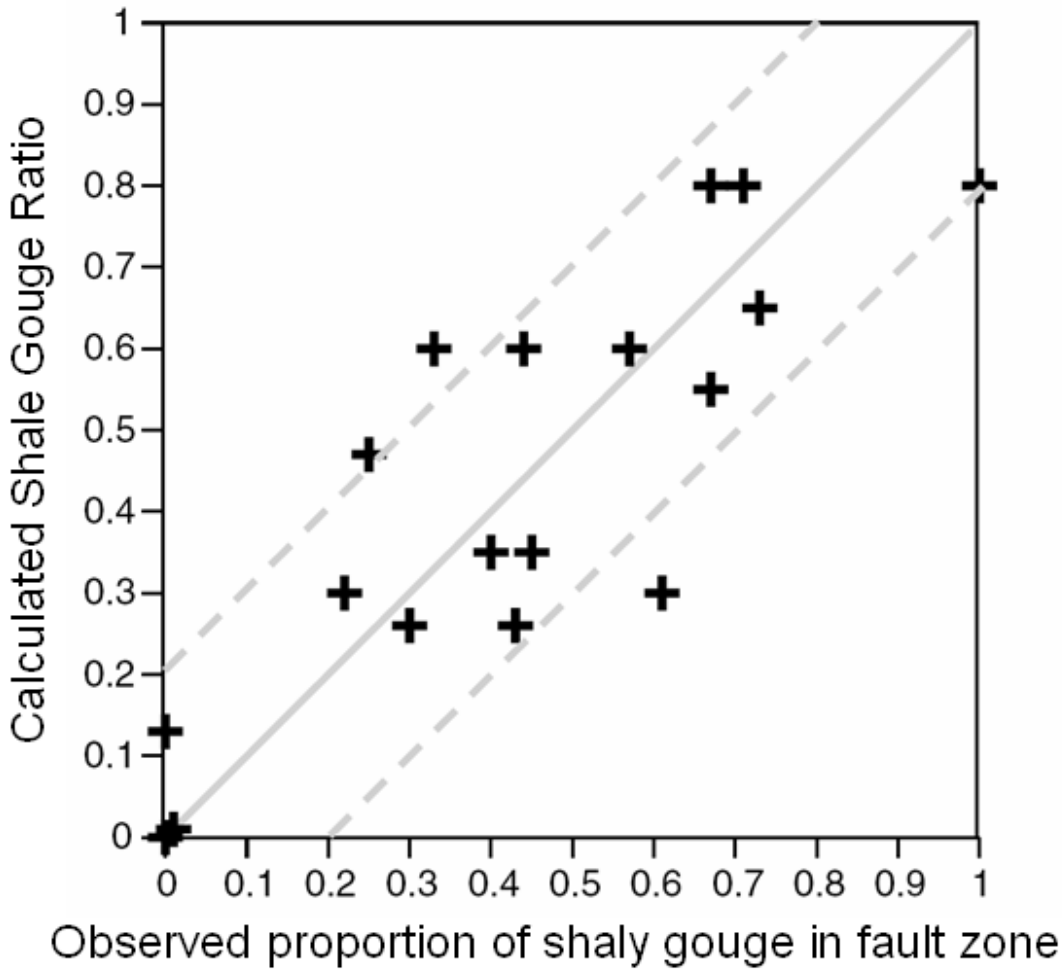

Figure 1.3. *Comparison of observed fault-zone compositions with calculated shale gouge ratio, for locations on the Moab Fault figured by Foxford et al. (1998). Observed compositions are based on the logged transects of Foxford et al. (1998, their fig. 5) and the calculated SGR's are based on a 'triangle' juxtaposition diagram (cf. their fig. 9). Note that there is a general correlation between observed composition and calculated SGR. The dashed lines bound the field where observed and calculated values agree within 20% (After Yielding, 2002).*

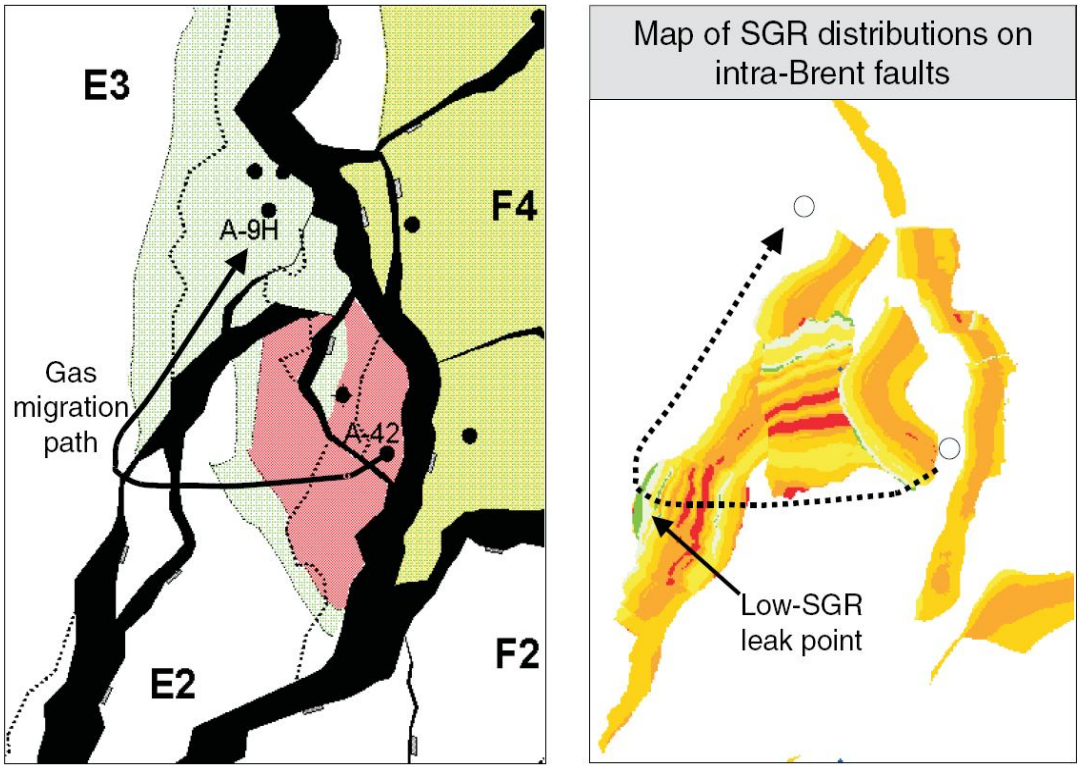

Figure 1.4. *Example of compositional control on dynamic behaviour during production on the Gullfaks field. In the map at left, green and red areas show Brent Group oil and gas respectively. The gas migration path from the injector A-42 to the producer A-9H crosses the fault away from the shortest route (Hesthammer and Fossen, 1997). The SGR distribution on the Brent–Brent overlaps (right map) shows that this location corresponds to the low-SGR window on the fault surface (SGR colours: green D <10%, red D >30%; Yielding et al., 1999). (After Yielding, 2002).*

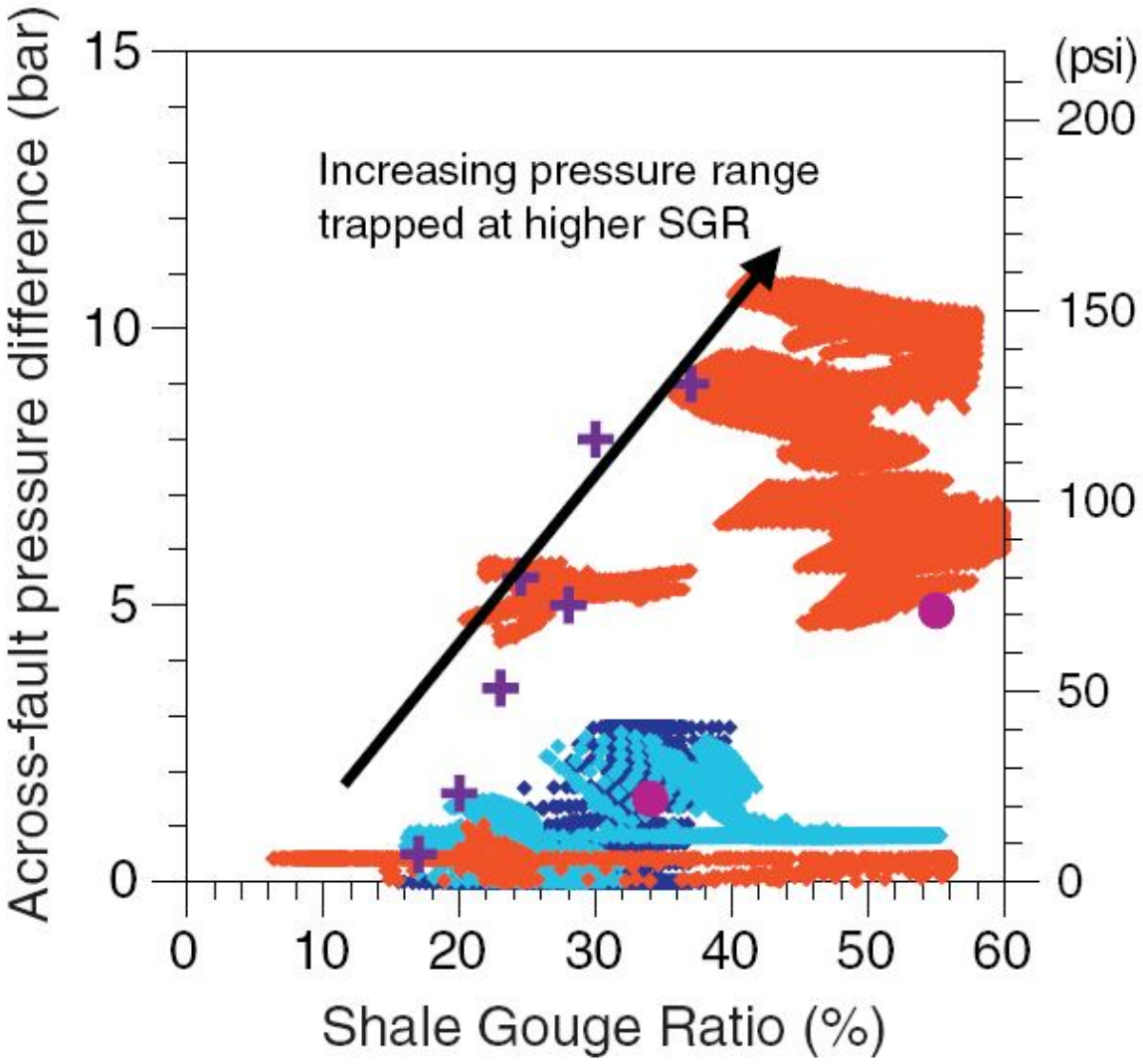

Figure 1.5. *Comparison of shale gouge ratio and in situ across-fault pressure difference for faults in the Brent Province, northern North Sea. Data are derived from pressure profiles acquired in wells located at the two sides of the fault. Since isobars are horizontal in each reservoir interval, the pressure profile can be mapped onto the fault plane from the wells on each side. Where reservoirs are juxtaposed at the fault, the difference between the two pressure profiles is the pressure difference across the fault. Each colour represents a different dataset. Clouds of small points correspond to entire reservoir juxtaposition areas. Large points correspond to 'trap-critical' locations that represent the highest pressure difference at a particular value of SGR on that fault. Includes data from Fristad et al. (1997) (recalculated with updated Vshale data provided by S. Sperrevik, pers. commun.), Yielding et al. (1997, 1999), Sverdrup et al. (2000). (After Yielding, 2002).*

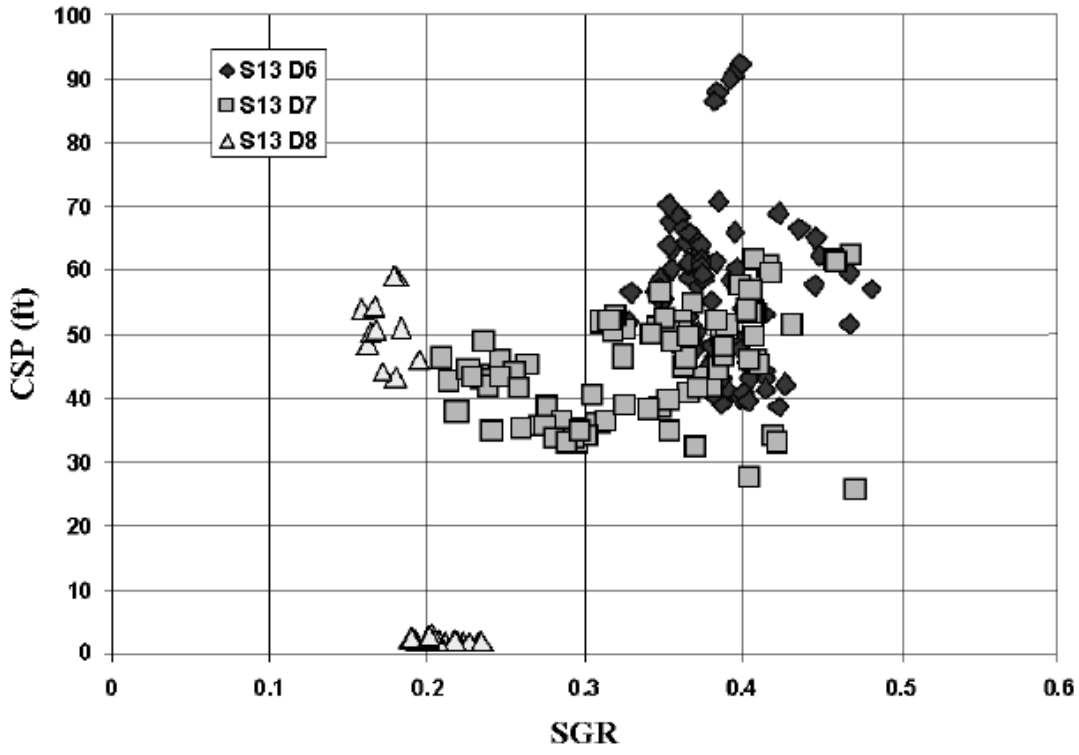

Figure 1.6. *Cross plot of CSP as a function of SGR on three different reservoir-fault-reservoir contacts (S13 D6, S13 D7 and S13 D8). No simple or direct correlation of CSP with SGR is observed as they describe two significantly different physical processes. (After Naruk et al. 2002).*

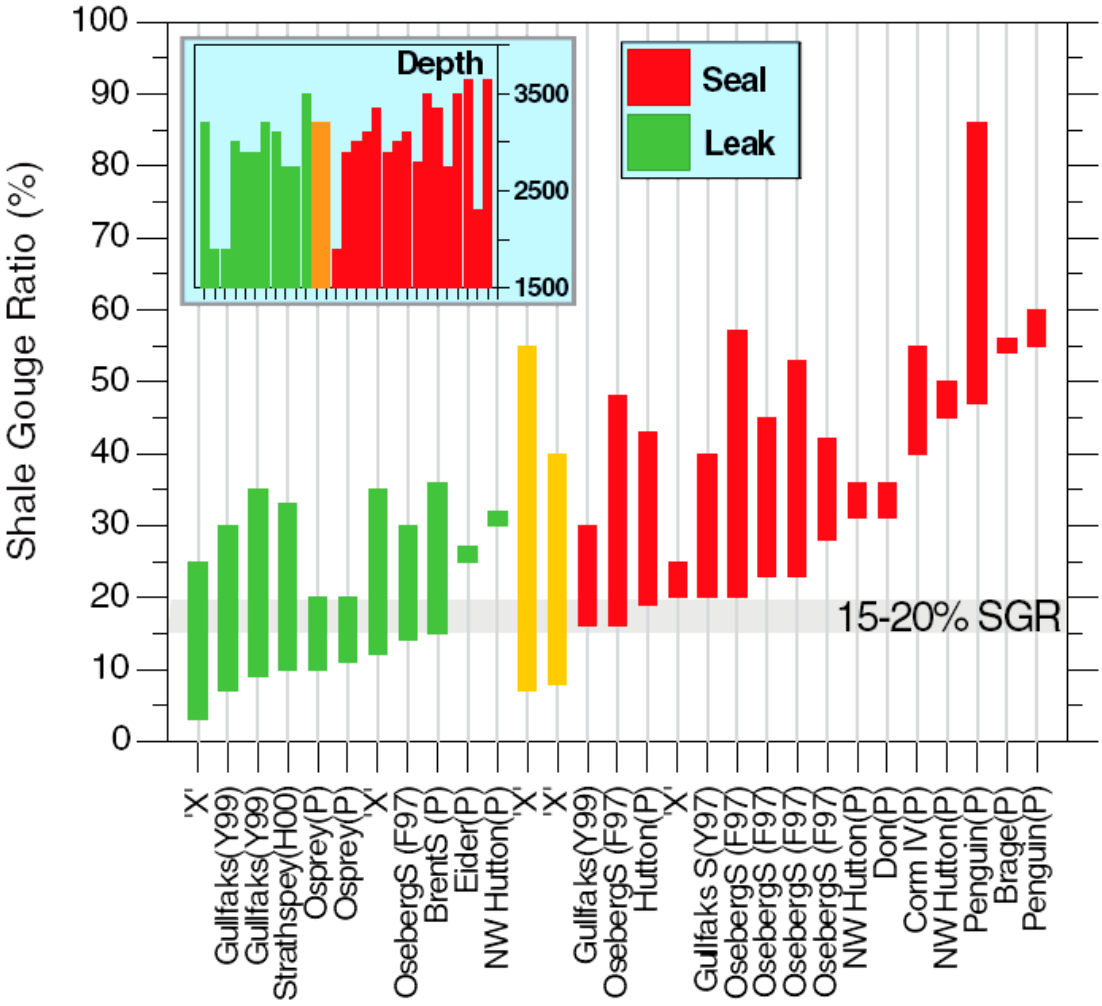

Figure 1.7. *Compilation of fault seal-leak observations from the Brent Province, northern North Sea. Vertical bars represent range of shale gouge ratio on individual faults. Faults are characterised as 'sealing' (red) or 'leaking' (green) depending on whether there is a change of hydrocarbon contact across the fault. SGR values of 15–20% provide a threshold between sealing and leaking behaviour (if a juxtaposition window with SGR < 15% occurs, the fault leaks). Orange bars indicate two faults which support OWC differences of <15 m, at 3200 m burial depth. The inset shows burial depths for the same sequence of faults: note the absence of any trend. References for the named faults are: F97, Fristad et al. (1997) (recalculated with updated Vshale data provided by S. Sperrevik, pers. commun.); Y97, Yielding et al. (1997); Y99, Yielding et al. (1999); P.. Phelps, pers. commun.; H00, Harris et al. (2000). (After Yielding, 2002).*

Here, the fault multiplier *T* is defined as a scalar between 0 and 1. This is meant to account for the impact of the fault seal on flow when a fault is in between cells *i* and *j*. Under such definitions, fault characterization used to rely on a matching practice that involves iterative changes on this fault multiplier, aiming to reduce the difference between production history and conventional simulations within a procedure defined as "production history matching". Yet, industry accepted the fact that fault characterization technology is needed to improve the fault definition within reservoir simulations.

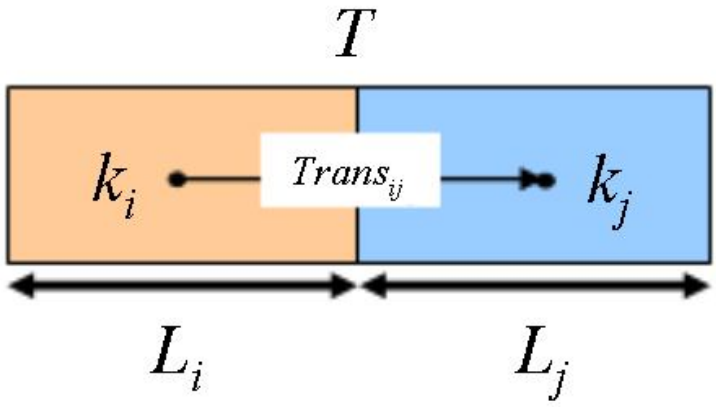

Figure 1.8. *The transmissibility multiplier T acts on the transmissibility $Trans_{ij}$ between two block centres. (After Manzocchi et al. 1999)*

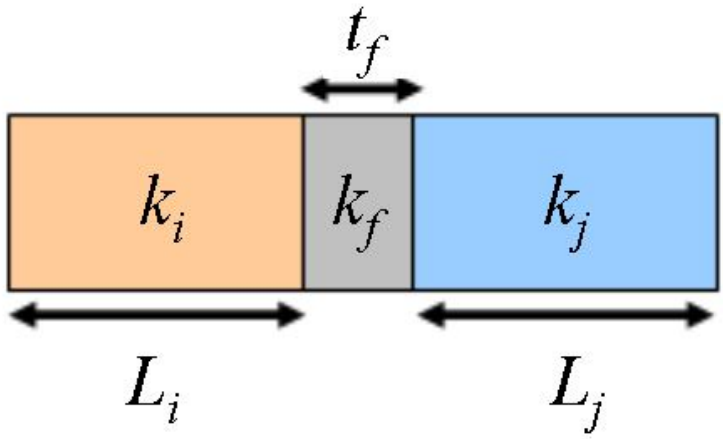

Figure 1.9. *Parameters incorporated in the calculation of the fault transmissibility multiplier. (After Manzocchi et al., 1999)*

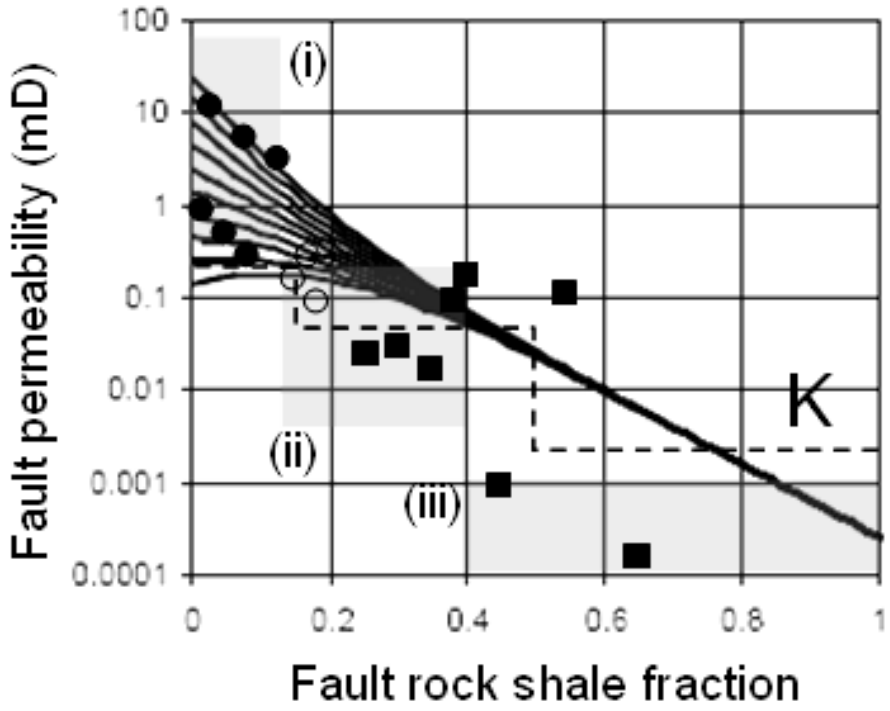

Figure 1.10. *Fault permeability (mD) vs. volumetric shale fraction for fault-rock. Data points represent plug permeability measurements from core and outcrop samples from a variety of locations (Gibson, 1998). Filled circles: cataclastic deformation bands. Open circles: solution deformation bands. Filled squares: clay gouge. Boxes are summaries of data from Sleipner field (Ottensen Ellevset et al. 1998). (i) Cataclastic deformation bands. (ii) Framework phyllosilicate fault rocks. (iii) Shale smears. The line labelled as K represents the average values based on core samples from the Heidrun Field, used in a full field flow simulation (Knai 1996). The curves represent the relationship used in Manzocchi et al. 1999 for permeability as a function of SGR and displacement. (After from Manzocchi et al. 1999).*

Consequently, Manzocchi et al. (1999) define a fault transmissibility multiplier as a function of the fault zone properties and the grid-block geometries, allowing the incorporation of fault information into the flow simulators. To do so, this work assumes a model in which fault-rock properties are given by the fault thickness t_f and a fault permeability k_f (Figure 1.9). Then, the equivalent permeability between the centres of the blocks *i* and *j* is:

$$k_e = \frac{L_i/2 + L_j/2}{\frac{L_i/2 - t_f/2}{k_i} + \frac{t_f}{k_f} + \frac{L_j/2 - t_f/2}{k_j}} \tag{1.7}$$

and the equivalent transmissibility over this distance is:

$$Trans_{ij} = \frac{2}{\frac{L_i - t_f}{k_i} + \frac{2t_f}{k_f} + \frac{L_j - t_f}{k_j}} \tag{1.8}$$

providing a numerically more robust representation of the fault.

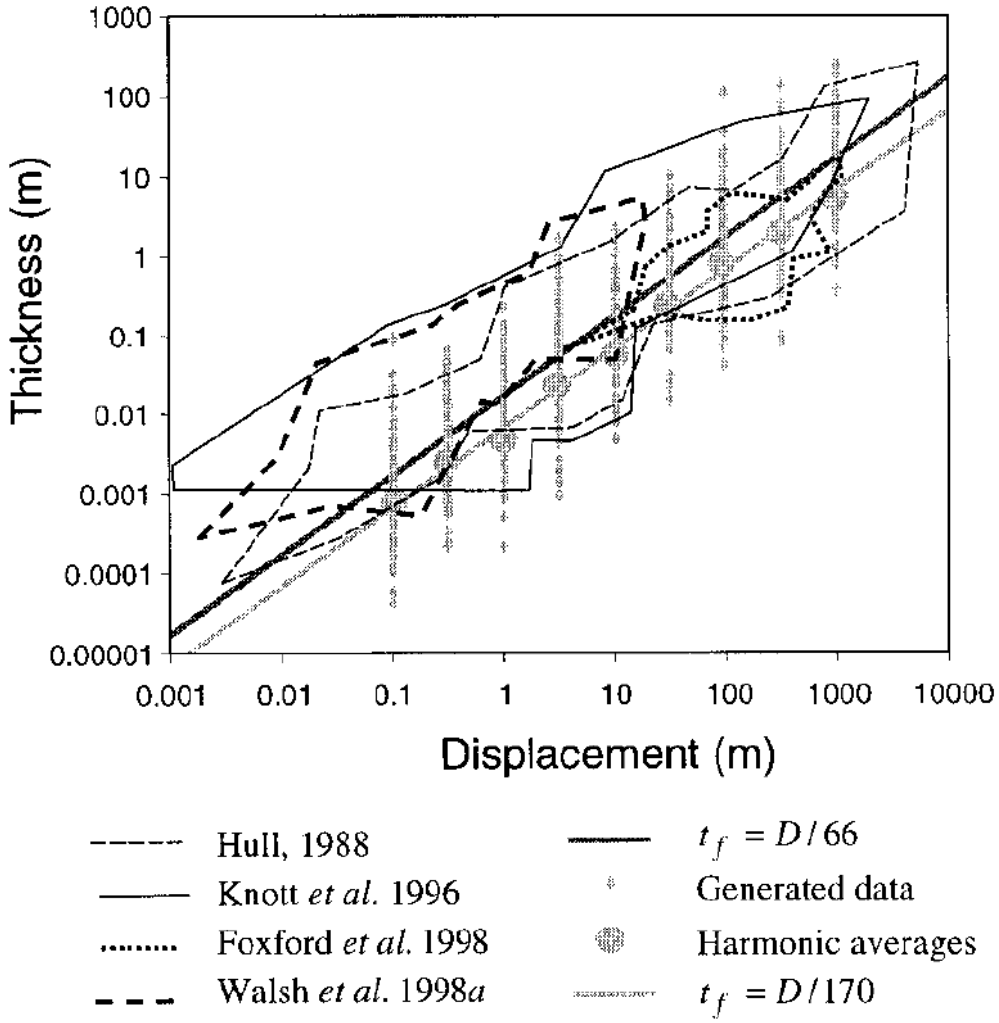

Figure 1.11. *Log thickness versus log displacement. Summaries of outcrop measurements are given as envelope defined from a variety of measurements (Hull 1988), from faults in Nubian sandstones in western Sinai (Knott et al. 1996), from Moab Fault in SE Utah (Foxford et al. 1998) and from faults in Westphalian sandstone/shale sequence from Lancashire, UK (Walsh et al. 1998). The harmonic average of these data (large circles) follows the relationship $t_f = D/170$. (After Manzocchi et al. 1999).*

To evaluate fault transmissibility using equation (1.8), an empirical prediction of fault zone permeability as a function of shale content (measured via shale gouge ratio) and fault displacement (measured along the fault plane) is proposed by Manzocchi et al. (1999) (Figure 1.10):

$$\log k_f = 0.4 - 4SGR - \frac{1}{4}\log(D)(1-SGR)^5 \tag{1.9}$$

where k_f is the fault permeability in miliDarcy, *SGR* the shale gouge ratio and *D* is the fault displacement in meters. Other empiric equations can be found elsewhere.

This is the case for Sperrevik et al. (2002), in which fluid flow properties of the fault rock are assumed to be controlled by the fault zone clay content (*SGR*), maximum burial depth (Z_{max}) and depth at time of deformation (z_f). Here fault permeability (mD) is defined by:

$$k_f = c_1 \exp\left\{-\left[c_2(SGR/100) + c_3 Z_{max} + (c_4 z_f - c_5)(1-(SGR/100))^7\right]\right\} \tag{1.10}$$

with constants c_1 = 80000; c_2 = 19.4; c_3 = 0.0403; c_4 = 0.0055 and c_5 = 12.5.

In this thesis, the equation postulated in Manzocchi et al. (1999) for the estimation of fault permeability is utilized due to proven versatility. In particular, the equation in Sperrevik et al. (2002) requires knowledge on burial history, and this information might be difficult to measure directly.

As for the fault zone thickness, compilations of fault outcrop data (e.g. Robertson 1983; Hull 1988; Foxford et al. 1998; Walsh et al. 1998) demonstrate an approximately linear relationship between fault zone displacement *D* and fault rock thickness t_f over a variety of scale-range with thickness values distributed over about two orders of magnitude for a particular displacement (Figure 1.11). Summaries of outcrop measurements show the harmonic average of these data follow the relationship:

$$t_f = D/170 \tag{1.11}$$

Equating (1.6) and (1.8) gives the transmissibility multiplier T as a function of the dimensions and permeability of the grid-blocks and the thickness and permeability of the fault:

$$T = \left[1 + t_f \frac{\left(2/k_f - 1/k_i - 1/k_j \right)}{\left(L_i/k_i + L_j/k_j \right)} \right]^{-1} \tag{1.12}$$

For the special case given by $L_i = L_j = L$ and $k_i = k_j = k_m$,

$$T = \left[1 + \frac{t_f}{L} \left(\frac{k_m - k_f}{k_f} \right) \right]^{-1} \tag{1.13}$$

which is equivalent to the transmissibility factor proposed in Walsh et al. (1998).

When $L_i \neq L_j$ or $k_i \neq k_j$, equation (1.13) can be used as a multiplier for one of the grid-blocks adjacent to the fault, therefore assigning the entire thickness of the fault-rock to this cell. This gives an identical transmissibility across the fault to applying (1.12) to the interface between the two grid-blocks, but also changes the transmissibility on the other side of the grid-block to which the permeability multiplier has been applied (Manzocchi et al., 1999). The method has been extensively proved in the North Sea reservoirs (e.g. Manzocchi et al. 1999, Harris et al. 2002). The geological based approach for the fault transmissibility calculation (Figure 1.12) provides much higher resolution than is usually required, but becoming appropriate as permeability heterogeneity increases (Figure 1.13). However, as fault zone content depends on the sedimentology modelling, any of its possible realizations requires the generation of the fault permeabilities, which in turn lead to a new set of multipliers, also depending on the grid-block permeabilities (Manzocchi et al., 1999) (Figure 1.14).

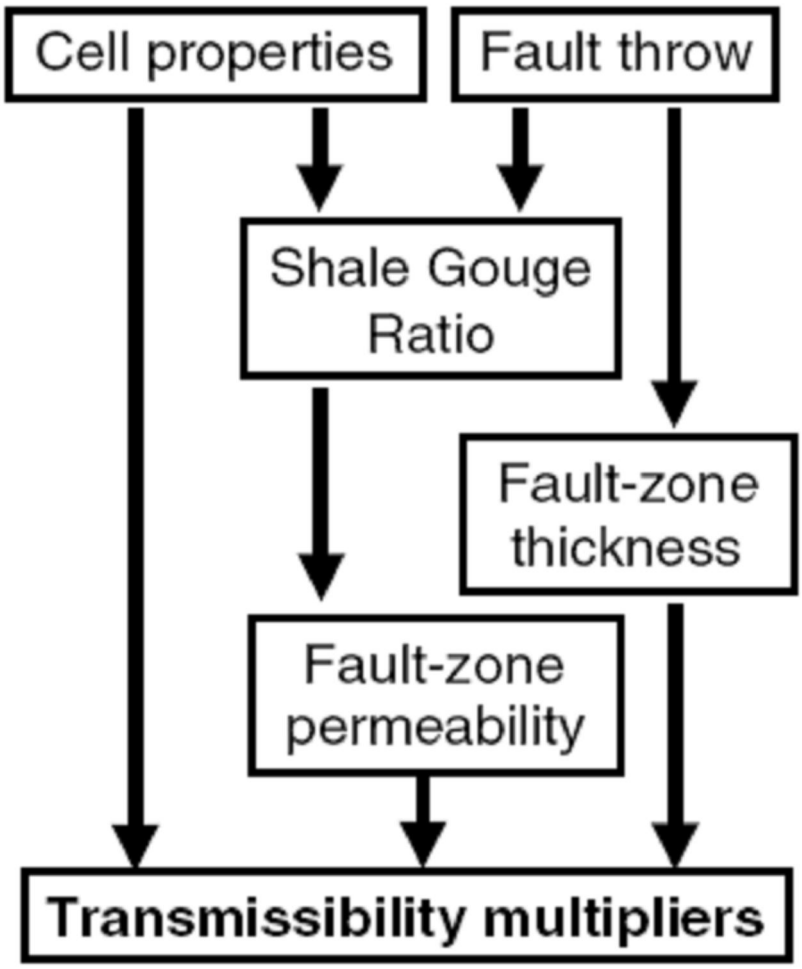

Figure 1.12. *Workflow for the calculation of the fault transmissibility multiplier for a reservoir simulation model. (After Manzocchi et al., 1999).*

Generally, the standard inter grid-block transmissibility equation underestimates fluid flow across the fault plane. This is because of the assumption that the area term in the transmissibility equation is given by the juxtaposition between the two grid-blocks, thus ignoring possible tortuous flow, which can increase the net transmissibility (Manzocchi et al., 2002). In spite of such errors, applications of the geological based method previously described have been proven useful. This has allowed incorporation of the fault properties for every grid-block fault-face considering:

- The clay content of the grid
- The grid permeability
- The grid geometry

Ultimately in this approximation, fault properties are integrated into the simulation model as transmissibility multipliers assigned to the grid. In this thesis, our objective is to evaluate these fault transmissibility multipliers using the time-lapse seismic signature.

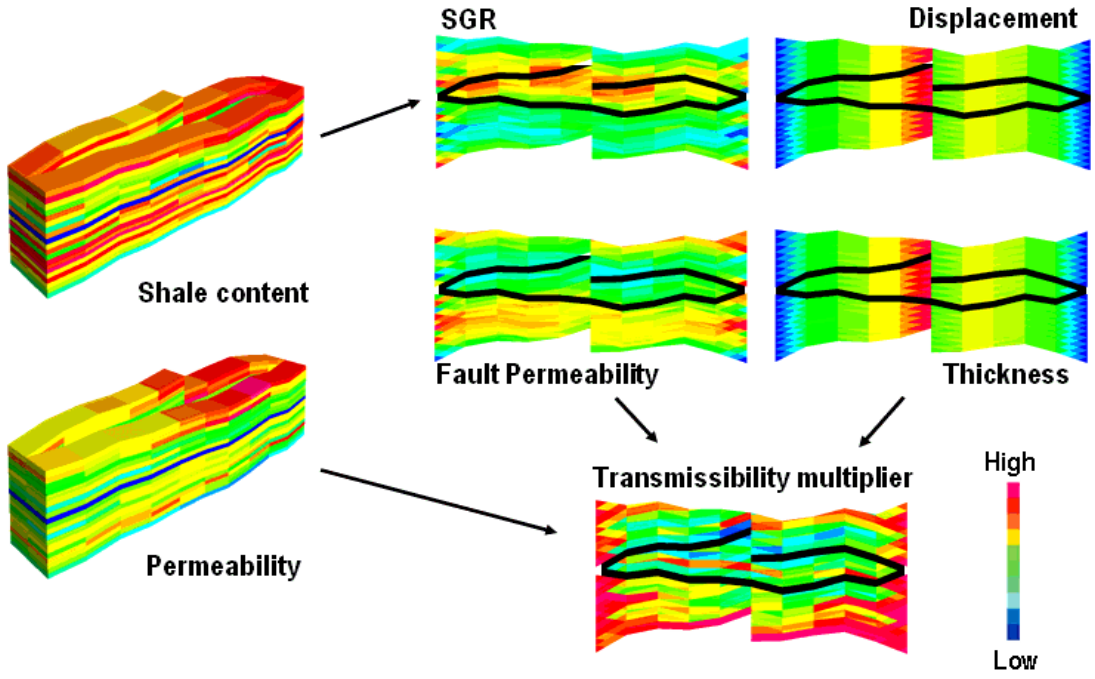

Figure 1.13. *Estimation of the fault transmissibility multiplier in a heterogeneous reservoir. At each cell–cell connection, shale gouge ratio is calculated from the local fault throw and the distribution of Vshale in the throw window. Shale gouge ratio is used to constrain upscaled fault-zone permeability. Fault-zone thickness is estimated from the local fault displacement. Each cell – cell transmissibility multiplier is then a function of the size and permeability of the juxtaposed reservoir cells and the thickness and permeability of the fault zone. (After Manzocchi et al., 2002).*

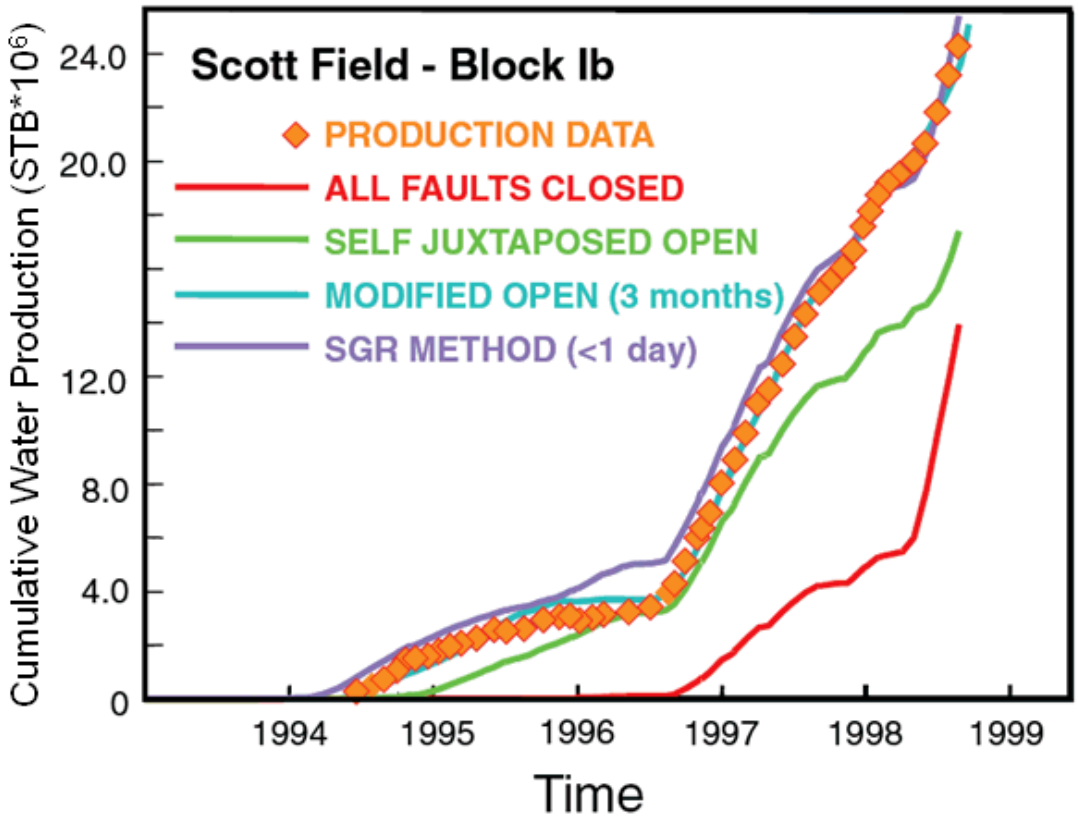

Figure 1.14. *Examples of reservoir simulation history-matches, using different fault properties, Scott Field, North Sea. Orange diamonds show observed cumulative water production for Block Ib of the field for 4 years from production start-up. The coloured lines show different models. The red line shows model production with all faults closed, i.e. no across-fault flow (Eclipse default). The green line is similar but with flow allowed at connections between the same reservoir units (self-juxtapositions). The blue line ('modified open') shows the result of history matching on a 3 months iteration process, manually adjusting transmissibilities at all the across-fault connections. The purple line ('SGR method') shows the first-pass result of calculating transmissibility multipliers using a transformation from shale gouge ratio to fault-zone permeability (method of Manzocchi et al., 1999, showed in Fig. 1.10). Courtesy of Marsden, Amerada Hess. (After Yielding, 2002).*

1.4 The state of the art in understanding reservoir faults using time-lapse seismic

In the context of the time-lapse seismic, recent progress has been addressed in the understanding of inter-compartment communication. The contribution shown in these previous works is focused in a qualitative or semi-qualitative framework which offers new insights in the evaluation of the sealing capacity of faults. Some of these examples are now discussed in this thesis:

Koster et al. (2000) put forward the use of repeated 3D seismic data in order to derive the sealing capacity of faults. Located in the Norwegian offshore, the Draugen field is shown as an example. In this case the reservoir and aquifer are in sand-to-sand juxtaposition across small fault throws that intersect the sequence at several places. To explain the possible communication paths in the field, several reservoir scenarios were constructed and the fluid-flow is then simulated. All of them matched the production data but differ in forecast profiles. To be able to design the production strategy for this field, seismic monitoring is introduced as a way to reduce uncertainty in the future production profile. Direct comparison between time-lapse seismic data and reservoir models allowed the selection of a best matching model for which sealing capacity of several faults in the reservoir was increased (Figure 1.15).

Sønneland et al. (2000) propose a methodology to detect flow barriers using saturation changes derived from the 4D seismic. Essentially, well production data in Gullfaks field is combined with the information of the fault network checking for dynamic reservoir changes across the faults. If the saturation change appears across a fault, a non-sealing fault is defined, the reservoir flow model might be updated (by manual adjustment) and the simulator re-run (Figure 1.16).

MacBeth and Al-Maskeri (2006) introduce a new technique in which transmissibility multipliers are derived from time-lapse seismic. The method is applied into a UKCS reservoir in which transmissibility values (ranging from 0 to 1) provide flow barriers intensity (Figure 1.17). The approach is based on pressure dominated 4D seismic as the pressure change helps to derive the horizontal permeabilities which in turn are used in the transmissibility estimation. However, in field cases with 4D seismic controlled by saturation changes (as in the Heidrun field), such methodology is not recommended as it

cannot deliver optimal permeability estimation (Al-Maskeri, 2005). Also, pressure changes need to be separated from the time-lapse seismic signature and this process requires further information as well as careful revision. Hence, when pressure changes are small, unavailable or in cases with limited knowledge on the lateral variation of permeabilities, it is difficult to invert for transmissibilities using this technique. Finally, the method implies all types of barriers (fault seals, fractures, lithology, and flow units) are treated equally, yet the elements defining their sealing capacity are different for each case. This might suggest a need for a sort of calibration (e.g. geological), which allows accounting for each barrier kind.

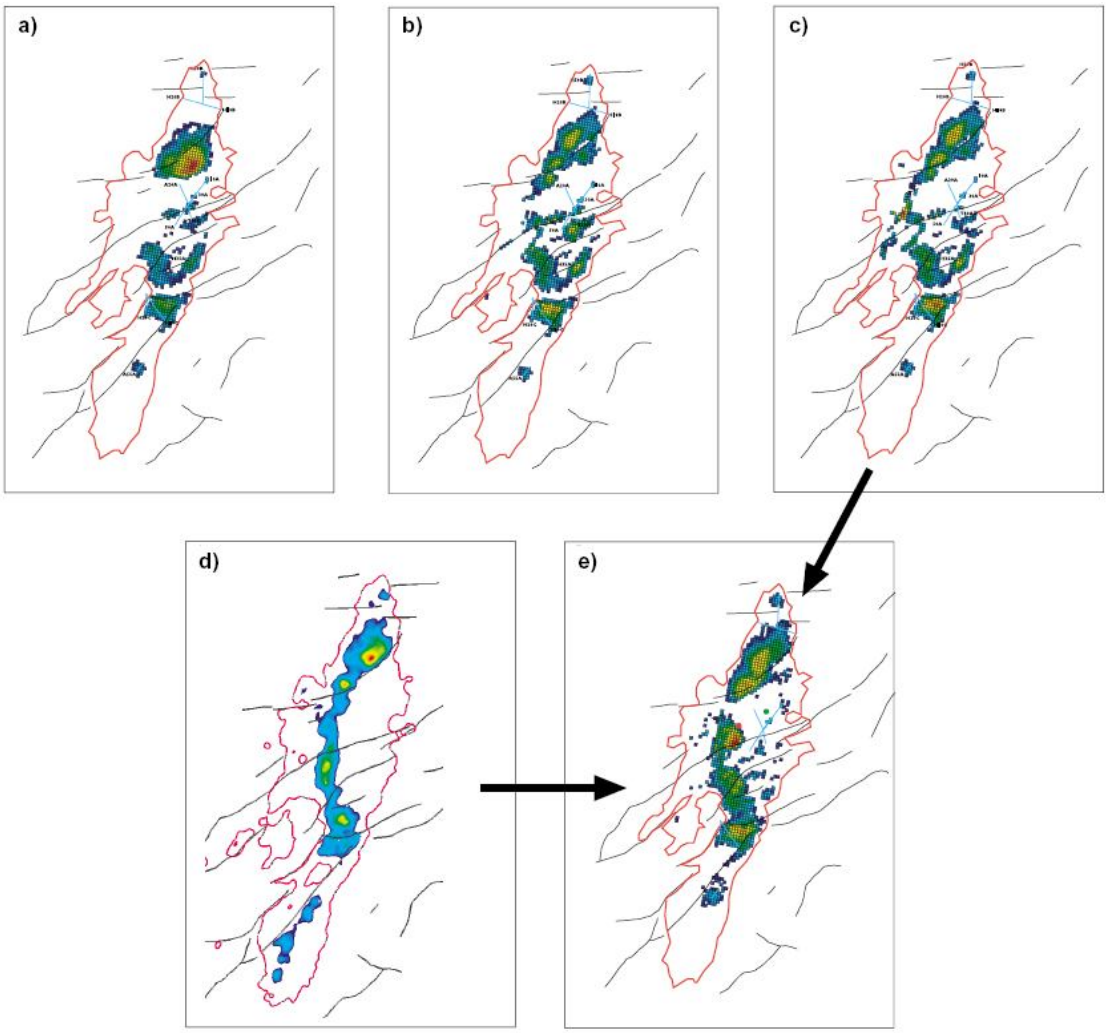

Figure 1.15. *Map over the Draugen Field of the change in equivalent hydrocarbon column as calculated by the reservoir simulator. Introducing different communication paths between the reservoir and the aquifer three models are constructed. (a) Communication in the north. (b) Communication through faults. (c) Communication in the west. This model best matches the time-lapse seismic results so it was used as a starting point for seismic matching. (d) Actual observation from time-lapse seismic. (e) Final model matched to seismic and production history. (From Koster et al., 2000).*

Kahar et al. (2006) analyse fluid flow in Heidrun field integrating 4D seismic responses, well log data and production data. Here, rock physics modelling shows that changes in fluid saturation seem to drive the 4D signatures in the Fangst Group. As water displaces either oil or gas in the reservoir, acoustic impedances are increased as hydrocarbon saturation decreases.

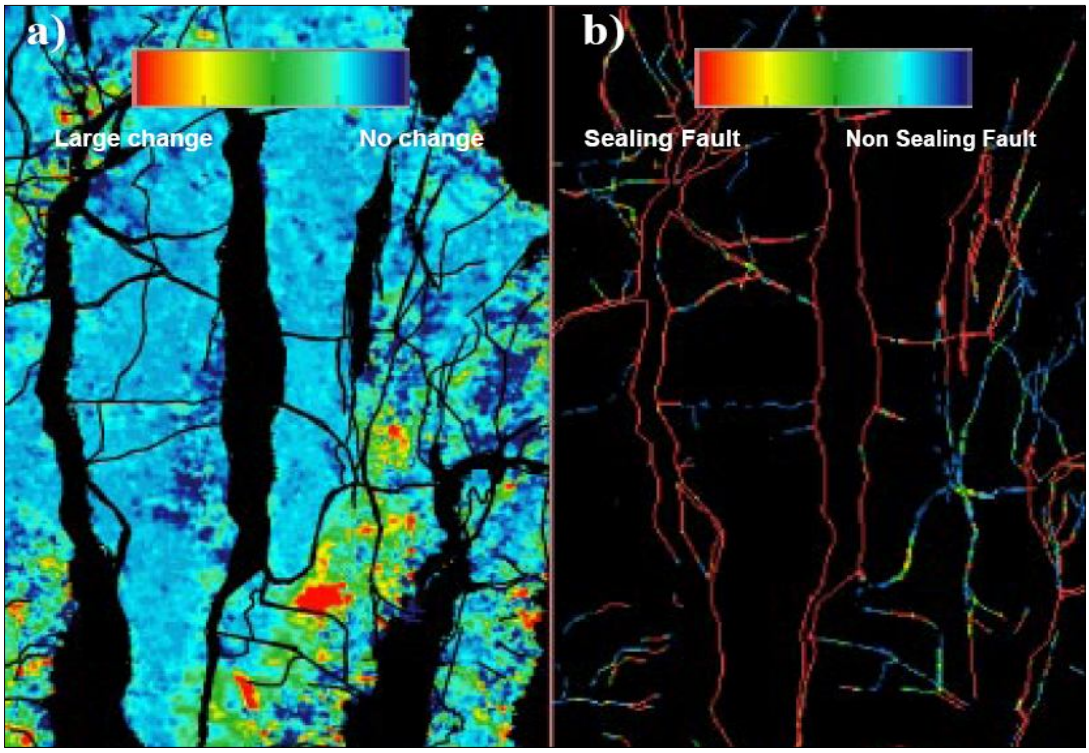

Figure 1.16. *a) Seismic saturation map where red indicates large differences in the seismic response and blue indicates no difference in the seismic response; b) shows the faults characterized after their sealing capacity. The red colour indicates sealing faults, while blue indicates non-sealing faults. After Sønneland et al. (2000).*

Based on the modelling and dataset, a fault-related phenomenon is identified as one of the main categories of fluid flow at Heidrun. This behaviour includes flow across the fault within the same and different reservoirs, fluid along fault conduits and flow near sealing faults. This observation suggests that accurate flow understanding must take into account the complex configuration of faults as barriers or conduits for fluids (Figure 1.18).

Irving et al. (2007) apply a new methodology that allows the calculation of fault properties at seismic scale using fault surfaces and inverted lithoseismic cubes. In this work, *SGR* formula is computed projecting the lithoseismic data onto fault slices and evaluating the fault throw at seismic scale. Comparison of the seismically-calculated *SGR* for a particular fault in a case example shows agreement with time-lapse seismic response resulting from the production strategy (Figure 1.19). Here, a negative 4D seismic anomaly change in the seismic impedance associated to gas injection in well B seems to be passing through the fault surface which is locally characterized by low values of the *SGR* algorithm showing consistency between the geological and the seismic tool.

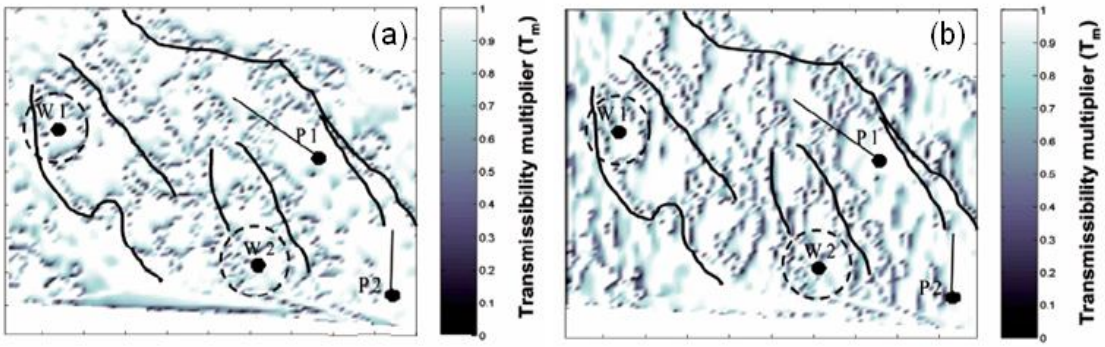

Figure 1.17. *(a) Map of barriers and degree of transmissibility from the 4D seismic signatures. Estimates are determined by moving along the Y direction. (b) Map of barriers and degree of transmissibility from the 4D seismic signatures. Estimation are determined by moving along the X-direction. Major faults picked on the 3D seismic are shown for reference. After MacBeth and Al-Maskeri (2006).*

Indeed, numerical simulations with transmissibility multipliers derived from *SGR* calculation provide a qualitative match to the 4D seismic observations (Figure 1.20). Nonetheless, the seismic data might be distorted in the vicinity of the fault planes as the seismic wave travels and get diffracted in the structural discontinuities. As a consequence, the projection of lithoseismic cubes against fault planes should be treated carefully.

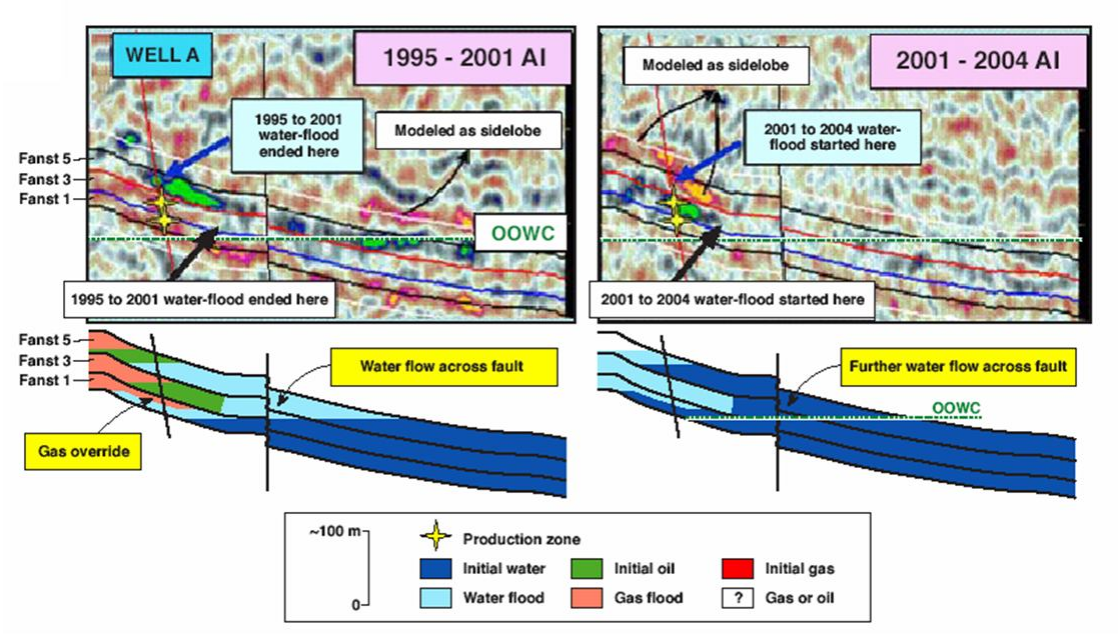

Figure 1.18. *Examples of flow across faulting and gas override. Inverted P-wave impedance differences 1995-2001 (left) and 2001-2004 (right) and associated interpretations are showed. After Kahar et al. (2006).*

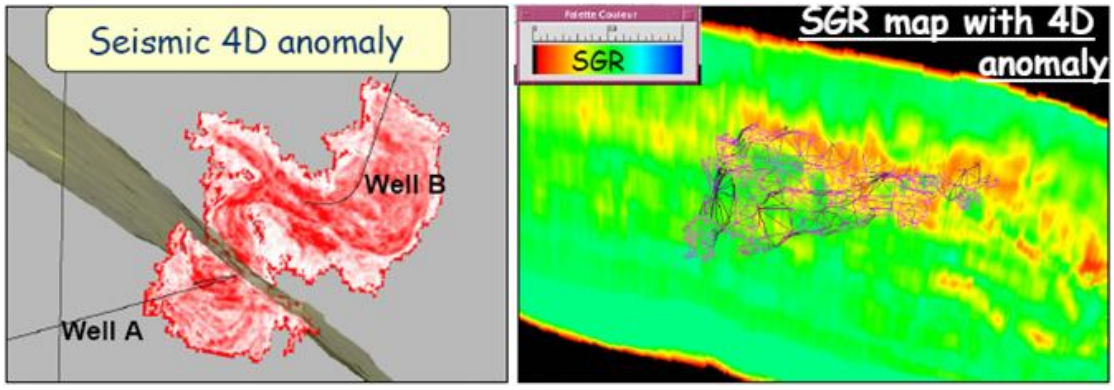

Figure 1.19. *4D seismic anomaly (-ve Δ impedance) due to gas injection in well B (Breton et al., 2005). (After Irving et al., 2007)*

Even though a great effort has been conducted to assess the fault sealing phenomena through time-lapse seismic data, most of the approaches integrate the observations from different disciplines in a qualitative or semi-qualitative stage. These analyses are generally based in a comparison of the 4D seismic response with production changes (e.g. in pressure and saturation), therefore showing the need for improvements in the quantitative aspects of the evaluations.

1.5 Motivation and challenges of this work

Table 1.1 summarizes main geologically driven methodologies that have been employed to assess the sealing capacity of faults. Most of them rely on the existence of particular data (e.g. thickness, shale/clay volume) concerning the shale-rich sections affected by faults. As a consequence, characterization of these parameters is achieved by incorporating well data into the fault property evaluation. This practice introduces uncertainties in the estimation which are related to the sparse nature of the information. Furthermore, uncertainties are included at each stage of the fault behaviour analysis. Yielding (2002) has separated them in two main groups: related to the mapping scale and to rock and fluid properties (Table 1.2). Incorrectly mapped horizon and/or fault geometries can lead to inappropriate reservoir juxtaposition. However careful mapping might be damaged during the structural modelling and the upscaling process needed for the construction of the static model. Structural uncertainty can be addressed with the generation of several models (including several algorithms) but this is a very tedious and costly exercise. Additionally, sub-seismic features are not correctly represented in those models, particularly in the presence of complex structures. In terms of the rock and fluid properties, well log data propagation is commonly employed to estimate the clay/shale portion affected by the fault surfaces. However, the location, completeness and quality of the information affect the integrity of the fault-seal analysis. Consequently, further improvement on the estimation of the fault sealing capacity is needed to boost reservoir management and hence ultimate hydrocarbon recovery. As shown previously, recent works introduce the use of time-lapse seismic in order to facilitate the evaluation of the fault sealing capacity. However until present, little improvements have been made in terms of the quantitative assessment of compartmentalized reservoirs via 4D seismic.

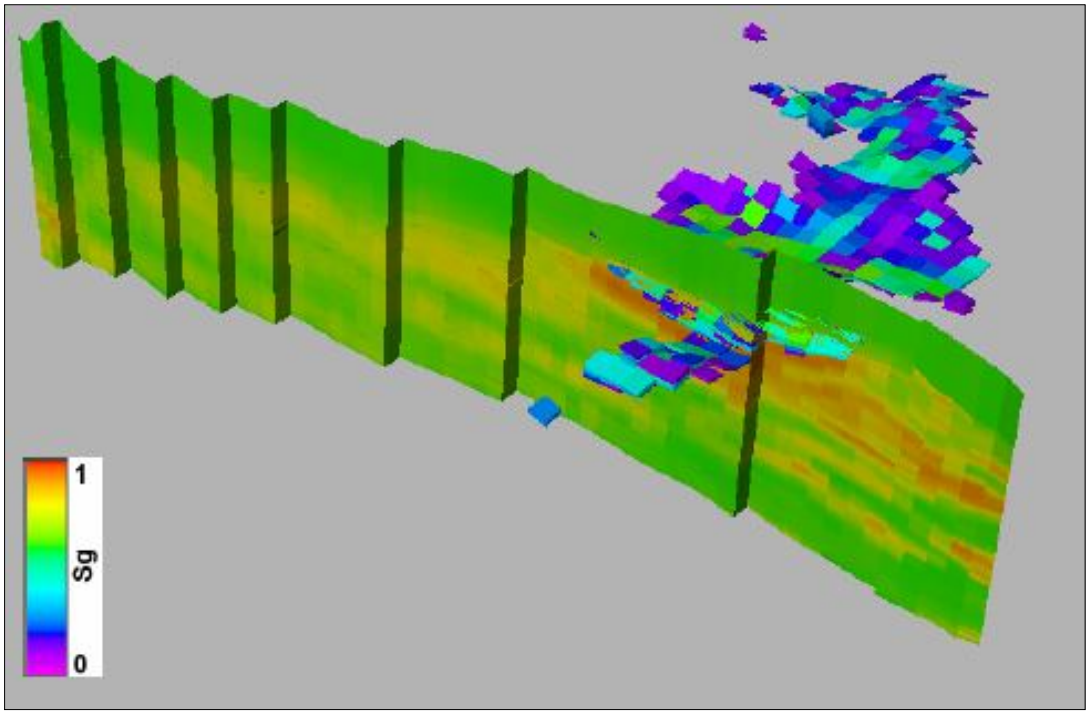

Figure 1.20. *Numerical simulations for gas saturation with transmissibility multipliers for observed fault plane provide a qualitative match to the 4D seismic observations. Low sealing capacity in the fault plane is indicated with red colour. (After Irving et al. 2007).*

Paper (Author, year)	Method	Advantages	Disadvantages
Bouvier et al. (1989) and Fulljames et al. (1996)	Clay Smear Potential (*CSP*)	• Calibrated against sealing/non sealing faults. • Successful in a field case. • Used to constraint reservoir simulations.	• Only measures continuity of clays. • Requires definition of individual shale beds. • Difficult to implement in thick heterogeneous reservoirs. • Threshold value for sealing not clear.
Lindsay et al. (1993)	Shale Smear Factor (*SSF*)	• Magnitudes classified in fault studies. • Represented by a constant value. • Easy to implement.	• Requires definition of individual shale beds. • Difficult to implement in thick heterogeneous reservoirs.
Yielding et al. (1999)	Shale Gouge Ratio (*SGR*)	• Successful in outcrop/field data. • Individual shale definition is not required. • The threshold value for sealing proven robust in many clastic/mixed sequences. • Linked to the petrophysics of the fault-rock. • Used to estimate fault permeability. • Used to calculate fault transmissibility multipliers for reservoir simulations. • Provides a very quick and geologically based route to a high-quality history match.	• Sparse nature of the clay fraction in sub-surface data.

Table 1.1. *Summary of publications related to the quantification of the sealing capacity of faults using lithological algorithms.*

Studies of fault properties utilizing the 4D product are required. As a consequence, this is the reason for the subject of this current work.

Group	Uncertainties
Mapping Scale	**Fault geometry** • Fault architecture (grid/size orientation) • Structural/Property modelling algorithm • Fault displacement **Horizon mapping** • Juxtaposition **Sub-seismic features** • Sub-seismic faults • Folds
Rock and Fluid	**Wells** • Number • Location • Logs • Fluid type

Table 1.2. *Classification of the uncertainties included in the analysis of the fault sealing capacity according to Yielding (2002).*

In view of the previous statements, the main challenge of this thesis is expressed in the development of a new technique that can be used to extract information related to the fault sealing capacity from the 4D seismic. The proposed approach aims to integrate the time-lapse seismic data with geological measurements to generate an intermediate product (i.e. fault permeability) that can be used in reservoir engineering studies.

By taking advantage of the coverage offered by 4D seismic data, the workflows described in this thesis are suggested as a way to overcome constraints in the fault seal

evaluation, which are mainly associated with the sparse nature of the data needed for the application of current methodologies (e.g. cores, well logs). Here, statistics of the time-lapse seismic are used in an effort to more fully resolve the spatial distribution of fault properties, particularly the fault permeability. By calibrating the 4D seismic measurements to the geology based estimates of the fault permeability, the methodology attempts the quantitative integration of the geophysical and geological techniques which in turn is targeted to improve the reservoir management decisions. Once fault permeability has been obtained using the time-lapse seismic signal, uncertainties are quantified. This information can be then implemented in fluid flow simulations (particularly in the estimation of the fault transmissibility multipliers) with the objective of decreasing the mismatch between the predictions and the observed production history. Finally, this thesis emphasises the implications of the dynamic fault behaviour of the fault properties in the 4D seismic response. This would bring valuable information in the understanding the complex behaviour of the flow in structurally compartmentalized reservoirs, particularly when changes in the trapping capacity are evaluated in the presence of two fluid phases.

1.6 Thesis outline

This thesis is divided into the following six chapters:

Chapter 2 presents a discussion over the Heidrun field. The geological setting is described as well as the production strategy associated with the Jurassic reservoirs included in the Fangst Group. Results from previous time-lapse seismic studies are shown.

Chapter 3 builds on the understanding of the 4D seismic character of this field by making use of the available dataset. Here, the spatial character of the time-lapse seismic signature is assessed. This helps to understand the implications that faults can have on the compartmentalization of the dynamic changes.

Chapter 4 describes a new methodology to estimate fault permeability from 4D seismic. Fault permeability introduces disruption to the pressure and saturation fields, which in turn control the time-lapse seismic signature within each compartment. To

sense these changes inter-compartment amplitude contrast and statistics of spatial variability are derived from 4D attribute maps. These 4D measures are then calibrated at the wells to the geology based estimates of fault permeability. Subsequently a quadratic polynomial is used as the best fit function for the fault permeability representation. Finally, to account for the uncertainty in the prediction using 4D seismic, Bayes rule is applied in order to obtain the posterior probability for the fault permeability at each location. The method is tested on a synthetic dataset showing encouraging results.

Chapter 5 shows the application of the developed technique to a Jurassic reservoir in the Heidrun field, located in the Norwegian offshore. The high degree of compartmentalization strongly impacts the way in which its individual compartments are being depleted. Due to well density, fault properties in the southern part of Heidrun field are not easily assessed by means of a geologically based algorithm. Here, 4D signature is employed to derive the fault permeability providing an improvement in the fault property estimation.

Chapter 6 provides the description of the reservoir model updating. Given the fault permeability calculated from the 4D seismic, fault multipliers are now introduced into the Heidrun simulation model to update the transmissibilities for the studied fault segments. A comparison of predictions for the well production data obtained from the original and the updated simulation model indicate some improvements when the 4D-derived fault multipliers are introduced. Also an automatic history match procedure is implemented which incorporates the 4D estimates as well as an uncertainty window defined by the errors in the 4D prediction.

Chapter 7 investigates the phase-dependent compartmentalization given by faults when considering a production scenario. Here, the study of the dynamic fault sealing potential is addressed using several 4D seismic surveys. Theoretical background on the two phase fault properties is explored. Tests are performed on synthetic examples allowing comparison with the 4D seismic signatures observed in the Heidrun field. Final insights on the dynamic inter-compartment connectivity are provided.

Chapter 8 shows the conclusions of this work. Additional recommendations are proposed for further development.

1.7 Contribution of this work

Fault transmissibilities inserted into the simulation model to represent the behaviour of faults are based on geological understanding and are uncertain because of the sparse nature of well data used in their estimation. Here, 4D seismic data is used in an effort to more fully resolve the spatial distribution of the fault properties. In a new effort to constrain reservoir flow, this thesis introduces a new workflow in which 4D seismic is employed as a tool to quantify the inter-compartment communication and hence enhance the fault property assessment. To achieve this task, inter-compartment amplitude contrast and statistics of spatial variability for the 4D signatures are considered. These 4D measures are then calibrated at the wells to the geology based estimates of fault permeability. Cross-plots of the above 4D-derived parameters against the fault permeability given by geological techniques such as the shale gouge ratio approach, reveal that for a well-controlled sector it is possible to directly invert for fault permeability. A quadratic polynomial can be used as the best fit function for the fault permeability representation, which for practical field cases must be calibrated with known (geologically based) fault properties. In addition, to account for the uncertainty in the prediction using 4D seismic, Bayes rule is applied in order to obtain the posterior probability for the fault permeability at each location. Application of this methodology to the Heidrun field produces encouraging results, and suggests that this can be used as a tool for deriving dynamic fault seal properties. Here the assessment of a geologically consistent 4D fault transmissibility can lead to improvements in fault characterization, constraining the fault behaviour in full field flow simulation models. This helps to enhance the matching between historical production data and simulated forecasts.

Also, implications of the dynamic fault behaviour in the 4D seismic response are discussed. In this case, the trapping capacity of the fault is evaluated in the presence of two fluid phases. In this study it is recognized that variations in the relation between the capillary pressure of the reservoir and the capillary threshold pressure of the fault-rock can introduce anomalies in the waterflooding pattern. Tests performed in synthetic models indicate that a phase–dependent behaviour of the fault might be detected by measuring the variance of the 4D seismic signature, yet similar results can be obtained if other scenarios are considered (e.g. strong changes in the fault transmissibility). As a consequence, if used as an interpretation tool, this 4D seismic statistic should be combined with additional information about the reservoir and faults. Application to the

Heidrun field suggests understanding of the two phase fault properties might help to explain unexpected watering pattern observed in particular compartments. Indeed, consideration of a phase-dependent behaviour in faults, can be also useful in the interpretation of the 4D seismic signature in compartmentalized reservoir settings.

Chapter 2

The Time-Lapse Seismic Signature of the Fangst Group, Heidrun Field

This chapter provides an overview of the Heidrun field. It describes the geological setting and the drainage strategy that has been employed since production began within the Fangst Group reservoirs. Contributions on the previous time-lapse seismic studies carried out in the field are shown. Here, 4D seismic is emphasized as a tool that has allowed the understanding of the dynamic changes occurring as a result of the field activities.

2.1 Introduction

Located in the offshore Norwegian shelf, the sandstone strata which make up the Heidrun field represents a major hydrocarbon accumulation containing both oil and gas. Tectonic history in the area has strongly affected rock beds in this field. In particular, faults are compartmentalizing the several reservoirs, shaping not only their spatial configuration but also the drainage pattern during production development. As a consequence, key challenges in the asset management strategy involve the understanding of the fault seal behaviour leading to the inter-compartment communication. Based on the connectivity analysis between compartments, the infill drilling strategy is designed utterly defining the field recoverable reserves. In order to locate remaining oil resources as well as monitoring reservoir performance, repeated seismic surveys have been undertaken in the area. This ongoing surveillance technique contributes with the management plan by allowing the understanding of the reservoir given the underlying dynamic changes (e.g. saturation, pressure) represented by the 4D seismic anomalies.

2.2 The Heidrun Field

2.2.1 General description

Heidrun field is one of the largest oil discoveries in the offshore Mid Norway area known as Haltenbanken (Figure 2.1 and Figure 2.2). Discovered by Conoco and partners in 1985 (Koenig, 1986) under 350 m of water, Heidrun field contains an estimated of 186 million Sm^3 of oil and 41.6 billion Sm^3 of gas at depths ranging from 2175 m to 2475 m below sea level. Production started in 1995, and included in the drainage strategy is pressure maintenance by up-flank gas and down-flank water injection together with gas cap expansion (Figure 2.3). Initial drainage strategy assumed recovery over 60% of the oil in place in the main reservoirs (Dargsten, 1994), however further understanding indicates that even in these relatively homogeneous reservoirs extensive infill drilling is required to improve production. Although additional production wells have been drilled achieving a present daily production of 25000 Sm^3 oil/day and 6.2 M Sm^3 gas/day, uncertainty related with fluid movement introduces a risk of a negative economic outcome. To avoid undesirable results, infill well planning integrates all available data, and in this case, time-lapse seismic seems to be the

appropriate tool to efficiently allow the integration of such information, hence several vintages have been acquired over the southern part of the field (Furre et al., 2006).

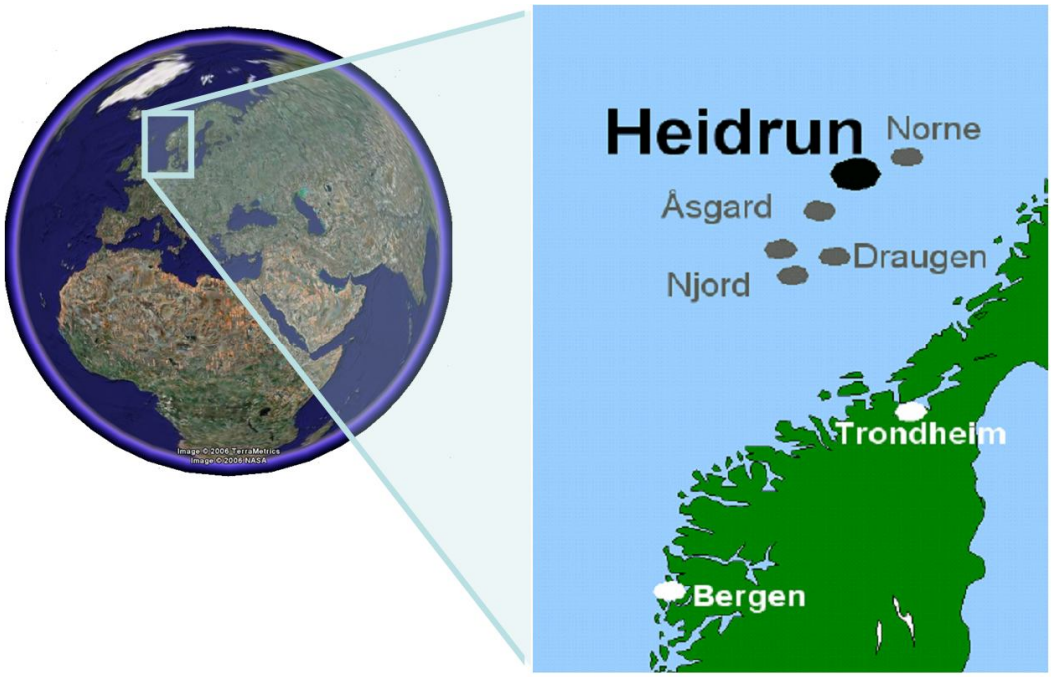

Figure 2.1. *Location of the Heidrun Field.*

2.2.2 Geological aspects

The hydrocarbon accumulation at Heidrun is trapped in a triangular shaped south dipping horst block. This structural setting has been linked to the accommodation of underlying Triassic salt during an intense extensional regime present at Mid-Late Jurassic times (Figure 2.4). The kinematic evolution of the region has led to the formation of a northeast – southwest trending fault zone with secondary fault planes observed in the east-west direction (Figures 2.5 and 2.6). Throws are in the range of 30 m reaching values up to 80 m, nonetheless, seismic resolution allows the detection of faults with throws down to 10 m (Reid et al., 1996).

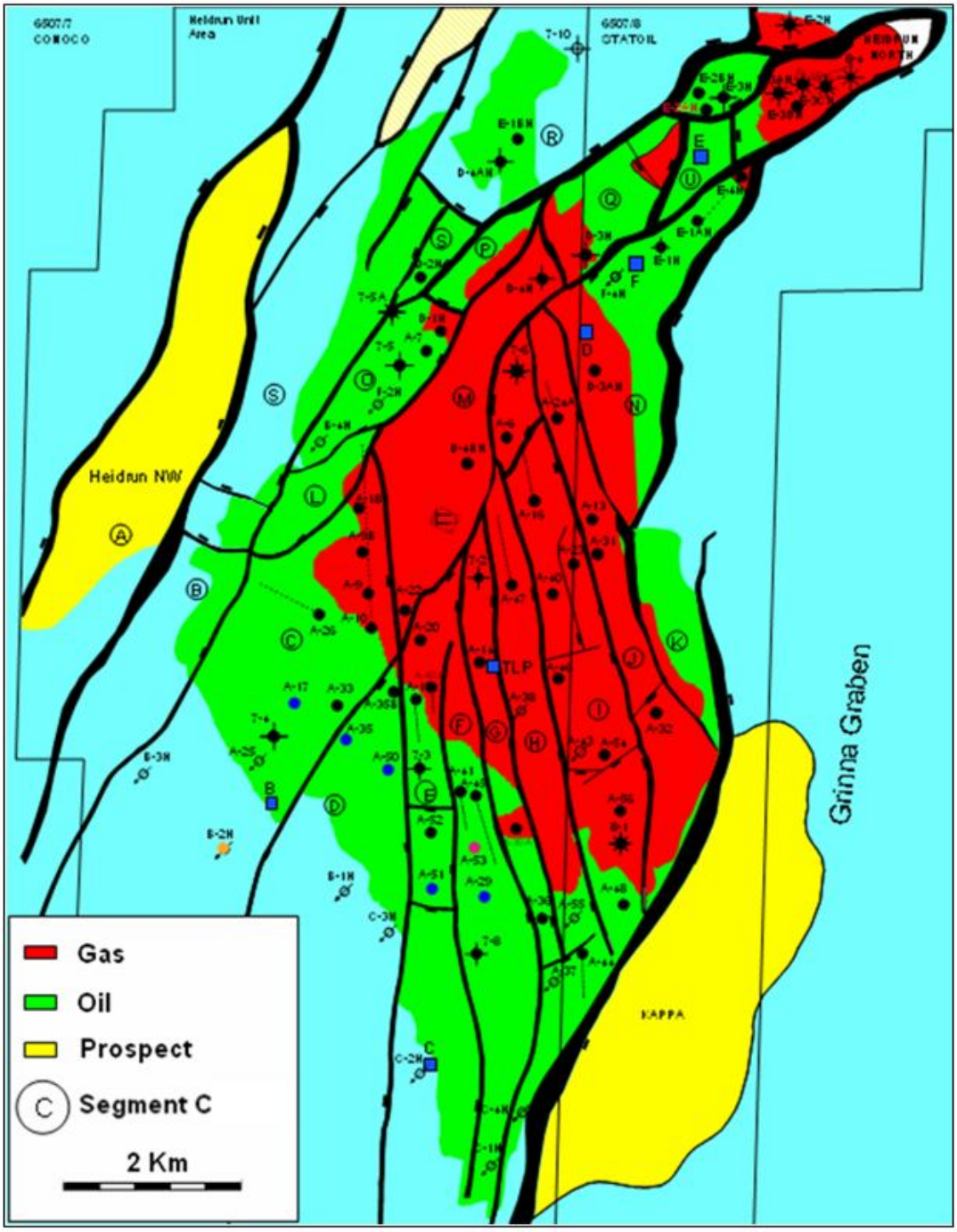

Figure 2.2. *Fluid distribution map for the Heidrun Field (modified from Statoil internal report).*

Field
Discovered 1985
Average Area 50 km^2
First production 1995
33 active oil producers (2005)
10 Water and 1 Gas injector (2005)

Rock
Porosity up to 35%
Permeability up to 5000 mD
k_v/k_h ~ 0.9 (average)
Caprock: Melke Shale (Viking Gp.)

Reservoir
Top reservoir 2300 m below sea level
Swc = 0.1 (average)
Sor = 0.12 (average)
Original GOR = 620 SCF/STB

Production
Discovery well flow rate 14,777 BOPD and 0.87 MMCMGPD
Hydrocarbon column (Fangst Gp.); gas 200 m; oil 190 m
Pressure @ 1995 = 250 bar (average)
Pressure @ 2001 = 243 bar (average)

Geology
Basin Name Halten Terrace
Shallow water reservoir
(Shoreface environment)
Unconsolidated fine to coarse grained sandstones
Middle Jurassic, Fangst Gp. sands
Fault and dip closed
Reservoir dip -5º
Other reservoirs: Lower Jurassic Tilje Fm.
Upper Triassic/Lower Jurassic Åre Fm.
N/G ratio ~ 0.9

Fluid
28º API
Temperature 85ºC
Viscosity 0.8 cp

Seismic
20 Hz peak frequency
Surveys 1986, 2001, 2004
Angle range 6º - 30º
350 m water depth

4D Changes
Oil sand → Water sand; ΔP = 0; ΔIp = 10%
Oil sand → Gas sand; ΔP = 0; ΔIp = -9 %

Table 2.1. *General Characteristics of the Heidrun Field.*

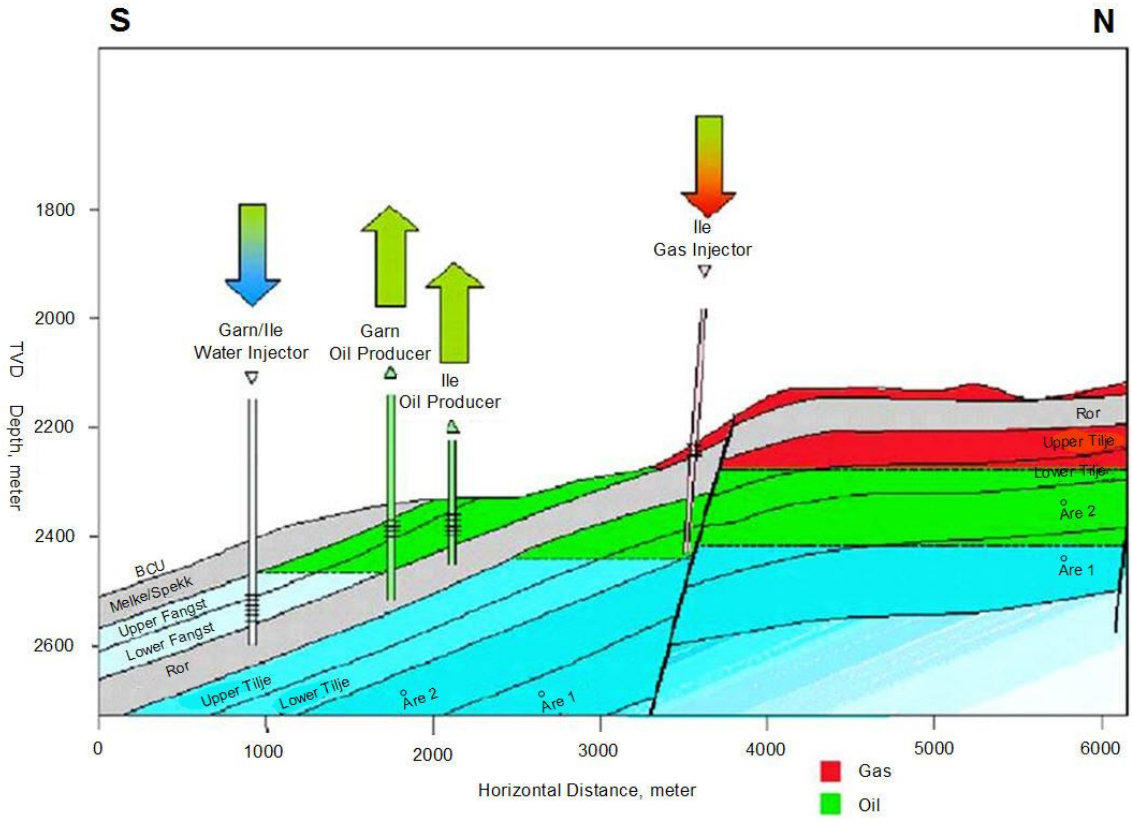

Figure 2.3. *North – South cross-section showing drainage strategy (after Hanssen et al. 2004).*

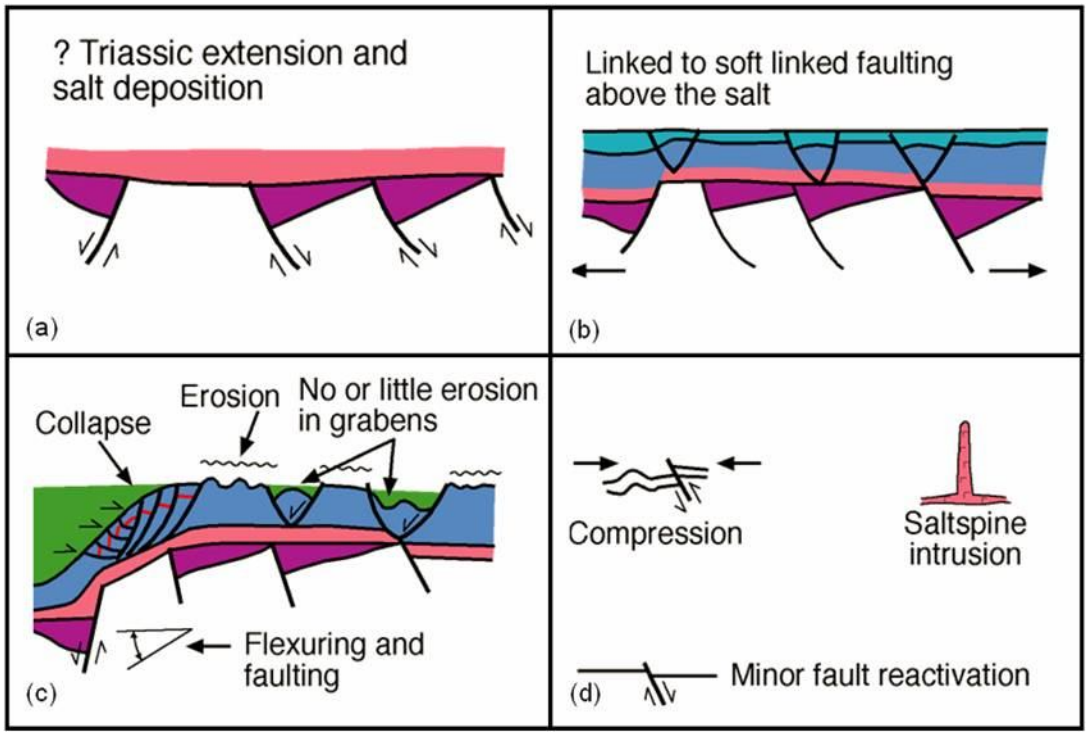

Figure 2.4. *Schematic evolution of the structural styles observed at the Heidrun field. (a) Rifting and posterior salt deposition during Triassic times. (b) Middle Jurassic extension during which the Horst and Graben system is developed within the cover as part of salt accommodation. (c) Early Cretaceous faulting due to basement rifting causing erosion on top of the horst blocks by Late Cretaceous sands. (d) Paleocene fault reactivation and Miocene compression with salt piercing (modified from Statoil internal report).*

From the stratigraphic point of view, the Jurassic reservoir section comprises a transgressive sequence ranging from continental to open marine deposits. A posterior uplifting during the Late Cretaceous rifting facilitates the erosion on horst blocks by Cretaceous sands deposited on top of the Jurassic reservoirs. Although these sand bodies are particularly difficult to map (low P-impedance in between Jurassic and Cretaceous sands), they trigger the presence of flow-related breaches across segments. The reserves are contained mostly in two clastic sequences: the Middle Jurassic Fangst Group (object of our study) and the Lower Jurassic Tilje and Åre Formations (included within the Båt Group) (Harris, 1989) (Figures 2.7 and 2.8). Fangst sandstones are largely unaffected by diagenesis and its permeability seems to be controlled by depositional factors such as grain size and detrital clay content. The permeability and porosity are extremely high; they commonly exceed 500 mD and 30 % respectively (Figure 2.9). These observations indicate favourable reservoir characteristics for the Fangst Group, particularly for Garn and Ile Formations; hence the main production is derived from those units.

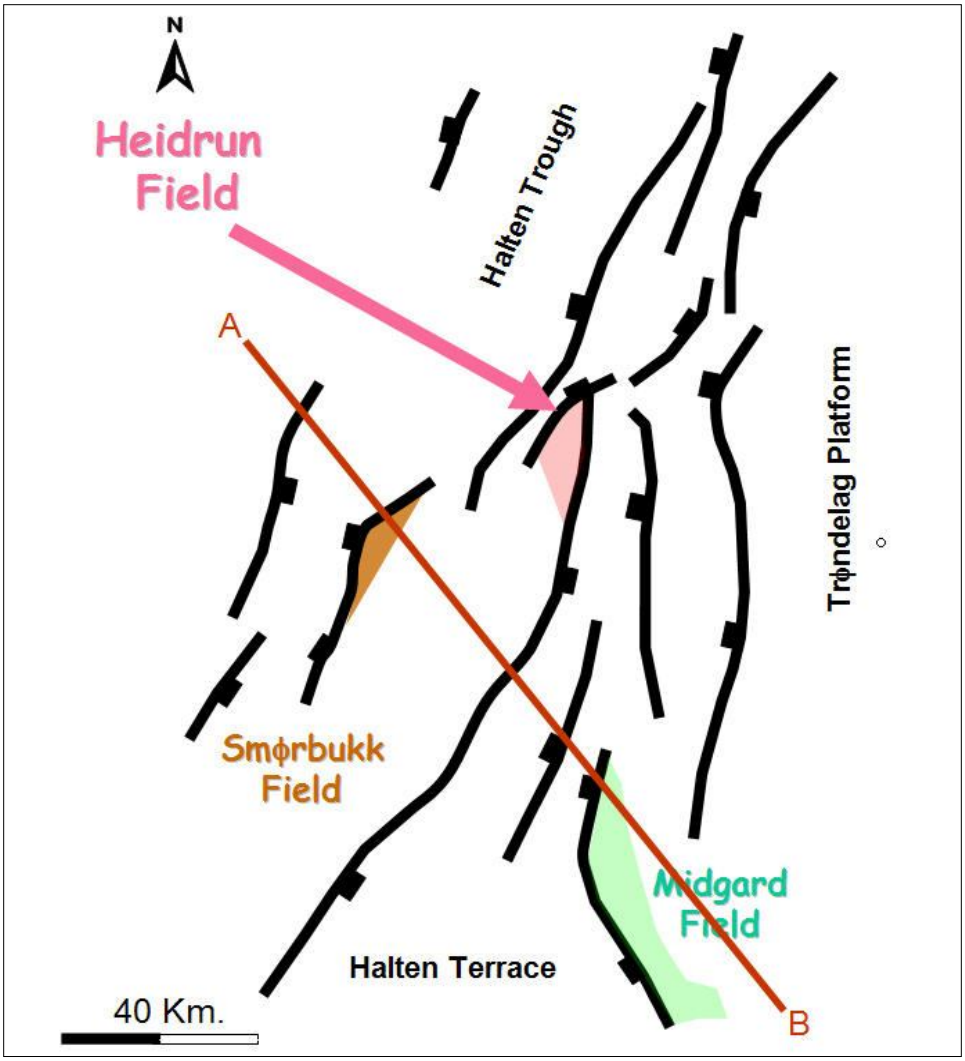

Figure 2.5. *Regional structural setting in the vicinity of Heidrun field (modified from Harris, 1989).*

The field is heavily faulted and it is being produced by draining its separate compartments (Furre et al., 2006) (Figure 2.10). The primary drainage strategy included a set of producers located in the thickest part of the oil column; meanwhile its pressure is being maintained constant. To do so, water injectors are placed in the southern flank of the field as well as gas injectors located in the gas cap at the top of the structure. As the waterfront moves toward the producers, new infill wells are drilled to produce the up-flank part of the reservoir and by-passed oil areas (Figure 2.11). However, to accomplish the difficult task of positioning of new producers and injector wells in those regions for recovery improvement, the drainage pattern should be understood. In particular, the permeability reduction along the fault planes influences the way in which major compartments are being depleted. As a consequence, the success in the reservoir

management is strongly linked to the understanding of the fault impact as a flow barrier to the fluid**.**

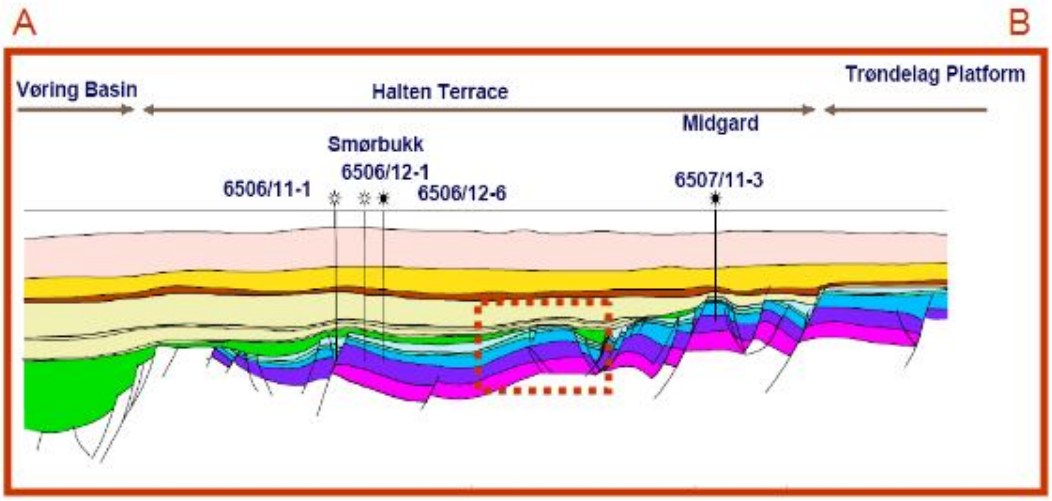

Figure 2.6. *Northwest – Southeast cross-section showing main structural styles. The profile is displayed in the figure 2.5 (red segment). The Heidrun field is located in the dashed rectangle (modified from Statoil internal report).*

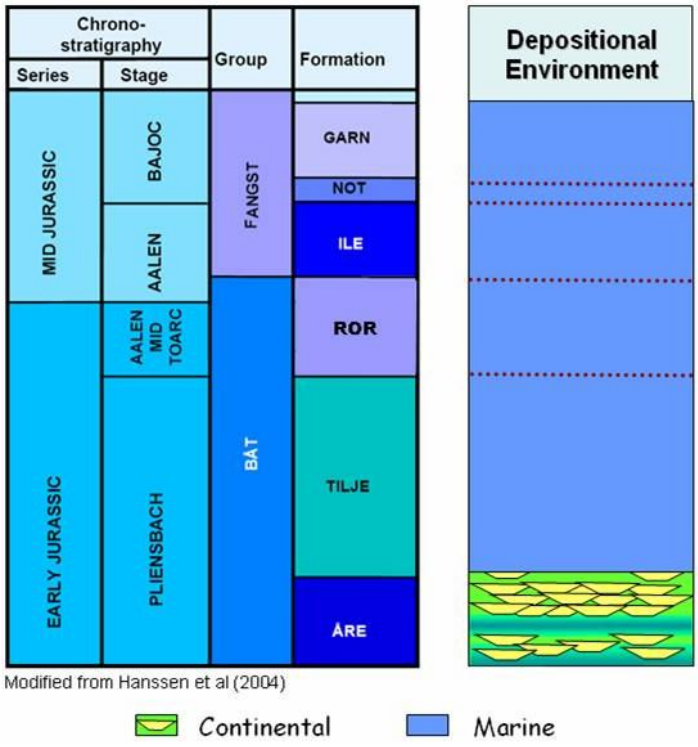

Figure 2.7. *Chronostratigraphic column for the Heidrun field (modified from Hanssen et al., 2004).*

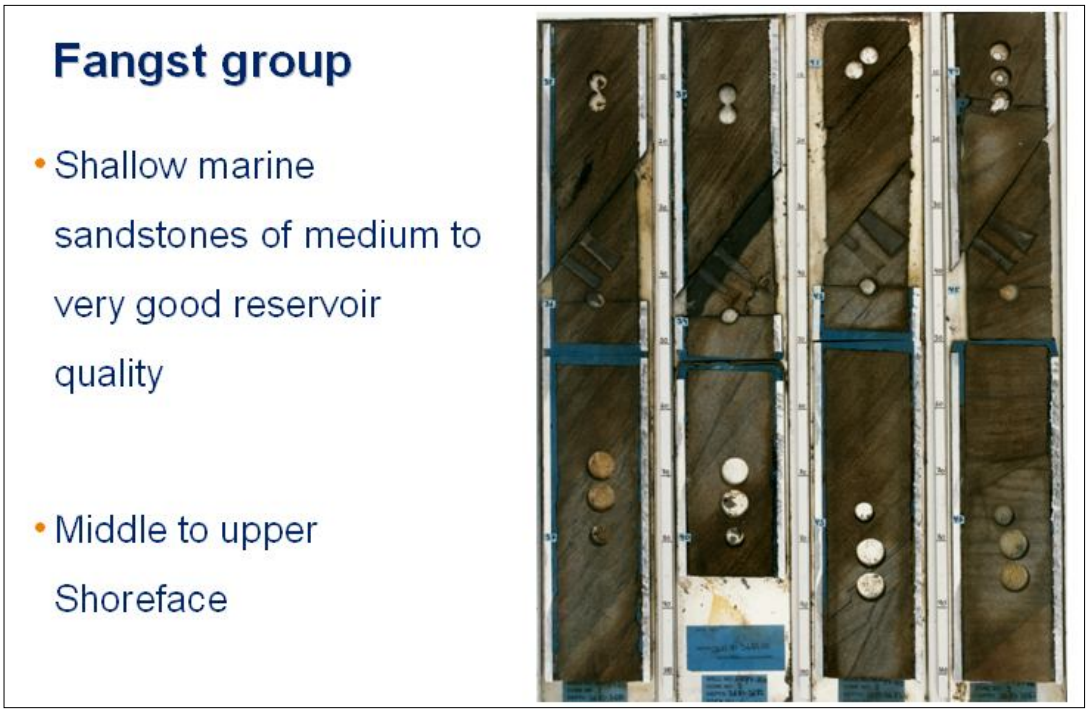

Figure 2.8. *Core view for the Fangst Group. The depositional environment is associated with the Middle to Upper Shoreface (from Statoil internal report).*

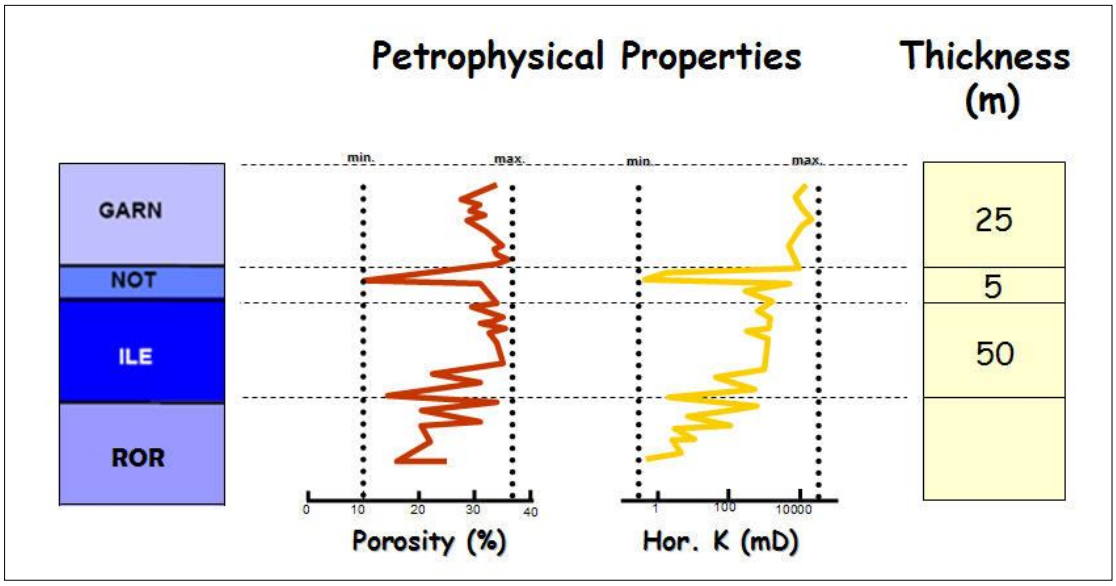

Figure 2.9. *Petrophysical properties for the Fangst Group. Porosity and Horizontal Permeability logs are displayed as red and yellow respectively (modified from Hanssen et al., 2004).*

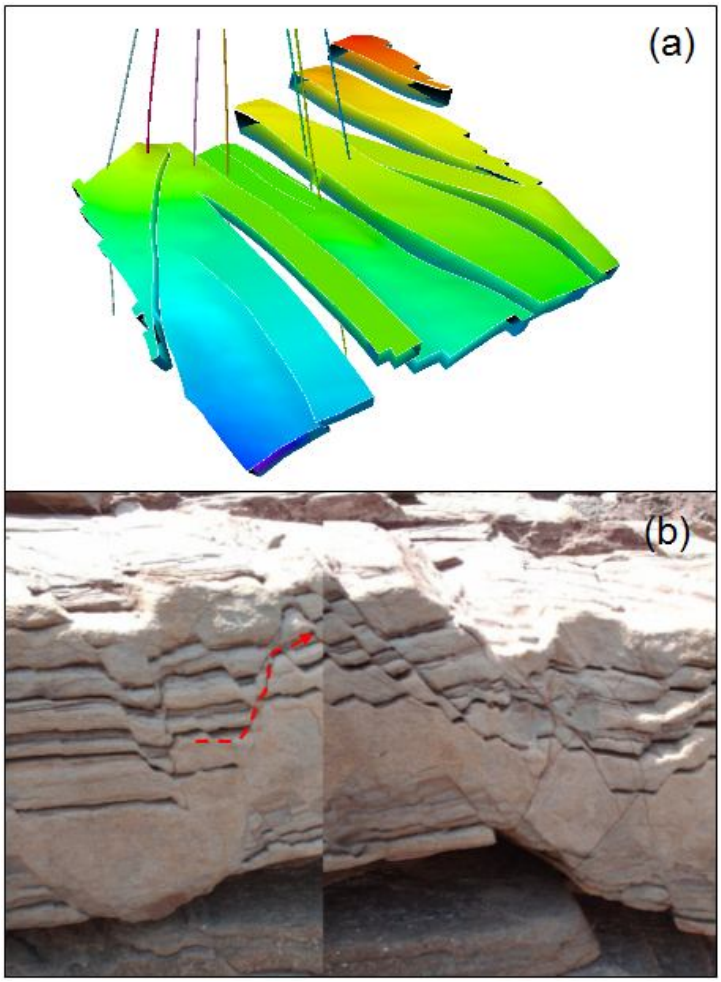

Figure 2.10. *(a) 3D sketch of the Heidrun field and its different production compartments. (b) Analogue reservoir model showing faults altering connectivity (modified from Baquero et al., 2009).*

2.3 Previous time-lapse seismic studies in the Fangst Group, Heidrun Field

2.3.1 Acquisition and data quality

In order to target marginal reserves, time-lapse (4D) seismic monitoring projects have been carried out in the southern flank of the field. The first repeated seismic survey was acquired in August-September 2001 using Q – marine technology. This method allows cable steering up to 3º against natural feather. It also permits to the acquisition boat to go as near as 100 m to the production platform enhancing the 3D migration in the zone of interest (Eiken et al. 2003).

The main target for the time-lapse study was the south-flank Fangst reservoir, which had been proved promising for time-lapse seismic in a feasibility study (Brevik, 1997) and in a time-lapse pilot study (Jørstad *et.al.*, 2000). The high porosity measured at Fangst Group, as well as its production activity (since 1995); seem to be the major factors contributing to the observed changes in the seismic response. The base 3D survey was acquired in 1986 through a towed streamer that included a single gun and two cable configuration. Nowadays, it is considered an "old" survey in terms of its repeatability, as the positional errors were rather large. Repeatability between the baseline and the first monitor (measured by means of the normalized root-mean-square or *NRMS*) was approximately 31 % and the observed time-lapse signal was relatively good for the Garn reservoir. To improve the repeatability levels between both vintages simultaneous re-processing was performed with an objective during the processing of multiple removal. In this process lateral positioning errors were revealed (~ 50 m) and tow-depth shifts in the 1986 survey were necessary to balance in order to enhance the match.

Following the first monitoring survey acquired in September 2001 and to better understand the role of the drainage strategy on the field recovery a new repeated survey was acquired on June 2004. The main purpose of this survey was to identify the present fluid distribution in the Fangst and deeper Upper Tilje reservoirs at the south flank. As in the 2001 survey, this second time-lapse survey was acquired over the south flank of the Heidrun field (Figure 2.12). The new 2004 survey is also acquired with Q – marine technology from a towed streamer with an identical single source and six cable configuration. Subsequent processing between 2001 and 2004 surveys resulted in *NRMS* values of 21% while differences of 34% were present between the 1986 and the 2004 survey. Analysis of the time-lapse seismic data revealed fluid movement information and the character of the seismic attributes is consistent with the initial fluid contacts and main faults (Hanssen et al., 2004) (Figure 2.13).

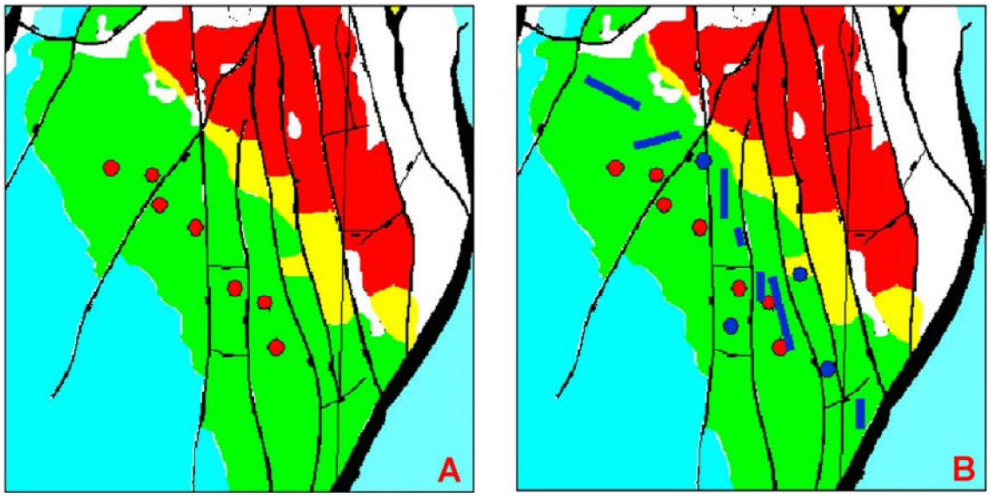

Figure 2.11. *Left hand side: Primary development (red) and infill (blue) well targets for the Garn and Ile Formations (from Hanssen et al., 2004). Areas highlighted in green, red and yellow are associated to oil, gas and transition zones.*

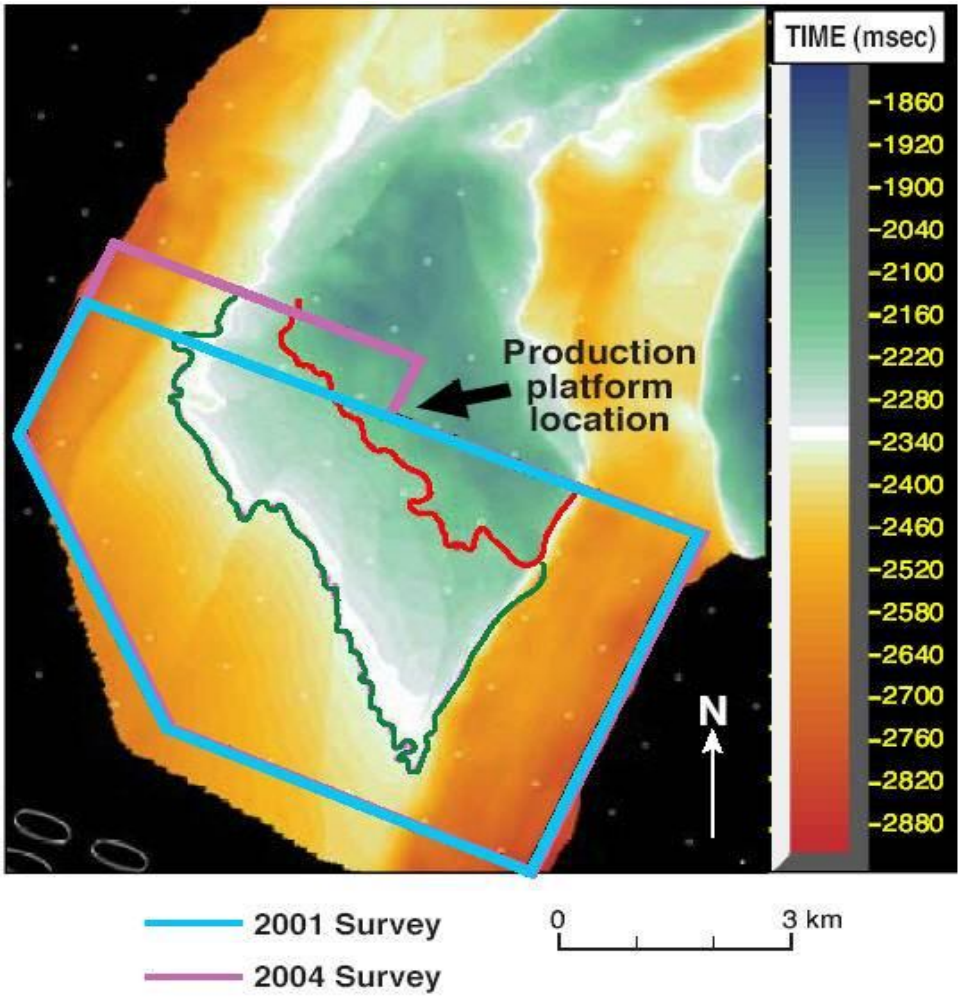

Figure 2.12. *Location of the repeated seismic surveys acquired in the Heidrun field relative to the top Fangst Group interpretation (based on the legacy). Blue line represents the 2001 survey which is partially overlapped by the 2004 survey indicated by the purple line. Both vintages were acquired with the Q-marine technology (from Furre et al., 2006).*

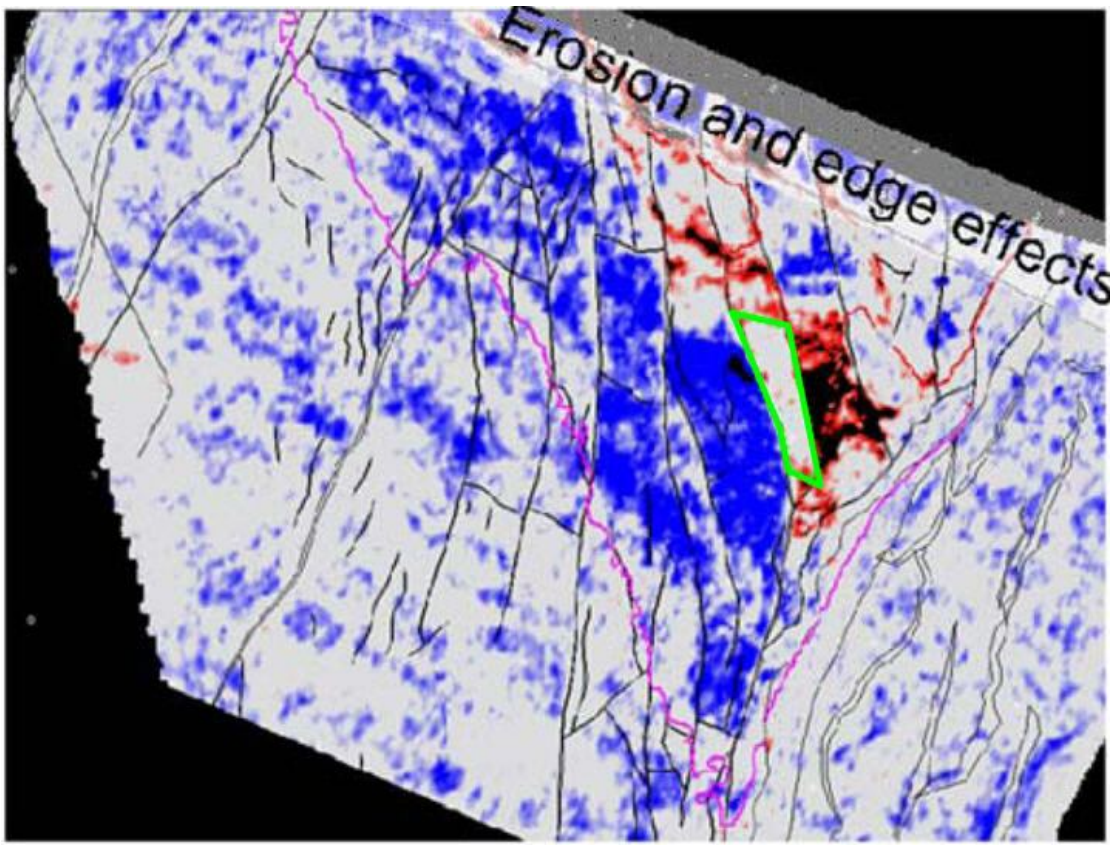

Figure 2.13. *Time-lapse seismic attribute map seems to honour faults (black segments) and contacts. Water-flooding and gas expansion signatures are indicated as blue and red respectively. The green segment highlights an undrained oil compartment (from Hanssen et al. 2004).*

2.3.2 The time-lapse seismic interpretation of the Fangst Group, Heidrun Field

The time-lapse seismic signature within the Fangst Group is strongly linked to the drainage strategy imposed on the Heidrun field. Figure 2.14 schematically illustrates the expected seismic changes for two different vintages: the pre-production or base (Figure 2.14, left) and the post-production (Figure 2.14, right) scenario. Here, the reservoir rock (sandstones in the Fangst Group) has lower P-wave impedances relative to the overlying rock Formation (as in shales in the Melke Formation above the Fangst Group) and other inter-reservoir shales (as the Not Formation). In the pre-production scenario, the P-wave impedance values in the reservoir increase with depth in each fluid leg observed in the model. By imposing a water injection strategy in a post-production stage, the reservoir gets flooded (in the updip direction) and an increase in the P-wave impedance is expected at the base of the oil leg. As a consequence a positive reflection coefficient (RC) at the new water oil contact appears in the RC log associated with this post-production stage, leading to a negative spike in the RC difference log monitor minus base. Convolution of a European polarity wavelet with differences between the monitor

and base RC logs leads to the presence of a trough amplitude at the position of the new oil water contact as well as a peak amplitude at the original oil water contact. Yet the presence of the Not Formation as laterally extensive intra-reservoir shales might impact the final outcome. Indeed, although it has been proven that fluid contact movement between Garn and Ile reservoirs is coupled (Kahar et al., 2006), the position of the shale relative to the fluid contacts might interfere with the signal derived from the fluid information. If gas expansion is assisting the water flooding, the expected RC log for the post-production scenario will also include a decrease of the P-wave impedance at the top of the oil leg leading to a decrease in the spike associated to the original gas oil contact and a new positive spike at the new gas oil contact in the post-production RC log. This will be evidenced in the RC difference log (monitor minus base) which when convolved with a European polarity wavelet will introduce a peak at the original oil gas contact and a trough at the new oil gas contact. As in the water flooding case, interference might be present in each vintage due to the presence of the thin shale beds close to the fluid contacts. This phenomenon might ultimately affect the final 4D seismic amplitude. Nonetheless, predicted changes seem to be in agreement with the observations at the production sites. They are particularly consistent with the boundaries between compartments as well as with the mapped original fluid contacts.

To evaluate the 4D signature in the Heidrun field, Furre et al. (2006) extracts amplitude maps for the main reflectors within each vintage to finally calculate differences by subtracting the newer map from the oldest. Within the Upper Fangst Group, Top Garn Formation has been described as a "good reflector" to be picked and analysed (with polarity preserved). Water flooding effects have been studied in the 2001 – 1986 and 2004 – 2001 difference maps. Water flooding can be followed in both difference maps, and particularly in the 2004-2001 map where the new oil-water contact is located above the one identified in the 2001-1986 difference (Figure 2.15). Even though the 4D signature is quite well identified in most of the top Garn difference map, non-repeatable noise is an intrinsic issue within the interpretations. Further qualitative inspection on low-angle stacks seems to indicate this noise could be related to the presence of multiples (Furre et al., 2003). Moreover, gas withdrawal influenced by the gas injectors up to the north-east sector (e.g. segment G) combined with the water-flooding effect given by the water injectors at the south-east, complicates the separation of pressure and saturation changes from the time-lapse seismic due to no sufficient well information or accurate fluid flow simulations allowing calibration of such 4D effect. Ultimately, the

interpretation results were used by Statoil, together with other data, to construct a suite of flooding or drainage maps, indicating remaining oil, brine-flushed and gas-flushed areas in addition to areas of uncertain flooding. The drainage maps were generated based on all available data, such as 4D data, the reservoir simulator, well logs and measured production (Nordby and Furre, 2002; Furre et al. 2004**)** (Figure 2.16). Because of the impossibility of updating the reservoir model with all available data, flooding maps can also be used as an integration tool. Within these maps, observed lateral seismic changes can be expressed from the reservoir management perspective (Anderson et al., 1996).

Furre et al. (2003) compares the fluid-flow simulator output and the 4D seismic maps especially for a layer within Upper Fangst Group (i.e. Garn Formation). In this study similarities and disparities are highlighted:

- The time-lapse seismic confirms the gas-flooding pattern along the G segment but less gas flooding as compared with the simulation model.
- Water – flooding is stronger within compartments E and F when compared with predictions from the simulator.

In a new attempt to understand the changes on the elastic properties (e.g. P-impedance) an inversion technique for 4D data has been developed internally by Statoil (El Ouair et al; 2005). In this method acoustic impedance changes are calculated by means of pre-stack seismic difference data within a Bayesian formulation which also provides posterior uncertainties for the estimates. This inversion technique has been successfully applied to the Heidrun post-stack seismic dataset and it has been useful in identifying water-flooding and gas flooding areas as well as being powerful in the detection of changes within thin layers (Figure 2.17). Due to the noise levels observed in 1986-2001 and 2001-2004 seismic data, the application of this inversion method was only possible for the 2001-2004 set. The result has been considered very valuable, particularly for the analysis of the intra-reservoirs contained in the Fangst Group.

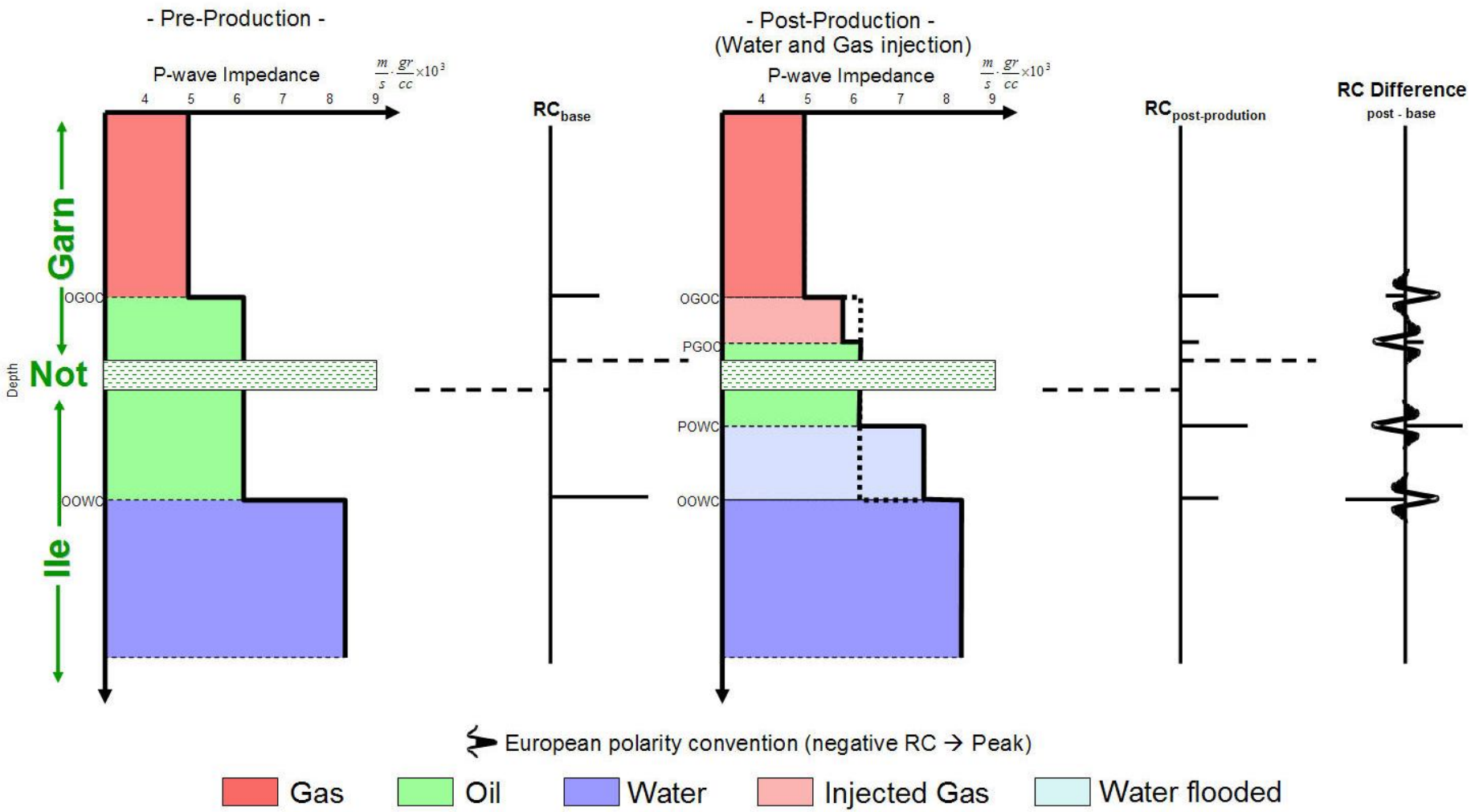

Figure 2.14. *Expected time-lapse seismic response for the Fangst Group at Heidrun field in two different vintages: the pre-production or base (left) and the post-production scenario (right). Reflection coefficient (RC) differences are calculated between the post-production or flooded stage minus the pre-production stage or base. OGOC = original gas oil contact, OOWC = original oil water contact, PGOC = gas oil contact after production, POWC = oil water contact after production.*

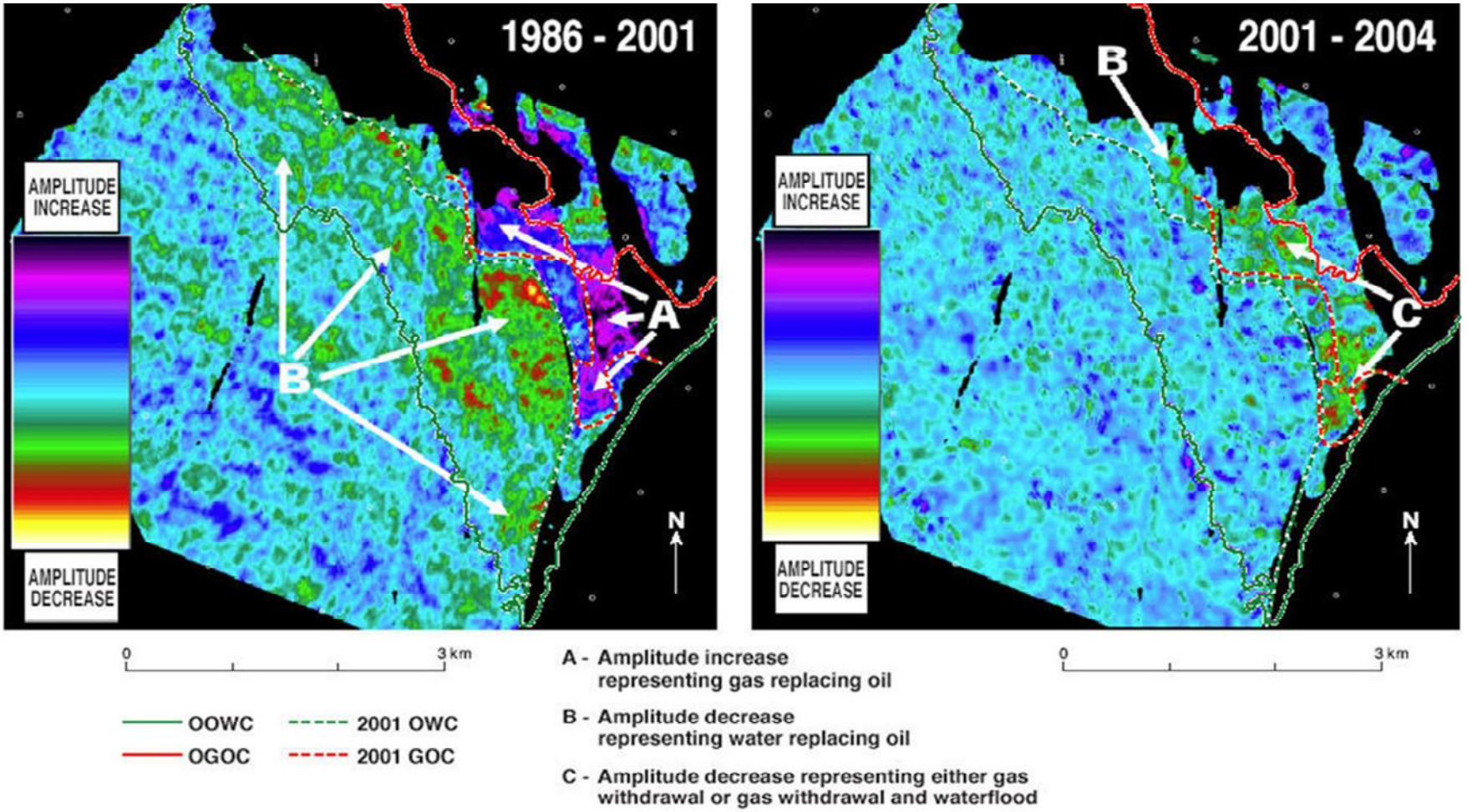

Figure 2.15. *4D signature at Top Garn Fm (Upper Fangst Group). Left hand side: 2001-1986 difference map. Right hand side: 2004-2001 difference map. Interpretations have been made in the maps for the original oil water (OOWC), original gas oil (OGOC), post-production oil water (OWC) and gas oil (GOC) contacts (from Furre et al., 2005).*

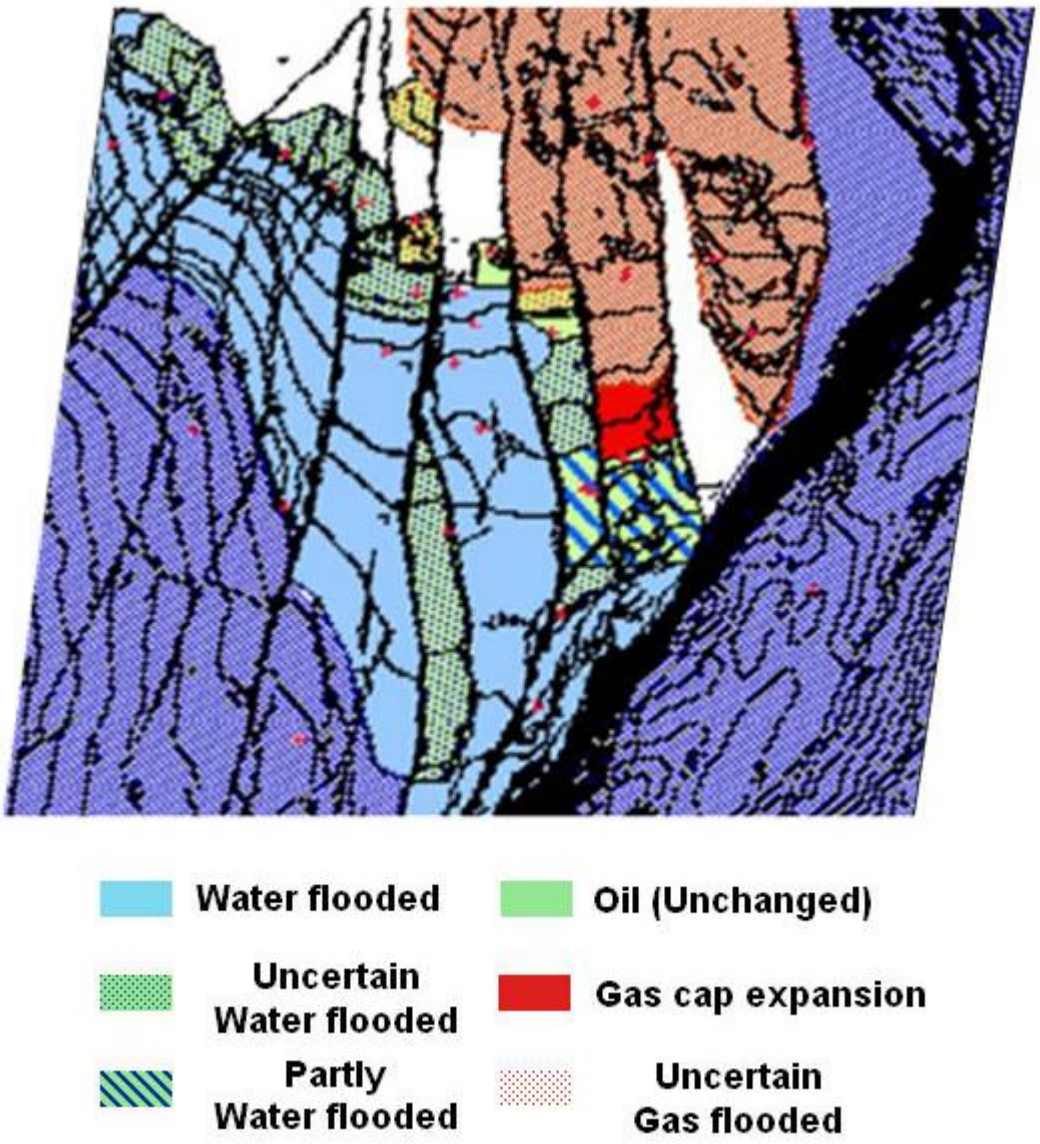

Figure 2.16. *Flooding map for the Garn reservoir (Upper Fangst Group) by 2001 (from Statoil internal report). Missing (eroded or not deposited) reservoir sectors appear as white patches.*

Several flow units are included in the Fangst Group (i.e. Garn Fm. and Ile Fm.), and these are mainly bounded by shaly sequences (Not Fm.). Production changes within those intra-units seem to be contributing to the seismic changes observed in the major reflectivity boundaries (sand/shale contrast) such as the Top Fangst Group. However, as the individual effects of each unit are being "absorbed" by the main reflectors, little is known about the specifics of the 4D changes. Even more, the shaly boundary between the Garn Fm. and Ile Fm. changes laterally between peaks and troughs, so the seismic cube difference is quite difficult to interpret, particularly in the vertical trace domain. Alternatively, these intra-reservoir features can be followed in the inverted data which

seems to contribute to a correct localisation of the 4D seismic anomalies (Figure 2.18). This observation helps to overcome the 4D interpretation difficulties (Furre et al., 2005).

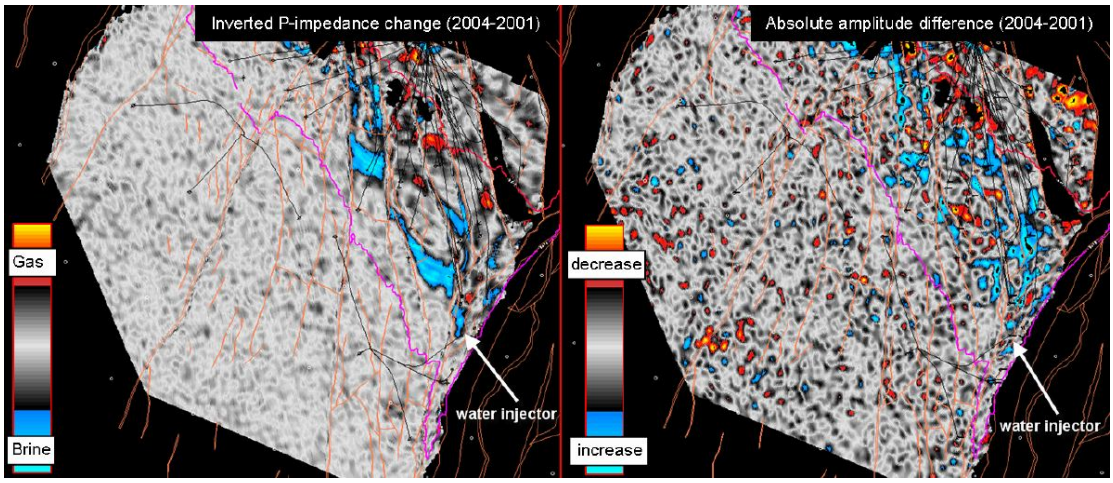

Figure 2.17. *4D seismic changes extracted from an Intra-Fangst reservoir considering a time window equivalent to 20 meters. Left hand side: Inverted P-impedance change from 2001 to 2004. Right hand side: 4D amplitude map given by the 2004-2001 difference (extracted from the same window). The inversion output facilitates the interpretation of the water flooding effect as the noise level has decreased (from El Ouair et al., 2005).*

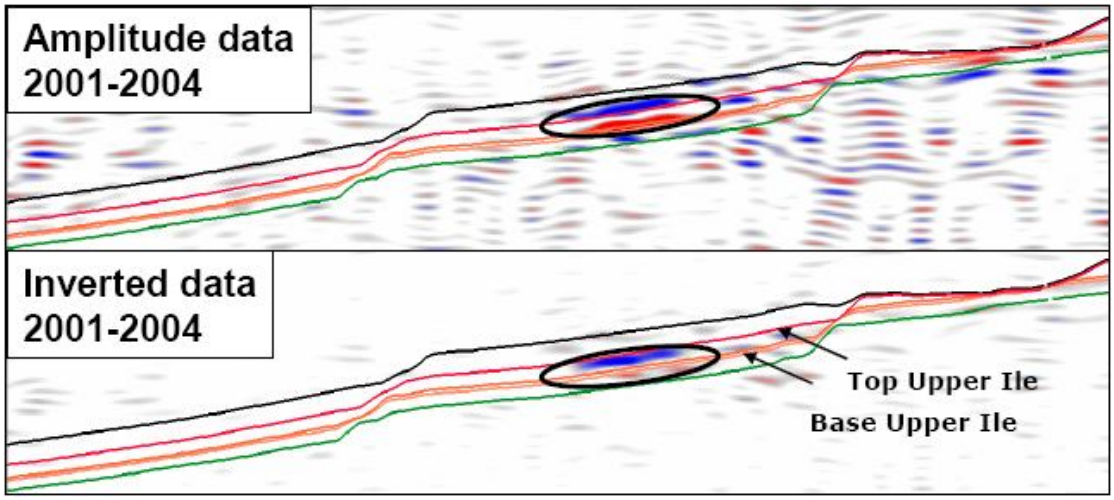

Figure 2.18. *Comparison of the 4D amplitude difference (upper) and inverted data (lower) for the 2004-2001 difference. Both sections are in the time domain. Blue colour indicates an increase in P-impedance (hardening) in between 2001 and 2004. The 4D signature cannot be accurately associated to a specific layer in the seismic amplitude difference; however the inverted data has repositioned the anomaly within the Ile Fm. (from Furre et al., 2005).*

Looking for the integration of the time-lapse seismic data with the fluid flow simulator output, Furre et al. (2006), make use of designed colour-coded flooding maps which integrate the geophysical and the engineering contribution (Figure 2.19). In spite of the impossibility of updating the simulation model to match the 4D seismic observations, these flooding maps have proven to be very practical to locate new strategically-placed wells. This qualitative approach has been proposed as an alternative way to deal with the inconsistencies between the 4D seismic and the simulator output.

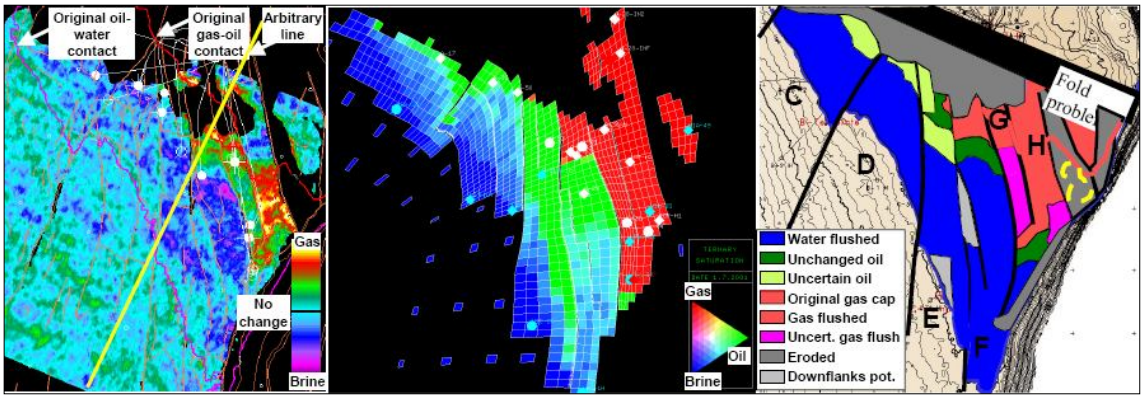

Figure 2.19. *Left hand side: Amplitude difference map extracted at Top Fangst Group. Middle: Reservoir simulation map for the top layer in Fangst. Right hand side: Flooding map for the Upper Fangst Group (from Hanssen et al., 2004).*

In this regard, time-lapse seismic has been quite useful in updating the model for individual sectors leading to the planning of new infill wells. A particular case example is discussed by Furre at al. (2006). In this study a new production well (C-C) is planned to be drilled up-flank (within Ile Fm.) providing pressure support by two water-injectors located down-flank. An erosion of the reservoir unit has been added to the old realization and the geological model is updated for the new configuration. Simulation output differences concluded that the final well placement depends on the model selection (hanging-wall to be drilled in the old model and foot-wall drilled in the new model) as the waterfront differs for each case (Figure 2.20).

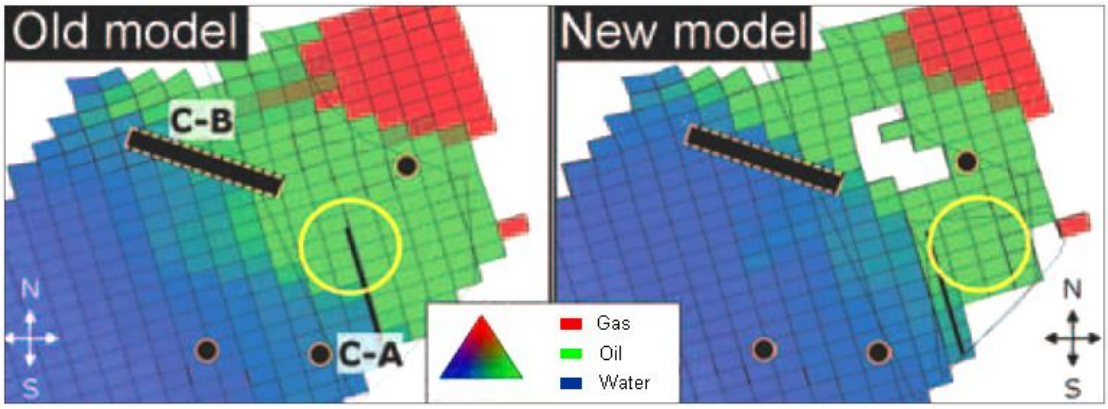

Figure 2.20. *Left hand side: Old reservoir model. Right hand side: New reservoir model where the erosion has been included. Producer wells C-A and C-B. Yellow circle indicates optimum position for new infill well C-C in each model: In the hanging wall (west of the fault) for the old model and in the footwall (east of the fault) for the new model (from Furre et al., 2006).*

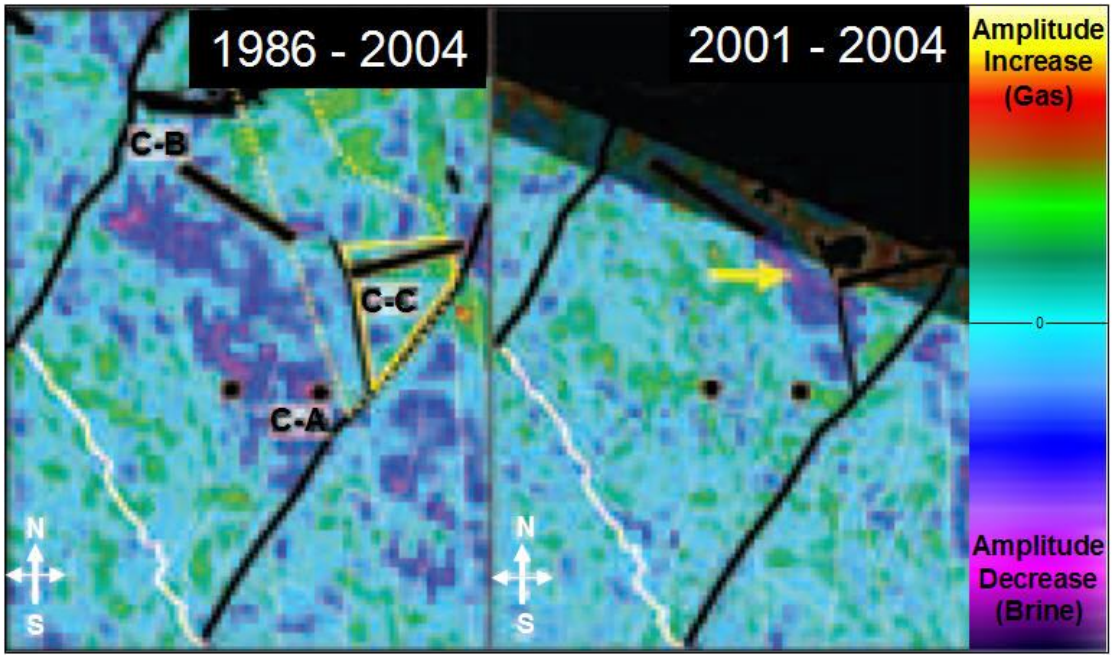

Figure 2.21. *1986-2004 (left) and 2001-2004 (right) seismic difference maps for the base of the Ile Fm. Faults are represented by the black segments. Original water-oil contacts represented by the white line. C-C denotes the location of the new infill well (red line). A 1986-2004 seismic difference map seemed to indicate there were remaining reserves, but the 2001-2004 difference map (higher S/N ratio) showed water reaching onto the fault segment. (from Furre et al., 2006).*

To address this issue the 1986-2004 and 2004-2001 differences are used. Although a 2004-1986 seismic difference map seemed to indicate there were remaining reserves, the 2004-2001 difference map (higher S/N ratio) not only showed that water reached the fault separating the minor compartments but that the water flooding is even passing through the fault (Figure 2.21). As the observation was detected in 4D maps for lower levels of the reservoir, a final decision was made on drilling the footwall (to the east of the fault) without crossing the fault. No water breakthrough was observed during early production. However, the well watered out after one month. This outcome supported the decision of not producing the hanging-wall sector (to the west of the fault) which might have caused water production from the start of the well activity.

2.4 Summary

Heidrun field is one of the major oil accumulations in the Norwegian offshore. Its drainage strategy includes water and gas injection looking for pressure maintenance as the reservoir is depleted. In spite of the high porosity (up to 35%) and permeability values (1-5 D) for the Jurassic reservoirs, challenges in the field management need to be addressed as the compartmentalization given by faults strongly influences the connectivity between different reservoir segments of the field. In order to track dynamic changes, a time-lapse seismic campaign has been implemented. In spite of the noise levels, the signal coherency is strong enough to extract useful and meaningful information. Certainly, the strong and relatively clean 4D seismic signal has allowed the mapping of fluid changes, using as guidance for the interpretation, the engineering and geological information. Previous studies combine various data sources which appear to be perfectly integrated as well as consistent with the observed reservoir signature.

Chapter 3

Assessing the Time-Lapse Seismic Signature of the Fangst Group, Heidrun Field

This chapter extends the previous analyses building on the fundamentals and the understanding of the compartmentalised character of the time-lapse seismic signature of the Fangst Group in the Heidrun field. Using the available database, this study leads to the identification of a major fault seal control on the dynamic changes, which in turn control the observed 4D seismic signature in the field.

3.1 Introduction

The time-lapse seismic data acquired in the Heidrun field reveals for the Fangst Group a clear signature which appears to be consistent with different sources of information. In particular, 4D changes in the reservoir seem affected by structural compartmentalization. Indeed, previous studies have recognized that faults are capable of influencing the fluid flow in this field (Kahar et al., 2006). In this real case example, further analysis of this phenomenon has been recommended. Consequently, this chapter builds on previous analysis of the observed time-lapse signature by making use of the available dataset. Additionally, we assess the spatial character of the 4D seismic signal to understand the regional effects that faults might have on the compartmentalization of dynamic changes.

3.2 Available database

In order to follow this study, the operator of the field (Statoil) kindly provided to the Edinburgh Time Lapse Project (ETLP) a dataset comprising a set of wireline logs, seismic data, seismic interpretations, the fluid-flow simulation model and specific production information. In terms of the seismic information, the data encloses the acquired vintages collected in 1986 (base line), 2001 (monitor 1) and 2004 (monitor 2). For each survey migrated volumes for partial (near – mid – far) and full offset stacks are supplied covering an estimated area of 100 km^2 (Figures 3.1 and 3.2). Also particular P-wave inversion products have been included.

Several seismic horizons are also available. They were directly derived from the base line survey which was used to describe the morphology of seismic reflections on top, base reservoir, in the overburden and underburden. The well data consist of seven wells and their associated well-logs (Figures 3.3 and 3.4). Each of them includes their associated trajectories, well-tops and time-depth conversions curves. Additionally, the full field reservoir model and the fluid-flow simulation output have been delivered (Figure 3.5).

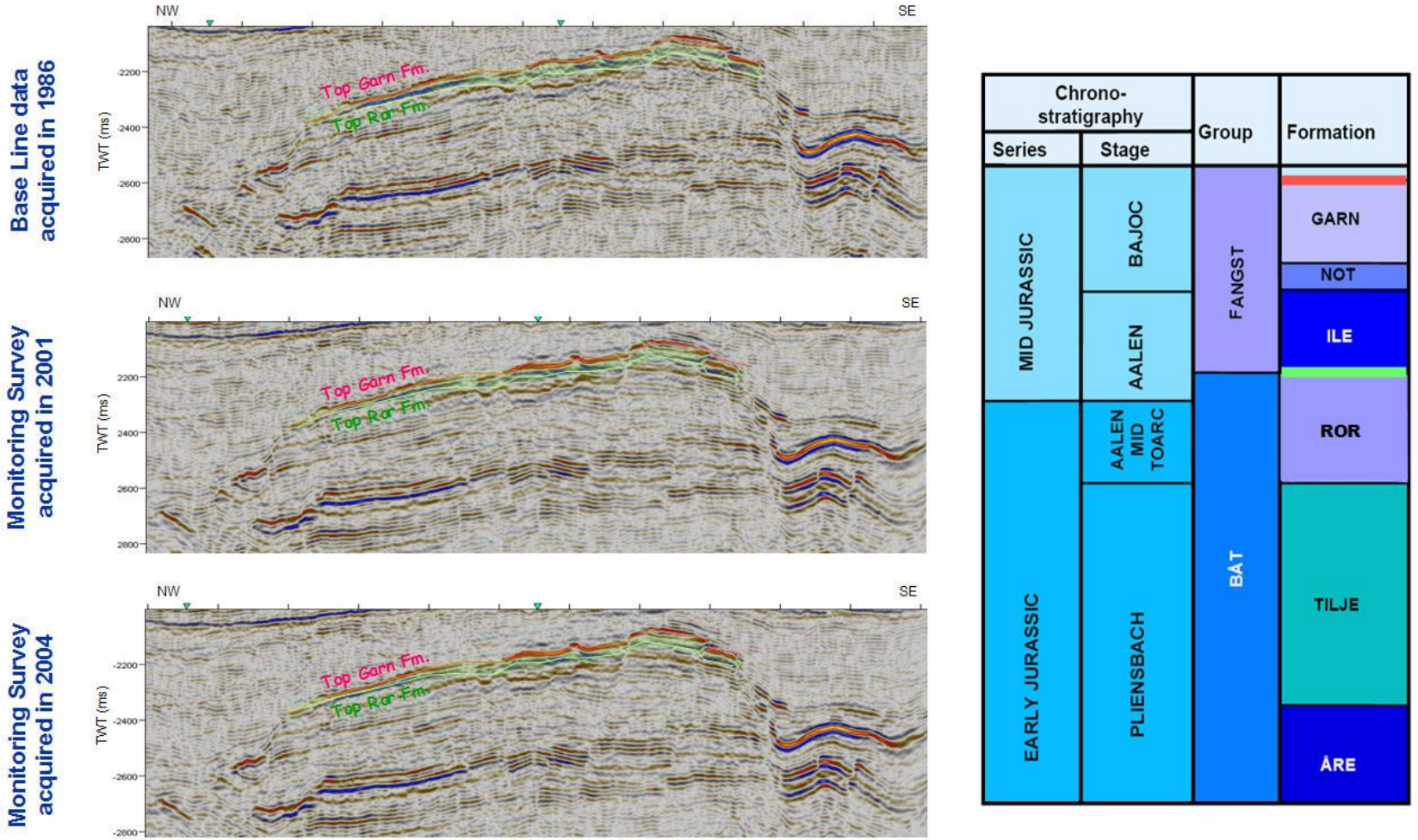

Figure 3.1. *Left: Full offset stacks associated to each seismic vintage acquired in the Heidrun field. Interpretation of top Garn and top Ror Formation are displayed as red and green horizons respectively. Right: Location of the picked horizons (highlighted according to their colours) in the chronostratigraphic table.*

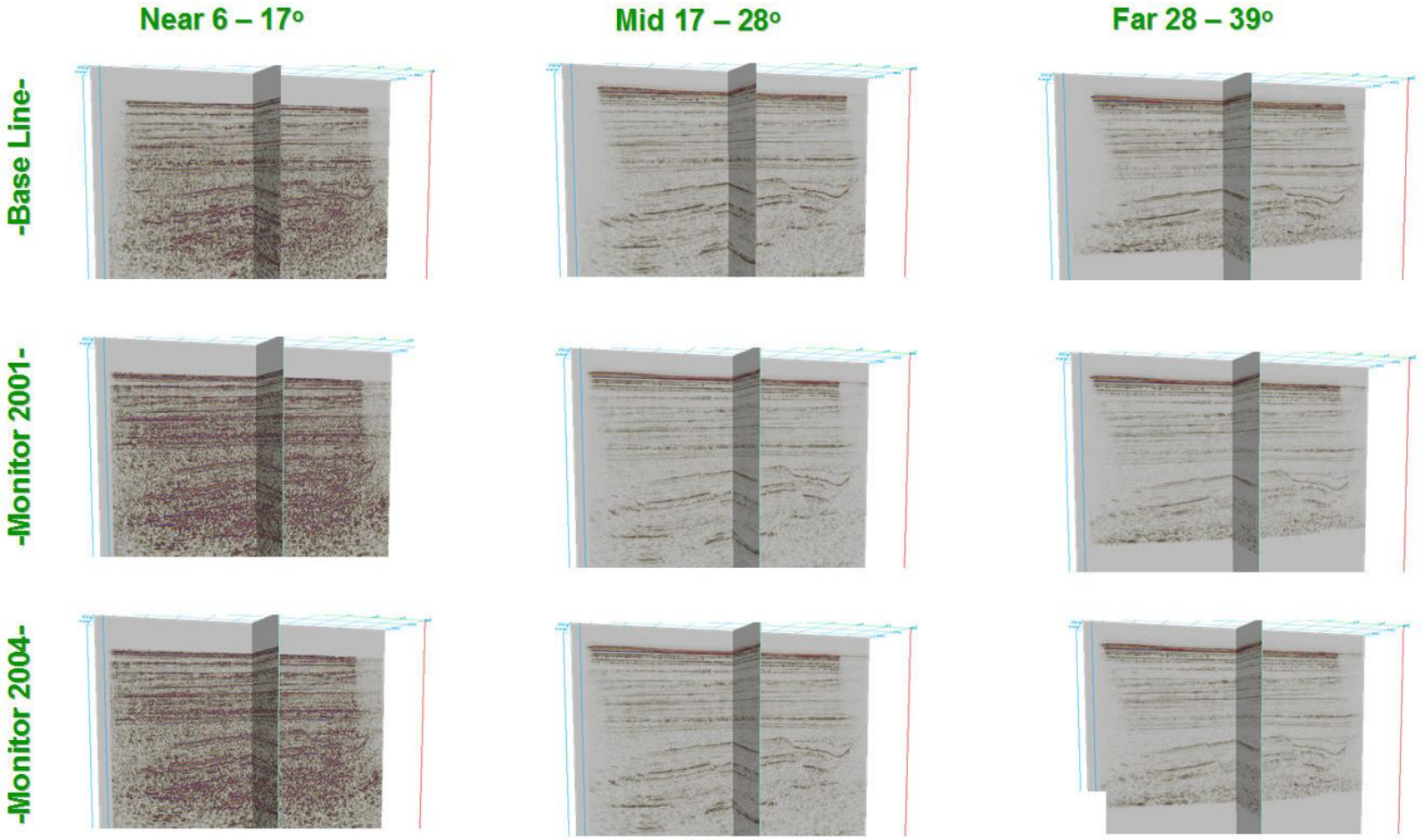

Figure 3.2. *Partial angle stacks associated to each seismic vintage acquired in the Heidrun field.*

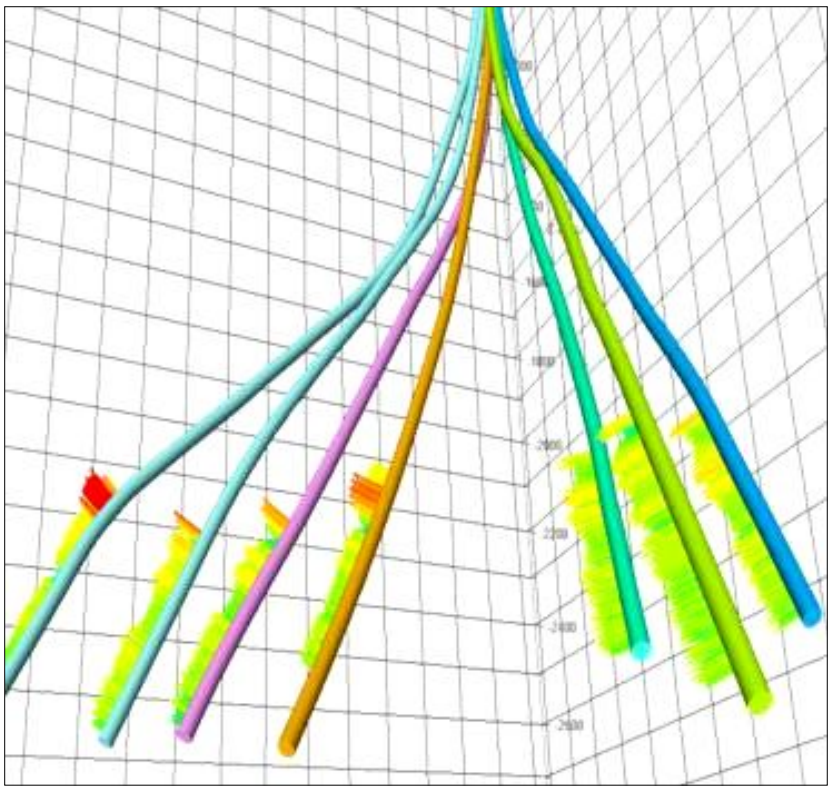

Figure 3.3. *Available well data.*

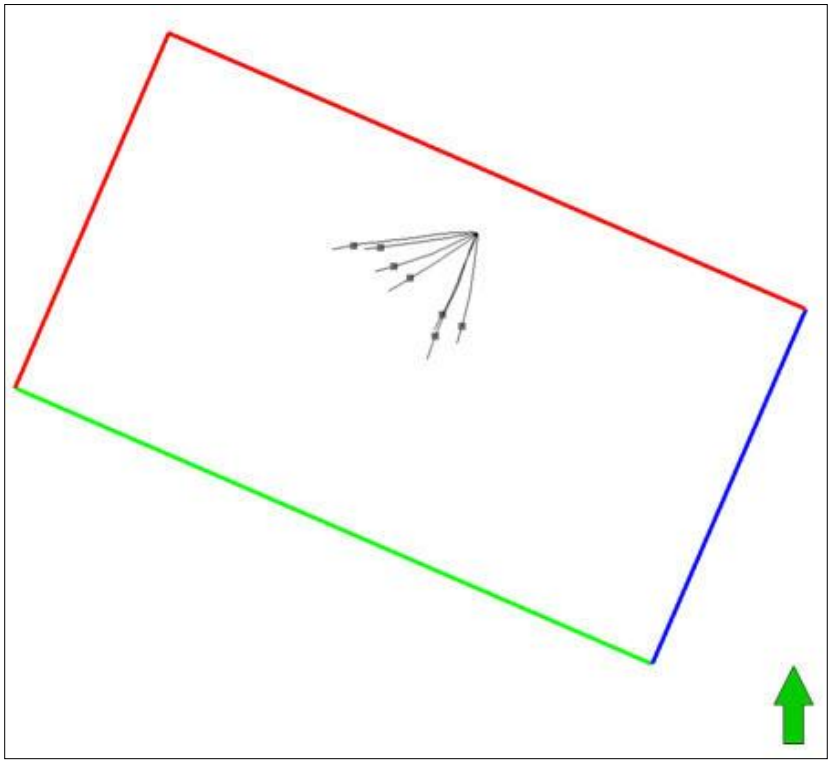

Figure 3.4. *Location of the well dataset relative to the seismic data coverage. Reservoir tops (Garn Fm.) are represented by squares plotted on the well trajectory.*

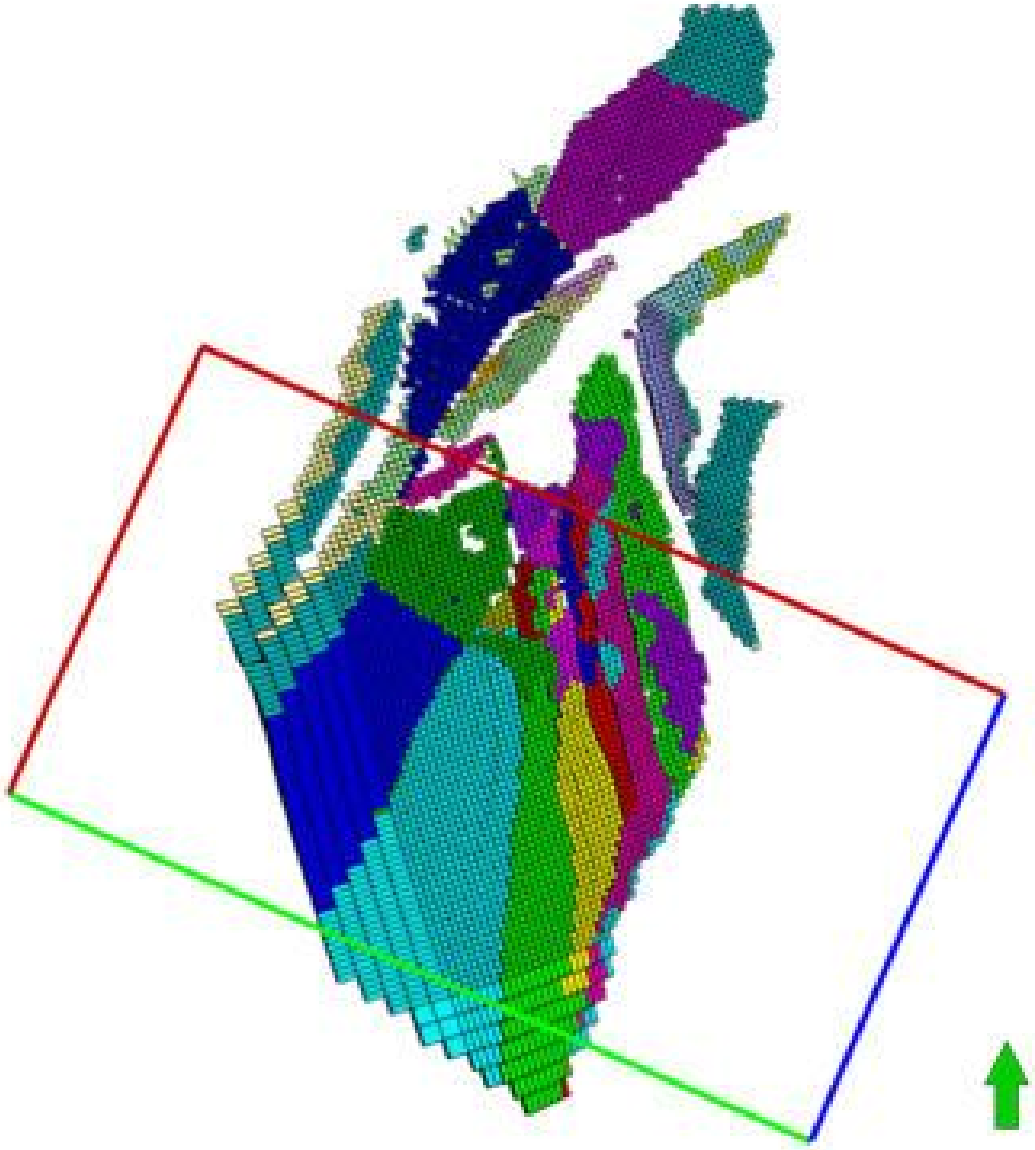

Figure 3.5. *The geo-cellular representation of the reservoir model is intentionally segmented in several blocks which have been discretely colour-coded indicating the fluid-in-place regions. The separation is strongly linked to the identification of major faults compartmentalizing the field. The seismic data boundary has been plotted on top (rectangular polygon) to highlight its relative location related to the simulation model.*

3.3 Detectability and sensitivity of the 4D seismic response

The 4D seismic response within the Fangst Group is characterized by a strong and relatively clean signal. The production strategy introduces time-lapse effects within 2 inner reservoir units known as Garn and Ile Formations. Their elastic properties changes seem to contribute to the total 4D seismic effect in the Fangst Group (particularly at its top) which has been associated with fluid substitution (during the water and gas injection drive) in previous rock physics modelling analysis (Kahar et al., 2006). According to these studies, an increase of the water saturation level dominates the time-lapse seismic response by increasing the P-wave impedance (from connate water saturation S_{wc}) up to 14% (measured at residual oil saturation S_{or}). This appears to be the case for the waterflooded leg where changes in pressure seem to perturb the P-wave impedance by less than 1% given the pressure maintenance strategy that has been imposed in the field. However, gas movement has been also evidenced in the vicinity of the gas cap which also contributes to the occurrence of major 4D seismic effects.

To evaluate the ability to detect changes in the seismic signature due to perturbations in the saturation and pressure field during production, a rock physics analysis is now performed as part of a feasibility study. In this case, the feasibility study will be tied to a particular production scenario as represented in Figure 2.14. In this regard, the following form of Gassmann equation (1951) is used to link changes in fluids to the seismic response:

$$K_s = K_d + \frac{\left(1 - K_d / K_{gr}\right)^2}{\frac{\varphi}{K_f} + \frac{1-\varphi}{K_{gr}} - \frac{K_d}{K_{gr}^2}} \tag{3.1}$$

where K_s is the saturated-rock modulus, K_d the dry rock modulus, K_{gr} the grain bulk modulus, K_f the bulk modulus of the fluid mixture and φ the porosity. The empirical relations proposed in Batzle and Wang (1992) are used to express those effects in the fluid phase. Also, to assign the pressure sensitivity properties for the dry rock-frame, the following equations presented in MacBeth (2004) are used:

$$K(P) = \frac{K_{\inf}}{1 + \left(S_K / \left(1 - S_K\right)\right) e^{-P/P_K}} \tag{3.2}$$

and,

$$\mu(P) = \frac{\mu_{\inf}}{1 + \left(S_\mu / \left(1 - S_\mu\right)\right) e^{-P/P_\mu}} \tag{3.3}$$

where K_{inf} and μ_{inf} are high pressure asymptotes, P_K and P_μ are constants, S_K and S_μ define the maximum possible change in the moduli.

The sensitivity of the P-wave impedance differences given the fluid substitution and differential pressure is assessed by performing Monte Carlo simulations. Uncertainties related to each parameter involved in the Gassmann relation and MacBeth equation are represented as probability density functions (pdf's) to finally evaluate the contribution of each parameter uncertainty to the variance of the P-wave impedance difference. To model uncertainty sources, triangular density functions are defined given the available well dataset for Heidrun field (Figure 3.6), but other distributions are tested yielding similar results. To avoid inconsistencies during the simulation process, K_d is modeled using the following empirical equation from Han and Batzle (2004), which applies to clean and shaly sandstones:

$$K_d = \left(1 - A \times \varphi + B \times \varphi^2 - C \times \varphi^3\right) \times K_{gr} \tag{3.4}$$

where, A = 7.16, B = 25.8 and C = 33.84 are obtained as a result of the least-square calibration of such equation with K_d values derived from the well logs values of the Fangst Group at the Heidrun field (Figure 3.7). For the purpose of the Monte Carlo simulation, pdf's associated with porosity and shear modulus are based on inspection of the available well logs for the Fangst Group at the Heidrun field. Pdf's for the bulk modulus of the mineral and fluids are based on 10% variation from its defined average value. Density values for the grain rock, water, oil and gas are constants and equal to 2650 kg/m^3, 1000 kg/m^3, 800 kg/m^3, 270 kg/m^3 respectively.

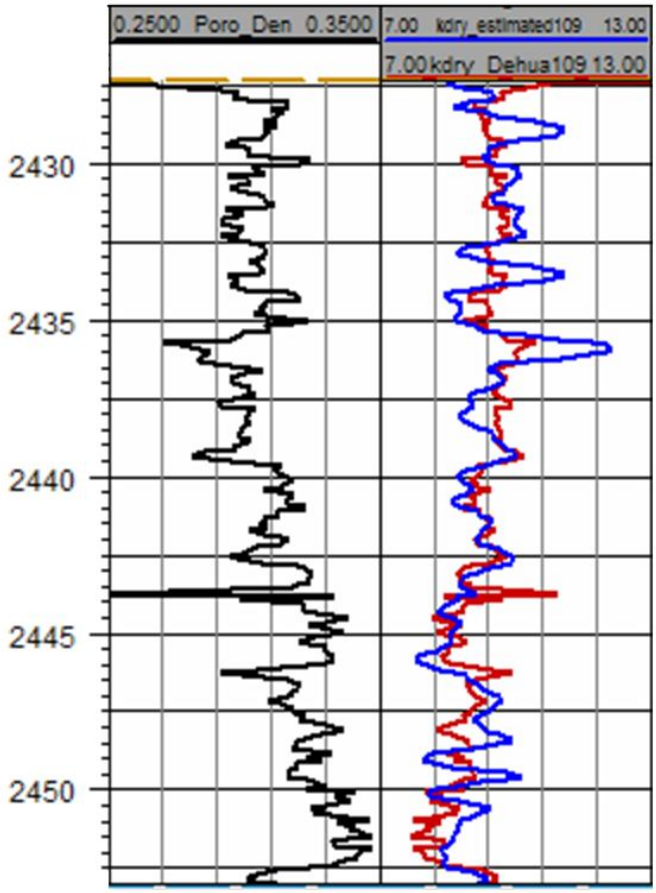

Figure 3.6. *Bulk modulus for the dry rock derived from the well logs in the Fangst Group at the Heidrun field. In the right hand side track, the blue line represents the dry rock modulus as estimated from the manipulation of the Gassmann equation (1951) whereas in red the Han and Batzle (2004) approximation based on the porosity log displayed in the left hand side track. Bulk modulus in GPa and depth values in meters.*

Two different fluid substitutions are performed by considering two different scenarios. In the first case, only the oil and water phases are considered. Here, the reservoir is initially fully saturated with oil (S_{wc} = 10%) and then fully waterflooded (S_{or} = 10%). For the second case the gas phase is also included. In the initial stage the reservoir is fully saturated with oil (S_{wc} = 10% , S_{gr} = 10%) to be fully gas flooded (S_{or} = 10% , S_{wc} = 10%) in the posterior stage. Finally the contribution of the pressure perturbation (a decrease in pressure of 7 % is estimated from the fluid flow simulation given for the Heidrun field) is evaluated and added to the fluid substitution taken in place.

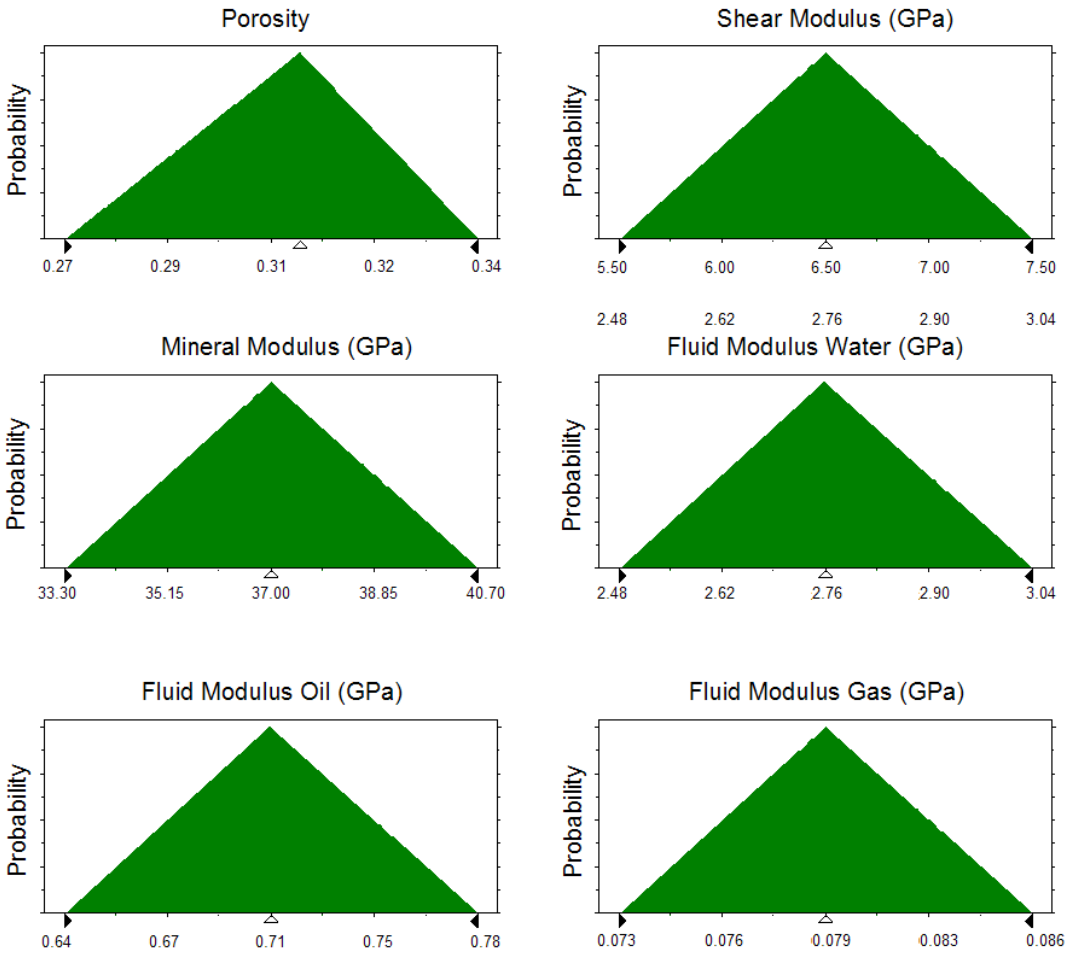

Figure 3.7. *Probability density functions (pdf's) used to describe parameters in the fluid substitution. Pdf's associated with porosity and shear modulus are based on inspection of the available well logs for the Fangst Group at the Heidrun field. Pdf's for the bulk modulus of the mineral and fluids are based on 10% variation from its defined average value. Density values for the grain rock, water, oil and gas are constants and equal to 2650 kg/m^3, 1000 kg/m^3, 800 kg/m^3, 270 kg/m^3 respectively.*

Forecasted P-wave impedance changes (Figure 3.8) and observed changes between monitor 1 (2001) and base line seismic surveys (1986) seem to be in agreement, as observed 4D changes in the waterflooded and gas expansion zones reach values up to 10% and - 6% respectively.

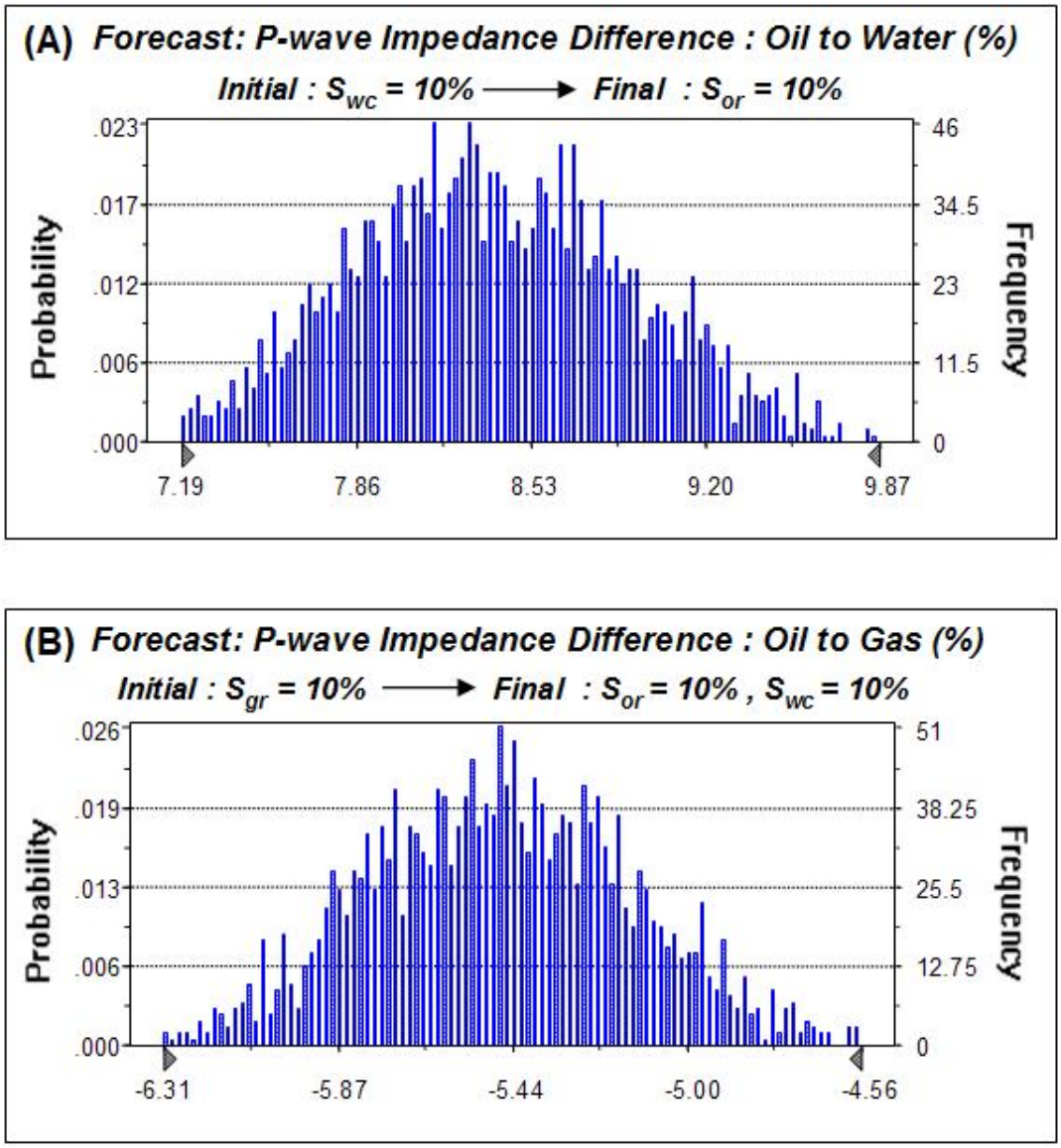

Figure 3.8. *Forecast for the P-wave impedance given fluid substitution and pressure contributions in two different scenarios. In (A) the reservoir is initially fully saturated with oil and then fully waterflooded. In (B) the reservoir is fully saturated with oil to be fully gas flooded. Connate water, residual oil and residual gas saturation are indicated as* S_{wc}, S_{or} *and* S_{grc} *respectively.*

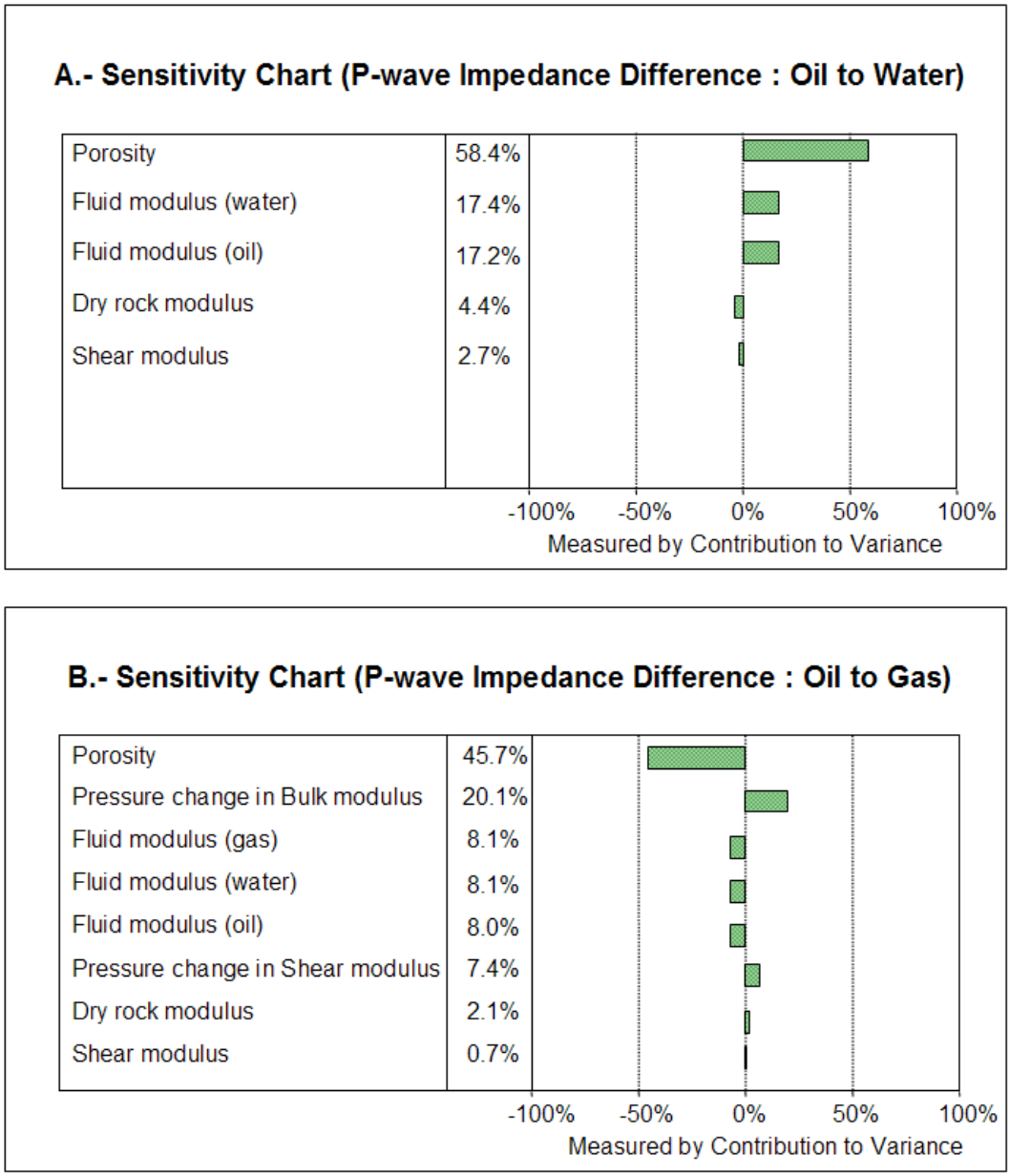

Figure 3.9. *Contributions to the P-wave Impedance variance from uncertainties associated with input parameters. In (A) the reservoir is initially fully saturated with oil and then fully waterflooded. In (B) the reservoir is fully saturated with oil to be fully gas flooded. Note that porosity in both cases seems to be controlling most of the P-wave Impedance change.*

Also sensitivities are calculated by computing the rank correlation coefficients between every assumption and forecast. The rank correlation method organizes assumption values from the lowest to the highest, computing the correlation coefficient providing a meaningful measure of the degree in which assumptions and forecast change together. If an assumption has a high correlation on the forecast (due to the model and uncertainty) the impact on the forecast increases. Positive coefficients indicate that an increase in the assumption is related to an increase in the forecast and negative coefficients imply the opposite situation.

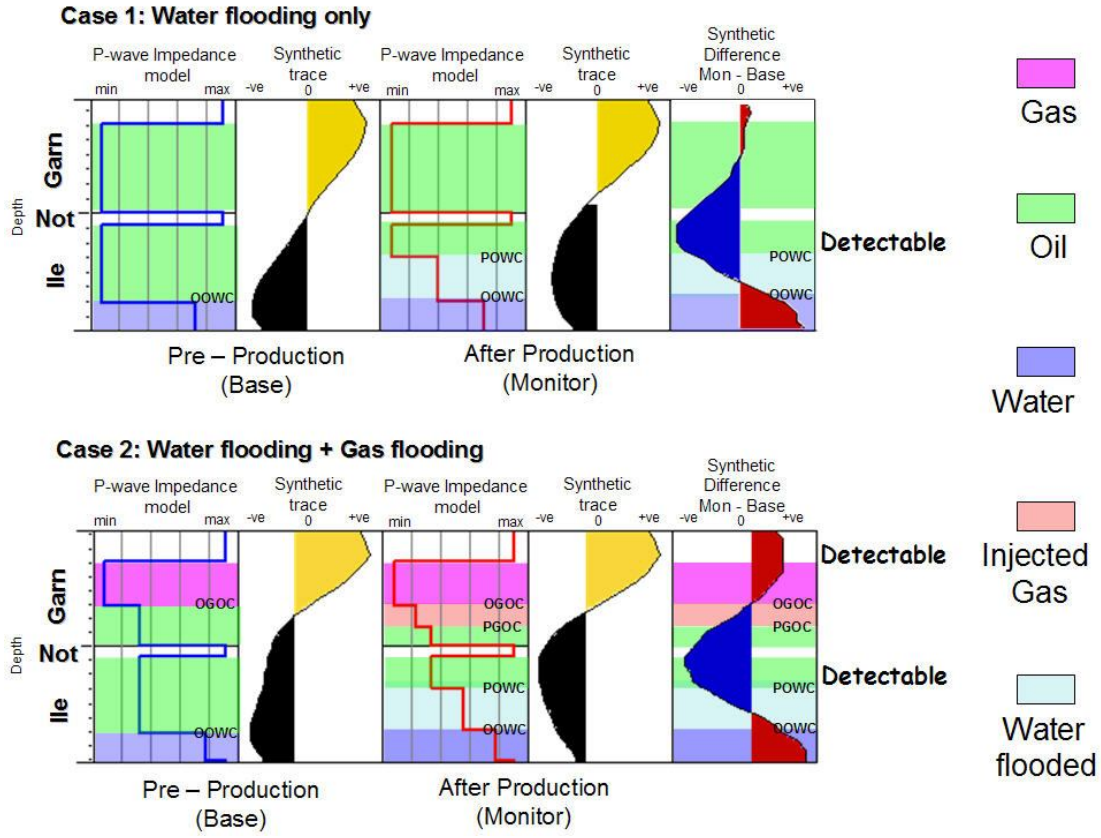

Figure 3.10. *1D synthetic models have been constructed for the water flooding (Case 1) and gas flooding (Case 2) scenarios. A negative seismic amplitude is detectable nearby the presence of the new oil water contact as well as a positive amplitude associated to the gas expansion is located at the top of the stratigraphic Group. OGOC = original gas oil contact, OOWC = original oil water contact, PGOC = gas oil contact after production, POWC = oil water contact after production.*

Here the simulations show that for the contributions to the P-wave impedance variance the porosity term seems to be controlling most of the seismic differences taking place for both production scenarios (Figure 3.9). This explains the strong 4D signature evidenced in the Fangst reservoir as the relatively unconsolidated sands with high porosity provides an excellent support for the P-wave impedance contrast due to elastic property changes during fluid substitution. Furthermore, when the fluid substitution only considers the oil and water phases the contribution of the pressure perturbation contributes negligibly to the total P-wave impedance change. However, as gas comes into system (gas expansion case), the effective fluid compressibility is quickly affected and consequently, the pressure change taking place in the reservoir leads to a major contribution in final P-wave impedance difference.

In terms of the predicted 4D seismic response, 1D synthetic models (Figure 3.10) have been constructed for the water flooding and gas flooding cases according to P-wave impedance diagrams displayed in Figure 2.14. As before, two scenarios have been selected according to the production setting. In the first case (Figure 3.10, top), the lower Fangst Group is waterflooded; while in the second case gas (Figure 3.10, bottom), expansion due to gas injection in the upper Fangst has also been included. A rising oil-water contact is considered in both production scenarios. Also during gas expansion, the production strategy results in a upward shift of the oil-water contact and a downward shift of the gas-oil contact leading to a 'displaced oil scenario' as discussed in Staples et al. (2004). In addition, a synthetic 20 Hz Ricker wavelet (European polarity convention) has been used in the convolution model. As predicted in the sketch illustrated in Figure 2.14, a negative amplitude is obtained near the new oil water contact as well as a strong positive amplitude (associated to the gas expansion) is being detected at the top of the stratigraphic Group. However the presence of inter-reservoir shales might impact in the final response as they might be interfering with the final amplitude depending on their relative position to the location of the fluid contacts. Also, as described in MacBeth et al. (2008) pressure depletion may introduce mechanical extension in the lower permeability shales to some degree. In that case, observed 4D seismic signature might consist in a combination of the reservoir changes (hardening) and shales response (softening).

3.4 The 4D seismic signature at the well location

In order to evaluate the 4D changes, two wells are analysed. In each case seismic traces at the well location are extracted for the base line survey and the monitor 1 by sampling the seismic traces along the well path. The seismic difference response is calculated by subtracting the base signal from the monitor in the vicinity of the Garn Fm. Also P-wave impedance logs extracted from a previous inversion strategy are displayed. In the oil and water movement case (Figure 3.11, top); the 4D seismic signature at the top of Garn reservoir is represented by a trough over a peak (blue over red) on the monitor – base difference (2001-1985). This observation is correlated to an average increase of the P-wave impedance in time as water displaces oil in this sand. When gas expansion comes into the system (Figure 3.11, bottom) the time-lapse seismic change is associated with a peak over a trough (red over blue). This phenomenon is expressed in a decrease of the P-wave impedance in the gas invasion zone. In both well examples, detailed examination of the P-wave impedance logs helps to understand the impact of fluid substitution on the trace. Looking into the P-wave impedance track, fluid substitution taken in place can be evidenced. In case (a) the lower sections of the reservoir sands have been watered out (blue-coloured area) meanwhile some remaining oil appears at the top of the produced interval (green-coloured area). In case (b) gas oil and water interact and particular 4D signatures associated with each fluid leg seem to interfere, thus seismic differences must be cautiously interpreted. However, in such case, changes in P-wave impedance can be analysed vertically. Indeed, by looking for increases and decreases in the P-wave impedance logs, the separation of the flooding phases can be achieved as shown in Figure 3.11 (bottom). In this example, a gas expansion zone (red-coloured area), remaining oil (green-coloured area) and water flooded sands (blue-coloured area) have been differentiated. Also, as previously discussed, the Not Fm. shales might impact in the effective 4D signature of the reservoir. The occurrence of laterally discontinuous intra-reservoir shales (e.g. within the Garn Fm. for the water/oil case) might intensify the complexity of local time-lapse response depending on the thickness and permeability of such low permeability layers as well as the net-to-gross of the depositional environment (MacBeth et al. 2008).

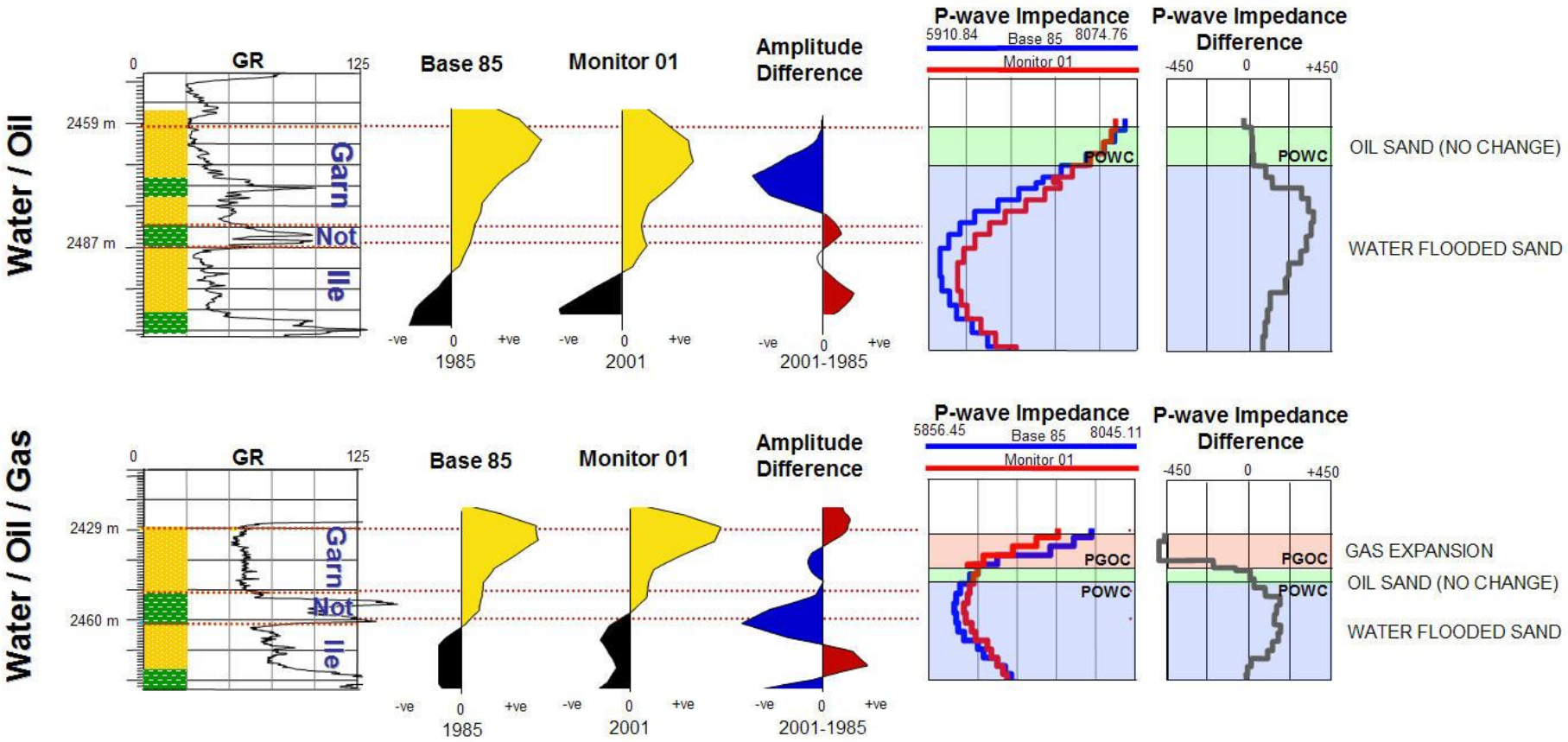

Figure 3.11. *Observed 4D seismic response at well locations. Top: Water – Oil and Bottom: Water – Oil – Gas cases. Seismic traces are extracted from the base and monitor 1 surveys (by sampling along the well path) which are used to evaluate the amplitude difference (monitor – base). Also P-wave impedance logs (derived from inversion products) are displayed for the base and monitor surveys which are displayed as blue and red logs respectively. In each example, the gas expansion (red) remaining oil leg (green) and water flooded sands are highlighted accordingly. PGOC = New gas oil contact after production. POWC = New oil water contact after production.*

This observation might explain the 4D seismic signatures present in the shaly layers; however a sidelobe effect cannot be neglected.

3.5 The 4D seismic signature along well intersection fences

To evaluate lateral 4D changes along the field compartments a well seismic fence is created (Figure 3.12). In this fence the seismic signature is extracted in the vicinity of the well trajectory. Five wells are selected according to their position in several compartments (C, D, F and G). Gamma ray logs (GR), seismic traces extracted from the base line seismic survey and the monitor 1 – base difference are displayed. For the base line, a seismic peak amplitude is observed nearby the top of the Garn reservoir. In terms of the 4D seismic responses within this unit, a trough over a peak signature is detected for wells in compartments C and D. This phenomenon is linked to the water flooding of the sands included in this reservoir. However a peak over a trough is evidenced in wells W-6 and W-7, signal which appears to be associated to the gas expansion in their associated compartments given the gas injection activity which takes place in this sector.

Changes in the 4D signatures can be laterally differentiated across the several compartments. In fact, a clear trough signal (blue) is detected in the well W-1 (compartment C), response which seems to gradually revert along each reservoir segment until a strong peak amplitude (red) appears in well W-7 (compartment G). These changes appear to be associated with the perturbation of the connectivity introduced by the faults separating major compartments, for which their respective sealing properties mainly influence the pressure dissipation and water flooding, by both building the 4D signal. To highlight lateral and vertical variations in the time-lapse seismic changes, a similar well fence is created (Figure 3.13). In this case gamma ray logs (GR), base (blue log in the AI track) and monitor 1 (red log in the AI track) P-wave impedance logs are displayed. Changes in impedances at well location can be used to track horizontal and vertical fluid replacement across the field. Increases in P-wave impedance are identified in between compartment C and F. These time-lapse effects are attributed to the watering of the reservoir sands (blue patch).

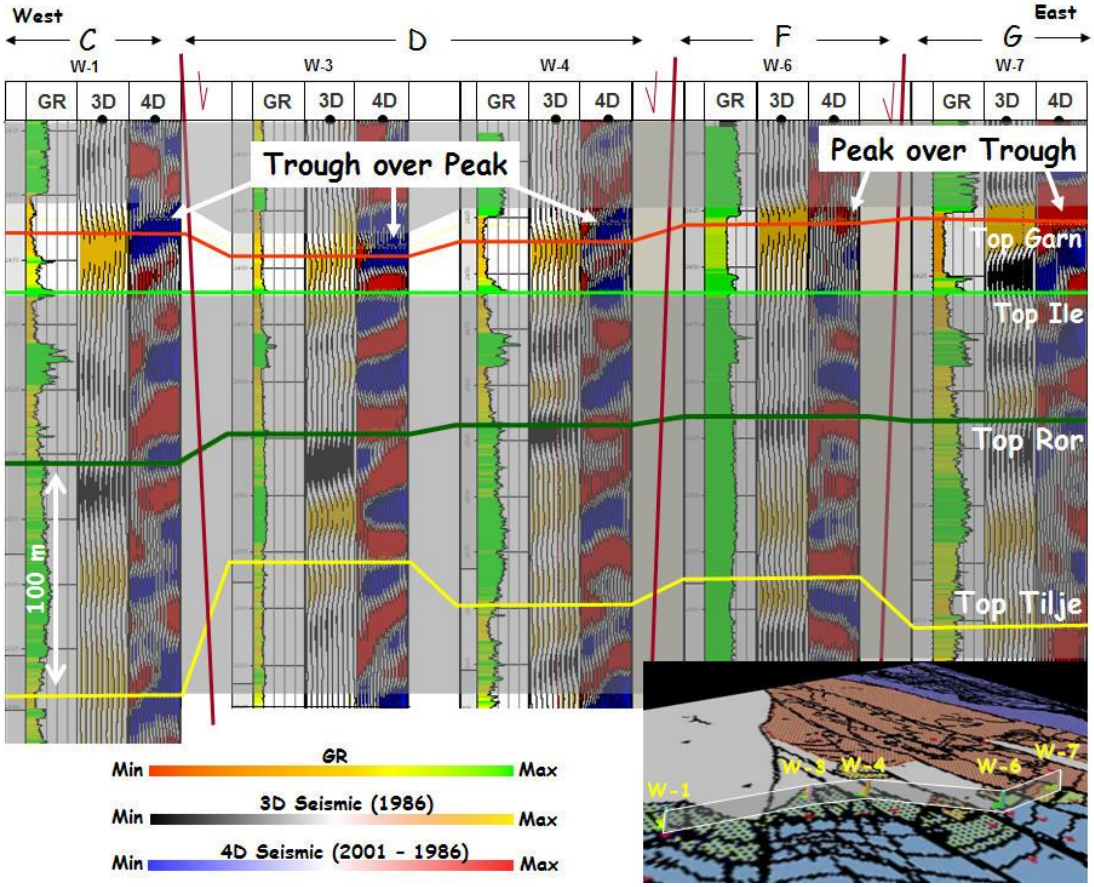

Figure 3.12. *Well seismic fence showing gamma ray logs (GR), 3D seismic (base line) and 4D seismic traces (monitor 1 – base line) for wells located in several compartments (C, D, F and G). The Garn reservoir is highlighted. Stratigraphic tops are identified using coloured lines. Major faults are represented as red segments. 4D seismic signatures for waterflooding (trough over peak) and gas expansion (peak over trough) are identified. Bottom right: location of the well seismic fence is displayed relative to the 2001 flooding map (see figure 2.16 for flooding map legend).*

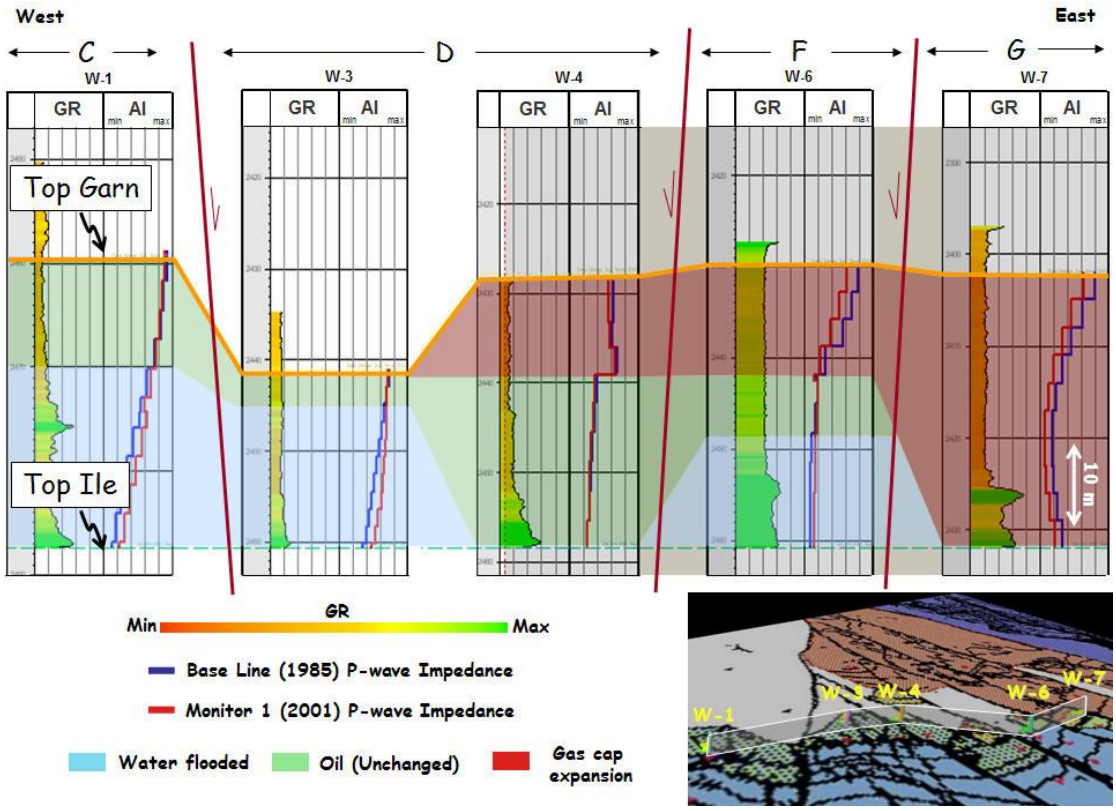

Figure 3.13. *Well P-wave impedance fence showing gamma ray logs (GR) and P-wave impedance logs (AI) for the base line seismic (blue) and the first monitor survey (red) for wells located in several compartments (C, D, F and G). Stratigraphic tops are identified using coloured lines. Faults are represented as red segments. Bottom right: location of the well seismic fence is displayed relative to the 2001 flooding map (see figure 2.16 for flooding map legend). Note lateral and vertical extension of the fluid replacement in the Garn Fm. Changes in the substitution seem to be associated with the presence of faults.*

Overlying the water flooded leg, an unchanged sector is observed in which no major P-wave impedance differences seem to be detected (green patch). This is particularly evidenced in compartments C and F. Also, in compartments F and G, gas expansion has been identified and it seems to be pinching out within compartment D.

Variations in the continuity of these fluid replacements help to highlight the connectivity between compartments. Changes in the oil and gas legs are evidenced when comparing wells located in compartment C, D, F, and G. Their vertical disparities across segments are strongly linked to the inter-compartment faults acting as flow conduits or barriers. Particular contrast is observed between compartment D and F where the reservoir seem to be water flooded in different proportions as indicated in well W-4 when compared to W-6, thus faults in between these segments seem to be controlling the drainage strategy. In terms of the gas expansion, a complex interaction in the fluid substitution is occurring in between compartments F and G. This might cause interference in the total 4D signature measured in the associated segments, not only in terms of saturation but also pressure changes.

3.6 The 4D seismic signature in seismic cross-sections

To evaluate the variation of the 4D character in the field a sequence of three seismic profiles are extracted across the field (Profiles 1-3). By means of these sections the time-lapse seismic response given by the difference monitor 1 - base is analysed following the 4D signal (peak and trough amplitudes represented in red and blue respectively) observed along the several compartments. To highlight the top of the reservoir, a blanketing has been applied in the overburden and underburden. Within each profile, compartments are identified (D to H), faults are represented as red segments and the top reservoir is also marked by the thin black line. Each section is located onto the 2001 flooding map (see figure 2.16 for legend) which is also used for correlation purposes.

At the top of the study area Profile 1 (Figure 3.14) shows a gas-related peak over trough (red over blue) between compartments F and G. The fault separating segments E and F seems to be expressing the limit for the gas expansion zone which according to the

flooding map dominates the north-eastern part of the field. Also a water flooding signature (trough over peak as blue over red) appears along compartments D and E.

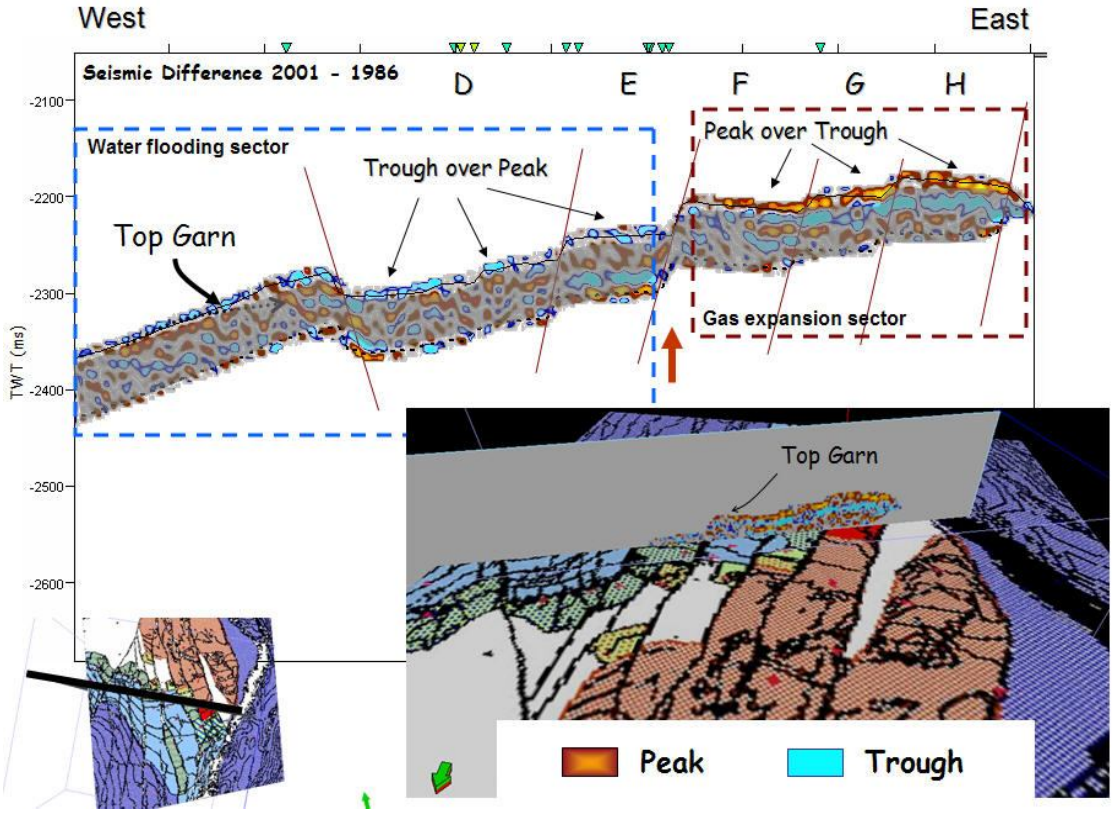

Figure 3.14. *Profile 1 showing seismic difference 2001 (monitor 1) – 1986 (base line). Top Garn interpretation (picked from 3D seismic) is highlighted and represented with a black line. Faults are shown as red segments separating compartments identified as D, E, F, G and H. Peak over trough (gas expansion) and trough over peak signal (water flooding) are identified. Bottom right: location of the seismic profile is displayed relative to the 2001 flooding map (see figure 2.16 for flooding map legend). A water flooding signature appears along compartments D and E. As in profile A the fault separating compartments E and D (indicated by red arrow) isolated the gas expansion.*

This observation suggests a fault-related fluid substitution taking place in which the fault properties dominate flooding extension. This behaviour is in agreement with the analysis shown in Kahar et al. (2006) who propose faults as one of the fluid flow mechanisms controlling drainage in the Heidrun field. Further south, in Profile 2 (Figure 3.15) the water flooding signal has fully swept compartment F while the gas expansion signature backs down towards compartment G and H. The gas-related peak is in this case bound by the fault separating segments F and G. This progressive flow

affecting the Garn reservoir suggests continuous oil substitution as water flows updip only being interrupted or enhanced by the faults acting as barriers or conduits.

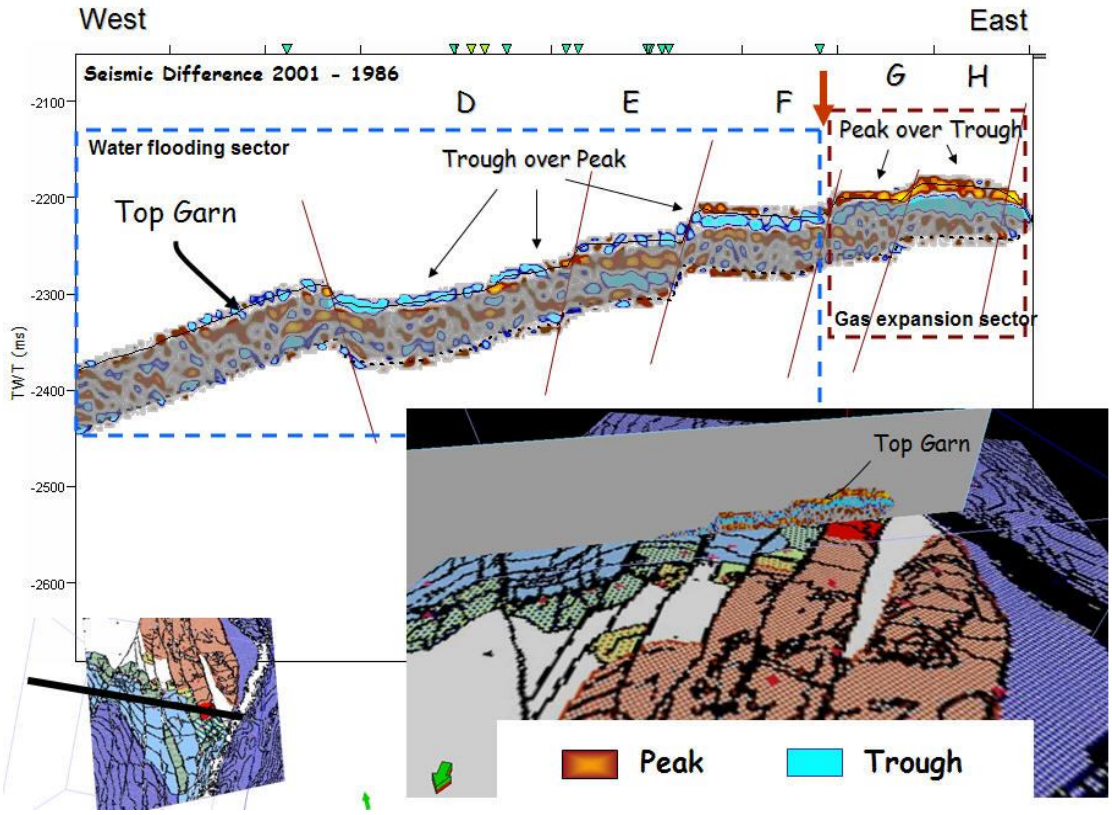

Figure 3.15. *Profile 2 showing seismic difference 2001 (monitor 1) – 1986 (base line). Top Garn interpretation (picked from 3D seismic) is highlighted and represented with a black line. Faults are shown as red segments separating compartments identified as D, E, F, G and H. Peak over trough (gas expansion) and trough over peak signal (water flooding) are identified. Bottom right: location of the seismic profile is displayed relative to the 2001 flooding map (see figure 2.16 for flooding map legend). The water flooding signal has fully swept compartment F while the gas expansion signature backs down toward compartment G and H. The gas related peak is in this case bounded by fault separating compartments F and G (indicated by red arrow).*

In the final profile (Figure 3.16) compartments D, E, F, G are completely watered out. An intricate interaction between the gas expansion is evidenced in compartment H. Water has fully invaded compartment G probably affecting also compartment H, however sidelobe interference challenges the interpretation on such a complex interaction. Nonetheless, the detected 4D effects have been cross-correlated with the associated flooding map. The blue-coloured trough amplitudes appear to be dimming

towards the south particularly in compartment D where the original water oil contact has been previously identified.

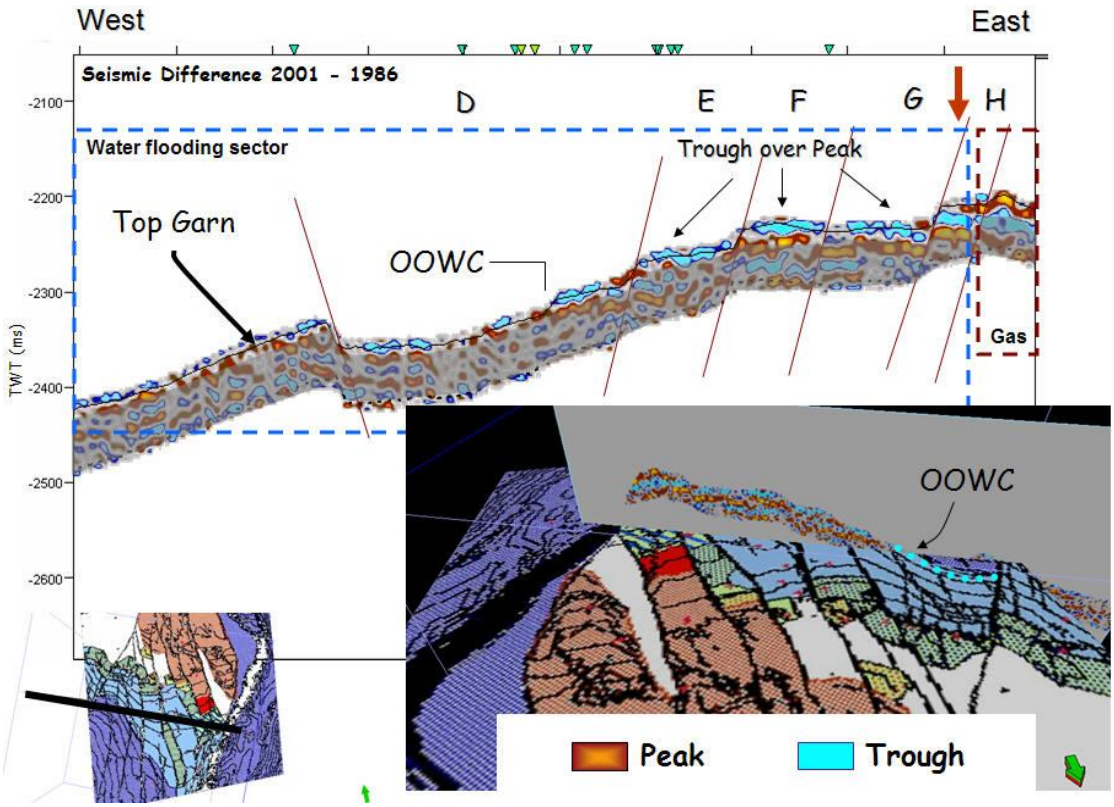

Figure 3.16. *Profile 3 showing seismic difference 2001 (monitor 1) – 1986 (base line). Top Garn interpretation (picked from 3D seismic) is highlighted and represented with a black line. Faults are shown as red segments separating compartments identified as D, E, F, G and H. Peak over trough (gas expansion) and trough over peak signal (water flooding) are identified. Bottom right: location of the seismic profile is displayed relative to the 2001 flooding map (see figure 16 for flooding map legend). Compartments D, E, F, G are completely watered out. The gas expansion is bounded by fault separating compartments G and G).*

3.7 The 4D seismic versus the fluid flow simulator output

In terms of the interaction between gas, oil and water phases during fluid replacement, the comparison between time-lapse seismic and the simulator output helps to identify those scenarios where the simulation model might introduce inconsistencies which lead to a mismatch between the forecast and the 4D signature. In order to highlight such a phenomenon, Profile 2 is selected to correlate the 4D difference monitor 1 (2001) – base

(1986) with the simulation results. As time-lapse seismic effects in the Garn reservoir have been mainly associated with the water breakthrough for the reservoir sands, water saturation changes have been calculated between base line production (1995) and the monitor 1 acquisition (2001) to qualitatively evaluate the mismatch between the 4D signal and the calculated forecast.

Figure 3.17 shows at the top the 4D seismic difference monitor 1 – base overlying the water saturation change (as derived from the simulator) in between those vintages. Three water injectors (in blue) appear to be flooding from the downdip reservoir toward the producer located in segment F (green). Seismic changes (trough amplitudes) are particularly observed in compartment D, E and F which are associated with the water flooding of the Garn Fm. These changes are useful to validate the forecast given by the water changes calculated from the 1995 and 2001 simulation steps. However a mismatch between both seismic and simulator (previous history matching) is observed in compartments F and G. Reservoir sands in compartment F have been watered out in the seismic difference but no changes appear in the simulator. An evaluation of the observed and predicted water cut (Figure 3.18) at the producer well (drilled in compartment F) shows higher water values for the well measurement relative to the simulator output. This observation is in agreement with the 4D seismic signal which also highlights full water breakthrough for this particular compartment. Similarly, gas-related peak amplitudes are observed in compartment G but no response associated with this change is evidenced in the prediction, pointing out another discrepancy in the same section. As in Garn Fm. fluid movement is typically affected by the flow properties of the faults affecting the reservoir, an underestimation of their transmissibilities compromises the quality of the outcome. This seems to be the case for faults separating compartments E, F and G which are controlling the simulator fluid influx not yet seismically validated.

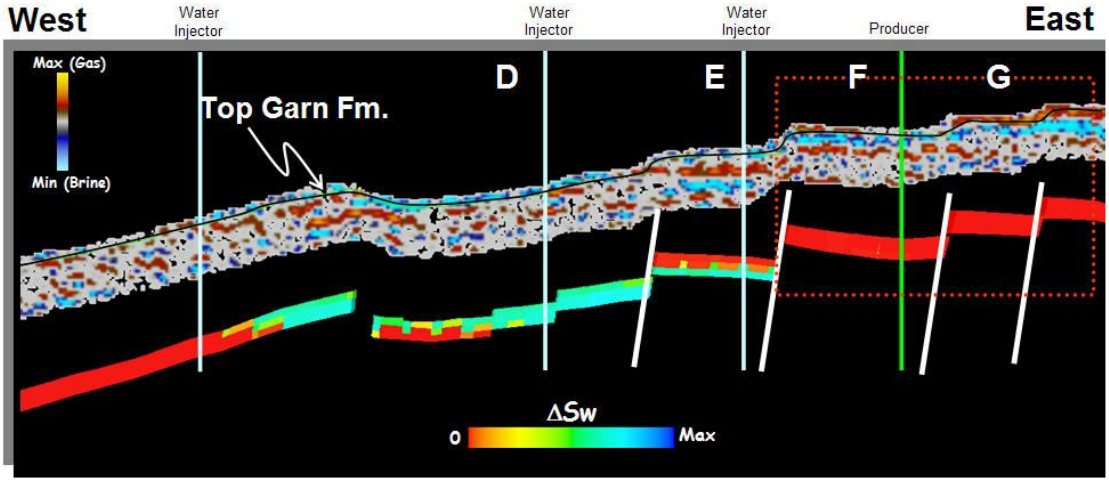

Figure 3.17. *Top: Seismic difference 2001 (monitor 1) – 1986 (base line). Top Garn interpretation (picked from 3D seismic) is represented with a black line. Below: Water saturation change given between seismic vintages as calculated from the simulation output at the seismic profile location. Three water injectors (light blue) and a producer (green) are identified. A mismatch between both seismic and simulation model (previous history matching) is observed in compartment F and G. Reservoir sands in compartment F have been watered out in the seismic difference but no changes appear in the simulator. Also gas-related peak amplitudes are observed in compartment G but no response associated to this change is evidenced in the prediction.*

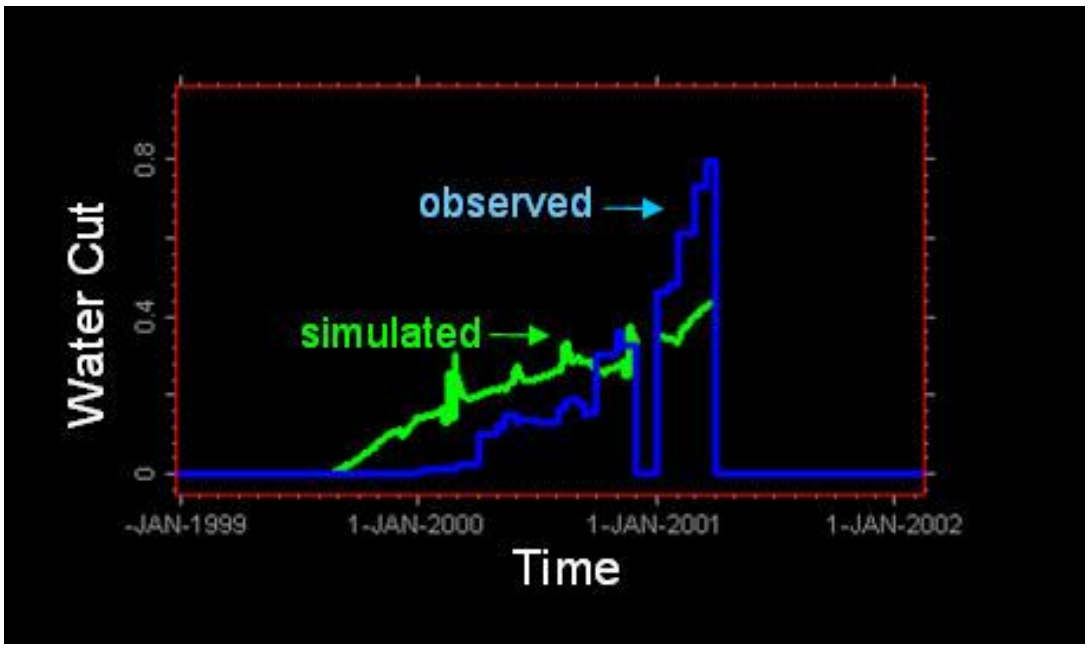

Figure 3.18. *Evaluation of the observed (blue) and predicted water cut (green) at the producer well drilled in compartment F (see Figure 3.17) showing higher water values in the well measurement relative to the simulator output. This observation is in agreement with the 4D seismic signal which also highlights full water breakthrough for this particular compartment.*

3.8 Evaluation of the water flooding distribution using 4D seismic

It is confirmed that 4D seismic changes can effectively be used to track water saturation changes in the reservoir. In a field with no pressure segmentation during production (e.g. pressure maintenance strategy) water saturation changes are strongly affected by the fluid-flow properties of the fault network. In this context a mismatch between 4D seismic changes (particularly in water saturation change) across compartments (i.e. lack of continuity) can lead to the evaluation the fault sealing phenomenon (Sønneland et al., 2000).

To evaluate the lateral continuity of the 4D seismic signal across compartments, an evaluation of the P-wave impedance (AI) differences between 2001 and 1986 is performed. For this purpose, a geocellular (or gridded) representation of the AI change data volume has been employed (Figure 3.19). Subsequent classification of the 4D impedance amplitudes into discrete facies allows separating three classes defined as Code 0, Code 1 and Code 2 (Figure 3.20) which have been locally correlated to gas expansion, backscatter (associated to random noise) and water flooding respectively using the information included in the flooding maps. The identified classes are then categorized by detecting connected volumes given the geocellular representation of the 4D seismic data (Figure 3.21). For the Garn reservoir a major water flooded volume (pink) is separated. This appears to follow the original and post-production water front geometries and is also linked to the wells in which water breakthrough has been observed (Figure 3.22). Also, the extracted 4D body appears to be correlated with the location of major fault segments as these structural elements affect the spreading of the 4D signal along the field. Nevertheless differences between the pink body and the flooding map in the south-eastern compartments are also identified suggesting the need for further integration of the 4D seismic data.

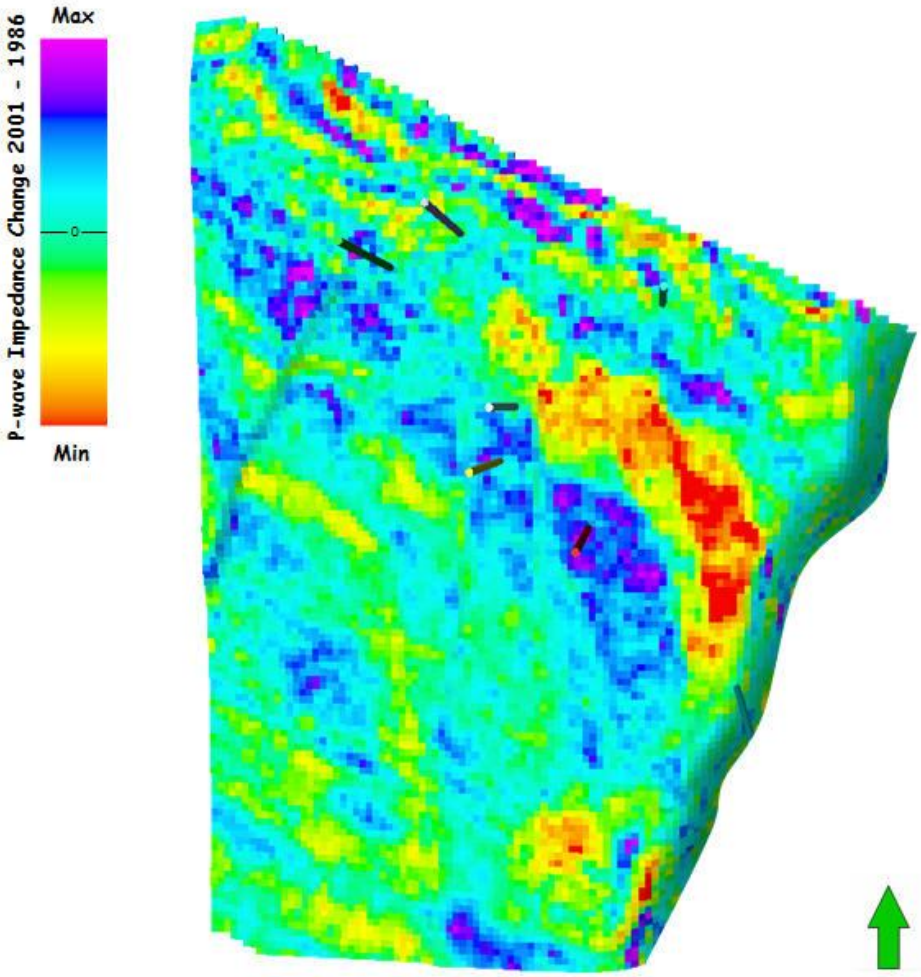

Figure 3.19. *Gridded representation of the P-wave Impedance change between 2001 and 1986 vintages.*

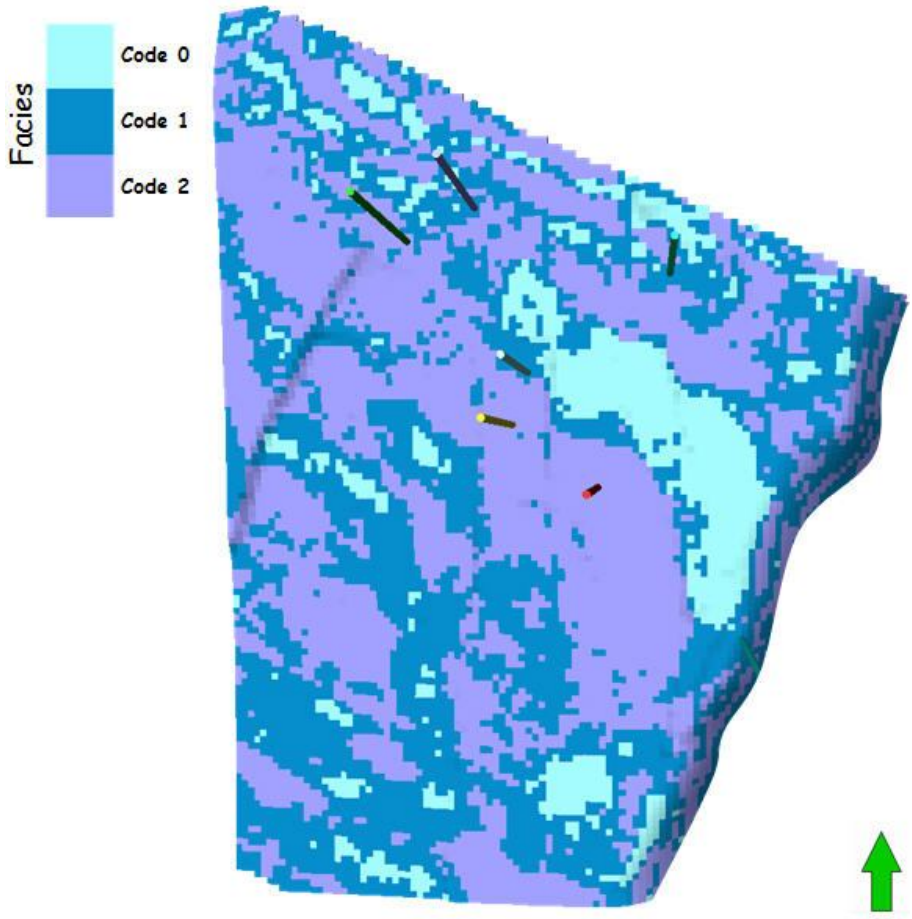

Figure 3.20. *Classification of the 4D impedance change (2001-1986) into discrete facies. Defined classes Code 0, Code 1 and Code 2 have been locally correlated to gas expansion, backscatter (randomized noise) and water flooding respectively using the information included in the flooding maps.*

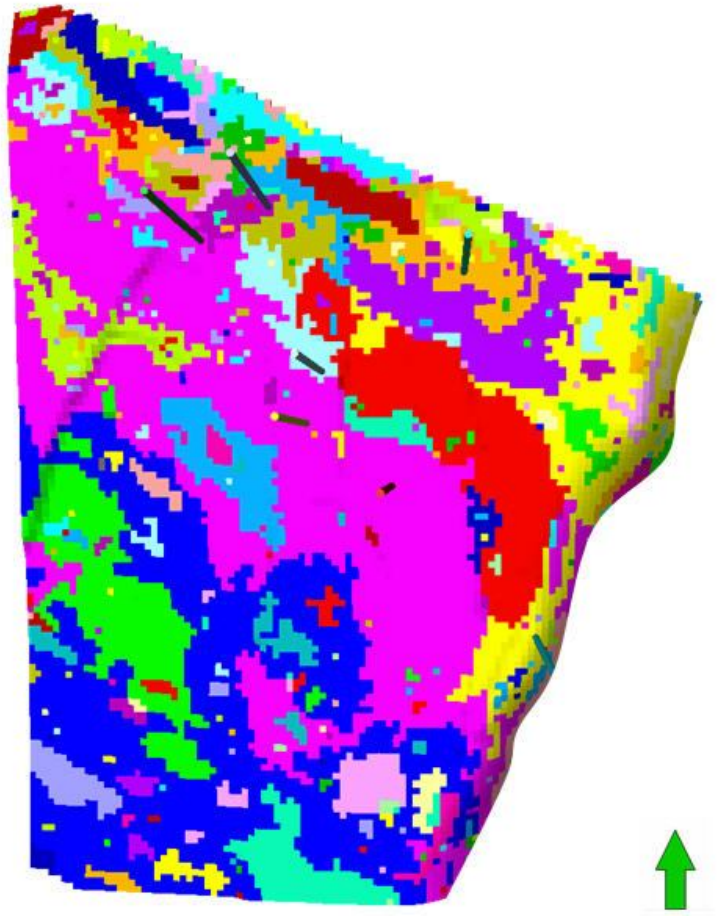

Figure 3.21. *Separation of connected volumes. Each volume is represented with a different colour.*

Using field activity information between 1995 and 2001 derived from 7 wells, differences in water cut at the survey vintages are calculated. Given the water cut change versus the P-wave impedance change at those particular well positions water saturation changes are now calculated using the 4D seismic attribute approach presented by Floricich et al. (2005). According to such technique the time-lapse change ΔA derived between two given seismic vintages can be approximated as follow:

$$\Delta A \approx C_s \Delta S_o + C_p \Delta P \tag{3.5}$$

for ΔA extracted on the area of interest, ΔS_o and ΔP the average oil saturation and pressure changes respectively and C_s and C_p constant coefficients of the expression (invariant in the reservoir) to be calibrated with the well activity.

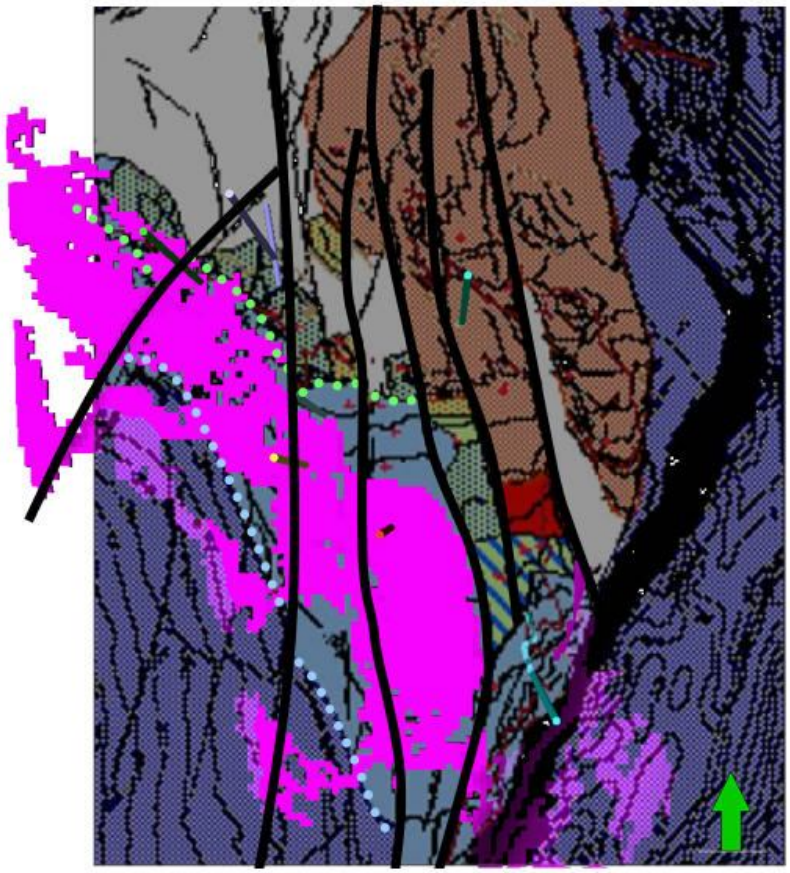

Figure 3.22. *Using the classification of the P-wave impedance difference as a filtering tool (Figure 3.20) and observed connected volumes (Figure 3.21), watered reservoir sands are isolated. For the Garn reservoir a major water flooded volume (pink) is separated. It appears to roughly follow the original and after production water front geometries (dotted blue line and dotted green line respectively) and is also linked to the wells in which water breakthrough has been observed (see figure 2.16 for flooding map legend). Faults separating reservoir compartments are represented by black segments.*

Related P-wave impedance changes can be approximated to water cut changes assuming a two phase system (only oil and water) and consequently the oil fraction (S_o) and the water fraction (S_w) complements in the total pore fluid volume:

$$S_o + S_w = 1 \tag{3.6}$$

where S_w has been directly related to the measured water cut when assuming the reservoir behaves as a oil filled tank.

Well	ΔS_w	$\sigma(\Delta S_w)$	ΔP (bar)
A	0.93	0.1	-8.51
B	0.23	0.1	-11.93
C	0.73	0.1	-8.14
D	0.07	0.1	-8.45
E	0.46	0.1	-10.24
F	0.80	0.1	-12.50
G	0.02	0.1	-17.68
			$\Delta P_{average}$ = -11.06
			$\sigma(\Delta P)$ = 3.4

Table 3.1. *Well data used for the pressure and saturation inversion. Relative location of wells is shown in Figure 3.23.*

Table 3.1 shows water saturation and pressure changes in the training wells employed for the inversion technique. This dataset has been also displayed in Figure 3.23. Differences between the water cut values between seismic vintages are calculated at each location and used as average in a pdf with normal distribution and standard deviation equal to 0.1. Pressure changes are extracted from the simulation as well measurements are not available. However, as the simulation model is not fully history matched, uncertainties are included in such observations. To tackle such drawback, a pdf with normal distribution is defined using the average of the pressure changes for the 7 wells. This assumption might impact on the final outcome, nonetheless, pressure changes in the reservoir between given vintages are low (average pressure decrease of 5 % in 6 years) and relatively uniform throughout the field (standard deviation $\sigma \sim 3.40$ bar) thus pressure change have limited impact on time-lapse seismic effects and major 4D amplitude changes are roughly proportional to water saturation changes.

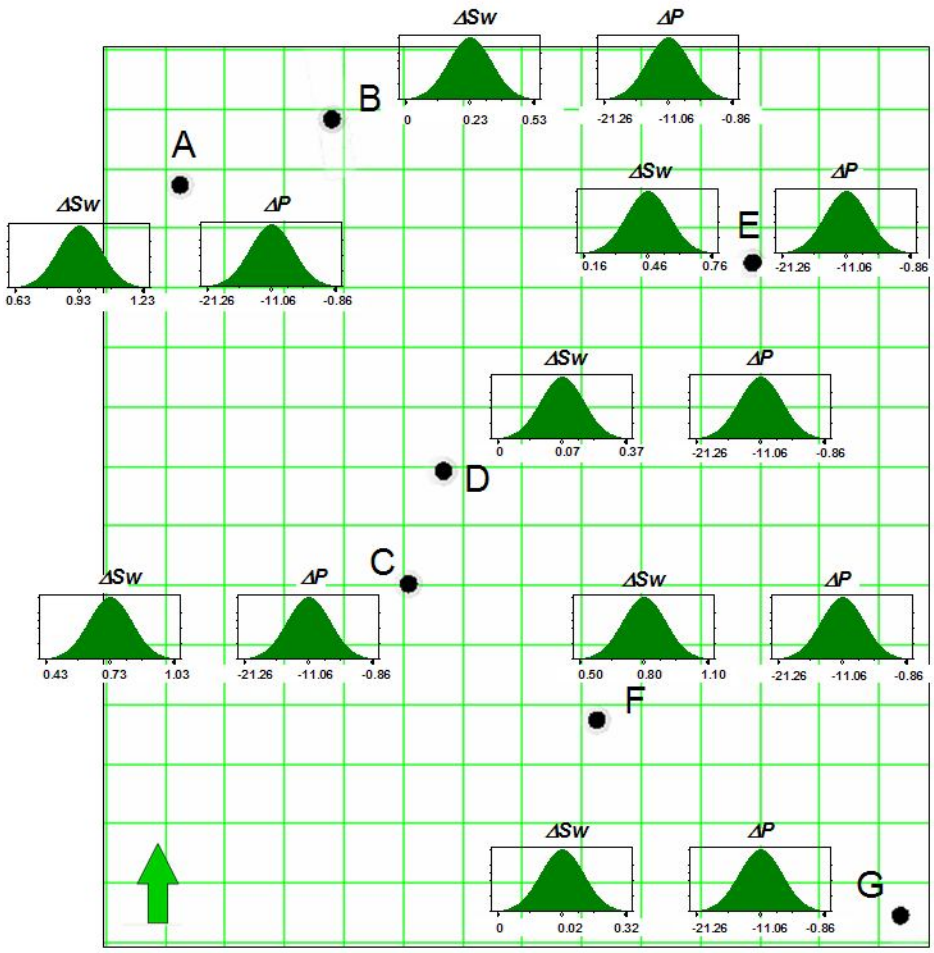

Figure 3.23. *Training wells and uncertainties for the calibration of the P-wave Impedance change.*

Indeed, the separation of the pressure and saturation changes by means of the P-wave impedance changes (Figure 3.24) indicates that the saturation coefficient *Cs* contributes the most to the final 4D signature (Figure 3.25). Cross-plot between the observed water cut change at the well position versus the estimated water cut given by the 4D seismic data is displayed in Figure 3.26. Inspection of the histograms for the water saturation changes derived from simulator and 4D seismic indicates a faster water breakthrough in the time-lapse seismic prediction as higher water saturation changes are observed in 4D seismic estimation when compared with the values from the fluid flow simulation (Figure 3.27). This observation might be associated with the dispersion of the water saturation changes in the simulation when compared with the geometry of the water-related 4D seismic signal (Figure 3.28). Consequently a consistent integration of the 4D seismic information into the reservoir model should allow increasing the water cut levels on the simulation output as indicated by 4D seismic and the well production data.

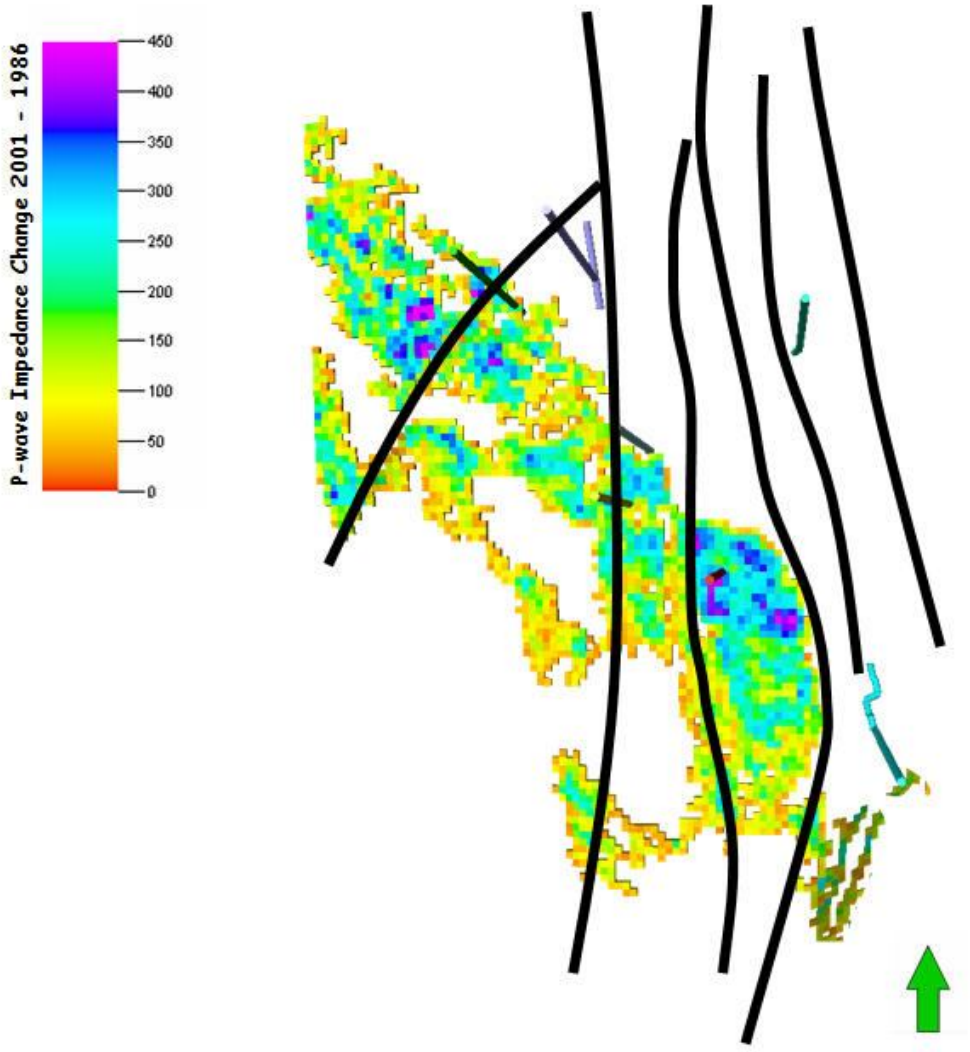

Figure 3.24. *Geocellular representation of the 2001 – 1986 P-wave impedance difference filtered according to the connected volume identified along the water flooded reservoir. Fault segments are displayed as black lines. Note that P-wave impedance changes within the filtered body are associated to a hardening response (positive values) as expected from a water flooded region.*

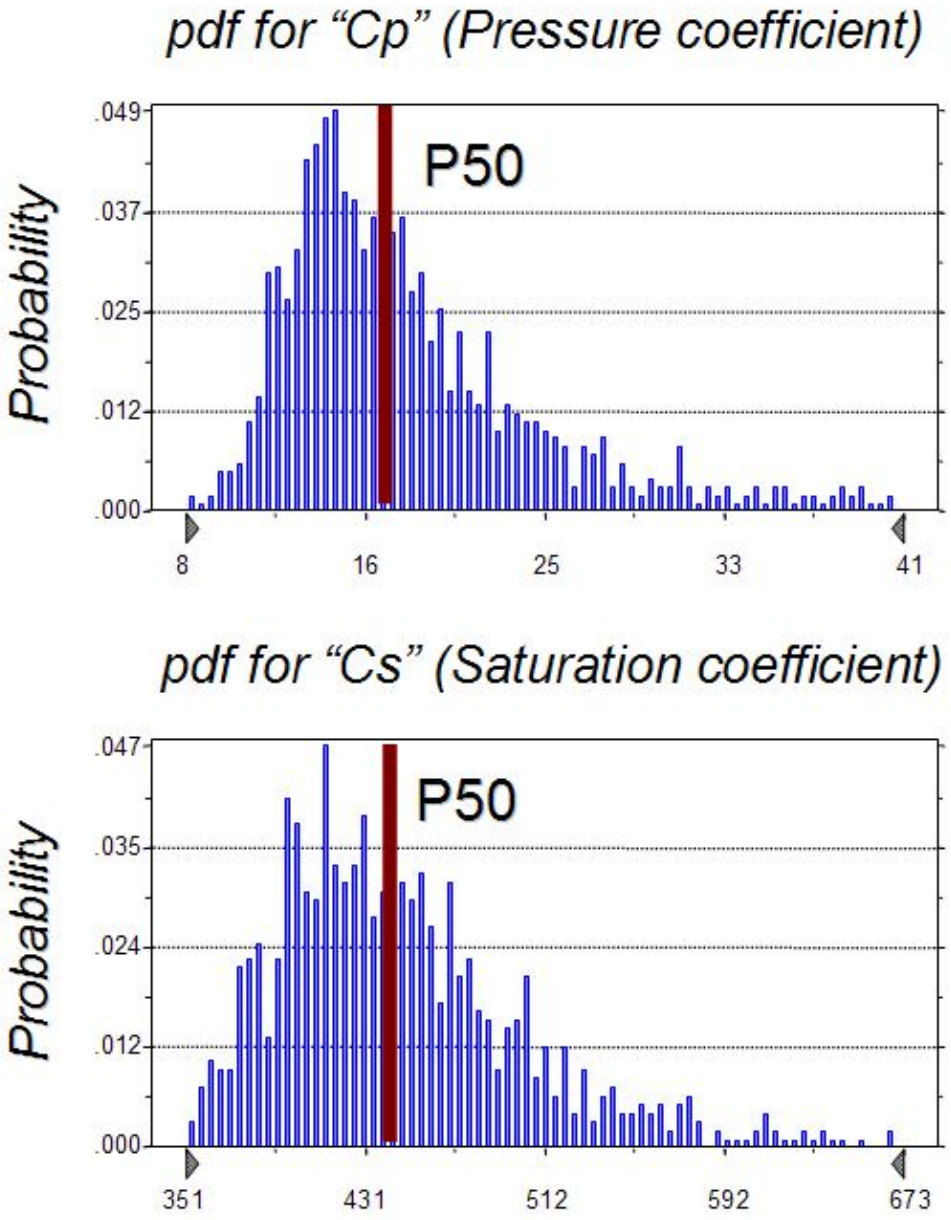

Figure 3.25. *Probability density functions (pdf) for the pressure (Cp) and saturation coefficient (Cs) estimated via the 4D seismic attribute approach presented by Floricich et al. (2005).*

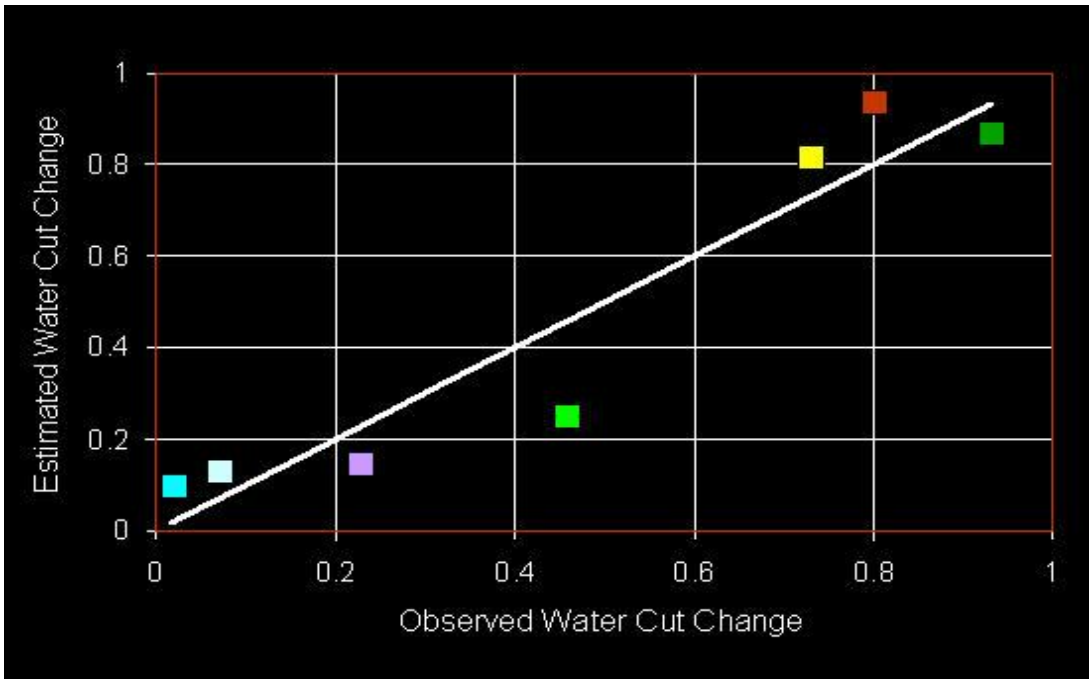

Figure 3.26. *Cross-correlation between observed water cut (measured from production logs) and predicted water cut changes (P50 estimation derived from P-wave impedance changes) at the well position. Perfect correlation has been represented with the white segment. (Standard error in the prediction ~ 16%).*

Also, as in the traditional 3D seismic analysis, lack of lateral coherence (continuity) of the 4D derived water changes seems to be in agreement with the presence of faults, hence lateral changes in *ΔSw* are also related to the inter-compartment communication given by the fluid-flow transmissibility properties of faults. This observation motivates the search of alternative procedures to assess flow-related fault properties using the time-lapse seismic data which can help to mitigate the lack of aerial coverage introduced in the well-dependent fault property assessment. Therefore, to decrease the mismatch between seismic and simulator, quantitative analysis of the continuity of the time-lapse seismic signal and its contrast across compartments is analysed in Chapter 4 in order to improve the evaluation of the reservoir fault communication in the Heidrun field.

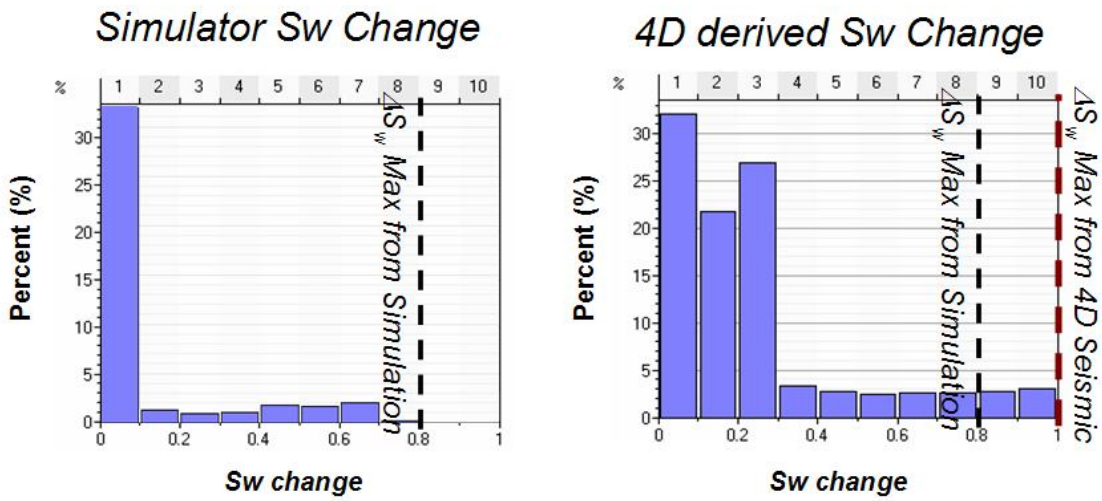

Figure 3.27. *Evaluation of the histograms for the water saturation changes derived from simulator (left) and 4D seismic (right) indicates a faster water breakthrough in the time-lapse seismic prediction as higher water saturation changes are observed in the 4D seismic estimation when compared with the values from the fluid flow simulation.*

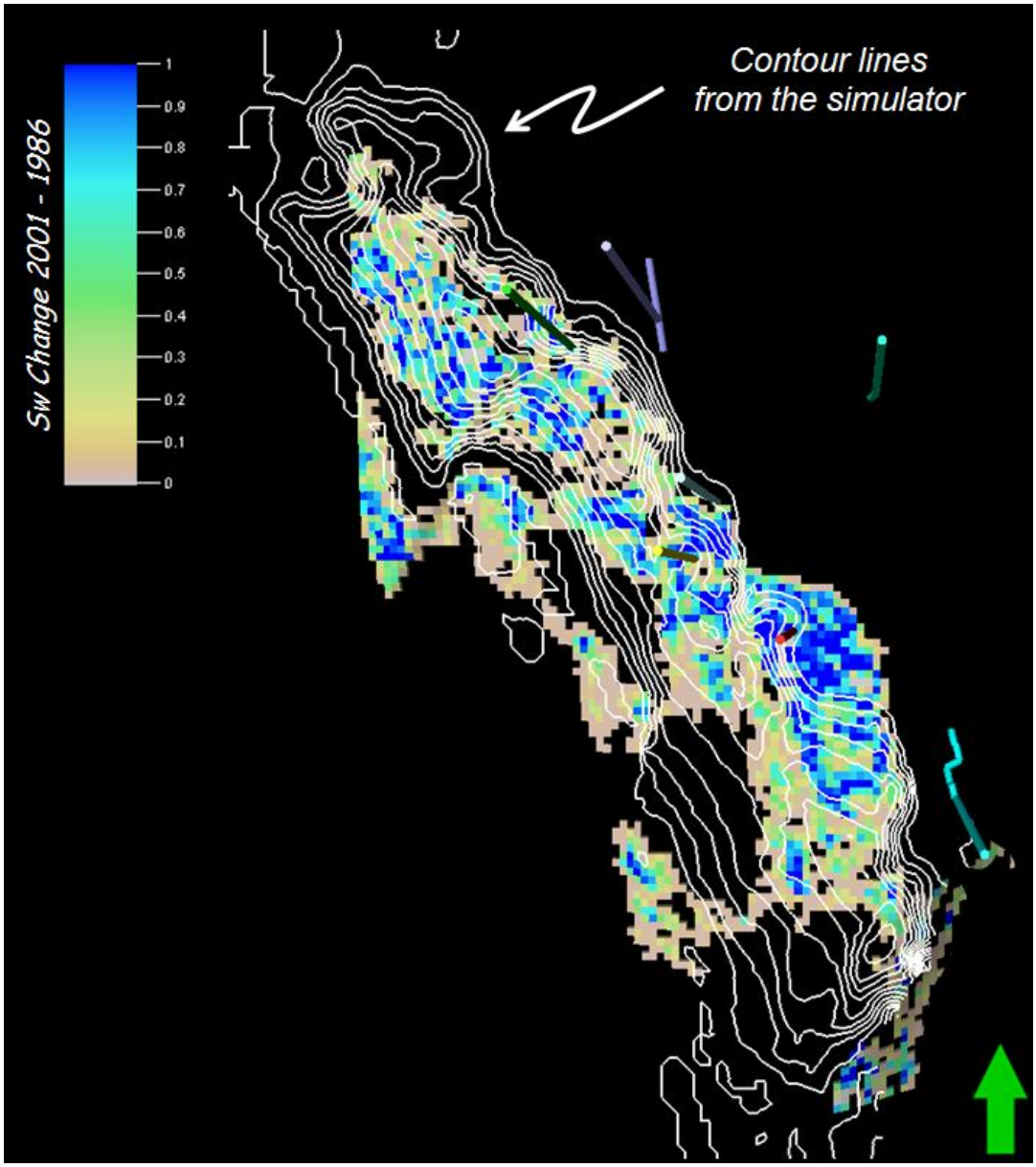

Figure 3.28. *Estimated water saturation change (P50) using the P-wave impedance difference in the 4D seismic attribute approach presented by Floricich et al. (2005). Contour lines (white) from the simulator water change are also displayed. Spatial dispersion of the water saturation changes in the simulation is evidenced when compared with the geometry of the water-related 4D seismic signal.*

3.9 Summary

The 4D seismic signature of the Fangst Group in the Heidrun Field is characterized by a strong character which appears to be coherent with field production. A sensitivity analysis reveals that the geological framework contributes a great deal to the petrophysical properties (i.e. porosities) which enhance such response. Yet, this study shows that structural compartmentalization affects importantly dynamic changes represented by the 4D seismic signature. Indeed, variation of the 4D seismic character in terms of continuity and amplitude contrast is identified between compartments as indicated in time-lapse cross-sections and maps. This seems to reveal a fault seal control on the extension of dynamic changes given by field production. In particular, faults separating compartments D, E, F, G, and H constrain the time-lapse seismic signature which is in turn dominated by saturation changes. Consequently, these faults appear to define the water-flooding as well as the gas expansion in the field. Also discrepancies between 4D seismic and simulator predictions are observed. This might occur as a result of limited understanding of the transmissibility capacity of faults. This observation motivates the study of finding alternative ways to quantitatively evaluate fault properties in the Heidrun field, particularly using 4D seismic as this seems a valuable tool to characterize the effects of the fault seal phenomena on the field production. Also, this can help with the lack of aerial coverage of the well data which is traditionally used in the fault property assessment.

Chapter 4

A quantitative approach to evaluate reservoir fault properties using 4D seismic

Fault transmissibility multipliers inserted into the simulation model to represent the behaviour of faults are based on geological understanding and are uncertain because of the sparse nature of well data used in their estimation. Also fault multipliers obtained in the history matching process are ambiguous as they might not be in agreement with the geological framework. In this chapter, a new technique is proposed in which 4D seismic data is used in an effort to more fully resolve the spatial distribution of the fault properties. To achieve this task, inter-compartment amplitude contrast and statistics of spatial variability for the 4D signatures are derived from a 4D attribute map. It is shown that a quadratic polynomial expression involving both measurement parameters can be used as the best fit function for the fault permeability. Application to modelled 4D seismic with a synthetic reservoir model and a typical production scenario produces encouraging results.

4.1 Introduction

The geological analysis of fault seal behaviour for the purposes of reservoir simulation is achieved by utilising well data. In particular, the shale gouge ratio method has proven to be an advantageous fault-seal predictor due to its versatility and applicability in reservoir models (Yielding 2002). Here, the net contribution of shale in a reservoir zone slipped in a fault throw interval is linked to the trap efficiency. Its capability to predict fault composition has been employed by Manzocchi et al., (1999) to derive fault permeability and hence fault transmissibility multipliers which are ultimately implemented in reservoir flow simulators. However, this approach is restricted by available well coverage, which can introduce considerable uncertainty.

More recently, time-lapse seismic has played a major role in the analysis of the dynamic connectivity (Sønneland et al. 2000). Its effects are in general a combination of pressure and saturation changes (MacBeth et al. 2006) which, for compartmentalized reservoirs, seem to be associated with the sealing behaviour of the faults. Based on this observation, and in a new effort to constrain reservoir flow, this chapter introduces a new workflow in which 4D seismic is employed as a tool to quantify the inter-compartment communication and hence enhance the fault property assessment.

4.2 Estimating fault properties using 4D seismic: The new approach

The time-lapse seismic signature given by the difference between two seismic attributes extracted from acquisition vintages has been employed to deduce reservoir changes during production. As part of the qualitative interpretation, 4D seismic anomalies are linked directly to changes into the reservoir (Sønneland et al., 1996; Anderson et al., 1997; He et al., 1998). They are commonly associated with changes in water saturation in case of nearby injector or producer exhibiting a watercut. If gas appears in the reservoir as a result of breakout depletion or if watercut is not observed for the production wells, anomalies are then associated with pressure changes (MacBeth et al., 2006). When calibrated with historical data from producers and injector wells, the signature of the seismic change given between repeated seismic surveys can be quantitatively related to pressure and saturation changes in the reservoir. Following this understanding, the overall spatial variability of the 4D attribute represents a valuable

tool to assess the continuity of the dynamic changes in the reservoir. Indeed, for a given structural framework, dynamic reservoir changes lead to a compartmentalization of the 4D seismic signature which in turn is influenced by the fault rock properties controlling fluid flow communication (i.e. fault permeability).

4.2.1 The model

Typical hydrocarbon recovery processes such as water flooding are implemented in reservoirs to maximize flow and recovery. Resistance to flow is essentially controlled by coefficients related to viscosity and pressure gradient, such as permeability and length.

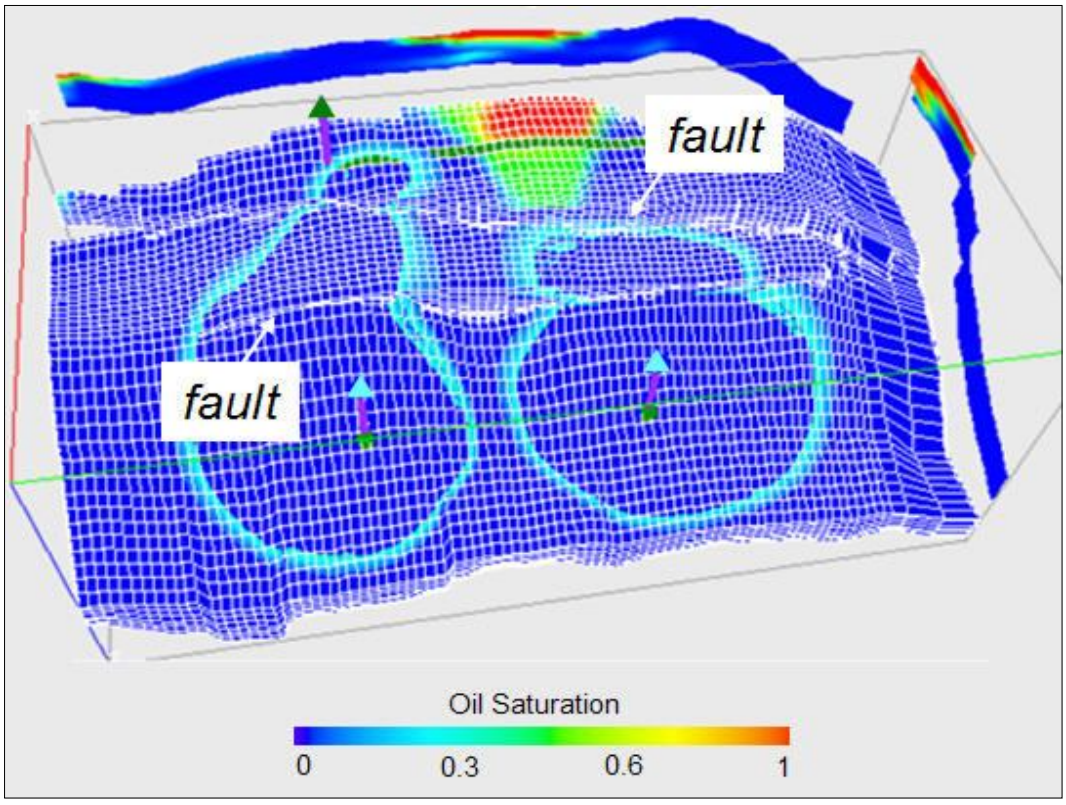

Figure 4.1. *Simulation model showing fault segments influencing the geometry of the water saturation front. During the fluid flow simulation, fault properties control the spreading of the water breakthrough. Note that the upper fault acts as a complete seal on the right hand side whereas on the left hand side the same fault behaves as a baffle. Injectors and producers are represented as blue and green triangles respectively. (Modified from MacBeth, 2007).*

When faults are present in the reservoir, flow is controlled by permeability and thickness of the fault and these properties act on the fluid phases influencing flow and defining the saturation profile (Figure 4.1). Based on such phenomenon, consider a homogeneous reservoir defined by the compartments *i* and *i*+1 (macroscale), both separated by a fault rock (microscale) approximated by a fault plane (Figure 4.2).

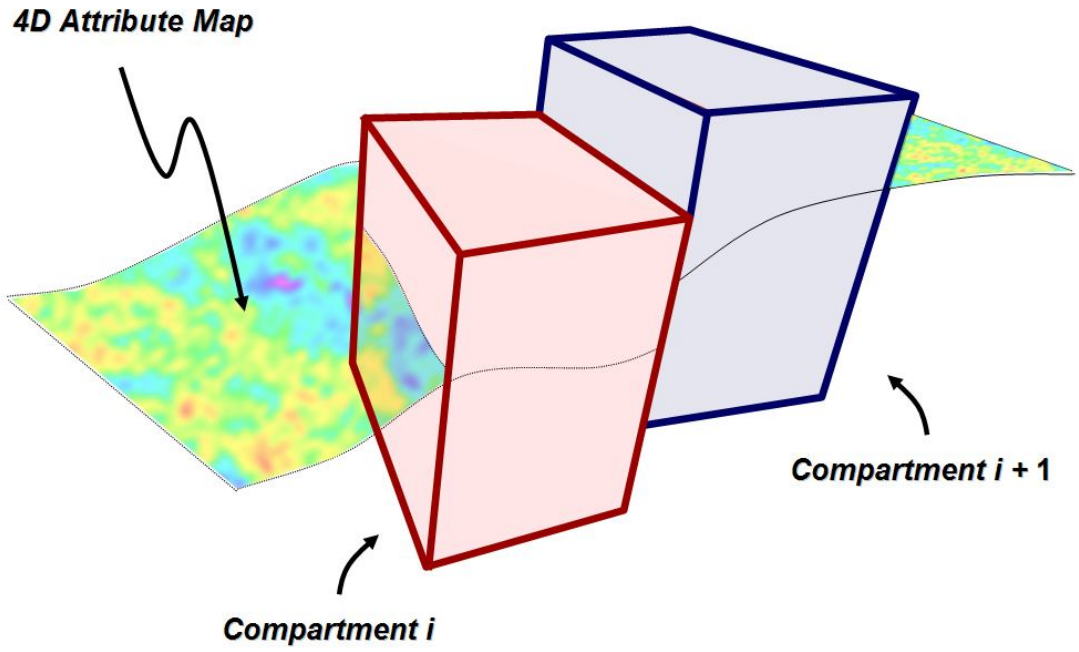

Figure 4.2. *Schematic configuration for a faulted reservoir. Compartments i (red) and i+1 (blue) are separated by a fault which in turn controls the dynamic changes expressed in the 4D attribute map.*

Each compartment has significantly better quality flow properties when compared to the fault rock. Also for a time frame allowing interaction of production changes (imposed by production and/or injector wells) with the fault-rock, bulk flow is altered by the pressure dissipation through the inter-compartment fault, affecting the water saturation profile in the reservoir. For this reason, major anisotropy in the dynamic changes can be associated with the altered flow properties of the fault rock. Under these assumptions, it is consequently expected that a coherent and non-patchy long period time-lapse seismic signature (integrating pressures and saturation changes) can be evidenced. This represents the support for the evaluation of strength and spatial continuity of the 4D signal which should be altered accordingly (Figure 4.3). In such scenario, the fault seal introduce the major control in the dynamic perturbation, utterly defining its regionalized character.

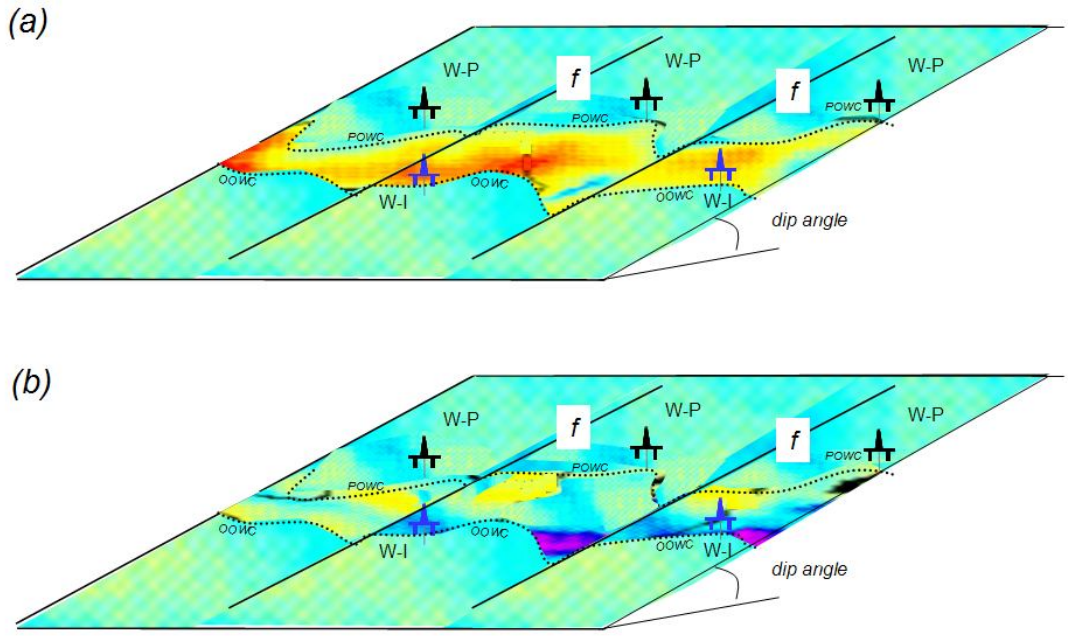

Figure 4.3. *4D seismic attribute map revealing anomalies due to drainage strategy defined by water injectors (W-I) and producers (W-P). Here we consider the strength of the resulting 4D seismic signature is linked to the production time frame will allows interaction of dynamic changes with the fault rock. (a) In the new approach, a coherent and non patchy long period 4D seismic anomaly is assumed. This acts as support for the evaluation of contrast and spatial continuity of dynamic changes. (b) A patchy short period 4D seismic signal showing no apparent regionalized character. Here the 4D signature might be difficult to relate to the interaction of flow with faults alone. Faults separating reservoir compartments are indicated (f). Original oil water contact (OOWC) and production oil water contact (POWC) area also displayed.*

To sense or visualize these signatures, a seismic attribute is estimated as measure of the seismic data. A good seismic attribute should be sensitive to reservoir properties enabling the prediction of a particular feature or property of interest (Chopra and Marfurt, 2007). The extraction of a seismic attribute map (as of 3D or 4D data) from a particular horizon can be expressed in terms of its sampling 2D grid. Figure 4.4 schematically represents a particular array of grid points organized in an array of evenly spaced rows and columns which discretize the estimated time-lapse seismic signature. The signature values are stored at the grid points representing the surface.

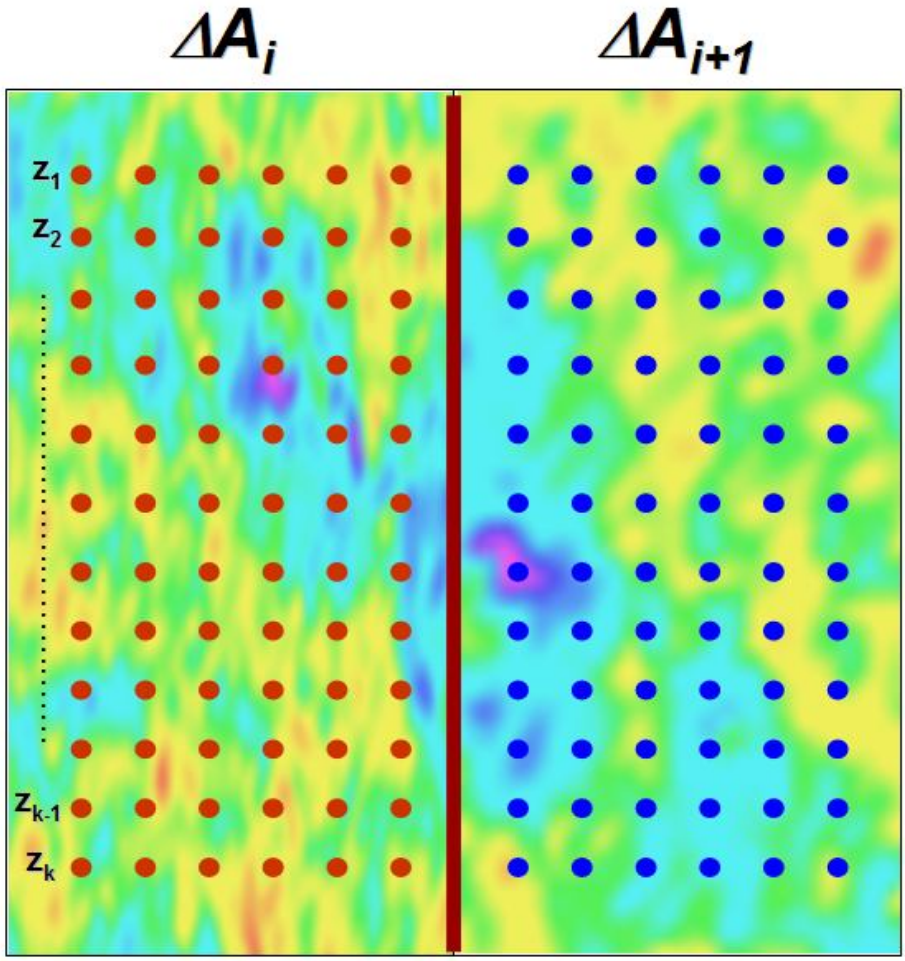

Figure 4.4. *Map view of the 4D attribute map showing time-lapse seismic signatures ΔA_i and ΔA_{i+1} associated to compartments i and i+1 respectively. Within the attribute map, its associated grid points are displayed and coloured according to each compartment (red and blue). The fault segment is represented by the thick red line.*

In terms of the production changes occurring in the reservoir and assuming no geomechanical effects, each sample measures a weighted contribution of pressures and saturations changes taking place at that particular point.

4.2.2 The method

As the saturation and pressure and saturation fields get perturbed by the fault rock properties (i.e. fault permeability), disruptions in the associated 4D seismic signature

are evidenced. To sense these changes, statistics of the 4D seismic signature are evaluated; in particular two measurement parameters are derived from the 4D seismic maps (Figure 4.5):

a) 4D inter-compartment difference: defined in this study as variable *x*, this parameter measures the 4D amplitude contrast between adjacent compartments using the average of the centred differences between neighbour compartments, defined at each fault segment position.

b) 4D Spatial Variability: defined in this study as variable *y*, this measurement captures the continuity of the 4D signatures. Several 1D variograms are calculated perpendicular to the fault segment and along the fault dip direction. The correlation lengths, as defined by the range of the variogram, are extracted in each case.

Based on both measurements, an empirical model is proposed in which dynamic changes expressed by the 4D seismic signature are linked to the fluid flow properties of the fault, particularly the fault permeability. The following quadratic polynomial model (or response surface) is postulated as the best fit function for the fault permeability representation:

$$k_f(x,y) = a_0 + a_1 x + a_2 y + a_3 x^2 + a_4 y^2 \tag{4.1}$$

where *x* and *y* are the parameters extracted from the 4D seismic as described above. For a given number of samples *k* included in a fault segment, equation (4.1) can be alternatively written as the following system of equations:

$$\begin{bmatrix} k_{f1} \\ k_{f2} \\ \vdots \\ k_{fk} \end{bmatrix} = \begin{bmatrix} 1 & x_1 & y_1 & x_1^2 & y_1^2 \\ 1 & x_2 & y_2 & x_2^2 & y_2^2 \\ \vdots & \vdots & \vdots & \vdots & \vdots \\ 1 & x_k & y_k & x_k^2 & y_k^2 \end{bmatrix} \begin{bmatrix} a_0 \\ a_1 \\ a_2 \\ a_3 \\ a_4 \end{bmatrix} \tag{4.2}$$

Consequently, the derivation of fault permeability from the 4D seismic attribute map requires the determination of the five coefficients of this polynomial expression. Their estimation can rely on the calibration of such expression in a sector with known (geologically based) fault properties (i.e. *SGR*-derived fault permeability). Once, these coefficients are known, it is possible to calculate fault permeability values for segments included in areas with poor well data control.

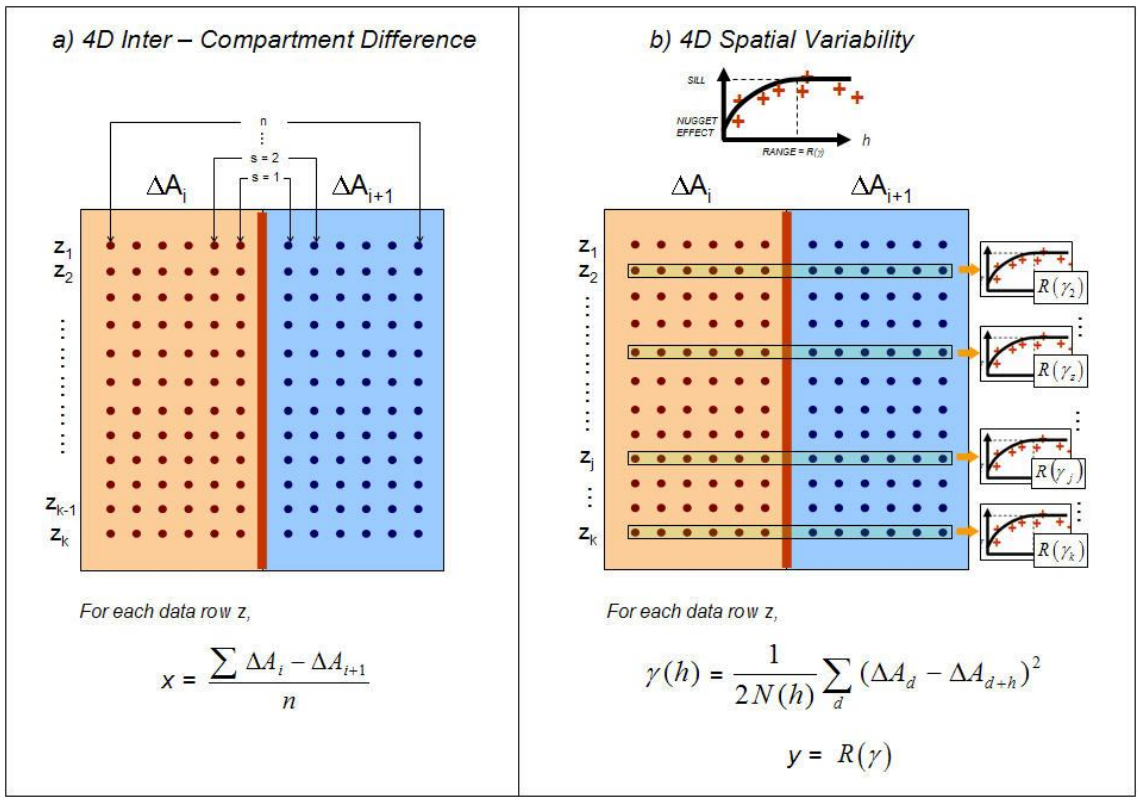

Figure 4.5. *Measures of the time-lapse seismic signature for fault seal analysis, derived for any specific reservoir sensitive 4D-seismic attribute: (a) the inter-compartment difference and (b) multiple 1D variograms with their respective correlation range extracted along the fault segment for each dataset row. Both measures appear to be correlated with fault seal behaviour.*

4.2.3 Uncertainty approach

In the application of the proposed methodology, uncertainties are introduced by means of the variogram modelling. Indeed, to extract variogram parameters (e.g. range) a model is fitted in a trial-and-error approach which leads to a non-reproducible solution.

To account for uncertainty in this inverse problem a simplified Bayesian approach (Bayes, 1793) is used in which the prior distribution is considered uninformative (all models are equally plausible a priori), and a consequence the posterior distribution becomes a likelihood function (Aster et al., 2005). With an error model based on individual data points *d*, noise measured in data assumed to be independent and normally distributed with standard deviation σ and expected *m* values for a particular model, the posterior distribution for each measured sample can be expressed as the truncated likelihood function:

$$p(m|d) = \frac{1}{\sigma\sqrt{2\pi}} e^{-\frac{(m-d)^2}{2\sigma^2}} \tag{4.3}$$

where *m* is limited by:

$$k_{f\ \min} \leq m \leq k_{f\ \max} \tag{4.4}$$

for $k_{f\ min}$ and $k_{f\ max}$ minimum and maximum fault permeability respectively.

Now, in order to evaluate the standard deviation of the noise included in measurements extracted from the variogram modelling, the following considerations are taken. In terms of the fitting of a model to capture the variogram range, it is a common practice to tackle this aspect by means of visual fitting using a graphical computer interface. This approach is strictly determined by the experience or additional information (e.g. from geology or geophysics). Nevertheless, if a statistical measure needs to be associated with such a procedure, an automatic variogram modelling can be used to assess the goodness of the fit via the statistical description of a population of measurements. Following the work presented by Pardo-Igúzquiza (1999), an automatic modelling helps to quantify the process by performing a statistical fitting in which each variogram point is weighted according to its uncertainty. By performing a non-linear minimization of the weighted squared differences between the experimental variogram and the model, a value for the variogram parameters (i.e. range) is therefore obtained. As illustrated by Pardo-Igúzquiza (1999) in the implementation of the automatic program, a selection of five different weighting functions can be performed yielding various estimates for the variogram range. These include:

1. An ordinary least squares fitting.
2. A weighting function which considers the number of data pairs used in each experimental variogram point (more weight is given to points with a higher number of data pairs).
3. A weighting function that considers the variogram model, meaning the experimental variogram points more closely to the origin receive more weight than experimental variogram points for larger distances.
4. A weighting function which considers the number of data pairs and the variogram model.
5. A weighting function which considers the variance of the variogram estimation.

Also four different variogram modelling can be employed (spherical, exponential, Gaussian and power models). In practice the selection of such models might be biased by additional screening of the data or based on assumptions related to the nature of the process controlling the spatial variability of the data.

Now, as a result of the statistical population for the variogram range, several realizations of 4D spatial variability are gathered. Assuming 4D inter-compartment difference invariant relative to the errors introduced by the variogram modeling, calibration of the coefficients in the quadratic polynomial expression (describing fault properties) is repeated for each 4D spatial variability realization yielding several representations of the response surface which are used to obtain fault property estimates (i.e. fault permeability) according to each model realization. Changes in the fault property estimates at each point included in the fault segment are used to derive a measurement of the standard deviation which is employed as indicator of the variability and is in turn appropriately used in the likelihood function described above. Minimum and maximum fault property estimates can be used to constraint the resultant likelihood function assigning end-member cases to be defined for this function (Figure 4.6). This process leads to a map representation of probable fault property values at each point included in the fault segment. Also, probability intervals (e.g. P10, P50 and P90) can be subsequently extracted. They represent limiting values for the intervals defined.

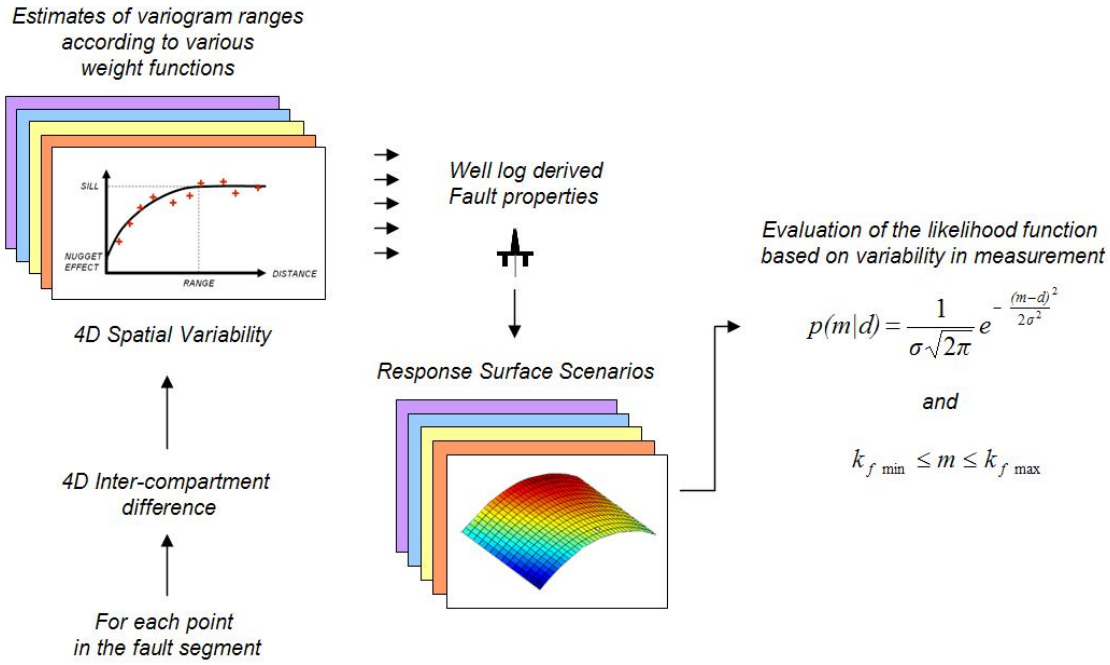

Figure 4.6. *Workflow in the evaluation of the uncertainty related to the variogram modelling. Calibration of the coefficients in the quadratic polynomial expression yielding to several of representations of response surface which are used to obtain fault properties estimates according to each model realization. The standard deviation in the fault property estimates is employed as indicator of the variability and is in turn appropriately used in the likelihood function.*

4.3 Application to a synthetic case

The method described above has been applied to a synthetic seismic data calculated from fluid flow simulations performed on a synthetic reservoir model based on Fangst Group reservoir of the Heidrun field. The workflow is employed to recover the initial fault permeability values inserted into the model given its 4D seismic signature. The implemented workflow for this objective is now discussed.

4.3.1 Geological modelling

To create the corner point geometry grid to be used for the fluid flow simulations, a field scenario has been set up by utilising the Heidrun dataset in a particular sector of the reservoir of interest (Figure 4.7). The selection of the area has been centred on the

presence of a fault which seems to be compartmentalizing the reservoir. The reservoir geometry has been defined by using upper and lower horizons constraining the Fangst Group as interpreted from the 3D seismic. They establish the vertical limits of the reservoir and define the juxtaposition between reservoir block as consequence of the fault occurrence. Following this structural framework, a grid is posteriorly defined (16 x 10 cells) allowing population of the static reservoir properties by upscaling and interpolating well log data associated with the reservoir compartments. Having defined the fault geometry during the structural modelling, fault properties are assigned according to the fault displacement and a shale smear definition given by the shale gouge ratio algorithm (Yielding et al., 1997) as described in Chapter 1. Indeed, the net content of shale/clay in the volume of rock as estimated from log data (gamma ray logs) in the Fangst Group reservoir as well as fault throws are used to compute the shale gouge ratio estimator. Then, as described by Manzocchi et al. (1999), an empirical equation is utilized to derive fault permeability which is in turn employed to calculate fault transmissibility multipliers as shown in Chapter 1.

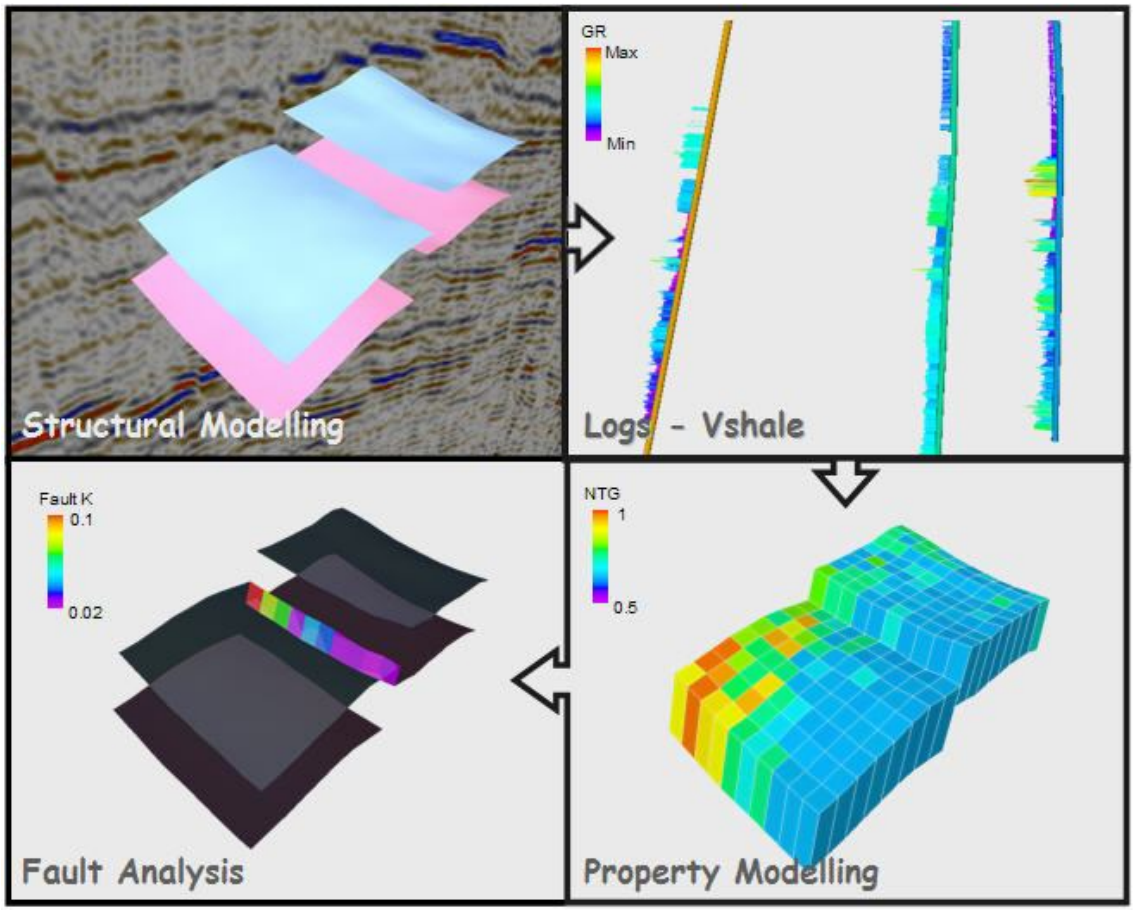

Figure 4.7. *Schematic workflow for the static model generation.*

Thus, by introducing fault permeabilities into the model it is possible to derive a geologically consistent fault transmissibility multiplier in which the juxtaposition between reservoir compartments (given by the fault displacement) and the shale smear definition are taken into account in the fault representation (Yielding et al., 1997 and Manzocchi et al., 1999). In this scenario the modelled fault plane acts as an interface between each compartment with grid cells aligned along the fault segment in each reservoir block. The fault segment is formed by 10 grid cells which have been numbered from 1 to 10 and consequently fault properties are assigned accordingly to each cell number. Fault displacement and associated shale gouge ratio values fluctuate along the fault segment as shown in Figure 4.8. Consequently lateral changes in fault permeability are introduced into the geological model. As discussed in Chapter 1, this will lead to lateral variations of the fault transmissibility multipliers which are in turn inserted into the fluid flow simulation (Figure 4.9).

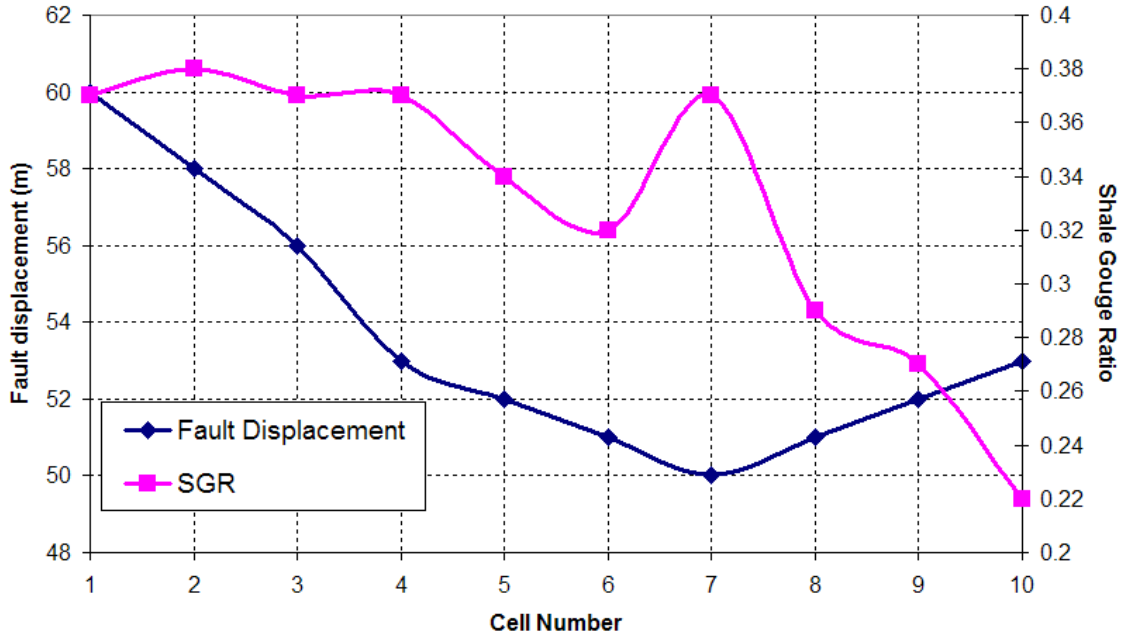

Figure 4.8. *Lateral variation of the fault displacement and the shale gouge ratio after well data propagation against the fault surface. Data points in the plot represent values included in the modelled fault. These are connected by an interpolation line.*

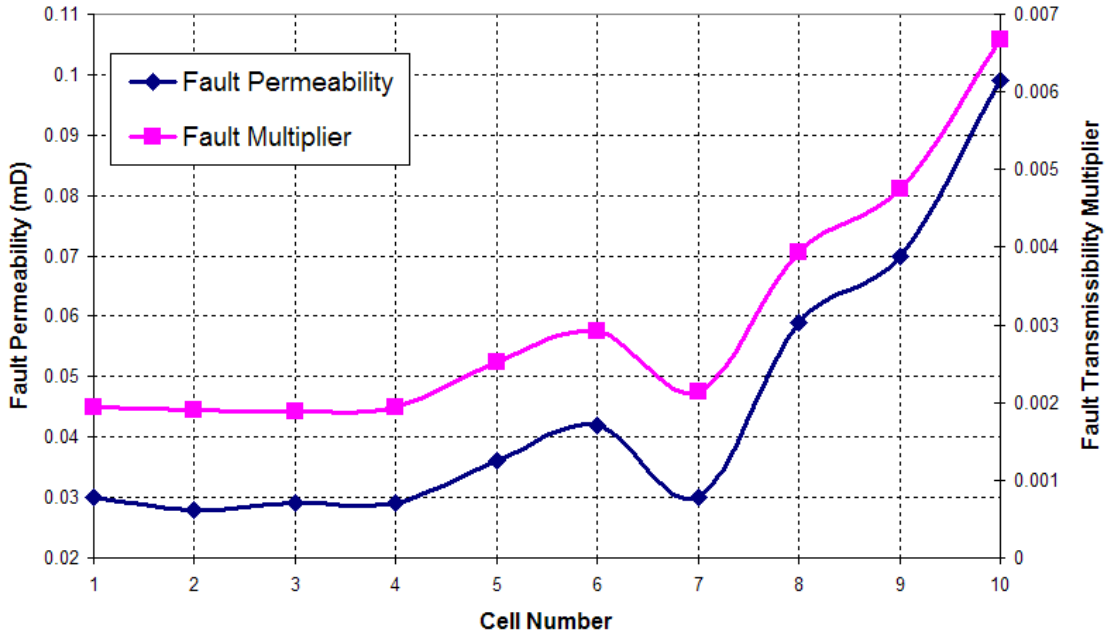

Figure 4.9. *Lateral variation of the fault permeability (derived from the SGR values) which is in turn used to derive a geologically based fault transmissibility multiplier to be inserted into the simulation model. Data points in the plot represent values included in the modelled fault. These are connected by an interpolation line.*

4.3.2 Simulator to seismic modelling

In order to evaluate fluid flow in the static model, a production scenario is numerically simulated. A water flooding strategy is designed, in which a producer and a water injector wells with rates set to 400 Sm^3/day, are located in each corner of the model. The initial conditions within the model are given by the information representing the reservoir rock and the fluid (Table 4.1). An initial pressure is assigned and an initial fully oil saturated scenario is considered. In spite of the introduction of the Heidrun field information, the numerical model is kept as simple as possible to highlight the role of the fault properties on the fluid flow. As a consequence the simulation deals with an oil-water system where only the buoyant force and/or fluid pressure gradients drive fluid flow. Two different time steps are selected to evaluate the time-lapse signature: the pre-production or base line and the post-production case given by 6 years of depletion.

Rock	Top and base reservoir	From 3D seismic interpretation in Heidrun field
	NTG	From clay content in reservoir log data (0.6 up to 0.9)
	Porosity	From reservoir log data (0.25 up to 0.30)
	Permeability	From reservoir log data (1 D up to 1.5 D)
	Rock compressibility	0.0000682 bar^{-1} @ 245 bar
Fluids	Water density @ standards conditions	1033.0 kg/m^3
	Oil density @ standards conditions	700 kg/m^3
	Oil viscosity	1.60 cP @ reservoir pressure
	Water viscosity	0.38 cP @ reservoir pressure
	Water compressibility	4.0e-5 $bars^{-1}$
	Oil and Water relative permeability	From Heidrun simulation model
	Water/Oil capillary pressure	From Heidrun simulation model
	Oil formation volume factor (FVF)	1.04 Rm^3/Sm^3
	Water formation volume factor (FVF)	1.00 Rm^3/Sm^3
Wells	Producer rate	400 Sm^3/day
	Water Injector rate	400 Sm^3/day

Table 4.1. *Input data in the fluid flow simulation.*

Pressure and saturation at each time step and their associated differences are shown in Figure 4.10. Essentially during 6 years of production, pressure depletion and fluid substitution (oil to water) takes place, nonetheless lack of communication between the two reservoir blocks is observed as the introduction of a fault leads to a compartmentalization of the pressure and saturation signatures. Differences for the pressure values between the post-production stage and the base line show a drop of 60 bars for the compartment including the water injector (hanging-wall) whereas a decrease of 150 bars appears in the block associated with the producer (foot-wall). Oil saturation differences also get affected by these changes as oil saturation values drop by 0.1 to 0.4 in the block associated with the injector but no major change appears in the other block. Indeed, the reduction in permeability introduced by the fault, deflects the flow across the compartments slowing the imposed waterflooding, particularly for the reservoir segment with no injector.

Using the simulated pressure and saturations and the static reservoir properties included into the model, a synthetic seismic response is estimated for the base line and the post-production stage. To do so, Batzle and Wang (1992) is used to derive the oil and brine acoustic properties under the reservoir conditions associated with the pre and post – production stages. Then, using the Gassmann's equation (1951) changes in bulk modulus and fluid density are computed according to the fluid substitution taking place. Additionally, the pressure sensitivity properties for the dry-frame rock frame are considered by implementing experimental curves obtained in the laboratory. This workflow, also known as petro-elastic modelling, allows conversion of the pressure and saturation values (obtained in the fluid flow simulation) into seismic velocities and densities used for the estimation of P-wave impedance for each particular grid cell included in the reservoir model. Differences between the modelled post and pre-production impedances seem to emulate the observed impedance change evidenced in a sector of the Heidrun field as shown in Kahar et al. (2006). Here, the Upper Fangst Group (Garn Fm.) shows a hardening response which appears compartmentalized as a strong contrast is observed between juxtaposed reservoir blocks (Figure 4.11). Considering a Ricker wavelet (European polarity) with 30 Hz as dominant frequency and the Zoeppritz formulation (1919) to compute the reflectivity series, the full offset stacked seismic volume is generated. Seismic profiles for the full stack seismic volume are displayed in Figure 4.12 (top).

RMS amplitude maps in a time window of 16 ms centred at picked top reservoir are also calculated (Figure 4.12, bottom). Differences between seismic volumes and maps after 6 years of production are also evaluated. An increase of seismic amplitudes is observed in the block associated with the water injection well (hanging-wall) whereas a general amplitude decrease is observed in the producer compartment (foot-wall). The contrast of the 4D signal between the two reservoir blocks is related to the flow-related properties of the fault. Now, having measured the time-lapse seismic signature the proposed methodology is applied to invert for the fault permeability values to recover the initial input introduced into the geological modelling.

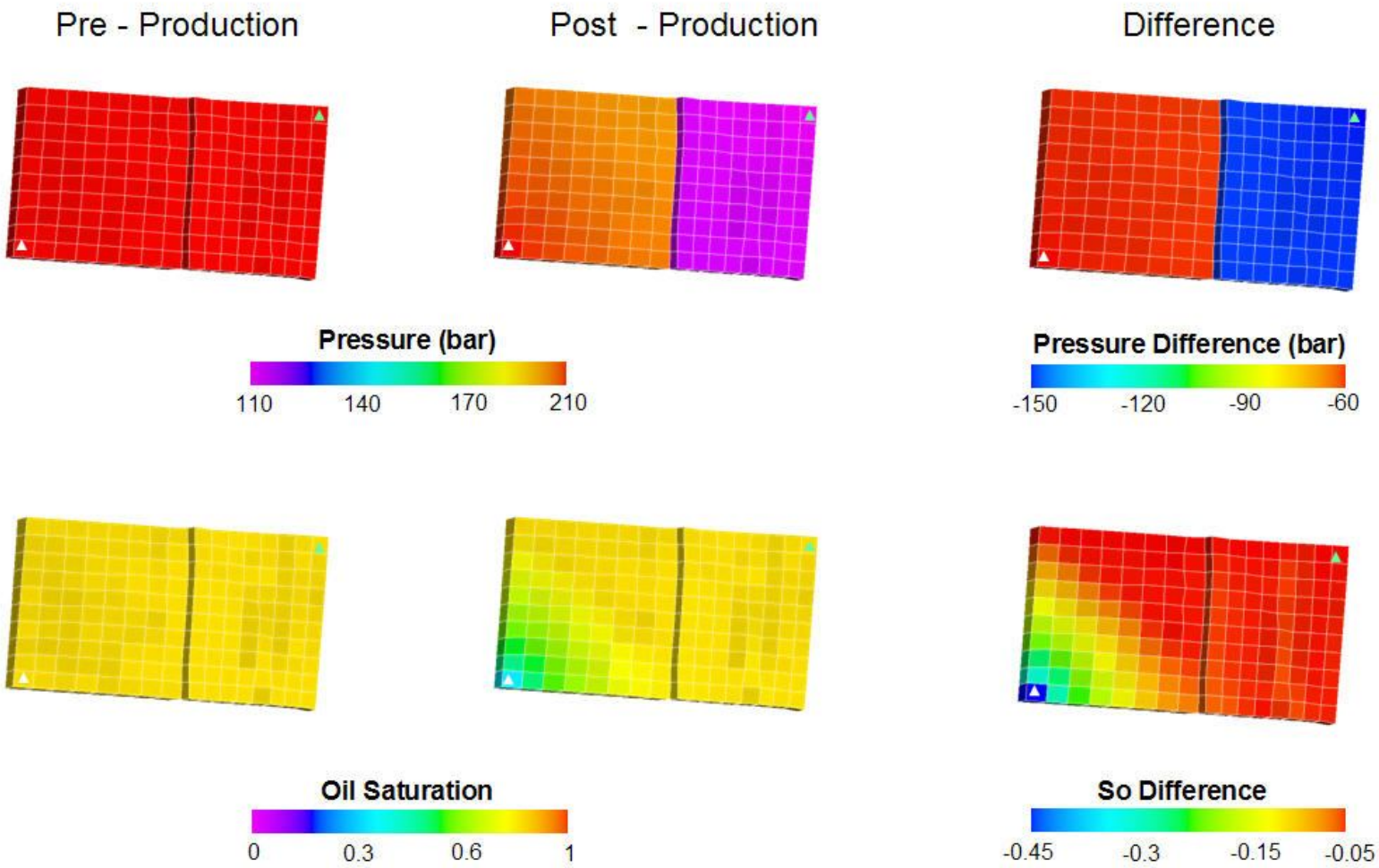

Figure 4.10. *Simulated pressure (above) and saturation (bottom) at the initial stage and after 6 years of production. A water injector (white triangle) and a producer (green triangle) are located in each corner of the model. Pressure and Saturation differences are calculated between the post-production and the initial stage.*

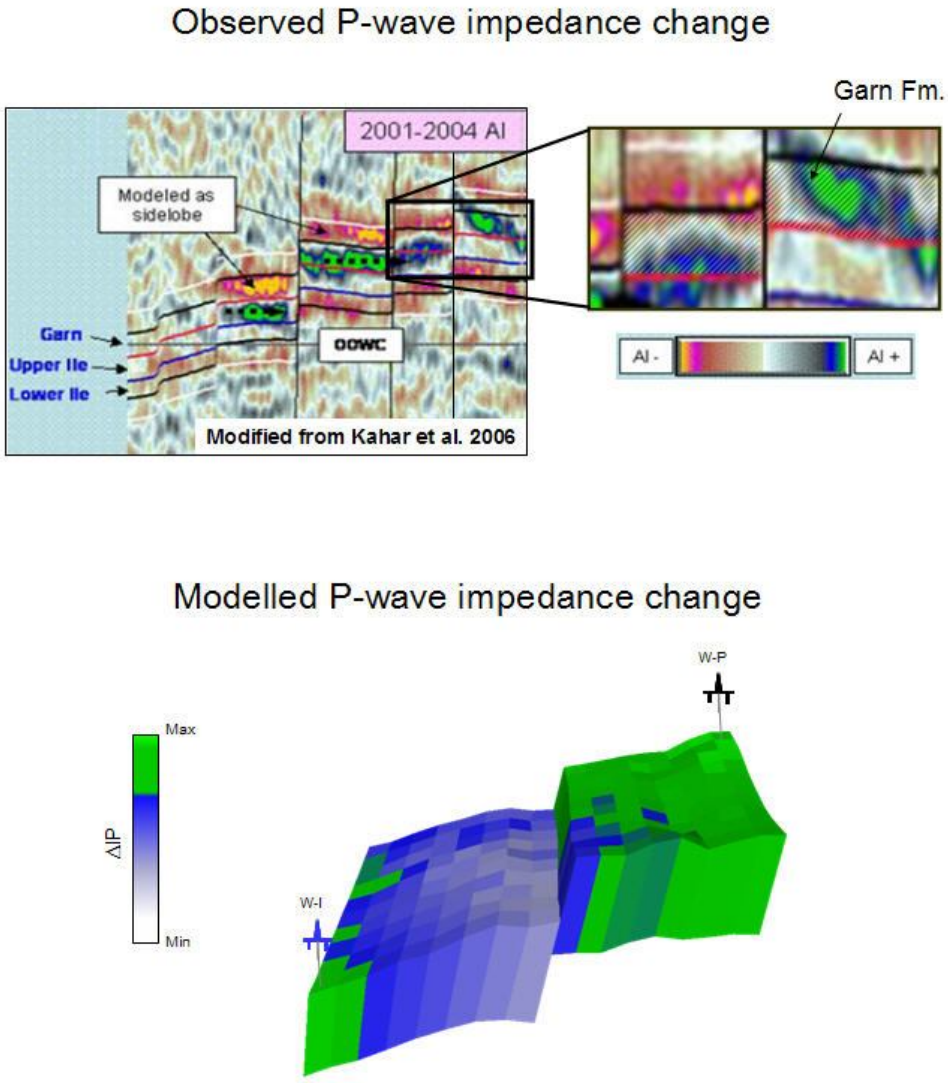

Figure 4.11. *Observed (above) and modelled (bottom) P-wave impedance difference. The synthetic scenario seems to simulate the observed impedance change highlighted in Kahar et al. (2006). A hardening response appears as water displaces oil in the Garn Fm. Reduced flow across faults affects the waterflood strategy; hence the 4D seismic signature appears to be compartmentalized.*

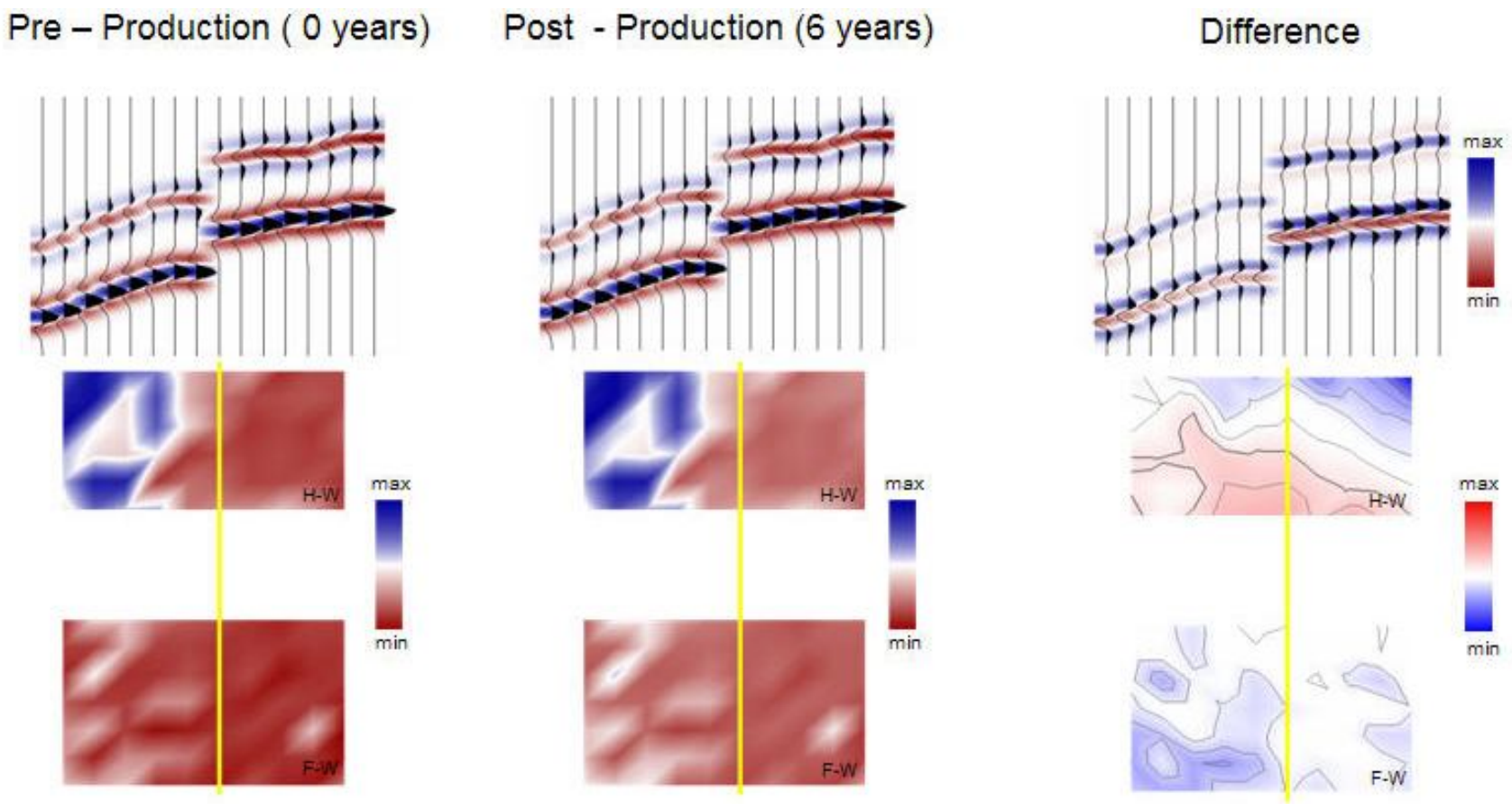

Figure 4.12. *Modelled seismic amplitudes are evaluated for full offset synthetic stacked sections. 4D amplitude maps are calculated considering the seismic differences after six years of production. Location of the seismic line (top) is displayed as a yellow segment in the amplitude map (bottom). Within the faulted reservoir Hanging-wall and Foot-wall are indicated as H-W and F-W respectively.*

4.3.3 Extraction and calibration of the 4D seismic statistics

Using the methodology described in section 4.2, 4D inter-compartment difference and 4D spatial variability are extracted using the difference map (time-lapse signature) between the pre and post-production amplitude maps. The grid representation of the 4D seismic map is used to extract both measured parameters for the dataset included in each row as shown in Figure 4.4. Given the geometry of the synthetic model 10 data rows are assembled from the difference map with 16 samples included in each row. In the 4D spatial variability case, an estimation of the range values along unidirectional variograms is performed by selecting the best fit option during variogram modelling (Figure 4.13). The fitting of a model to the experimental variogram (calculated from the observational data) is part of a trial-and-error process which continues until fitting is considered satisfactory. The non-reproducible nature of such approach is later addressed to assess uncertainties within the estimation methodology.

Once both 4D statistics are obtained, both measurement parameters are gathered for each sample included in the fault segment as shown in Table 4.2. In order to compare such results with the fault permeability included within the geological model, a cross plot is assembled (Figure 4.14). Modelling of the overall observed trend reveals that a quadratic polynomial expression can be used as the best fit function for the fault permeability (Figure 4.15). Indeed, a regression analysis, in which a least-squares adjustment between the 4D statistics and the included fault permeability values is performed, showing a correlation coefficient (R^2) of 95%. This observation is used to postulate a response surface which can be used for prediction purposes. Indeed for this synthetic scenario, a regression involving all the available samples (10 in all fault segment) shows the following as the best fit function for the fault permeability k_f:

$$k_f = 0.25 - 157.39\ x\ -\ 3326.05\ x^2 - 25.35\times10^{-5}\,y + 1.51\times10^{-7}\,y^2 \qquad (4.5)$$

where x and y are the 4D inter-compartment difference and 4D spatial variability respectively.

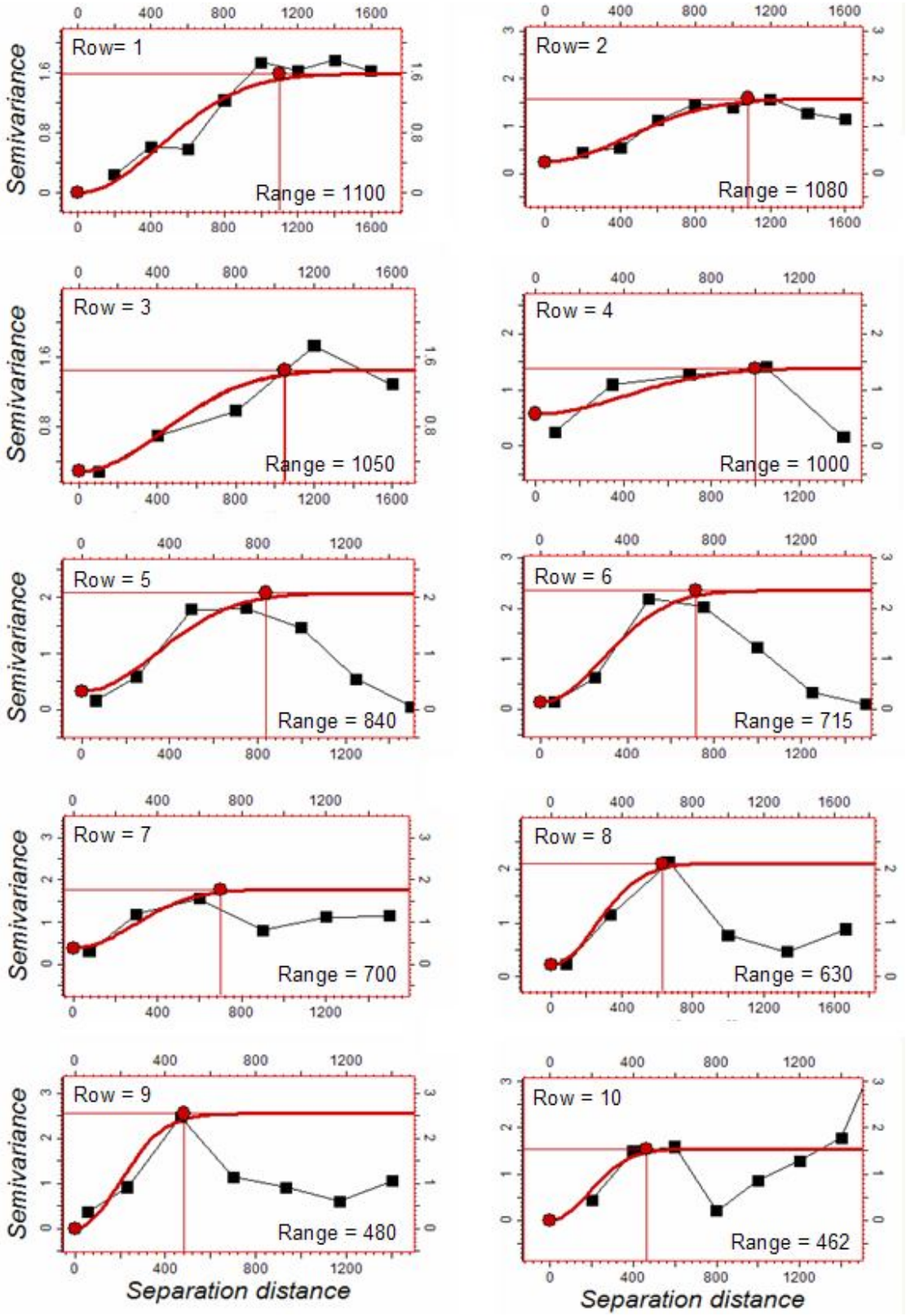

Figure 4.13. *Unidirectional variograms for each data row within the 4D attribute map. The fitted model in each case is used in the range estimation.*

Row	4D Measurements		Fault Permeability ($1x10^{-2}$ mD)
	4D Inter-compartment difference ($1x10^{-5}$)	4D Spatial Variability	
1	75.849	1100	3
2	75.986	1080	2.8
3	76.853	1050	2.9
4	74.129	1000	2.9
5	70.851	840	3.6
6	67.749	715	4.2
7	62.133	700	3
8	58.502	630	5.9
9	52.741	480	7
10	45.006	462	9.9

Table 4.2. *4D measurements per each data row.*

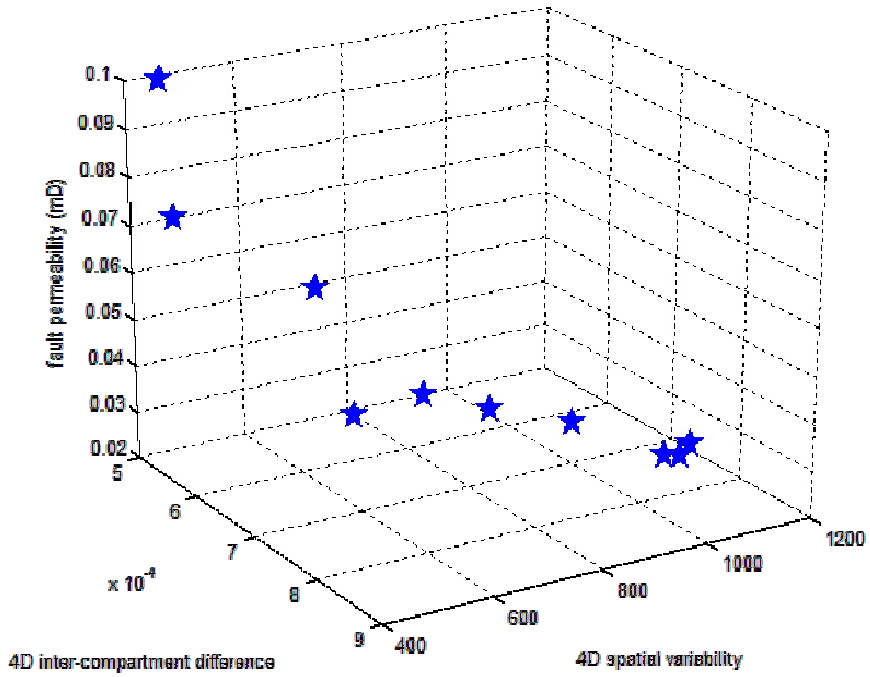

Figure 4.14. *Cross-plot between the 4D statistics and the true fault permeability. Each sample is displayed as a star.*

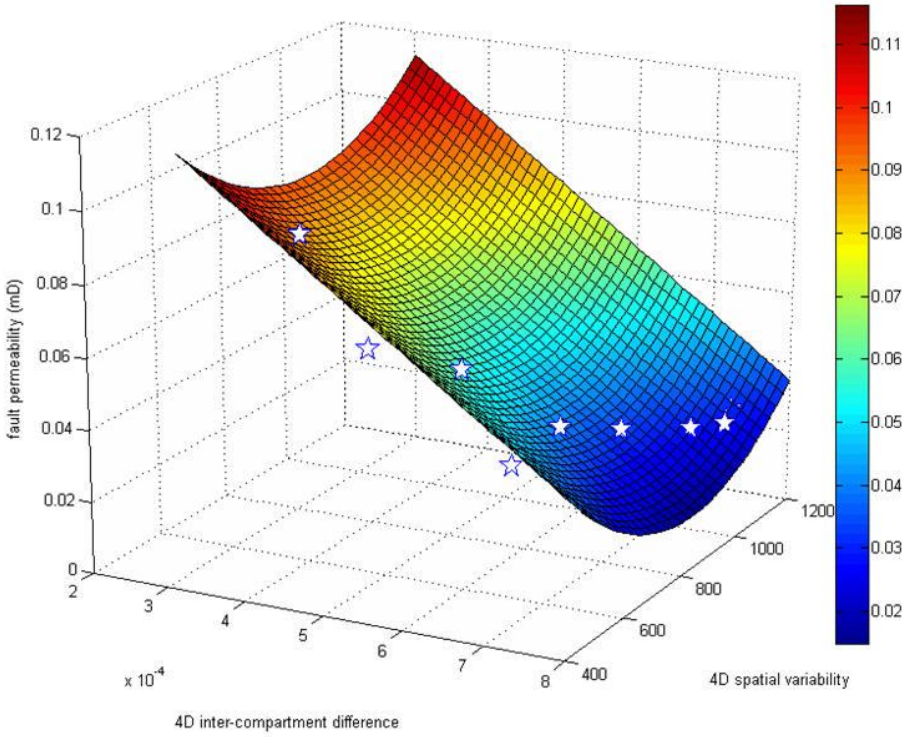

Figure 4.15. *Response surface given by the quadratic polynomial fit of the available samples (displayed as stars). Magnitudes in the surface are in mD and associated to the colour bar.*

Using such quadratic polynomial expression, fault permeabilities are inverted from the 4D seismic statistics (Figure 4.16). The response surface prediction compares favourably with the true fault permeability values in the model, nonetheless small differences between the 4D seismic prediction and the true values can be detected. Indeed, the flexibility of the quadratic polynomial approximation relies on the simplification of the inversion process; nonetheless it can deliver under/over estimations if strong variations in the fault properties are taking place as evidenced in cell number 7. This is because the selected model is only able to capture a smooth representation of the fault permeability, delivering only its regional behaviour. This is a limitation in the proposed methodology, which also depends on the resolution of the seismic. This allows evidencing compartmentalized long period anomalies that appear to be related to the fault seal. However, small heterogeneities in the signal can be difficult to capture with the seismic measurements. This restraints the quantitative analysis, as it might not be able to solve beyond the overall trend.

In practice, the restricted coverage of the well dataset (i.e. logs) very often does not allow population of the necessary geological information to predict fault properties. In some cases it is also noted that the information included in a well located in the vicinity of a fault does not necessarily apply to the geology immediately adjacent of a fault. As a consequence, limited well data information can be used to partially constrain fault properties (i.e. fault permeability) in a sector (or sectors) of the full fault segment. The position of such sector depends on the number of wells, location and their trajectories relative to the fault segment. Here, the statistics of the 4D seismic signature are proposed to extend the quantitative evaluation of fault properties by calibrating the coefficients of the quadratic polynomial expression in a sector with known (geologically based) properties, which is in turn later used as an estimator in zones with no well control. To evaluate the predictive capacity of the polynomial model in the synthetic model, a cross-validation technique is applied in which calibration of the coefficients has been performed by arranging all plausible combinations of sub-sectors (only iterative samples are used to generate each possible combination) to be used as training data and inverting for fault permeability values away from the input values (Figure 4.17).

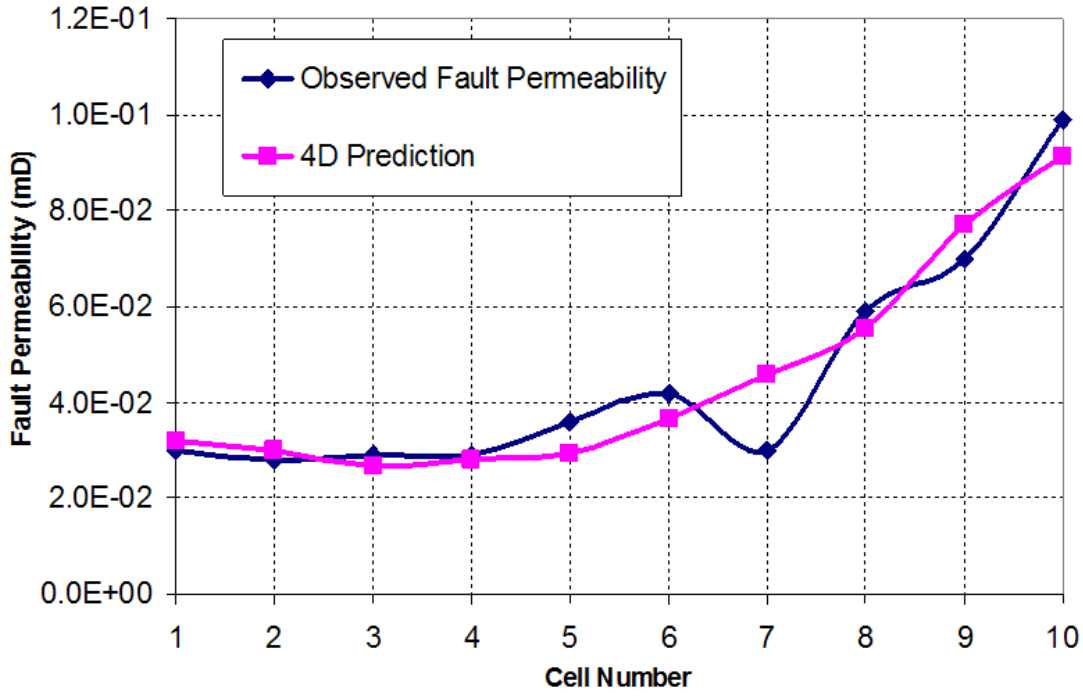

Figure 4.16. *Comparison between the true fault permeability values derived from well data (included in the geological modelling process as shown in Chapter 1) and the prediction given by the measurement parameters extracted from the 4D attribute map for the 10 samples included in the fault segment.*

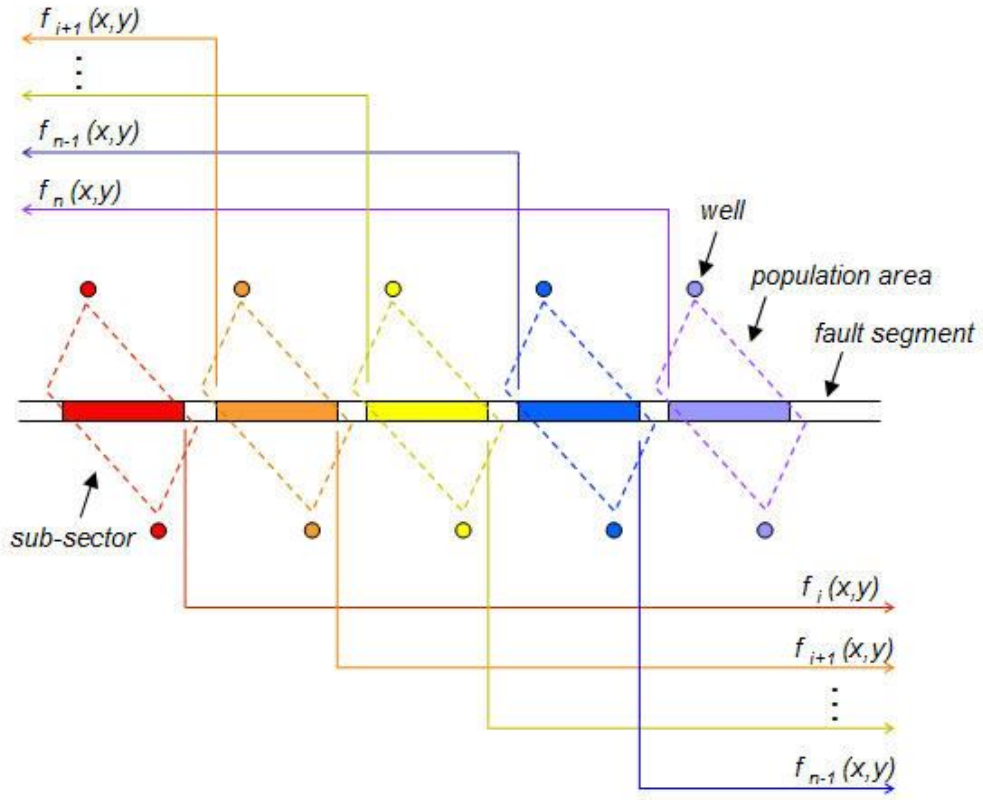

Figure 4.17. *Limited well data information can be used to locally determine (populate) fault properties in a sub-sector of the fault segment. The position of such sub-sector depends on the number of wells and location relative to the fault segment. In the diagram, several groups of wells are displayed. These are represented with a particular colour. For each well arrangement, a sub-sector is defined where the well data can be propagated against the fault in a limited area (colour coded according to wells used). Using a specific sub-sector (represented in the diagram with a different colour) as a calibration tool for the polynomial coefficients, it is possible to expand the fault permeability estimation away from the populated area given by the wells. In the synthetic model, a cross-validation technique is applied. Here, calibration of the coefficients is performed arranging all plausible combinations of sub-sectors and evaluating errors. The sub-sector can change in size (number of samples) but also in terms of its position along the fault segment.*

Combinations include variations on length and position of the training samples which are posteriorly used to invert for coefficients in the quadratic polynomial approximation accordingly (Table 4.3). This means that for a given number of training samples, all viable positions are tested during the calibration stage (Figure 4.18).

Combination number	Number of samples used for calibration
1 - 6	5
7 - 11	6
12 - 15	7
16 - 18	8
19 - 20	9
21	10

Table 4.3. *Number of samples included in each combination (used for training purposes) as extracted from various sub-sectors of the fault segment. The complete fault segment is formed by a total of 10 samples. As more samples are included into the calibration of the polynomial expression, the number of possible combination decreases. For a fixed number of samples, variation in the combination number is associated to different positions of the sub-sector along the fault segment.*

Then, mean errors are computed by calculating the average square difference between the true (included in the synthetic) and the predicted values for the full fault segment (given by the response surface). Mean errors during validation are displayed in Figure 4.19. Indeed, the number of training samples compromises the accuracy of the prediction. In this regard, non convergence of the quadratic polynomial approximation leads to variation in the estimation derived from each possible calibration (Figure 4.20). In general, larger calibration sectors help to reduce the average error in the estimation.

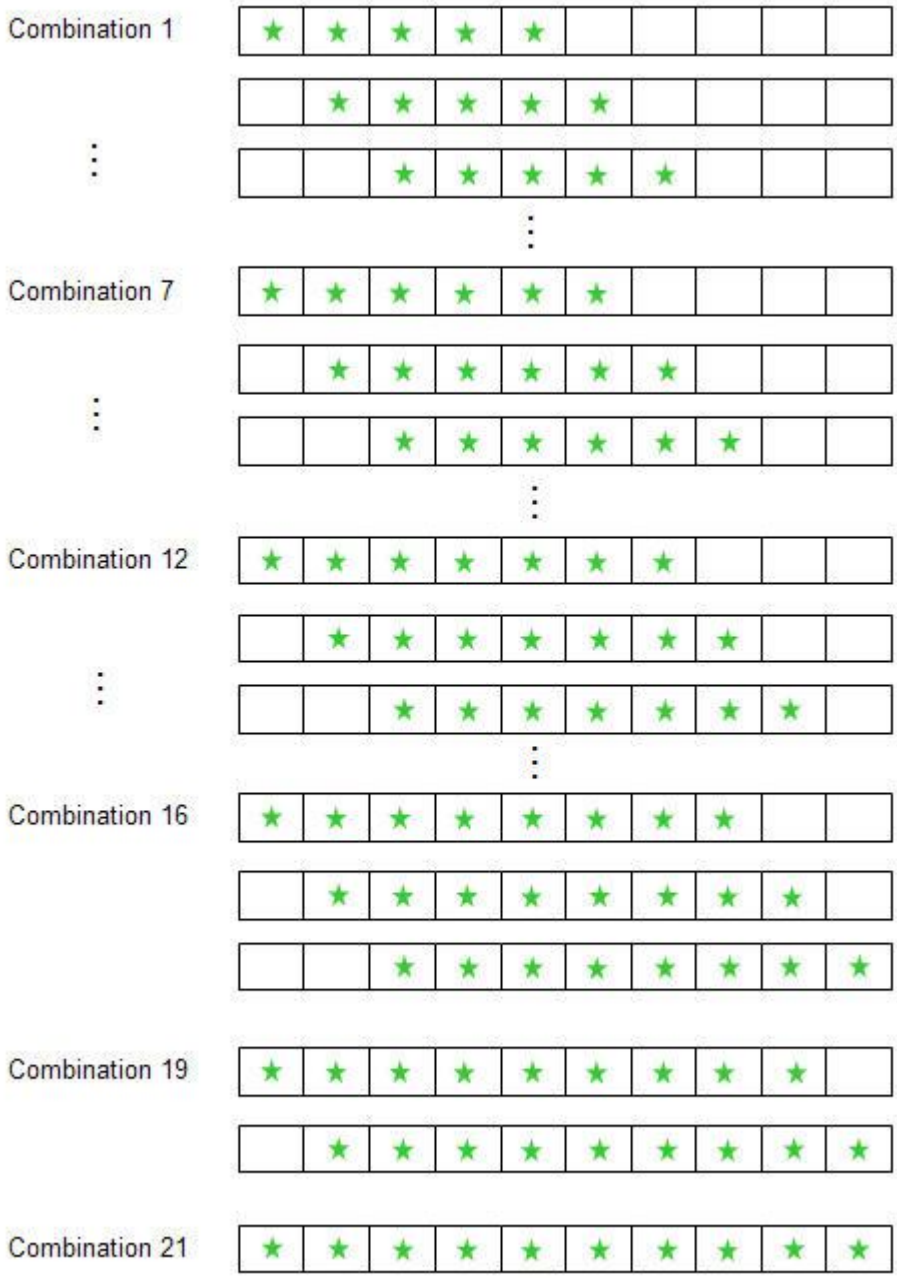

Figure 4.18. *Plausible combinations of sub-sectors in which length and position of the samples used in calibration are changed systematically. In the synthetic example, the total fault segment length is equivalent to 10 grid samples. Those used as training in the calibration process are indicated with a green star.*

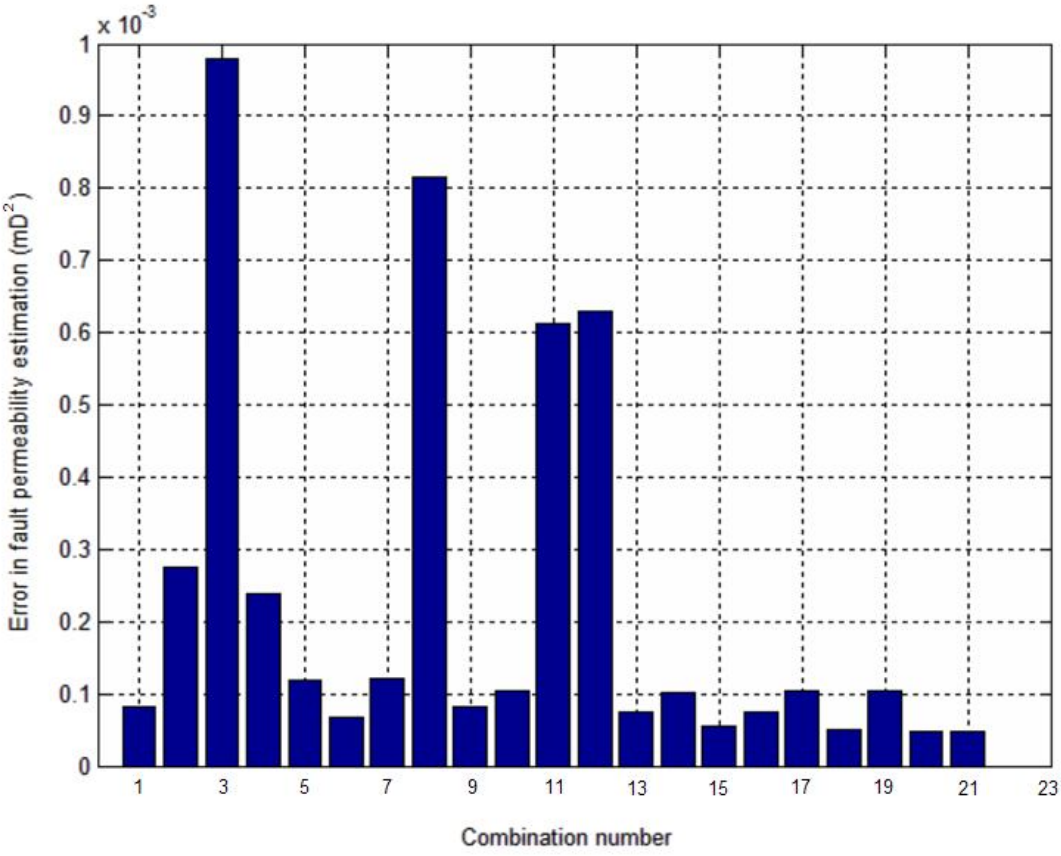

Figure 4.19. *Average cross-validation errors calculated for each combination (sub-sector) used as training data for the calibration of the coefficients in the quadratic polynomial expression. The number of training samples increases with the combination number.*

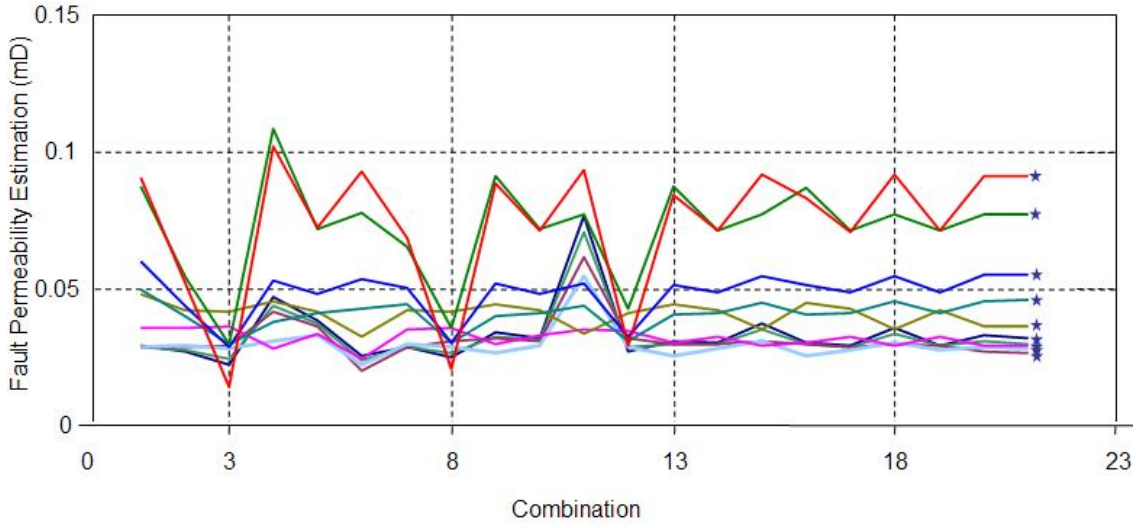

Figure 4.20. *Each colored line represents a particular sample included in the fault segment. By increasing the number of training samples, convergence to the true values (represented as blue stars in right hand side) is achieved.*

4.3.4 Uncertainty evaluation

The approach outlined in the section 4.2.3 has been tested on the synthetic scenario described above. The five weighting functions described in Pardo-Igúzquiza (1999) are taken into account in the estimation of range values. This means five different realizations for the 4D spatial variability are assembled in the process (Figure 4.21).

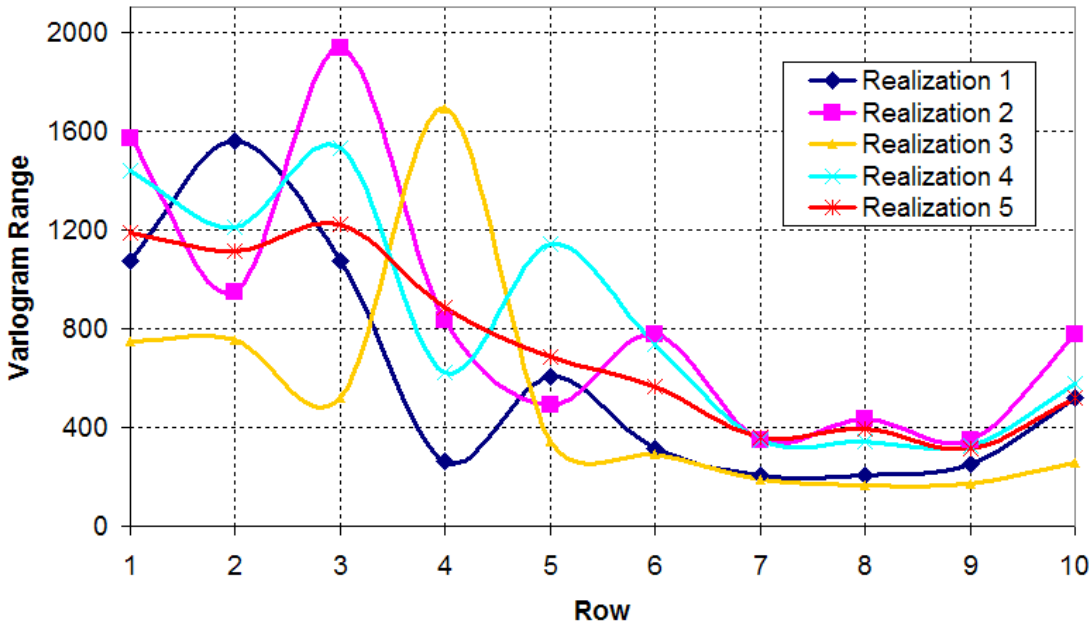

Figure 4.21. *Five different realizations for the 4D spatial variability.*

After calibration of the coefficients in each individual scenario, a quadratic polynomial expression is defined in each case which is used to generate the fault property estimates (i.e. fault permeability) associated with each point included in the fault segment (Figure 4.22). Variation in the fault permeability values along each realization (as derived from the best polynomial fit) is used to extract a measure of the standard deviation which in turn is employed as an input for the evaluation of the likelihood function discussed above. Note that for this synthetic study, the variogram range values show high variation in between cells 3 and 6 of the fault segment leading to an increase of the standard variation as shown in Figure 4.23. In addition an average square difference between each response surface realization and the true fault permeability values (included during geological modelling) is computed. Variation of such mean errors is shown in Figure 4.24.

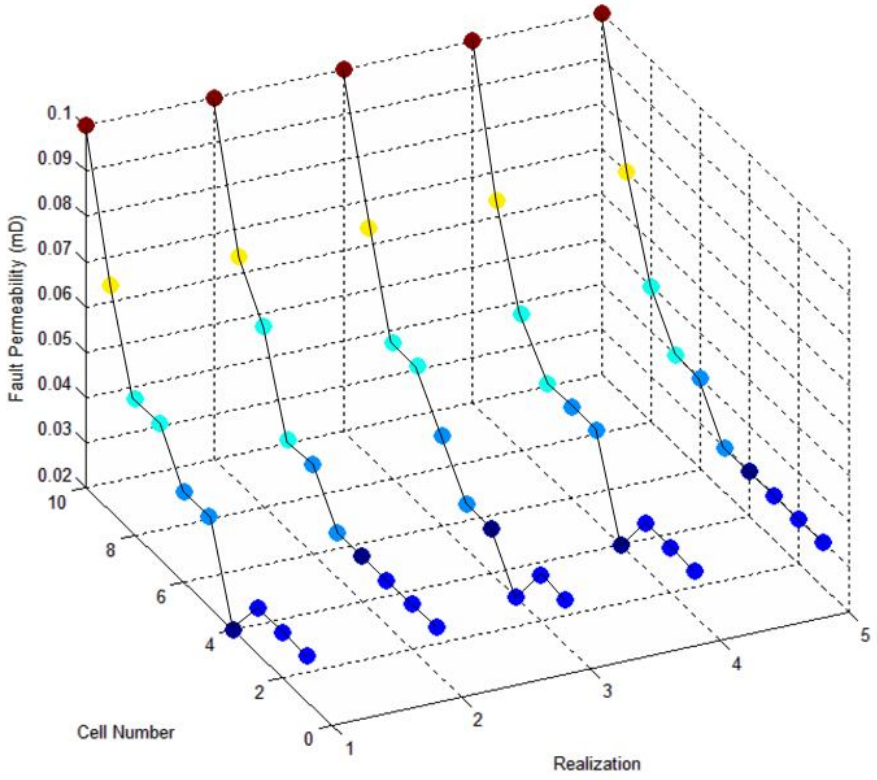

Figure 4.22. *Fault permeability estimations derived from each realization of the 4D spatial variability. Five possible models have been derived using for the calibration of the best polynomial model ranges derived from the various weighting functions.*

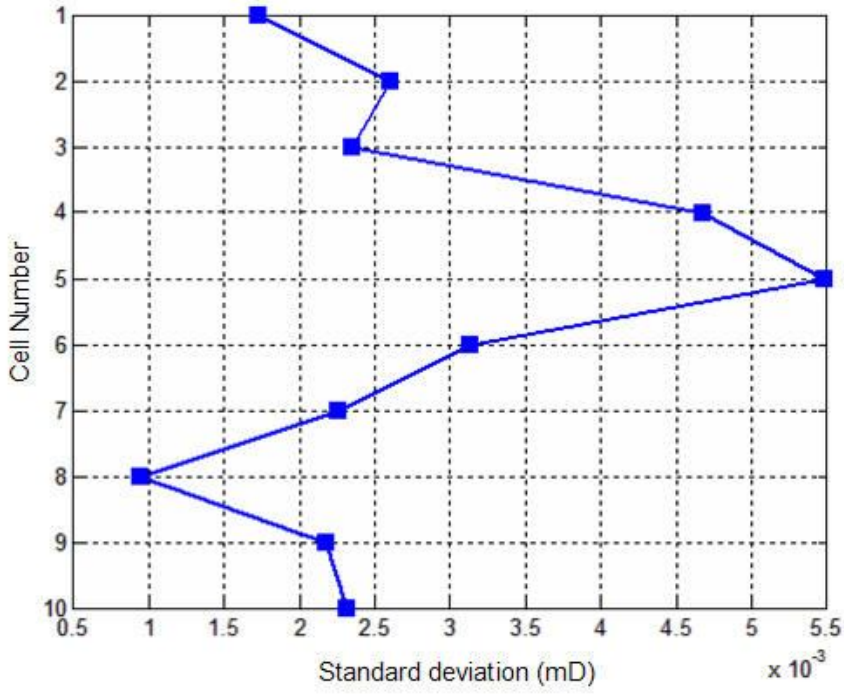

Figure 4.23. *Standard deviation derived from all possible fault permeability values given at each point included in the fault segment.*

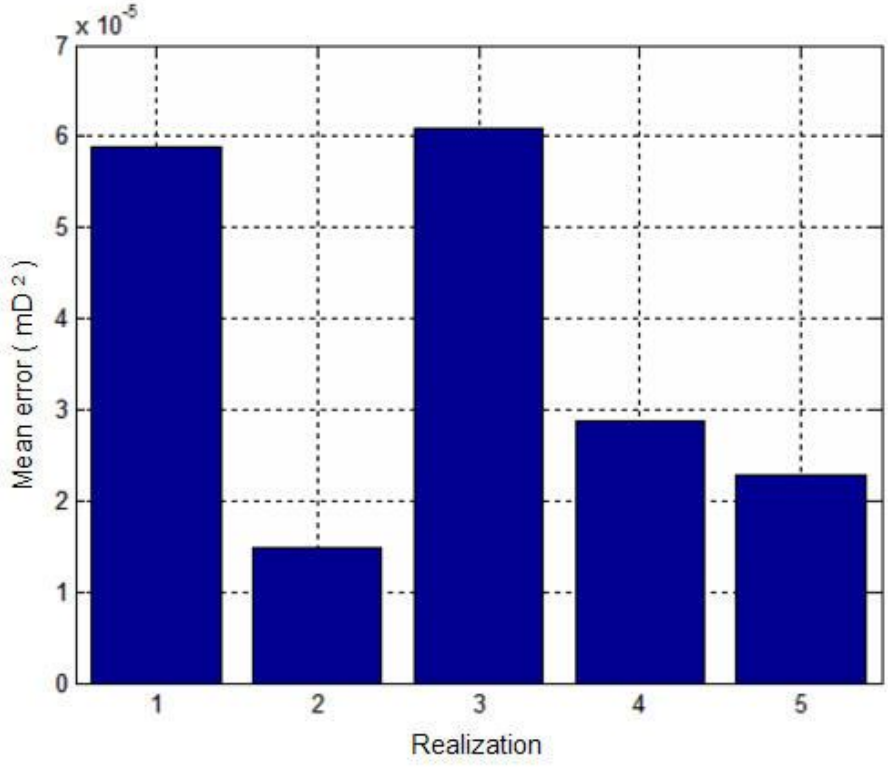

Figure 4.24. *Mean error for each response surface realization.*

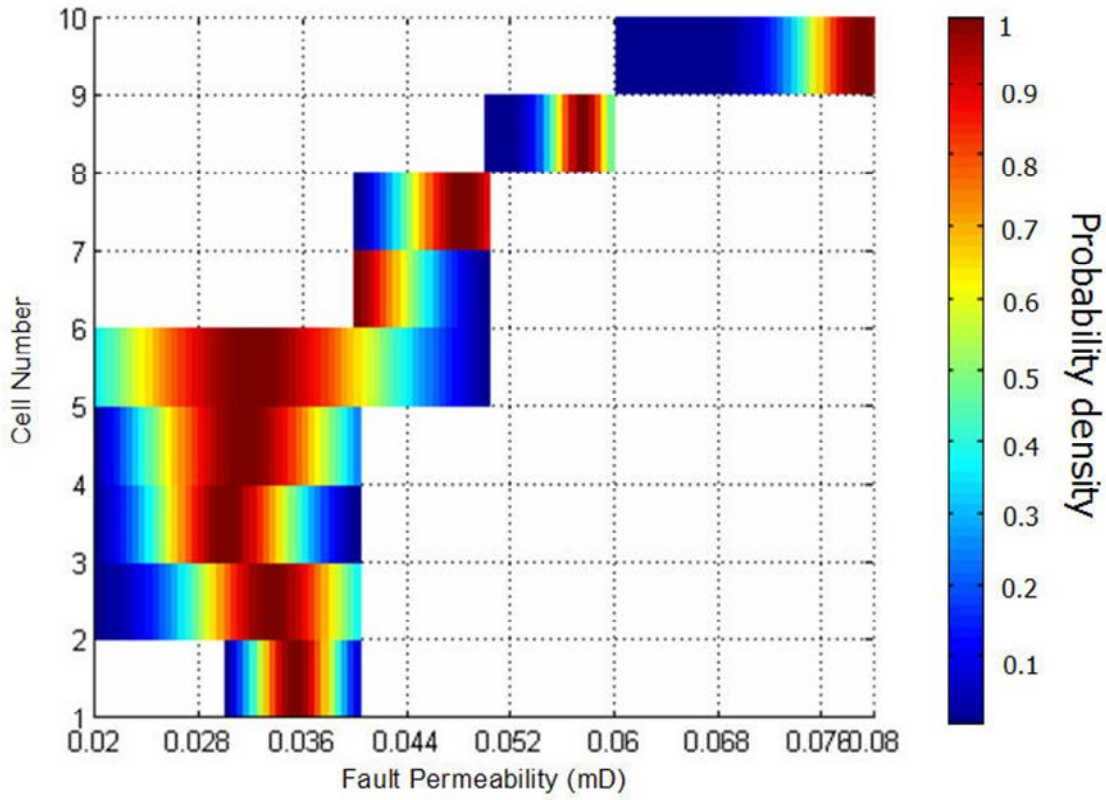

Figure 4.25. *Probability map showing for each cell included in the fault segment all possible fault permeability values which have been colour coded according to its probability of occurrence. Probability density values have been normalized.*

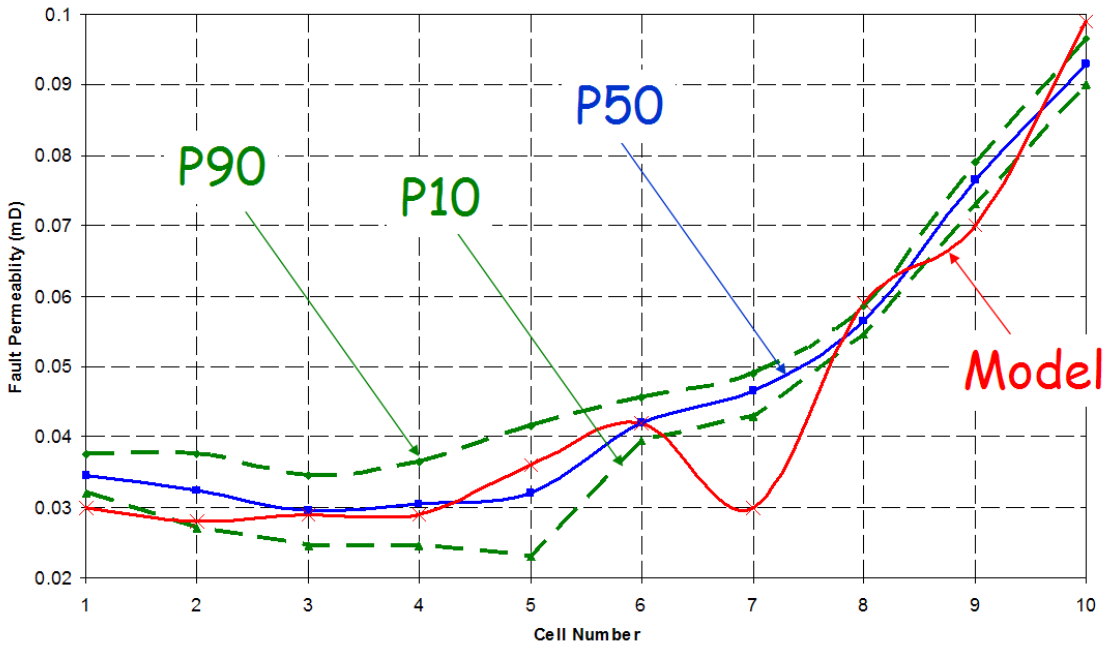

Figure 4.26. *Extracted percentiles from probability map. Here 10% (P10), 50% (P50) and 90% (P90) probabilities of finding a fault permeability value below that indicated by the curve. Fault permeability values initially included into the synthetic model are also plotted in the graph in red.*

Now, to measure the uncertainty related to the inaccuracy of the various response surface models, statistical probability density functions (pdf) given by the definition of the likelihood function shown above are used to describe the probabilities associated with all possible values for the fault permeability measurement. As indicated in Figure 4.25, a probability map has been created in which for each cell included in the fault segment a fault permeability window is displayed, which in turn is colour coded according to the probability of occurrence. Also, for each cell number, the associated pdf is used to derive a cumulative density function (cdf). The cumulative form is employed to estimate the 10% (P10), 50% (P50) and 90% (P90) probability intervals for which a fault permeability value is included (Figure 4.26). As expected, the P90 realization is predominantly acting as the high cut value for the 4D estimation when compared to the model input. However, the smooth nature of the polynomial model only permits to reproduce the overall fault permeability variation. As a consequence, local heterogeneities such as that presented in cell number 7 seem difficult to predict. This also introduces limitations for solving certainty windows that can capture the residuals which are separated from the regional trend. This result suggests that the evaluation of fault properties using statistics of the 4D seismic signature might be constrained at finer scales, and changes at higher resolution might difficult to reproduce. Yet, on the whole, comparison between fault permeability values initially included in

the geological model (derived by the well log information) and estimates from the proposed inversion technique (via the 4D seismic) encourages its application to a field case. Such a case example is shown in the next chapter.

4.4 Summary

Changes in the rock properties around fault planes lead to changes in the overall effective fault permeability. This modifies fluid flow behaviour and, in particular, can cause compartmentalisation. Such a phenomenon affects reservoir drainage by controlling pressure and saturation changes which in turn are responsible for the time-lapse seismic signature. Based on this observation, this chapter presents a new method in which 4D seismic is employed as a tool to quantify the inter-compartment communication and hence enhance the fault property assessment. To sense disruption in the pressure and saturation fields due to reduced permeability in the fault, two measurement parameters are derived from the 4D seismic maps: 4D inter-compartment difference and 4D spatial variability. Using the time-lapse seismic derived from a synthetic reservoir model and a typical production scenario, it has been shown that a quadratic polynomial expression (or surface response) combining the two measurement parameters can be used as the best fit function for the fault permeability representation. In practice, the coefficients of this polynomial expression must be calibrated in a sector with known (geologically based) fault properties. However, once a surface response is modelled, it is possible to calculate fault permeability in segments with poor geological control. In addition, to account for the uncertainty in the estimation, the non-reproducible nature of the variogram modelling (included in the analysis of the 4D spatial variability) is addressed. By considering a posterior distribution expressed as the likelihood function of a map representation of probable fault property values at each point included in the fault segment is computed. Application to the synthetic scenario produces encouraging results as indicated by similarities between the modelled values and the estimates from the inversion technique. These results suggest that 4D data can be used as a tool for deriving fault seal properties leading to improvements in fault characterization for the full field.

Chapter 5

Quantitative evaluation of reservoir fault communication using 4D seismic: An application to the Fangst Group, Heidrun Field

The methodology for estimating fault permeability from 4D seismic is applied to a Jurassic hydrocarbon reservoir located in the Norwegian offshore. Fault sealing properties are a subject of discussion as available well information cannot fully resolve such unknowns by means of geologically based algorithms. This chapter employs statistics of the 4D attribute map to propagate the fault permeability in three fault cases, providing an improvement in the characterization of the sealing properties of reservoir faults in the Heidrun field.

5.1 Introduction

It is known that in compartmentalized reservoir settings, fault seal properties impact on the pressure development and fluid flow affecting reservoir management decisions. The success in the prediction of the reservoir performance is strongly dependent on the evaluation of the sealing behaviour of the fault rock acting as barriers or flow retarders during the implementation of the drainage strategy chosen for the field production. Consequently the assessment of fault sealing properties of reservoir faults is critical in the characterization of the reservoir communication of the field.

As shown in Chapter 2, Heidrun field is severely compartmentalized by faults with trends NNE-SSW and ESE-WNW, and as a result reservoir faults introduce a dynamic hydraulic resistance between the several compartments of at least 2 bar (Heum, 1996 and Welbon et al., 1997). Such faults introduce juxtaposition by putting in contact different rock types across the fault (e.g. reservoir rock against non-reservoir rock). Also the fault rock seal, as a deformed low permeability rock along the fault plane is in contact with the reservoir rock introducing a major effect on the fluid flow. The fault juxtaposition is given by the geometry of the reservoir (commonly defined during 2D or 3D seismic interpretation assisted with well information) and is handled well in fluid flow simulators, whereas the evaluation of the fault rock seals needs to be addressed differently as it cannot be measured directly. Even more, the sealing capacity of a fault is far from constant in a given area as the properties governing the fault rock might vary laterally and vertically along the fault plane (i.e. stratigraphy and fault displacement). Consequently a particular fault might behave as sealing in some areas and open to fluid in others.

As discussed in Chapter 1, the shale gouge ratio (*SGR*) method has proven to be particularly useful in the evaluation of the sealing properties of the fault rock (Yielding 2002). Here, the net contribution of shale in a reservoir zone is linked to the trap efficiency. It has also been employed by Manzocchi et al., (1999) to derive fault permeability and hence fault transmissibility multipliers when needed in the fluid flow simulators. This geological analysis of fault seal behaviour is achieved by utilising well information. In particular, log data (e.g. Gamma Ray) is used to populate the fault sealing properties; however this approach is highly restricted to available well data

coverage which can introduce considerable uncertainty. Based on this phenomenon, this chapter presents the application of the methodology proposed in Chapter 4 in which statistics of the time-lapse seismic are used to quantify fault properties in areas with poor well data control. 4D seismic data is used in an effort to more fully resolve the distribution of the fault properties by utilising the spatial coverage of the seismic vintages to help determine the fault property estimates. To do so, 4D measures are calibrated at the wells to the geology based estimates of fault permeability. Here, the method is now employed to assess the fluid flow properties of faults separating four major compartments of the Heidrun field. As a heavily compartmentalized field case, Heidrun field represents an ideal case to evaluate the proposed new approach which can impact on the characterization of the complex inter-compartment communication taking place in the reservoir.

5.2 Geological fault seal prediction: The calibration tool

Faults defining major compartments in Heidrun Field (particularly those appearing in the Fangst Group) show NNE-SSW trends. Also, due to the drainage strategy set into the field, available well information is mainly focused in the oil window region. As a consequence, the sparse nature of the well log data means that it is not fully able to populate the properties (i.e. lithology) needed in order to perform a geological fault seal prediction. Nonetheless the available information seems enough to evaluate such unknowns in a sector of the field. In particular log data (i.e. Gamma Ray or *GR*) for the Fangst Group reservoirs included in between compartments D and G (see Figure 2.2 for compartments reference) serve to estimate the sealing properties (using the *SGR*) in a sub-segment of each of the three major bounding faults defined in this study as: Fault 1 (between compartment D and E), Fault 2 (between compartment E and F) and Fault 3 (between compartment F and G). The propagation of well log data implies the upscaling of such information according to a defined grid geometry (Figure 5.1). Particularly, shale content (V_{shale}) is estimated with the gamma ray values using the formula:

$$V_{shale} = \left(GR_{\max} - GR_{\log}\right) / \left(GR_{\max} - GR_{\min}\right) \tag{5.1}$$

and then populated towards the fault surface by means of an interpolation algorithm. To do so, a geocellular model is constructed for the each investigated fault with grid dimensions 100 m x 100 m x 1 m . Each grid cell within this model includes the estimated value for the shale gouge ratio value as defined in the equation 1.5 (Chapter 1). Finally *SGR* values are vertically averaged within the Fangst Group obtaining a mean representation of the fault sealing properties along the sub-segment of each fault in the well controlled sector of the field.

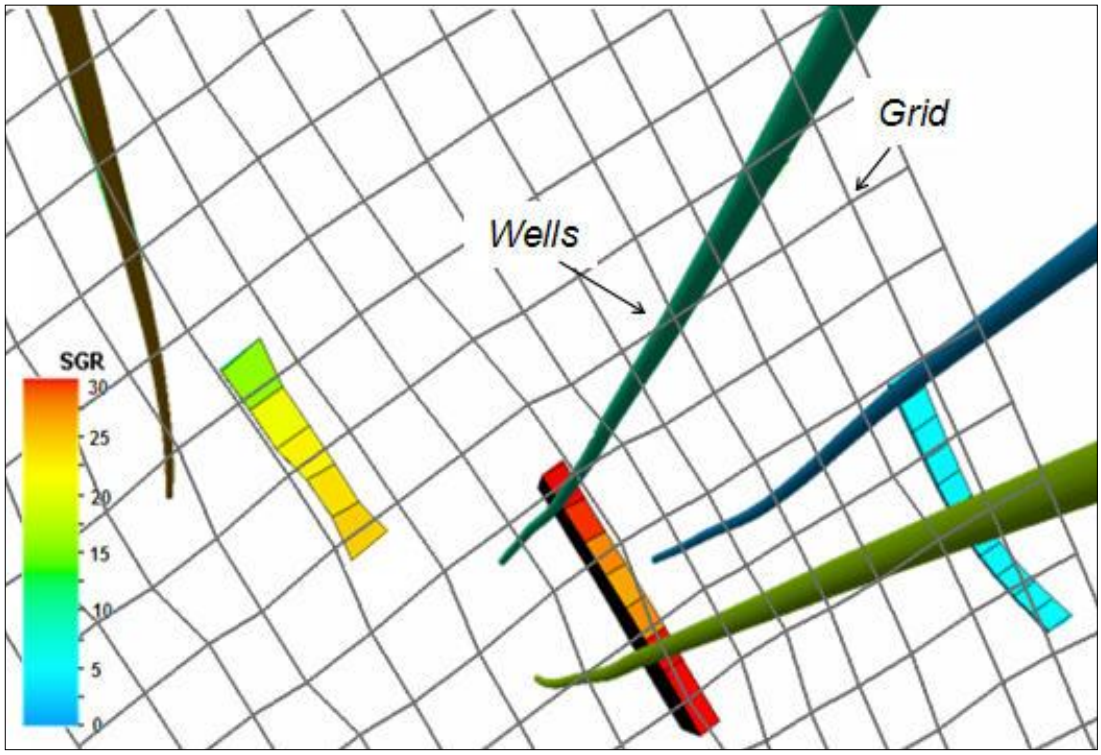

Figure 5.1. *Gridded representation of the shale gouge ratio values (vertically average in the Fangst Group) for a sub-segment of each of the three faults separating compartments D, E, F and G. From Left to Right: Fault 1 separating compartments D and E, fault 2 separating compartments E and F and fault 3 separating compartments E and F. Gray lines show the grid array employed for the population of the logs (clay content) associated to available wells.*

Estimation of the fault seal capacity of the fault sub-segments in the well-controlled sector of the field reveals low *SGR* values for faults 1 and 3 when compared with values for fault 2 in the north part of the field. Here, the sealing behaviour in fault 2 seems to be strengthened as *SGR* measures show values above 20 % (Yielding, 2002). Although the geological approach employed helps to characterize the sealing fault properties in a well-controlled sector of the field (Figure 5.1), the estimation of the fault sealing properties is compromised outside this area particularly in the south of the field where

only sparse water injection wells can be found in the vicinity of the original oil water contact (Figure 5.2).

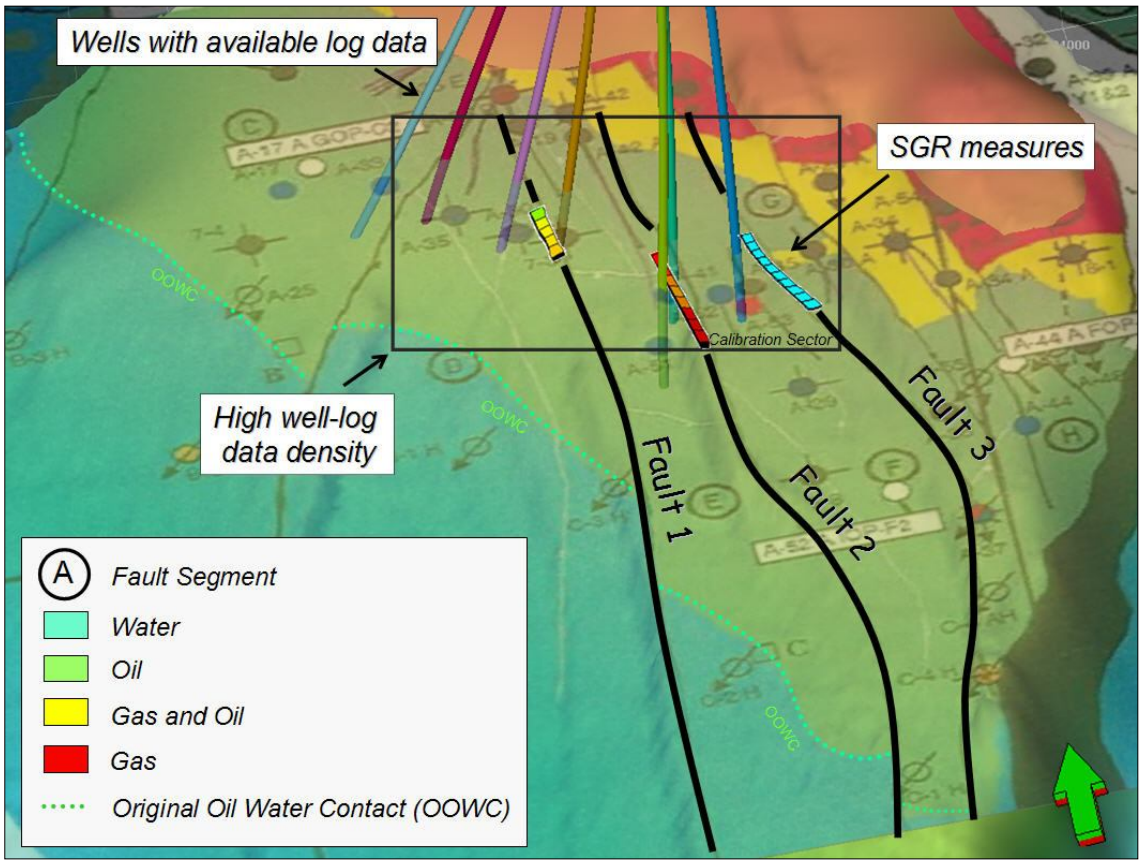

Figure 5.2. *Derived fault sealing properties along the fault segments in the well controlled sector of the field derived by means of the geological fault seal predictor (SGR). Wells with available log information are mostly located in the oil window allowing populating the clay content in that particular sector. The geological approach is highly restricted by the data density; as a consequence, the estimation of the fault sealing properties is compromised outside the well-controlled sector. Colour bar for the SGR measures is shown in Figure 5.1. Faults 1, 2 and 3 are separating compartments D and E, E and F, F and G respectively.*

However, time-lapse seismic data represents valuable information for the understanding of the reservoir fault properties. Now, utilising the methodology presented in Chapter 4, the next section takes into account the calculated *SGR* for each fault, using them as calibration measures for the statistics of the 4D seismic signature in order to predict fault sealing properties in areas with poor well data control, particularly in the southern part of Heidrun field where due to the well log data density, fault properties are not easily assessed by means of a geologically based algorithm. To do so, *SGR* values are transformed into fault permeabilities via equation 1.13 (Chapter 1).

5.3 Statistics of the 4D seismic

To evaluate the time-lapse seismic signature in this practical field example, two seismic vintages are employed: the base-line acquired in 1986 and the first monitor in 2001.

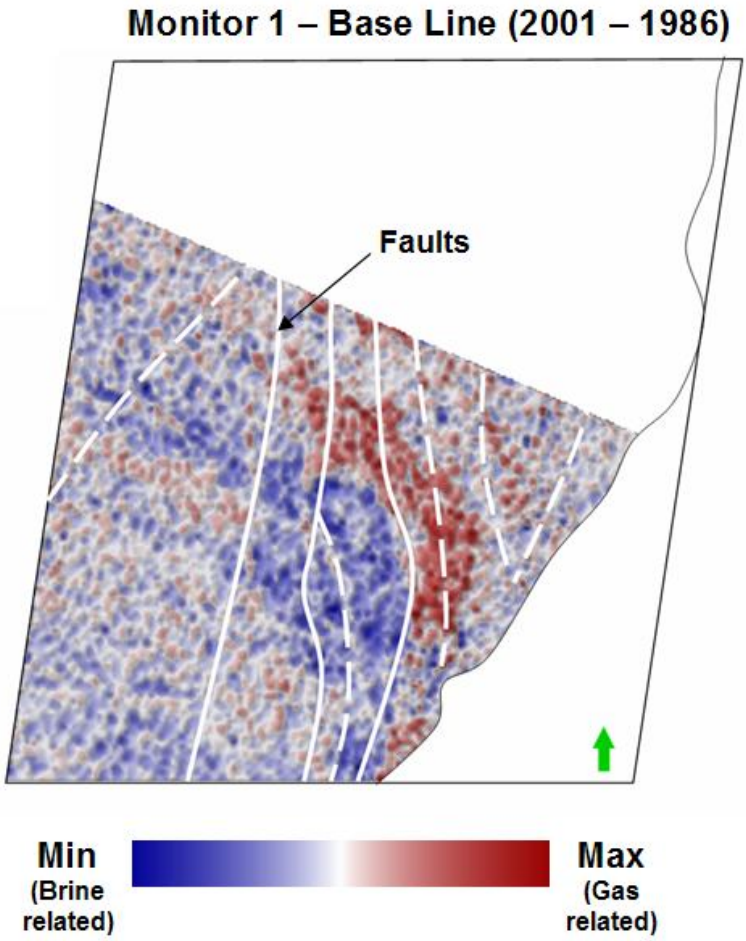

Figure 5.3. *Employed 4D signature (at top Garn Formation in the Upper Fangst Group) given by the RMS amplitude difference between the first monitor (2001) and the base-line (1986) seismic surveys. Faults are displayed as white lines. From left to right as solid segments, faults 1, 2 and 3 separating compartments D and E, E and F, F and G respectively. Other fault segments are shown as discontinuous lines.*

Both surveys have been simultaneously reprocessed to enhance their repeatability level (Furre et al. 2004). Considering these two surveys, *RMS* amplitude difference is extracted in a 16 ms window centred at the top Garn Formation in the Upper Fangst Group (Figure 5.3). Location of such 4D attribute on the flooding map is displayed in

Figure 5.4. Observation of the 4D signature for successive pairs of compartments suggests the presence of discrete long period anomalies which appear to be related to the fault seal phenomenon as they get laterally affected by the presence of the major fault segments.

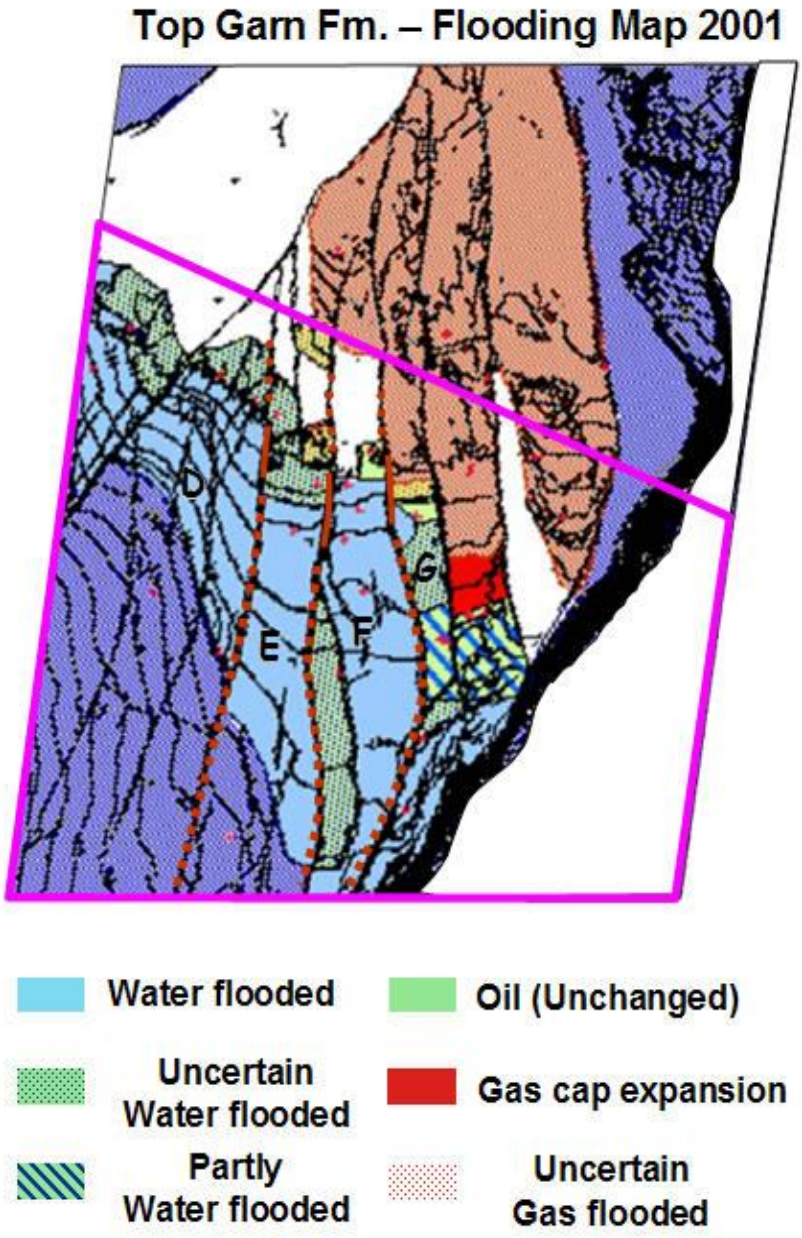

Figure 5.4. *Location of the 4D attribute map on the 2001 flooding map is shown with the purple polygon. Red solid lines indicate analysed fault sub-segments with geologically derived fault properties. Fault segments with unknown sealing character are displayed as red discontinuous lines. Faults 1, 2 and 3 are separating compartments D and E, E and F, F and G respectively.*

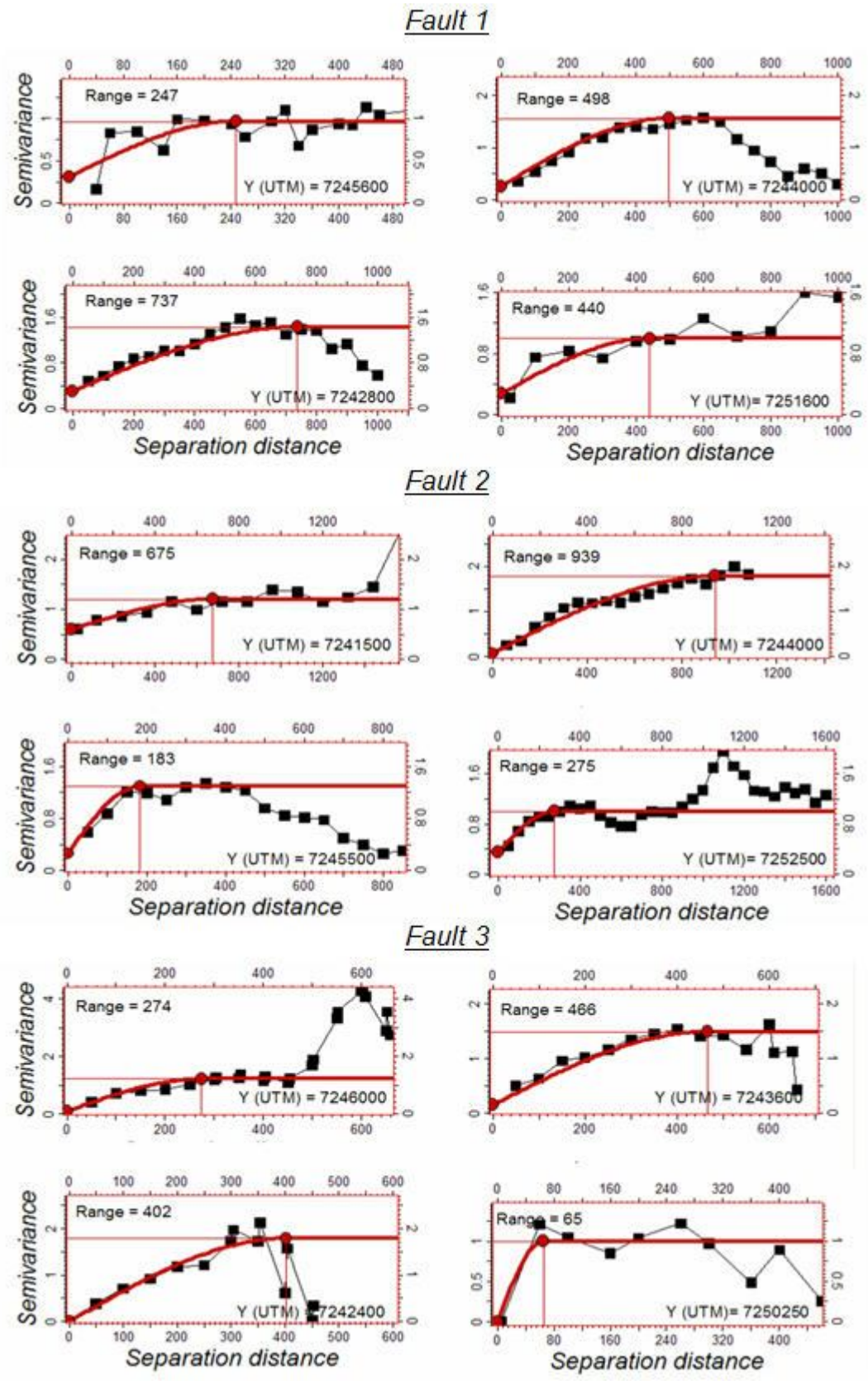

Figure 5.5. *Variograms calculated using the grid representation of the 4D attribute map (RMS amplitude difference) derived from the Upper Fangst Group, Heidrun field. Range values have been estimated within each variogram capturing the measurement variability along the each fault segment.*

Due to well density, fault properties in the southern part of Heidrun field are not easily assessed by means of a geologically based algorithm. Consequently 4D measurements (described in Chapter 4) are extracted for three pair compartments D-E, E-F, and F-G (Fault 1, 2 and 3 respectively) and used to extrapolate the fault property prediction into unknown segments of the connecting fault system. Using the grid representation of the 4D attribute map, 4D inter-compartment difference is calculated for each compartment pair. Also variogram ranges are estimated for each 1D experimental variogram calculated in the fault dip direction capturing the 4D spatial variability measurement (Figure 5.5). For each analysed fault, the 4D measurements are extracted along the fault segment associated with each of the three compartment pairs. Using such statistics, extrapolation of the fault property prediction into unknown segments of the connecting fault system is achieved by firstly calibrating the polynomial approximation via geological fault permeability (calculated from *SGR*) values in a well-controlled sector. In each fault case, the data associated to the calibration sector is assembled in order to estimate the coefficients of the polynomial approximation used as the best fit function for the fault permeability representation.

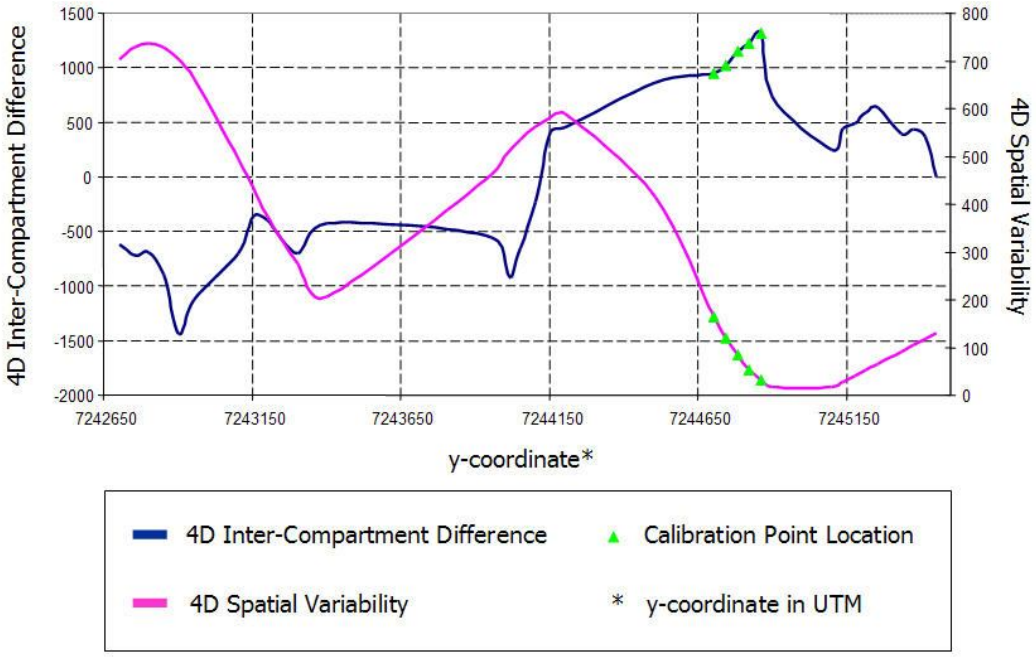

Figure 5.6. *4D statistics derived from the compartment pair D-E and associated to fault 1. The shale gouge ratio estimation in the well-controlled sector of the fault segment is used to derive fault permeability values acting as calibration points (in green). y-coordinate is in Universal Transverse Mercator (UTM) and represents Northing in the coordinate grid.*

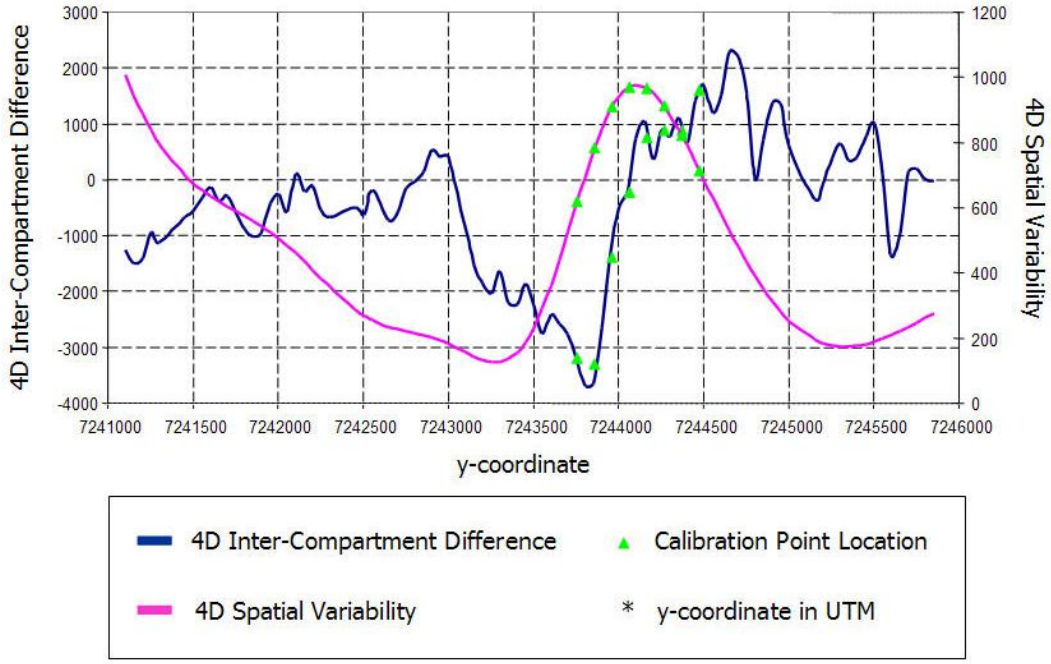

Figure 5.7. *4D statistics derived from the compartment pair E-F and associated to fault 2. The shale gouge ratio estimation in the well-controlled sector of the fault segment is used to derive fault permeability values acting as calibration points (in green). y-coordinate is in Universal Transverse Mercator (UTM) and represents Northing in the coordinate grid.*

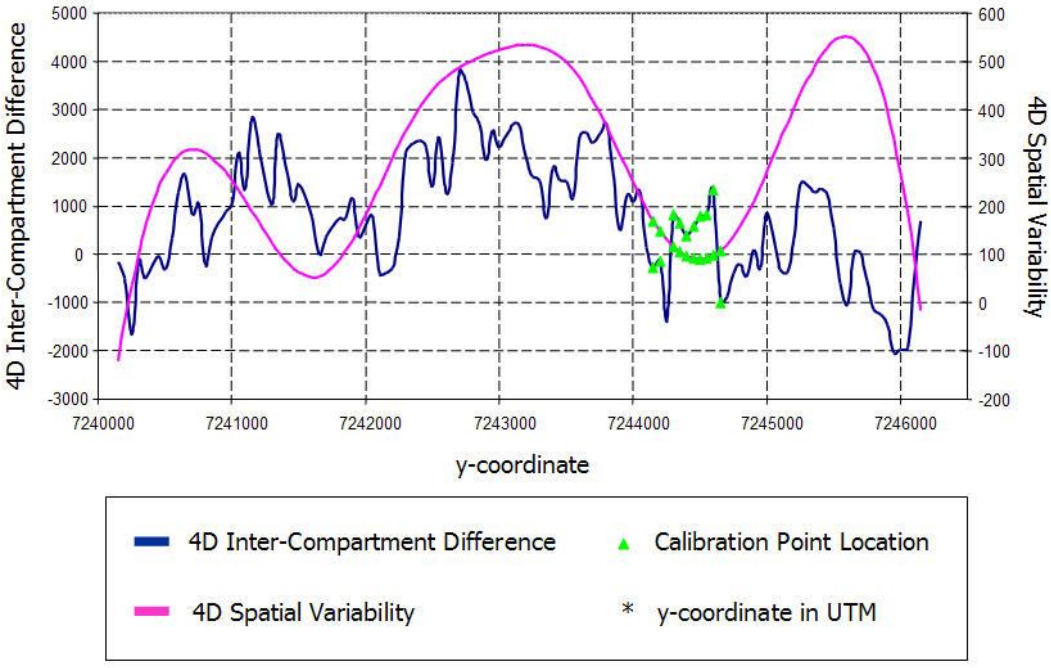

Figure 5.8. *4D statistics derived from the compartment pair F-G and associated to fault 3. The shale gouge ratio estimation in the well-controlled sector of the fault segment is used to derive fault permeability values acting as calibration points (in green). y-coordinate is in Universal Transverse Mercator (UTM) and represents Northing in the coordinate grid.*

As postulated in Chapter 4, the approximation for fault permeability to be considered is given by:

$$k_f(x,y) = a_0 + a_1x + a_2y + a_3x^2 + a_4y^2 \qquad (5.2)$$

where x and y are the 4D inter-compartment difference and the 4D spatial variability respectively. The coefficients of this expression are obtained using the calibration measures shown in Tables 5.1, 5.2 and 5.3.

Sample	x	y	Fault Permeability (mD)
1	943	164	0.217
2	1019	120	0.225
3	1154	83	0.231
4	1222	53	0.240
5	1317	31	0.250

Table 5.1. *Assembled calibration sector to estimate the coefficients of the polynomial approximation used as the best fit function for the fault permeability representation in fault 1. 4D inter-compartment difference and the 4D spatial variability are indicated as x and y respectively.*

A regression analysis consists of a least-squares adjustment between the 4D measurements and the fault permeability values, and is performed in the well-controlled sector. The calibration of the coefficients in the quadratic polynomial expression yields a response surface in each fault case. Table 5.4 gathers the resulting coefficients given by the calibration process. Obtained response surfaces given by the polynomial fit of the available samples are displayed in Figure 5.9, 5.10 and 5.11. Using the approximation given for each fault case, the prediction of the fault permeability values is propagated in the unknown fraction of each fault segment using measurement parameters extracted from the 4D attribute map.

Sample	x	y	Fault Permeability (mD)
1	-3197	619	0.073
2	-3300	783	0.073
3	-1386	910	0.107
4	-218	971	0.154
5	750	966	0.169
6	875	911	0.134
7	880	822	0.096
8	1595	715	0.079

Table 5.2. *Assembled calibration sector to estimate the coefficients of the polynomial approximation used as the best fit function for the fault permeability representation in fault 2. 4D inter-compartment difference and the 4D spatial variability are indicated as x and y respectively.*

Sample	x	y	Fault Permeability (mD)
1	-261	170	0.910
2	-147	149	0.920
3	828	116	0.938
4	638	104	0.942
5	396	96	0.938
6	595	91	0.929
7	800	90	0.921
8	818	92	0.915
9	1338	98	0.899
10	-987	108	0.867

Table 5.3. *Assembled calibration sector to estimate the coefficients of the polynomial approximation used as the best fit function for the fault permeability representation in fault 3. 4D inter-compartment difference and the 4D spatial variability are indicated as x and y respectively.*

Fault	Coefficients				
	a_0	a_1	a_2	a_3	a_4
1	7.89E-01	2.20E-05	-1.86E-03	-3.24E-07	2.43E-06
2	4.42E-01	1.27E-05	-1.33E-03	6.86E-09	1.07E-06
3	8.25E-01	1.43E-04	8.04E-04	-1.44E-07	0

Table 5.4. *Coefficients of the polynomial approximation for the fault permeability for each fault case. Faults 1, 2 and 3 are separating compartments D and E, E and F, F and G respectively.*

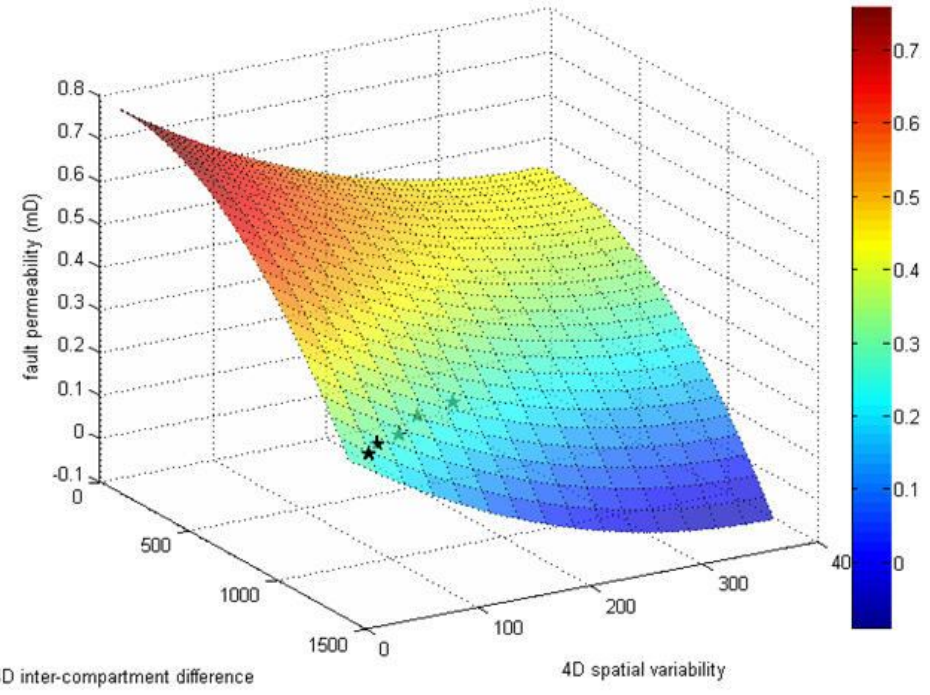

Figure 5.9. *Response surface given by the polynomial fit between the 4D measurements and the fault permeability values estimated in the well-controlled sector for fault 1. Calibration samples are displayed as black stars. Magnitudes in the surface are in mD and associated to the colour bar.*

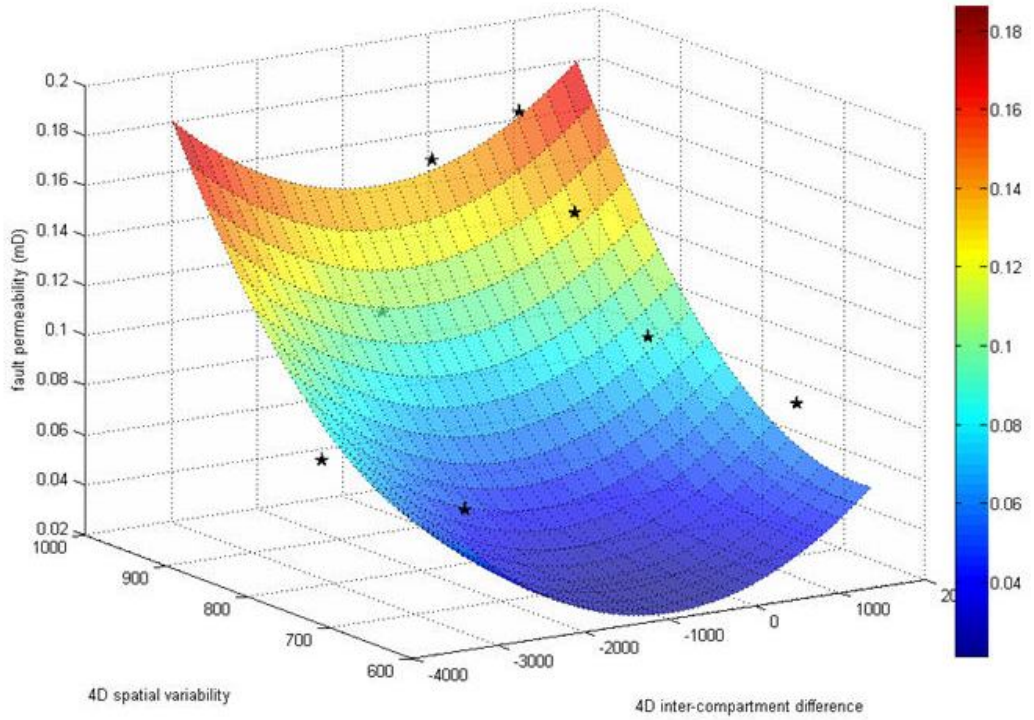

Figure 5.10. *Response surface given by the polynomial fit between the 4D measurements and the fault permeability values estimated in the well-controlled sector for fault 2. Calibration samples are displayed as black stars. Magnitudes in the surface are in mD and associated to the colour bar.*

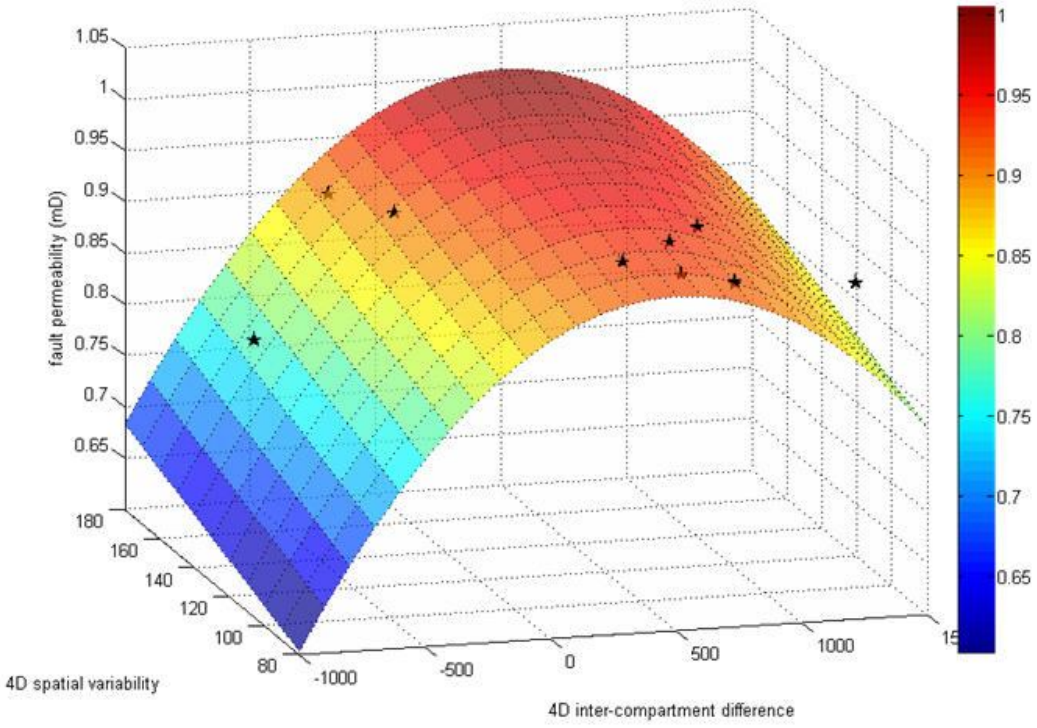

Figure 5.11. *Response surface given by the polynomial fit between the 4D measurements and the fault permeability values estimated in the well-controlled sector for fault 3. Calibration samples are displayed as black stars. Magnitudes in the surface are in mD and associated to the colour bar.*

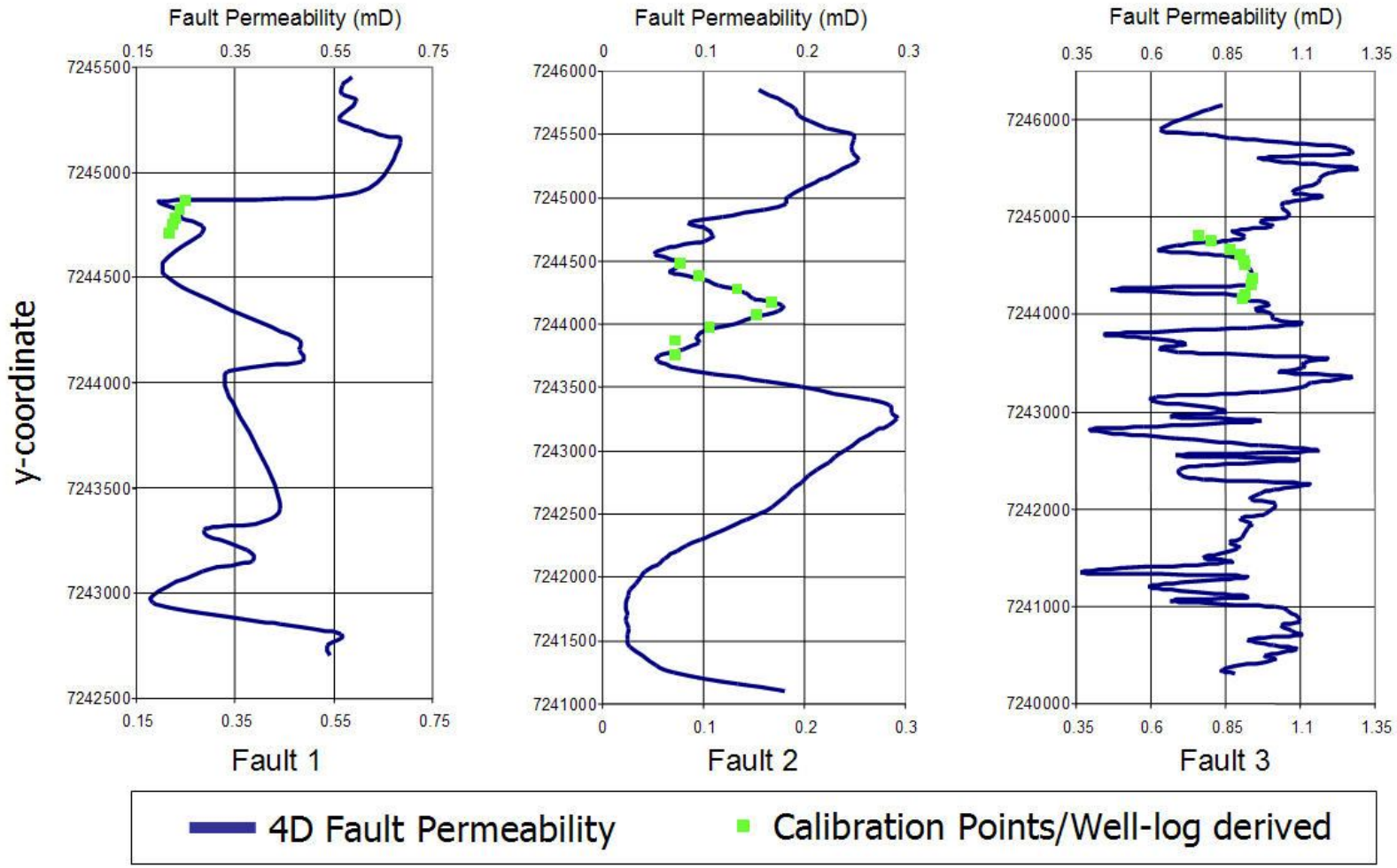

Figure 5.12. *Predicted fault permeability values given by the measurement parameters extracted from the 4D attribute map. Calibration points are also indicated. y-coordinate is in Universal Transverse Mercator (UTM) and represents Northing in the coordinate grid.*

As shown in Figure 5.12, prediction in the calibration sector compares favourably with the well-log derived fault permeability values. Yet, a decrease of the signal-to-noise ratio in the 4D attribute map, particularly in the vicinity of fault 1 (within compartments E and D), leads to a less robust calibration process. Indeed, the normalized root-mean-square difference between two seismic vintages *NRMS* values reveals the likeness of the traces between these surveys (Kragh and Christie, 2002). In particular, for two traces defined as a_t and b_t, the *NRMS* is defined here below:

$$NRMS = \frac{200RMS(a_t - b_t)}{RMS(a_t) - RMS(b_t)} \tag{5.3}$$

where *RMS* is expressed as,

$$RMS(a_t) = \sqrt{\frac{\sum_{t1}^{t2}(a_t)^2}{N}} \tag{5.4}$$

and N is the number of samples in the interval $t_1 - t_2$. *NRMS* values close to 0 in a window above the reservoir indicate higher repeatability, as no changes are expected in the overburden during the time frame in which both seismic vintages are acquired. In the Heidrun field, *NRMS* amplitudes (between 2001 and 1986 seismic vintages) calculated in a window of 150 ms above top reservoir show average values of 50; however regions with higher *NRMS* are detected (Figure 5.13). Most of the anomalies seem to be related to the lack of repeatability associated to the presence of faults, while others appear in the compartments from which both statistics of the 4D seismic are extracted. Such low repeatability zones introduce uncertainties in the analysis of the time-lapse seismic signature which might be related to acquisition footprints still remaining after the simultaneous reprocessing of the base and monitor surveys (Furre et al. 2004). In particular, *NRMS* values above 100 appear more frequently in compartments D and E. Indeed, average cross-validation errors for the fault permeability prediction are higher for the fault 1 when compared to the mean errors for faults 2 and 3 (Figure 5.14). Nonetheless, as shown in the discussion section of this chapter estimated fault permeability values seem to be in agreement with magnitudes showed in Knai and Knipe (1998) where fault rock types have been analysed in the Heidrun field.

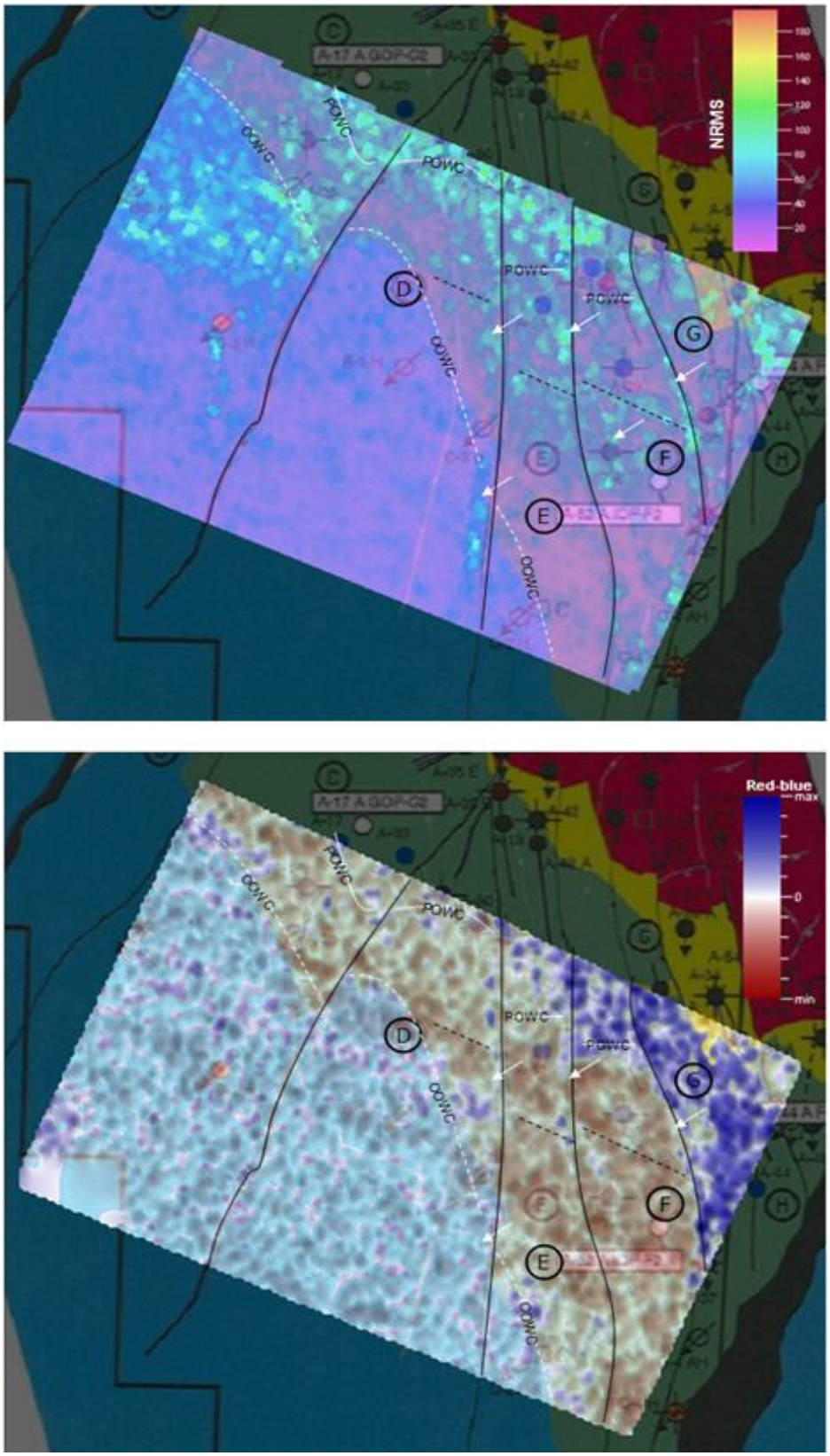

Figure 5.13. *Above: Repeatability measurements (NRMS) in a window of 150 ms window above top reservoir. White arrows point to low repeatability zones associated with the presence of faults. High NRMS magnitudes appearing parallel to the acquisition geometry are indicated as black dotted lines. Below: 4D seismic attribute map at top reservoir. Low repeatability regions discussed above are also shown. Original oil water and production oil water contacts appear as OOWC and POWC respectively.*

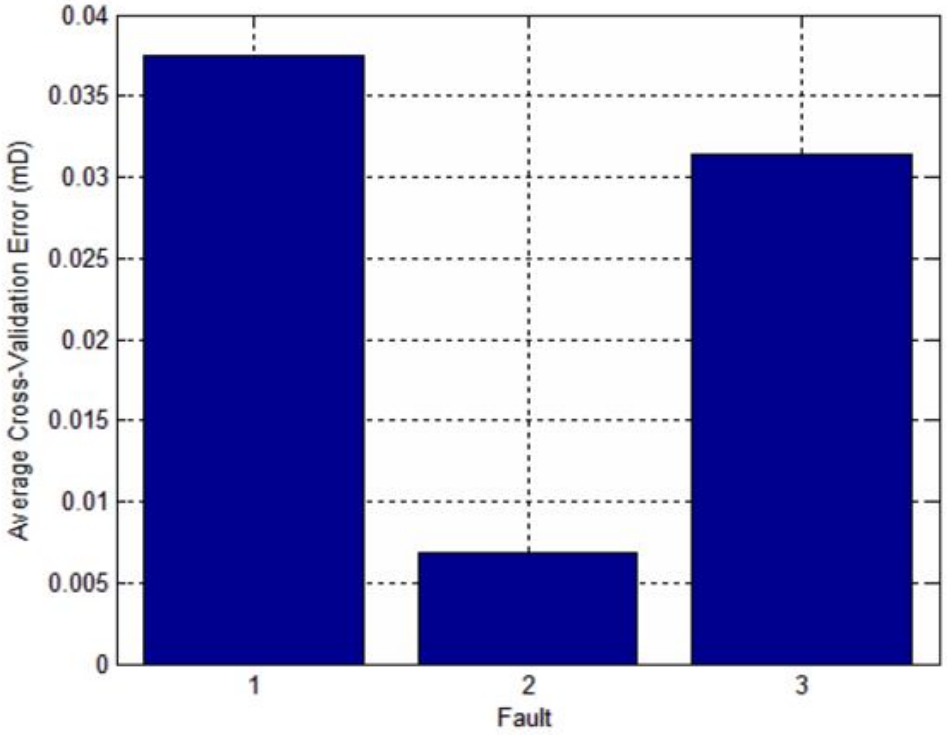

Figure 5.14. *Average cross-validation error for each analysed fault.*

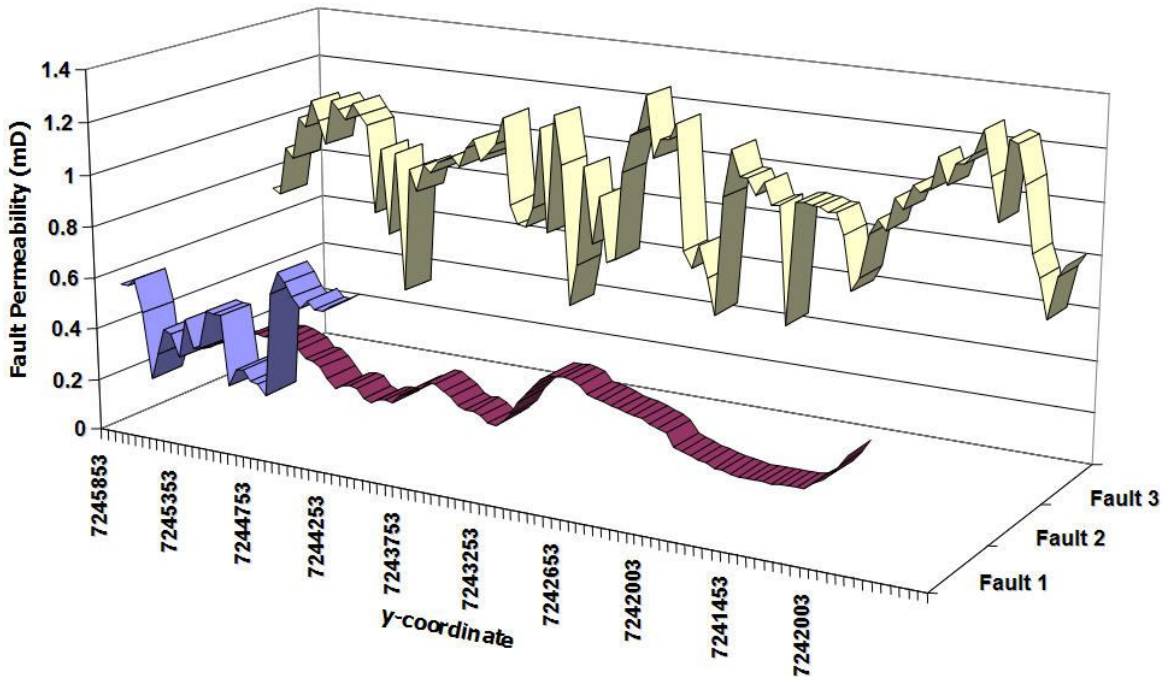

Figure 5.15. *Comparison between fault permeability values for the analysed fault segments. y-coordinate are in Universal Transverse Mercator (UTM) and represents Northing in the coordinate grid.*

Comparison between fault permeability values obtained in each fault case is displayed in Figure 5.15. Lowest fault permeabilities are shown in fault 2 whereas the higher values are included in the profile associated with fault 3. Also variations along each fault segment seem to respond differently in each in the fault case. These changes in the sealing behaviour strongly impacts the way in which the associated compartments are being depleted. In particular for the Fangst Group reservoirs, the reduction in permeability in the fault leads to disruptions in the saturation fields and hence the flooding strategy imposed in the field.

5.4 Uncertainty evaluation

In the study of the uncertainties introduced in the prediction of the fault permeability, an evaluation of the uniqueness of the variogram modelling is performed employed the approach outlined in Chapter 4. Using the automatic fitting program described in Pardo-Iguzquiza (1999) five different functions are used, yielding various estimates of the variogram range. Using such population of samples, five realizations of the 4D spatial variability are assembled for each of the three studied faults (Figures 5.16, 5.17 and 5.18).

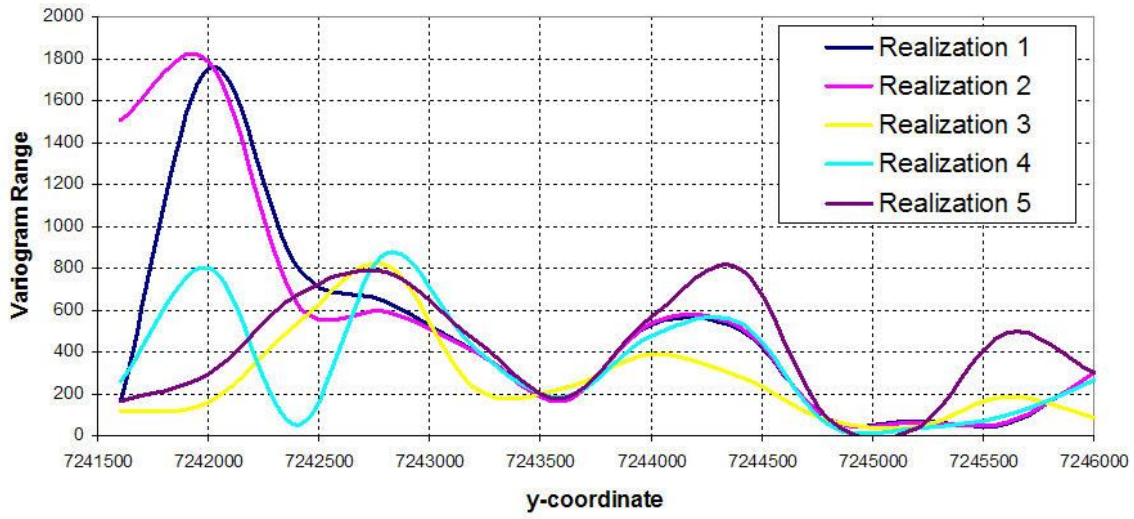

Figure 5.16. *Five different realizations of the 4D spatial variability associated with fault 1. This is derived from the RMS amplitude difference extracted at the Upper Fangst Group, Heidrun field. y-coordinate are in Universal Transverse Mercator (UTM) and represents Northing in the coordinate grid.*

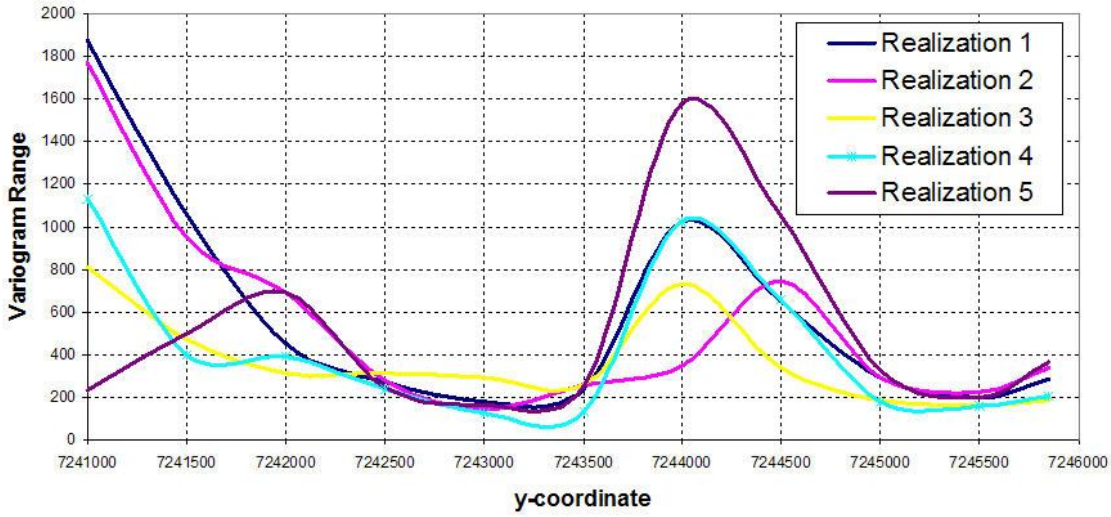

Figure 5.17. *Five different realizations of the 4D spatial variability associated with fault 2. This is derived from the RMS amplitude difference extracted at the Upper Fangst Group, Heidrun field. y-coordinate are in Universal Transverse Mercator (UTM) and represents Northing in the coordinate grid.*

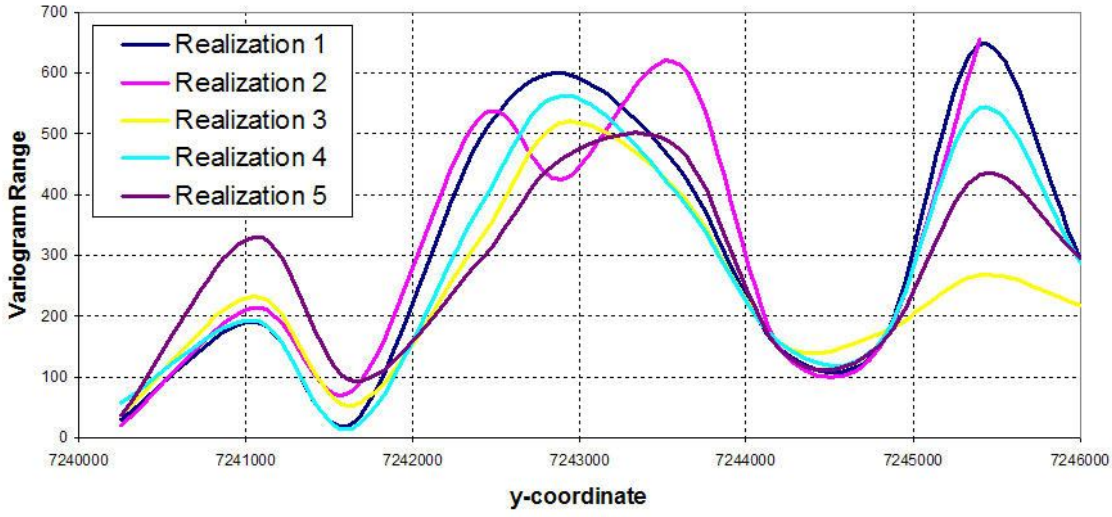

Figure 5.18. *Five different realizations of the 4D spatial variability associated with fault 3. This is derived from the RMS amplitude difference extracted at the Upper Fangst Group, Heidrun field. y-coordinate are in Universal Transverse Mercator (UTM) and represents Northing in the coordinate grid.*

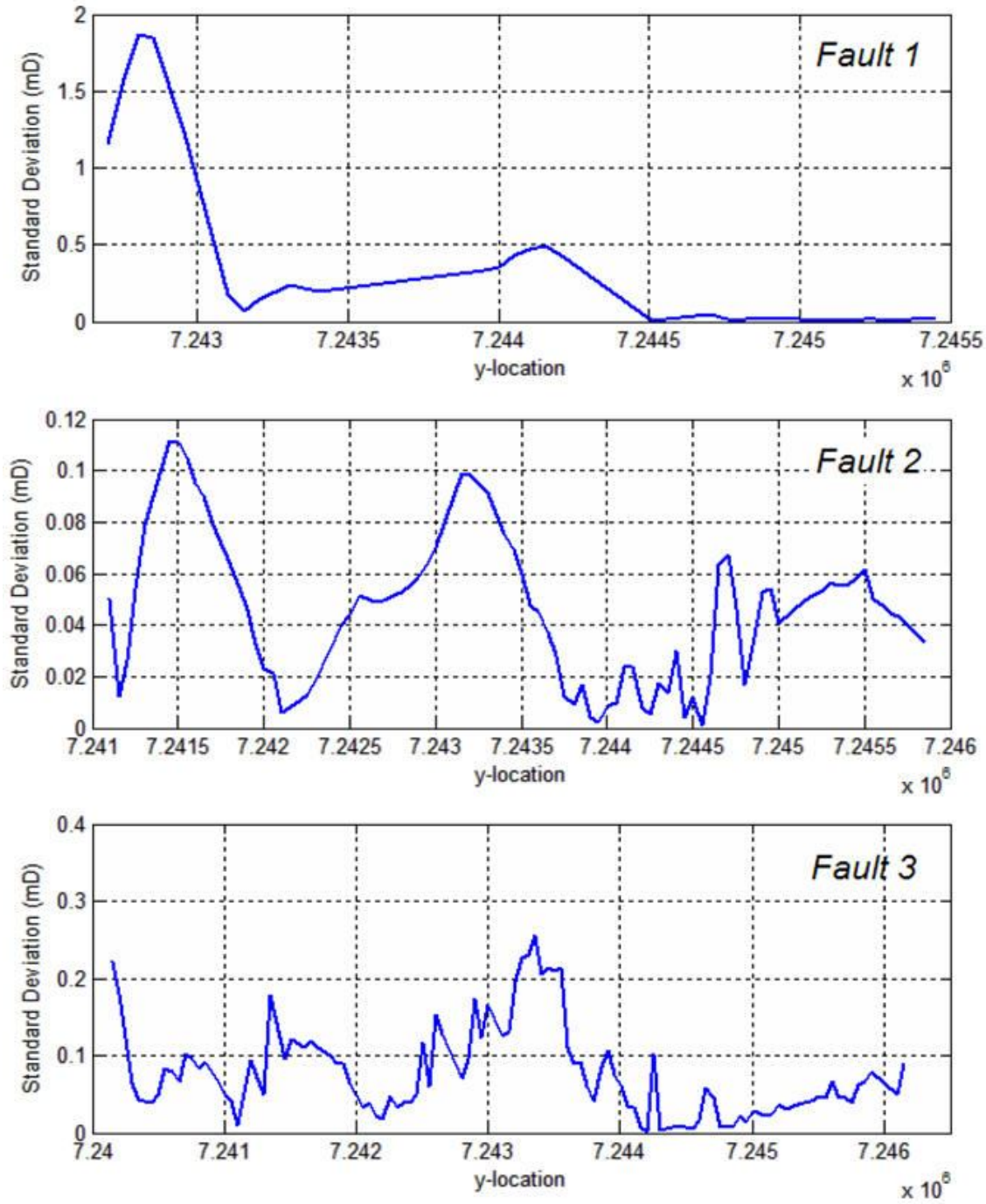

Figure 5.19. *Derived Standard deviation associated to a particular location for each fault segment. Values indicated in the y-location axis are expressed in Universal Transverse Mercator (UTM) system and represents Northing in the coordinate grid.*

Calibration of the coefficients included in the quadratic polynomial approximation of the fault permeability is repeated for each realization of the 4D spatial variability and the fault property estimates are then obtained for the each response surface scenario. In all cases 4D inter-compartment difference is assumed invariant relative to the errors introduced by the variogram modelling. The variation of fault permeability for a particular sample according to each polynomial representation (derived via calibration of the coefficient in each particular realization) is used to measure the standard deviation of the prediction at a particular location in the fault segment (Figure 5.19). Then, using the probability density function (pdf) defined by the likelihood function (equation 4.4 in Chapter 4), the probabilities associated with the possible values of fault permeability for each fault case are calculated. Probability maps have been generated for each fault in which possible fault permeability values for each sample (included in the fault segment) are shown according to their probability of occurrence (Figures 5.20, 5.21 and 5.22).

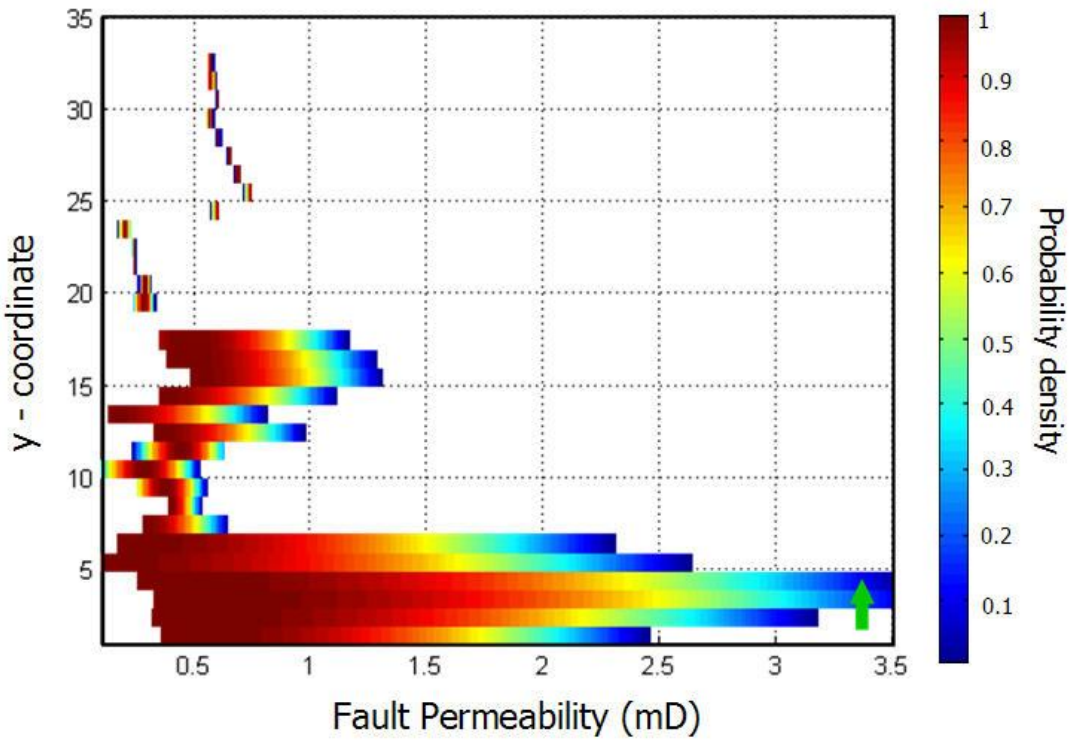

Figure 5.20. *Probability map showing for each sample in the fault segment 1 an interval with all possible fault permeability values which have been colour coded according the probability of occurrence. Probability density values have been normalized. Values indicated in the y-coordinate axis are displayed as sample number to enhance visualization.*

Observation of such probability maps reveals the presence of a narrower interval of possible fault permeability values for the samples used as training points during the calibration of the polynomial expression. Indeed, as such training samples have been kept constant for the inversion of the response surface realizations; they exhibit lower standard deviation values when compared to the points included in the unknown sector of the fault segment.

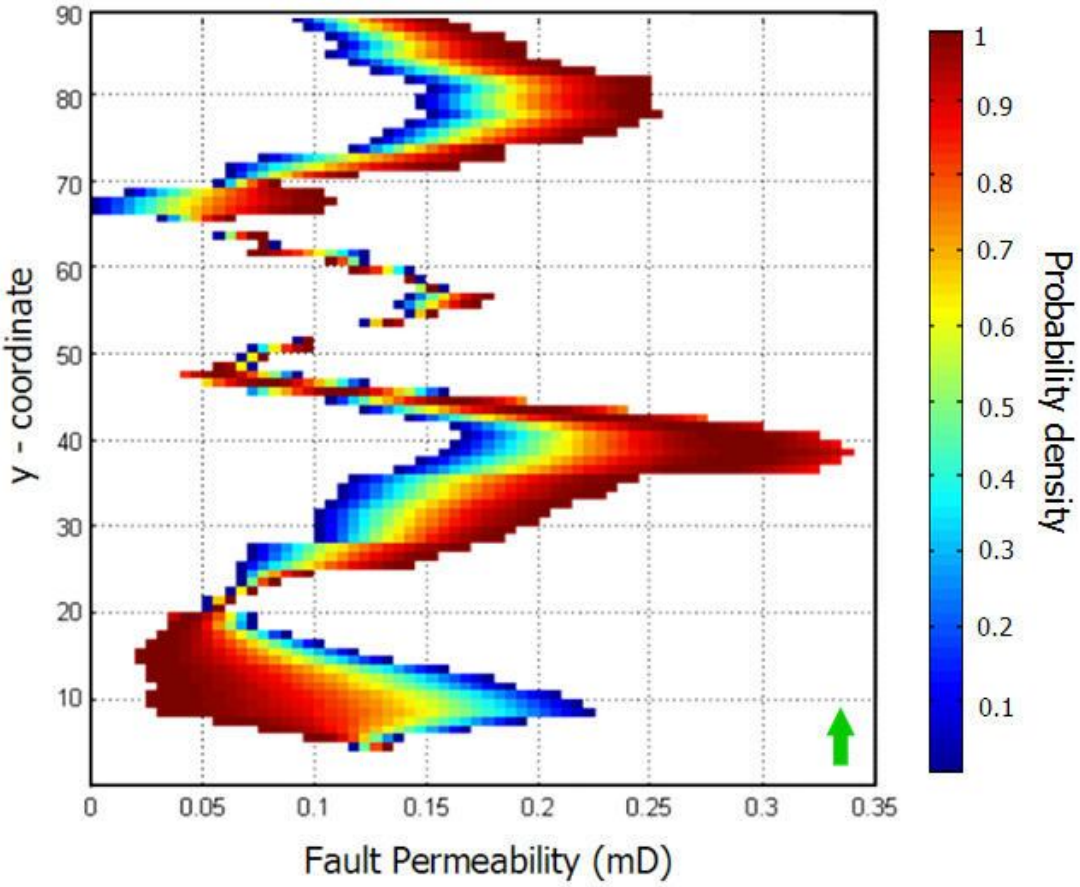

Figure 5.21. *Probability map showing for each sample in the fault segment 2 an interval with all possible fault permeability values which have been colour coded according the probability of occurrence. Probability density values have been normalized. Values indicated in the y-coordinate axis are displayed as sample number to enhance visualization.*

Evaluation of these probability maps serve to highlight regions in the fault segment with different levels of uncertainty related to the fault permeability prediction. The wider the interval of values for a particular sample is, the higher the uncertainty of the fault property. In particular a decrease of the signal-to-noise ratio in the 4D attribute map in the vicinity of fault 1 (compartments D and E) as shown above with the *NRMS* map, leads to a less robust calibration process translated in an increase of uncertainty. As

described in this specific fault case, the qualitative assessment of the information contained in such maps helps to quickly identify and quantify regions with ambiguities. Once these probability maps are assembled, cumulative density function (cdf) are derived for each sample located in each of the three fault cases. The cumulative form of these maps is employed to derive the P10, P50 and P90 percentiles for the fault permeability values associated to each fault segment (Figure 5.23).

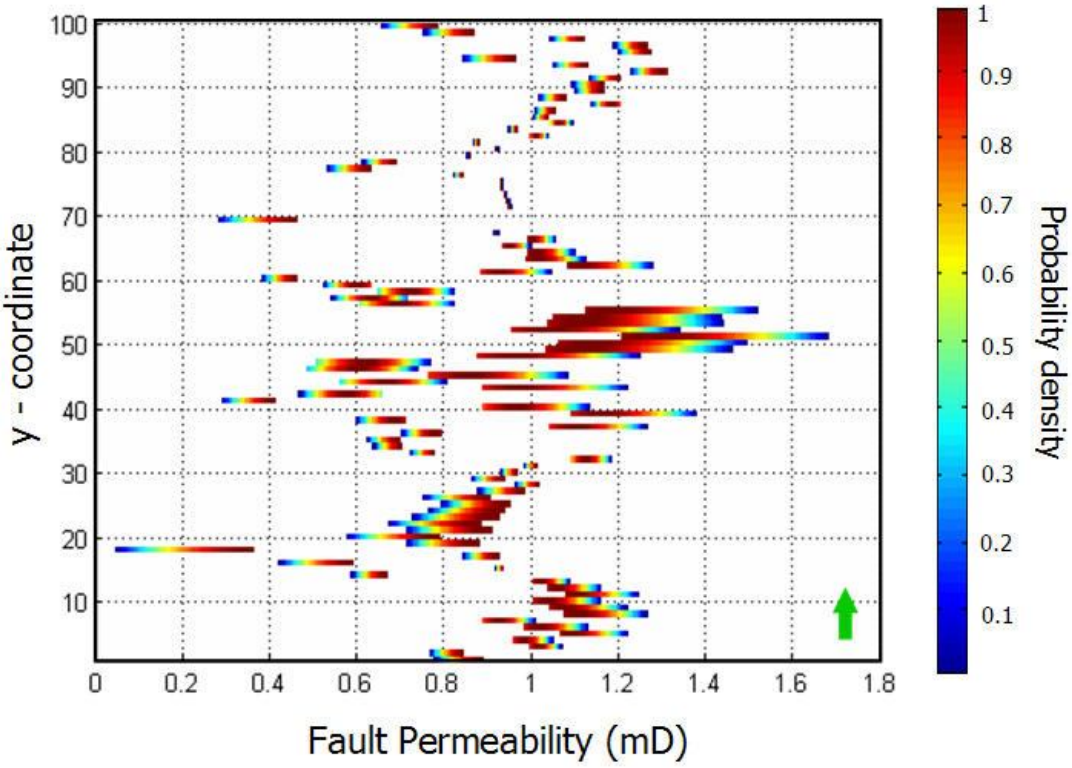

Figure 5.22. *Probability map showing for each sample in the fault segment 2 an interval with all possible fault permeability values which have been colour coded according the probability of occurrence. Probability density values have been normalized. Values indicated in the y-coordinate axis are displayed as sample number to enhance visualization.*

The estimation of the fault permeability as part of the reservoir parameters from 4D seismic, motivates the updating of such variable in the simulation model. The results presented in this chapter can be viewed as means of starting the optimization search in the history matching workflow. To address such subject Chapter 6 builds on the implementation of the 4D estimation as well as the uncertainties associated with such fault permeability prediction. By incorporating the results obtained in this chapter into the geological modelling of the Heidrun field, 4D seismic provides added value beyond current conventional approaches.

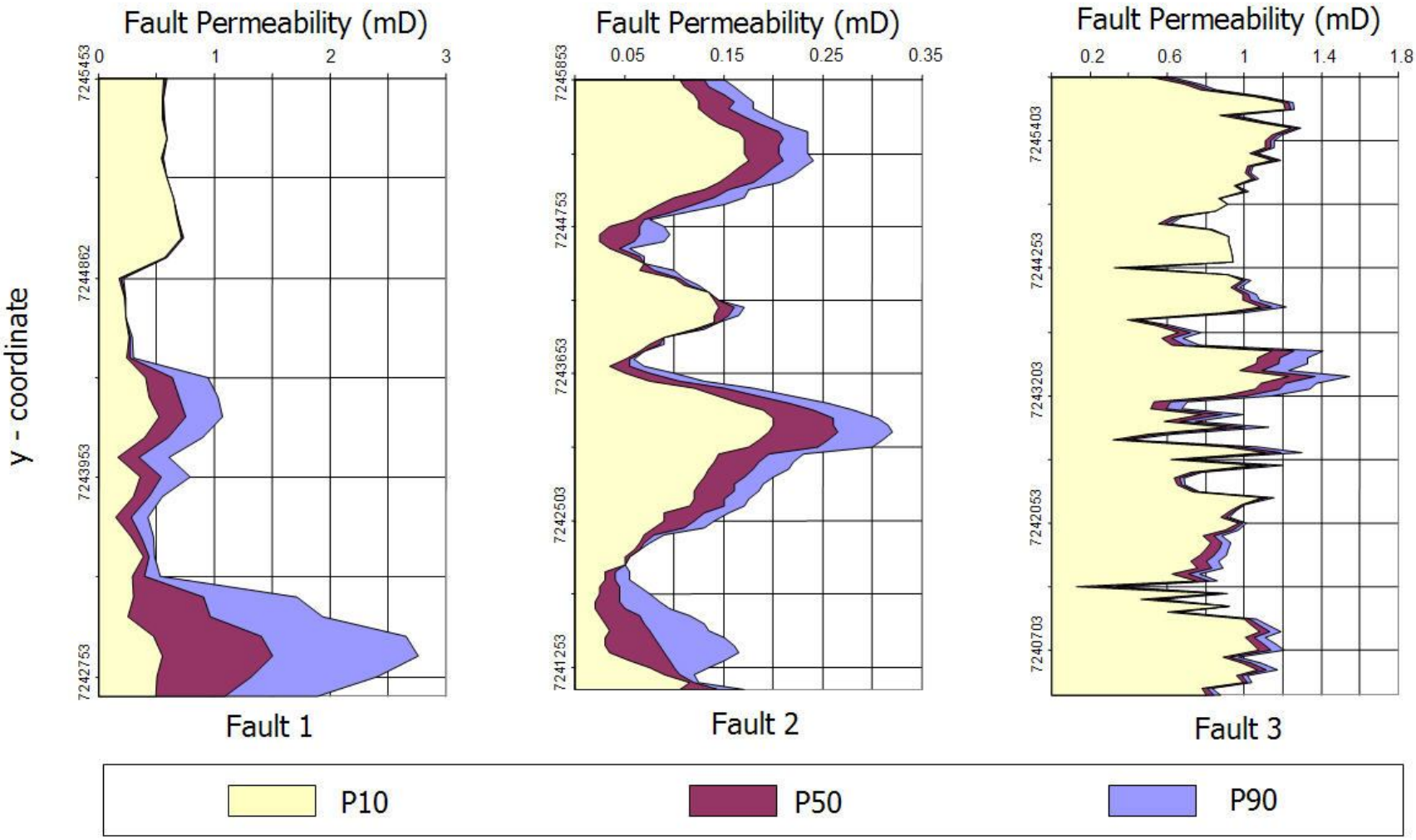

Figure 5.23. *Extracted percentiles for the analysed faults. Here P10, P50 and P90 are probabilities of finding fault permeability below that indicated by the curve. y-coordinate is in Universal Transverse Mercator (UTM) system and represents Northing in the coordinate grid.*

5.5 Discussion of results

As a first evaluation of the 4D-estimated fault permeability values, previous studies in the Heidrun field are brought here, in particular the quantitative analysis of the fault sealing properties presented in the Knai ad Knipe (1998). In this study, a microstructural and physical property analysis of the fault rock cores was implemented to evaluate the deformation mechanism and the petrophysical properties of the reservoir faults in the Heidrun field. Several fault rock types (presented in Fisher and Knipe, 1998) are identified in the Heidrun cores. Particularly cataclasites (developed from clean sandstones), phyllosilicate framework fault rocks (created from impure sandstones) and clay smears are observed in the reservoir faults. Based on such core analysis, representative fault permeabilities are assigned to each fault rock category. Such findings are summarized in Table 5.5.

Fault Rock Type	Fault Permeability (mD)		
	Average	Low	High
Cataclasite	0.14	0.006	0.3
Phyllosilicate Framework (low clay)	0.11	0.1	0.12
Phyllosilicate Framework (high clay)	0.018	<0.001	0.07
Clay smear	0.0014	<0.001	<0.003

Table 5.5. *Review of fault permeability values in the Heidrun field derived in the study presented by Knai and Knipe (1998) as observed from the fault rock analysis on Heidrun cores. Average, lower and upper limits are shown.*

For faults setting juxtaposed reservoir units within the Fangst Group, fault permeabilities are expected to be in the order of 0.3 mD, however the introduction of this value (as constant) along the faults in the simulation model (using fault transmissibility multipliers), later revealed that history match of the production is improved by considering fault permeability values up to 3 mD for those reservoirs with highest host rock permeabilities (i.e. Fangst Group). From the history match results implemented in that study, it is inferred that permeabilities for the cataclasite fault rock type (which might dominate the fault microstructure in the Fangst reservoirs) could also be higher than the measured upper limit of 0.3 mD observed in some core data. Ultimately, a constant value of 1 mD is finally introduced during their updating of the simulation model, and assumed best fit in that study. According to Knai and Knipe (1998), this adjustment in the fault permeability is justified as it has been also evidenced in other fields.

The first order solution previously discussed seems in agreement with the 4D seismic prediction obtained along this chapter. Fault permeability values calculated in our way are found to lie between 0.1 and 1 mD, with the magnitude of these results being in agreement with previous fault rock studies applied to the Heidrun field. Also, the uncertainty analysis shown in the previous section, revealed that the upper limit for the fault permeability magnitudes might be reaching the 3 mD cut for a particular sector of the fault segment (as in Fault 1). Nonetheless, to evaluate the implications of the estimated fault permeability values in terms of the reservoir development and production history match, the reservoir model needs to be updated and the fluid flow simulated. As shown in Knai and Knipe (1998), lack of core sampling for critical reservoirs such as in the Fangst Group strongly impacts the fluid flow understanding as the cataclasite developed in such reservoir setting is responsible for the dominant flow path. In the previous studies, available dataset provided by cores did not allow fully evaluation of the fault-rock permeabilities and, as recommended in such work, refinement of fault-related flow is required to improve the impact of the fault seal variable. In the next chapter, we implement our 4D estimation taking advantage of the spatial coverage offered by the time-lapse seismic signature, finally incorporating our fault permeability values by introducing them as 4D derived transmissibility multipliers, and closing the loop with the evaluation of the misfits of the production match offered by our update when compared to a base case model where 4D seismic is not considered.

5.6 Summary

In the classical fault sealing evaluation techniques, the construction of representative fault seal models included in the reservoir framework can be misunderstood as a result of the sparse nature of the geological information offered by cores or well logs. In the Heidrun field case; this phenomenon limits the way in which such unknown can be propagated in order to perform a geological seal prediction for faults defining major compartments. In this chapter it is found that time-lapse seismic helps the aerial resolution of fault seal determination beyond that produced by well-based estimation. In particular, prediction via the measurement parameters 4D inter-compartment difference and the 4D spatial variability of the signature given by a 4D attribute map allows propagation of fault permeability in three major fault cases separating compartments D, E, F and G of the Heidrun field. Also, analysis of the uncertainties related to the 4D seismic prediction is assessed. By understanding the levels of uncertainties associated with the fault permeability estimation it is possible to reduce ambiguities associated with the sealing behaviour of the faults. Comparison of the 4D estimation with previous studies related to the fault seal capacity, shows agreement as the fault permeability values calculated with our method are found to lie in the same order of magnitudes as those obtained in the study of fault-rock types analysed from Heidrun cores.

Chapter 6

Updating the simulation model using fault transmissibility multipliers derived from the 4D seismic signature of the Fangst Group, Heidrun Field

This chapter describes the updating of the reservoir simulation model of the Heidrun field. Fault permeabilities estimated via 4D seismic are now upscaled and used to derive fault transmissibility multipliers for the studied fault segments. Simulated results given by the base case and updated reservoir models are compared. An improvement of the match with history production is found in the model updated with the 4D seismic input. Also an automatic history match procedure which includes the 4D estimates and its uncertainty is implemented. By including such a workflow the mismatch with production data and the spatial correlation with the 4D data are enhanced.

6.1 Introduction

The implementation of fault transmissibility multipliers in reservoir simulation models to describe the fault zone properties is essential to represent the structural barriers affecting the fluid flow during reservoir depletion. In order to represent the sealing properties of the faults in a modelling framework, various kinds of information are employed. Current workflows rely on fault rock permeabilities (derived from core measurements or clay/shale portion in logs) and fault thickness which are commonly derived from geologically-based methods. Other assumptions, involving fault geometry, fault throws and reservoir juxtaposition are generally based on the information offered from seismic data (i.e. 2D and 3D). When available, well-testing techniques and injection of tracers might also help as part of the qualitative assessment of the reservoir compartmentalization. Ultimately, history matching techniques help to quantify fault properties but if this approach is used without calibration with other background information, fault assessment found in this way might be misleading. In spite of such efforts it is still difficult to fully understand the effects of the compartmentalization, as the prediction of fault properties is in most of the cases biased by the available data and the integration capability. To ensure that all sampling tools and associated measurements are used to characterize the sealing capacity of faults consistently, the sampled information should be combined in a single workflow. Here we make use of the results presented in the previous chapter, in which statistics of the 4D seismic signature are integrated with geologically-based estimates delivering a new fault property evaluation in the Heidrun field. Now, using this 4D prediction we update the Heidrun reservoir model introducing geologically-consistent 4D fault transmissibility multipliers. Taking into account their associated uncertainties, an automatic history matching workflow is implemented and misfits with the production data are evaluated.

6.2 The reservoir simulation model in the Heidrun Field

The reservoir simulation model of the Heidrun Field has been provided by the operator (Statoil) and it is used as a means to perform volume calculations and production forecasts as well as the uncertainty quantification related to the reserves and production rates. Also, it helps to design the plan of actions to be imposed in the field during its development, particularly the well planning and the ranking of well targets. The model

has been built by the operator at a vertically fine gridscale (with grid cell dimensions 120 m x 110 m x 10 m) with a total cell number of 910,248 and comprises all the producing reservoirs in the field. These are the reservoirs associated with the Fangst Group (i.e. Garn and Ile Formations) and the Båt Group (Tilje and Åre Formations). The reservoir zonation in the full field model contains 68 layers, each of them involving several modelling challenges which are associated with structural, stratigraphic and data management complexities. In terms of the structural aspect, the field is compartmentalized in major segments, but also minor interpreted faults have been incorporated. As for the stratigraphy, formations in the Fangst Group show good and relatively homogenous reservoir properties while those Formations included the Båt Group are highly heterogeneous units. The diverse information included in this single model is a result of the integration of all the available information and its manipulation might be complex and time consuming if an appropriate workflow is not implemented.

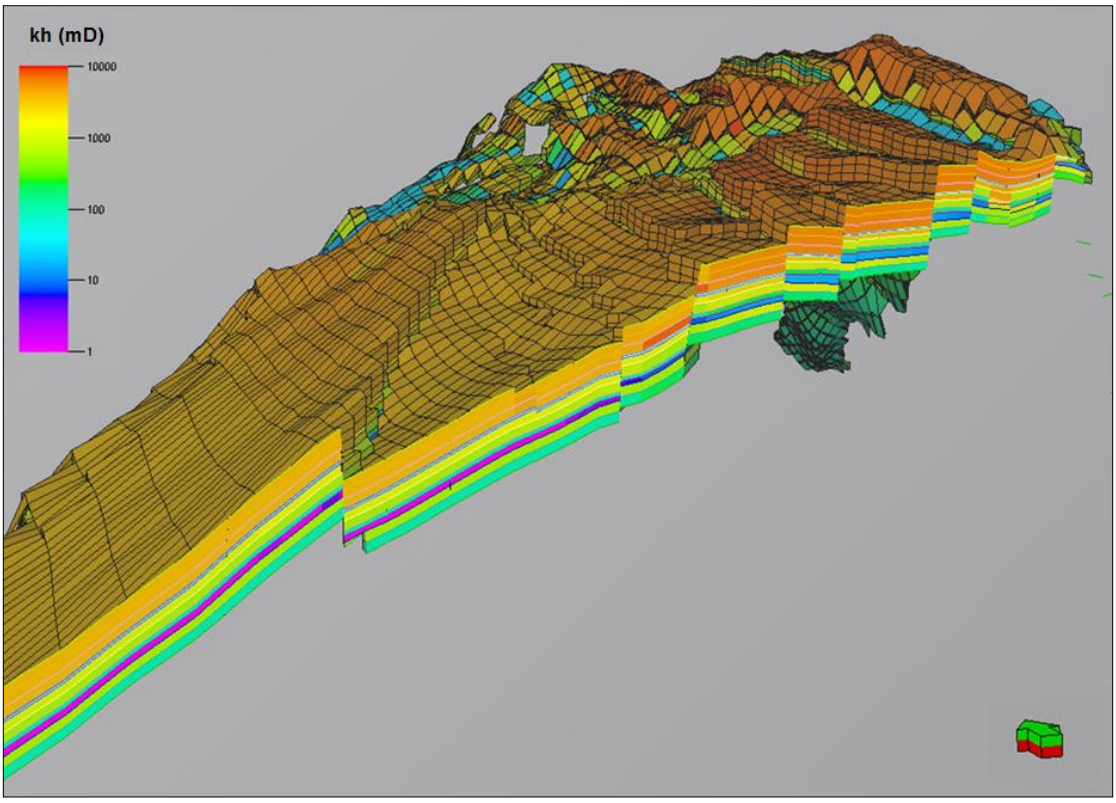

Figure 6.1. *The Fangst Group shows excellent and lateral continuous reservoir qualities. In particular, horizontal permeabilities are very high reaching values up to 10,000 mD. As a consequence major barriers to fluid flow in the field are related to the presence of faults.*

For the purposes of this thesis, the reservoir zonations used here are simplified to those included in the Fangst Group only (containing up to 13 layers) as the study of the 4D seismic signature of this field has focused on this stratigraphic unit. In here, laterally continuous properties (Figure 6.1) and excellent reservoir quality are present as average porosity values are high (20%) and permeability values reach 10,000 mD (Figure 6.2). Also the net-to-gross distribution in these layers has been kept constant and equal to 1 and based on the shallow marine facies which seem to dominate the stratigraphic unit. Hence changes in reservoir communication are highly dependent on the fault properties as the degraded petrophysical properties of the fault-rock act as a barrier to the fluid flow when compared to the reservoir characteristics.

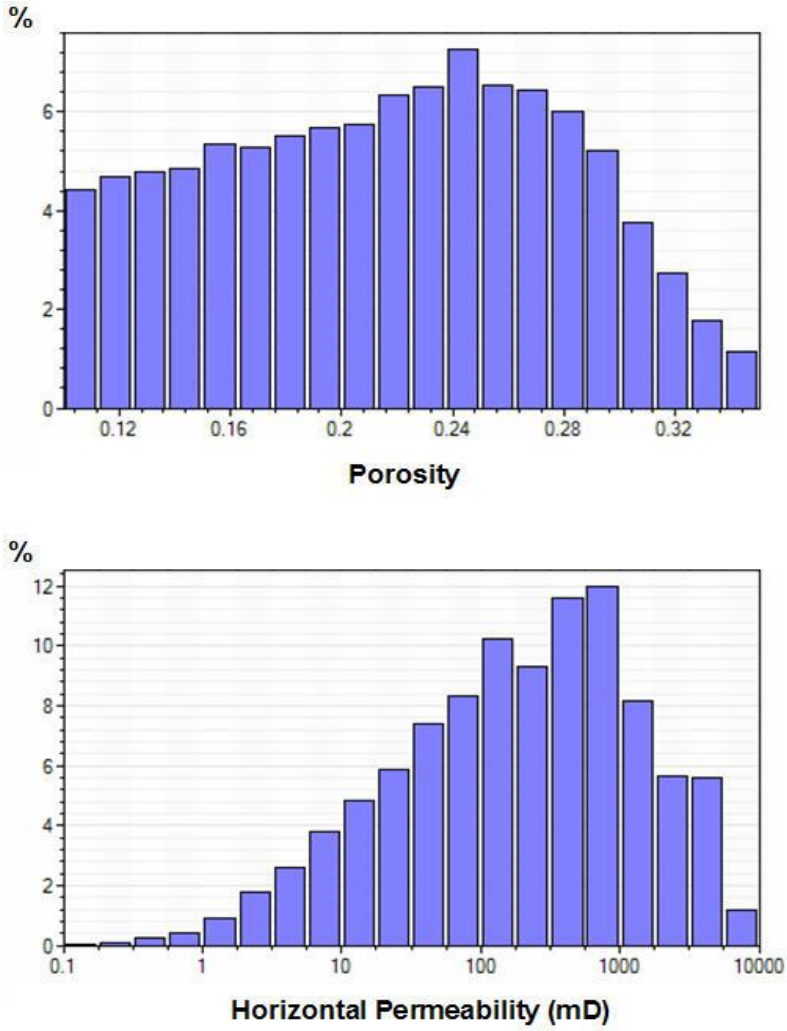

Figure 6.2. *Petrophysical properties included in the reservoir simulation model for the Fangst Group.*

6.3 The simulation results

The existing reservoir model for the Heidrun field provided by Statoil (base case) simulates a black oil system with water and gas flooding over several time steps. A strong water drive is imposed from the down-flank side of the field by water injectors. Also gas injectors are located in the up-flank edge of the field providing the pressure support needed during the production (Figure 6.3). In general, the water injection strategy serves to displace the reservoir oil towards the producer wells. These are located below the gas injection zone which in turn helps to maintain the pressure, ultimately controlling the inter-well communication.

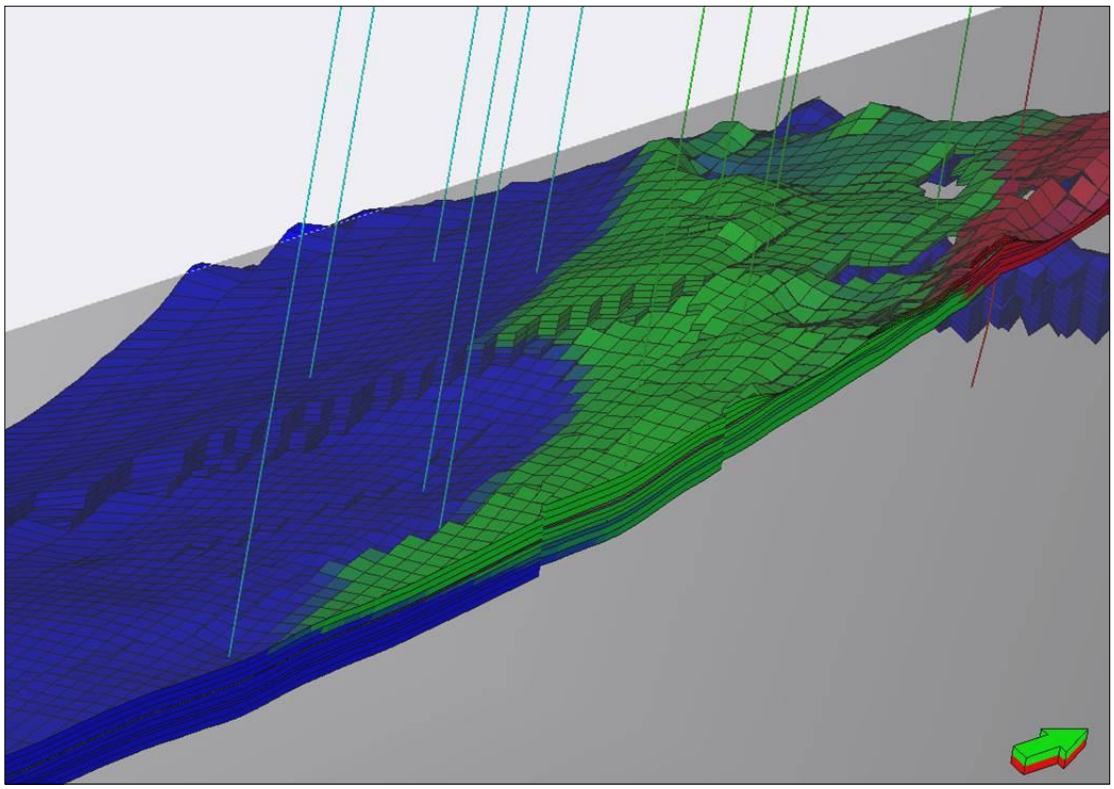

Figure 6.3. *Initial fluid distribution along the dip direction of the field. Water, oil and gas are represented as blue, green and red, respectively. Water injector wells located in the down-flank side of the field (in light blue) impose a strong water drive in the reservoir. Also gas injectors in the upside-flank edge (in red) help to maintain the reservoir pressure.*

Although work is currently being pursued by the operator to fully history match the reservoir simulation model, available pressure and saturation predictions at this point are used to analyse the 4D seismic signature observed in the reservoirs. In particular, simulated pressure, water and gas saturation changes between the 1995 (pre-production) and 2001 (post-production) stages are evaluated.

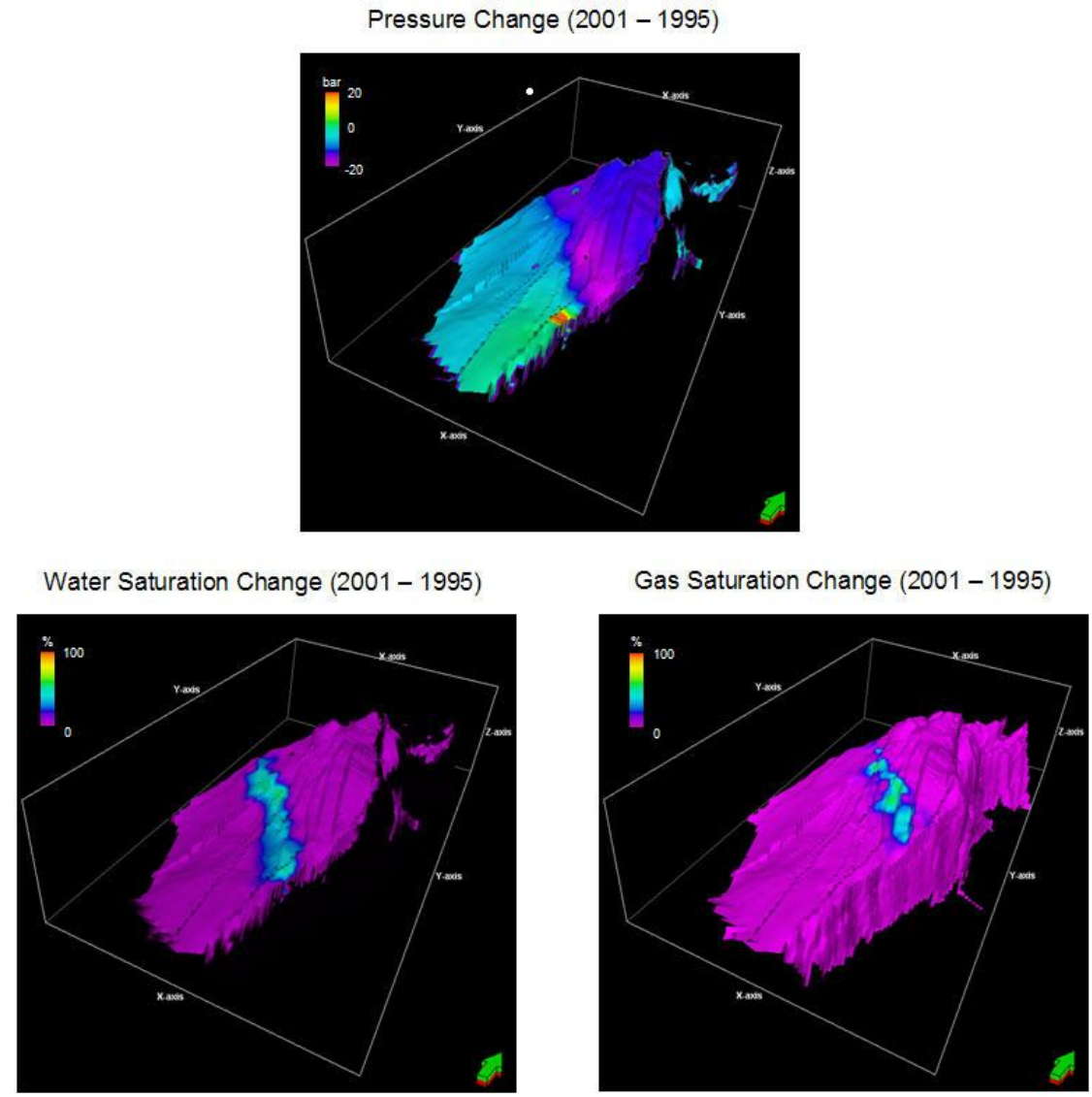

Figure 6.4. *Simulation predictions for the pressure (above), water (lower left) and gas saturation (lower right) changes. Differences have been calculated for the 2001-1995 time interval and represent average changes for the Fangst Group.*

For the simulated pressure change, a mean decrease of 7 bar is evidenced in the Fangst Group. In general, the pressure decreases towards the upside flank of the field. In terms of the water saturation change, a maximum increase of 50 % (average in Fangst) in the water levels is evidenced in the flooded zone. For the observed dynamic changes, their spatial distribution throughout the field can also be related to the extracted 4D seismic signature which has also been discussed in Chapter 3. RMS amplitude difference (2001-1986) extracted in a 16 ms window centred in the Upper Fangst Group has been compared with the simulation output. The 4D signal reveals a discrete long period

anomaly which is in turn characterized by positive magnitudes in the RMS difference attribute map. When associated with the simulated pressure change, the anomaly appears on the area affected by the highest pressure drop (- 20 bar), whilst a lack of a coherent signature exists where small pressure changes (-6 bar) occur (Figure 6.5). The anomaly seems to be also correlated to the gas cap expansion taking place in the up-flank edge of the field, where the increase in gas saturation reaches values of up to 70% (Figure 6.6). Here, the gas saturation increase and the pressure decrease are interacting in opposite ways by decreasing and increasing P-wave impedances respectively.

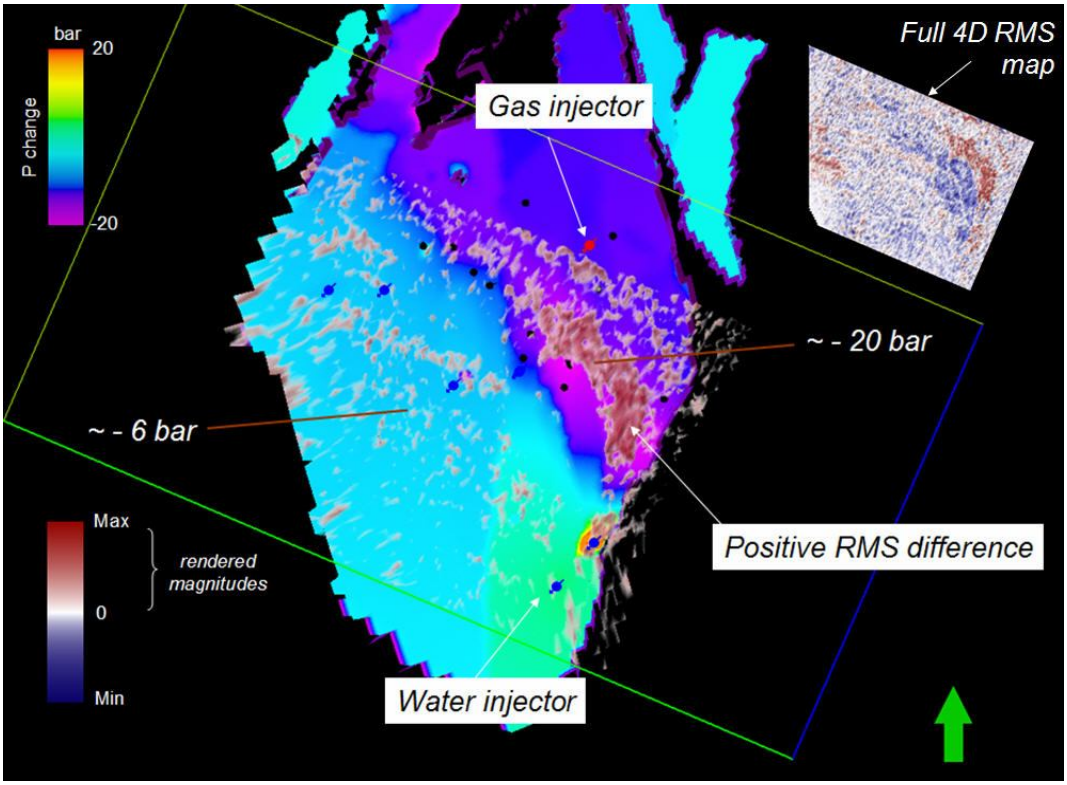

Figure 6.5. *Average pressure changes (2001-1995) in the Fangst group. Positive RMS difference appears on the area affected by the highest pressure drop (- 20 bar).*

In terms of the simulated water saturation change affecting the Fangst Group, a second long period anomaly is evidenced. This 4D effect has been correlated with the negative RMS difference appearing in the 4D attribute map. The regional geometry of the time-lapse seismic signature seems consistent with the simulated waterflood (Figure 6.7), however when analysed in detail, local adjustments in the simulation model might be needed in order to enhance the match between the 4D seismic signature and the simulation output.

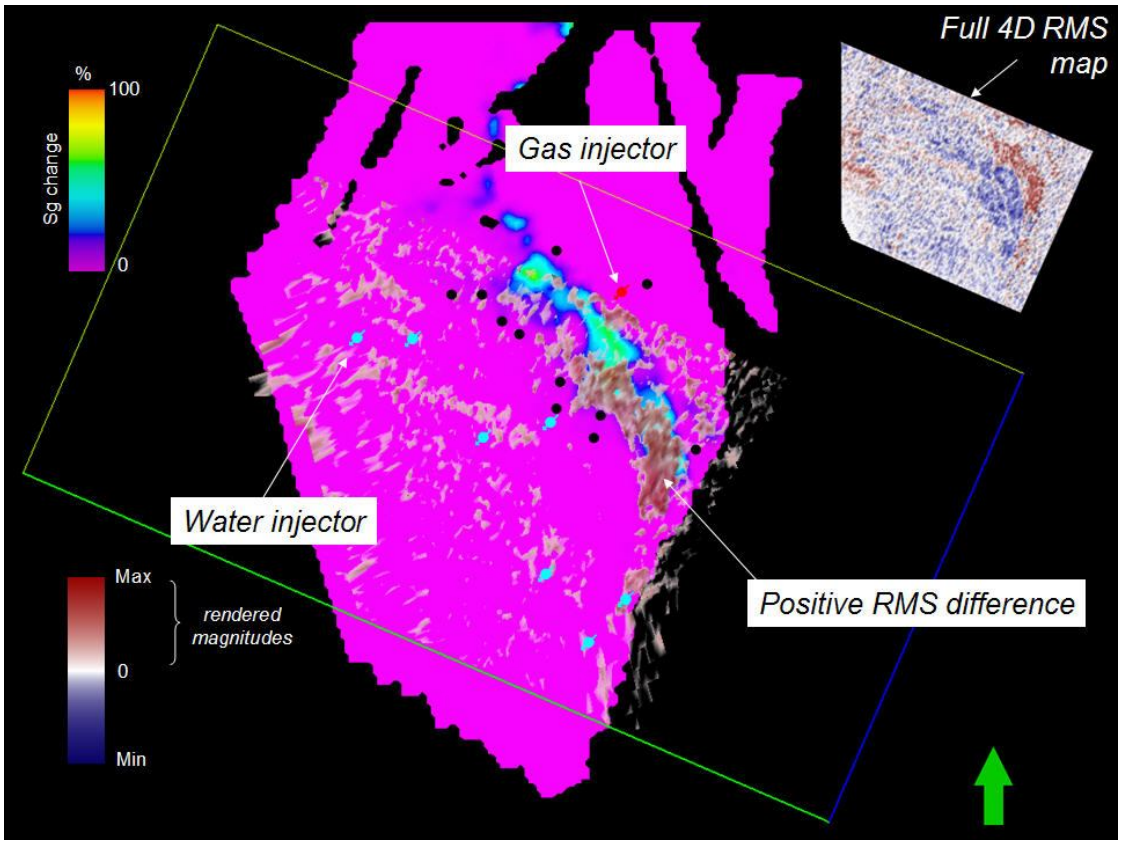

Figure 6.6. *Average gas saturation changes (2001-1995) in the Fangst group. Positive RMS difference shows correlation with the simulated gas saturation change.*

Here, fault transmissibility multipliers incorporated in the reservoir model; strongly affect the outcome provided by the simulation. These fault multipliers depend on fault permeability as described in Chapter 1, and they modify the fluid flow behaviour which is reflected in bottom hole pressures and production data at the well location. Now, in the following section of this chapter, we make use of the results shown in Chapter 5 where fault properties, in particular fault permeabilities, have been estimated using the statistics of the 4D signal. By calculating associated fault transmissibility multipliers, the reservoir simulation model is then updated.

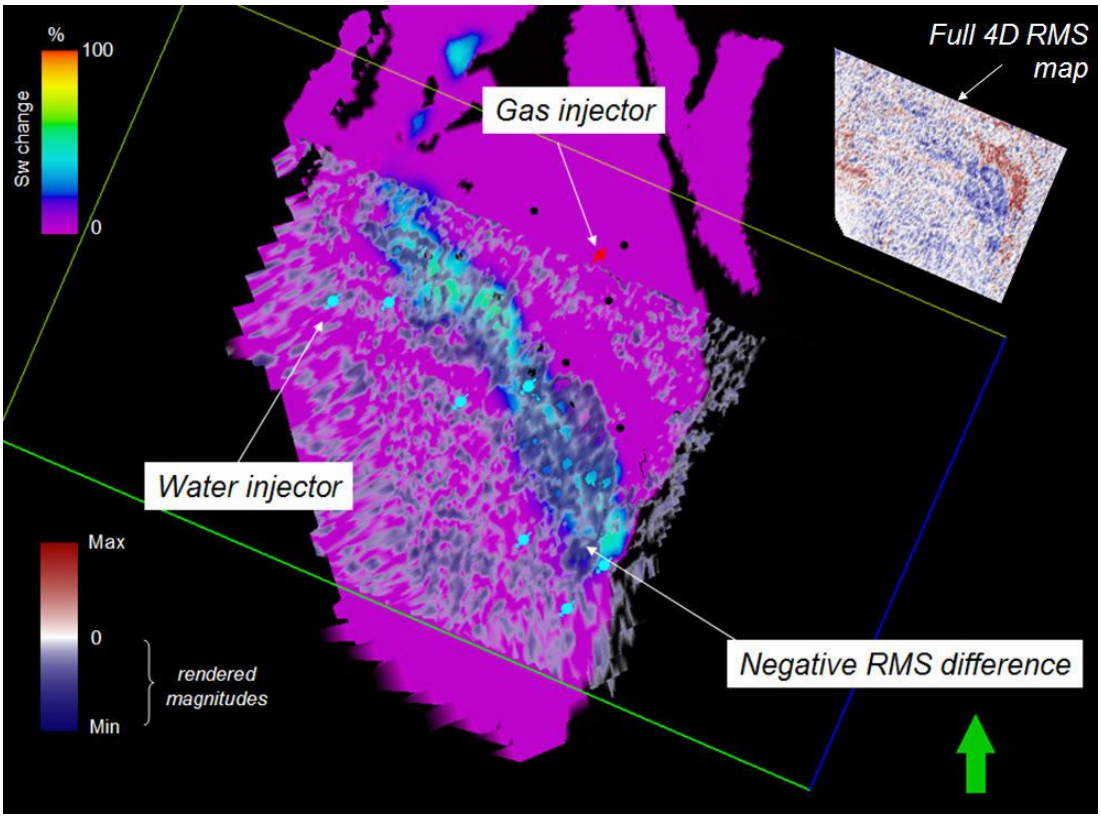

Figure 6.7. *Average water saturation changes (2001-1995) in the Fangst group. Negative RMS difference shows correlation with the simulated water saturation change.*

6.4 Upscaling the 4D seismic-derived fault permeability

The number of samples included in the estimated 4D seismic-derived fault permeability is initially incompatible with the number of grid-blocks included in the simulation model for each particular fault segment. Indeed, fine scale information is provided by the statistics of 4D seismic signal due to the grid representation of the attribute map used to carry out the predictions (Figure 6.8). To alleviate such scale mismatch, a coarse resolution representation of the high resolution data included in the fault permeability is generated. Therefore, an upscaling of the fine grid data is undertaken which minimizes the sample grid. To do so, the fine information is grouped into a number of aggregates equivalent to the number of grid-blocks representing the fault segment in the model. Finally, the equivalent fault permeability property of each aggregate is calculated by averaging the values constrained by each grid-block.

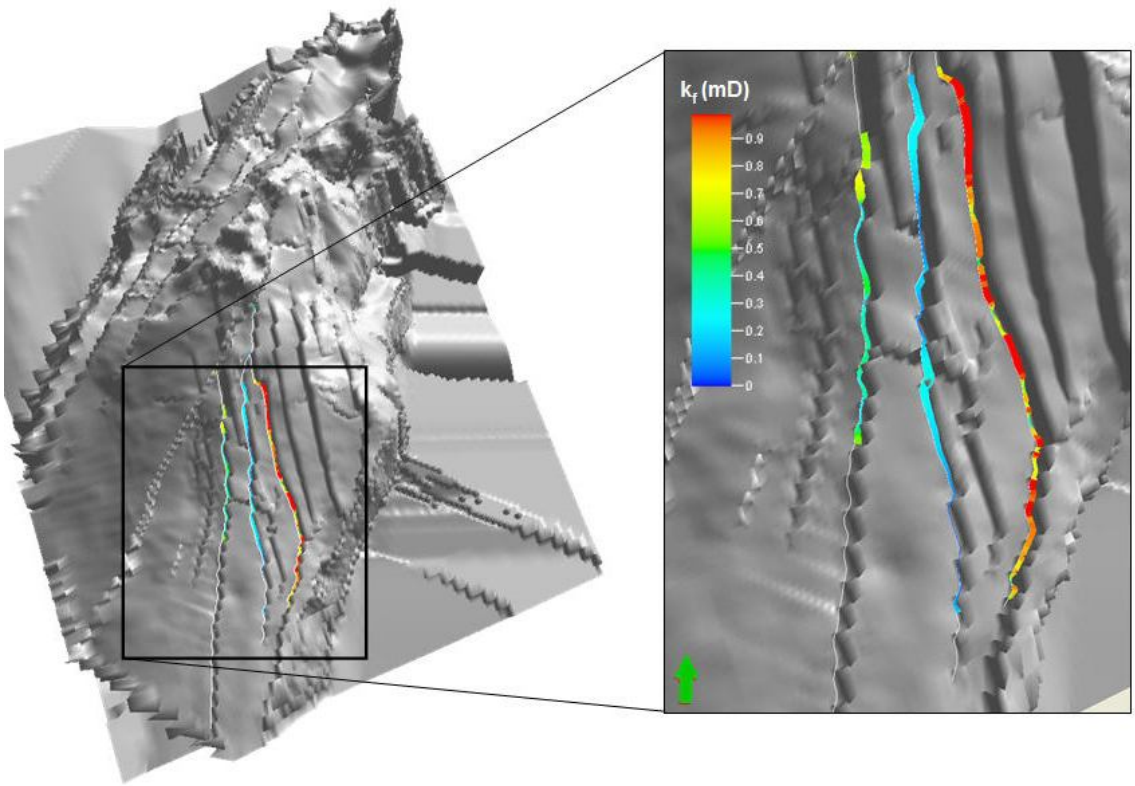

Figure 6.8. *High resolution representation of the fault permeability as derived from the statistics of the 4D seismic attribute (RMS difference). The fault permeability prediction has been performed for three major fault segments compartmentalizing the southern section of the field and this needs to be upscaled as the fine data sampling in this prediction is initially incompatible with the number of grid-blocks included in the simulation model.*

To perform the upscaling of the 4D fault permeability values, these are geo-referenced into the reservoir simulation model. Once this is done, the data points are re-sampled into the cells defined by the 3D grid (Figure 6.9). When upscaling the high resolution representation of the fault permeability, a quality control is also carried out. This means that major trends in the input data are kept when performing the upscaling process (Figure 6.10). Also, values captured in the upscaling are reviewed. Comparison between the high resolution data and its upscaled version shows agreement as the distribution of the upscaled values seems to represent the fine grid representation derived from the 4D attribute. Also, as discussed in Chapter 5, calibration of the statistics of the 4D signal is performed using vertically averaged fault properties derived from well log information in the Fangst Group. Consequently, no vertical variation in the upscaled representation of the fault permeability is introduced along the layering of this stratigraphic unit (Figure 6.11).

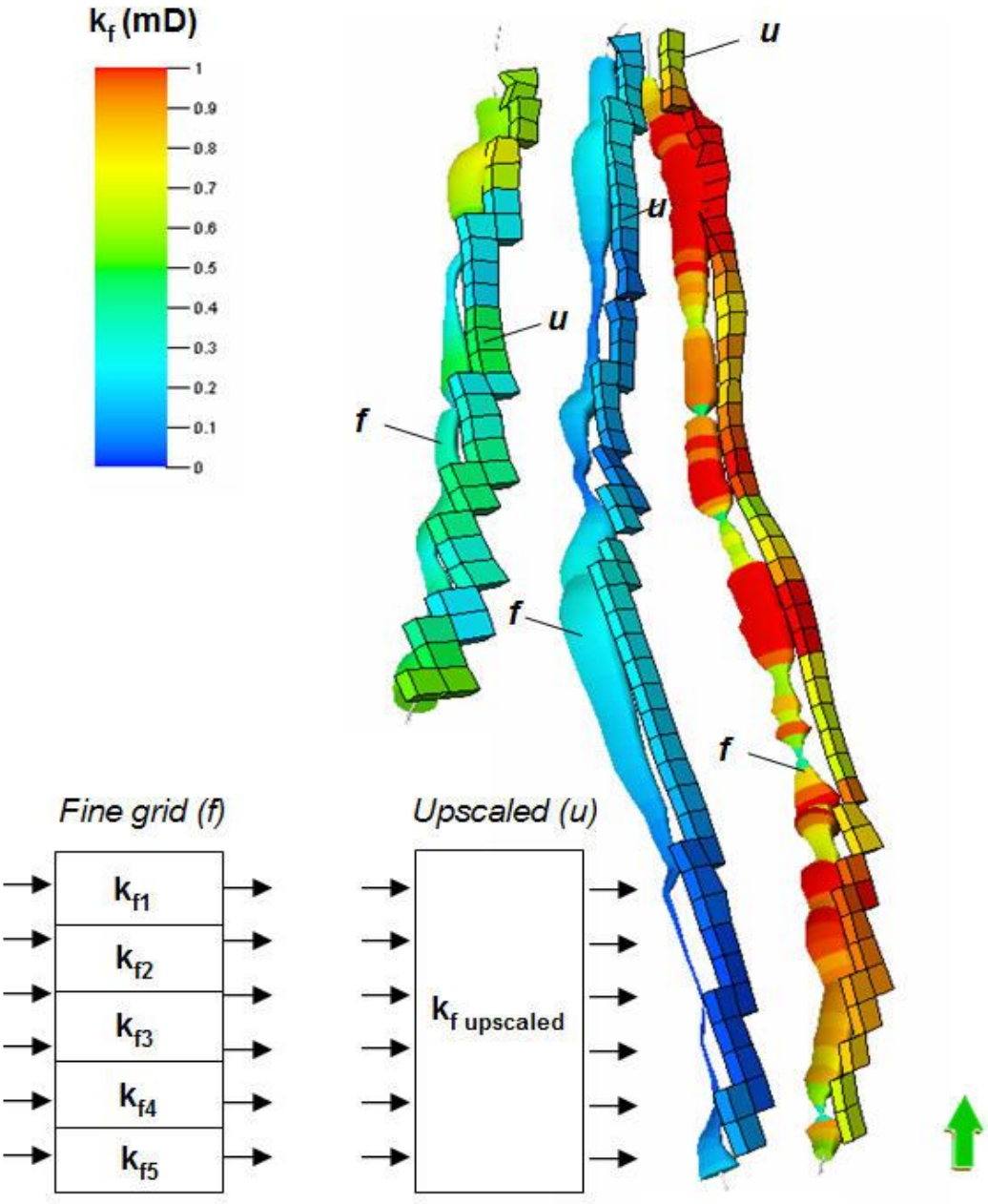

Figure 6.9. *Upscaled fault permeability values for the three fault segments. The fine grid representation of the fault property (f) is represented as a 3D pipe (with size proportional to the fault permeability values) displayed to the left of the upscaled representation of each fault segment (u). Upscaling of the high resolution data helps to derive an equivalent fault property for each grid cell. Trends observed in the input data seem to be kept in the upscaled version.*

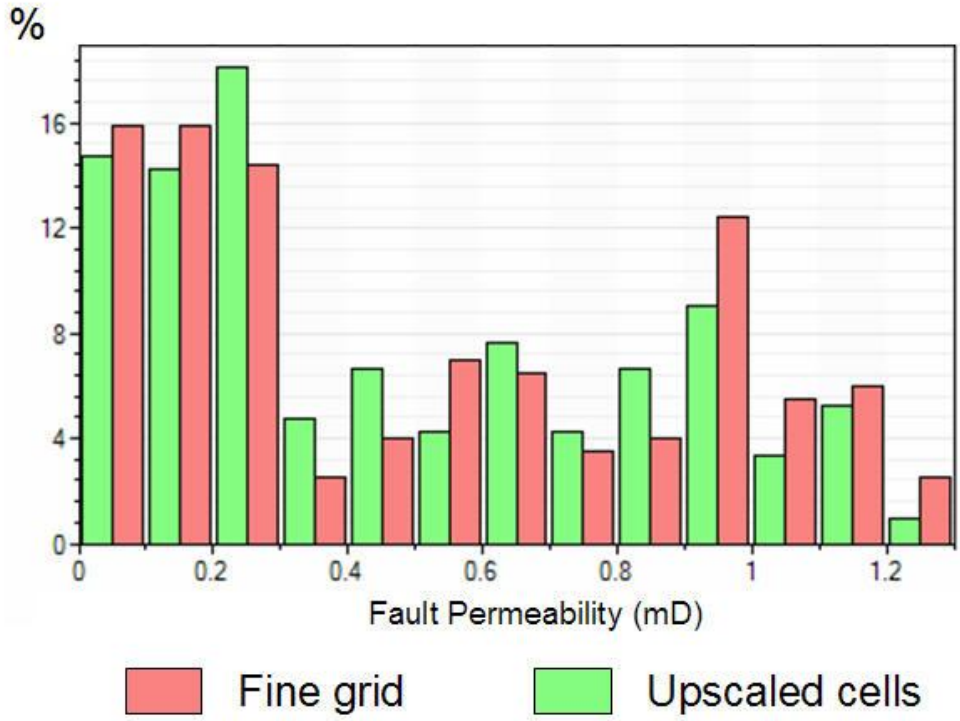

Figure 6.10. *Comparison between the fine grid representation of the fault permeability (as derived from the 4D attribute map) and the upscaled version (from the simulation grid) of the estimation. The distribution of the upscaled values seems to represent the fine grid values.*

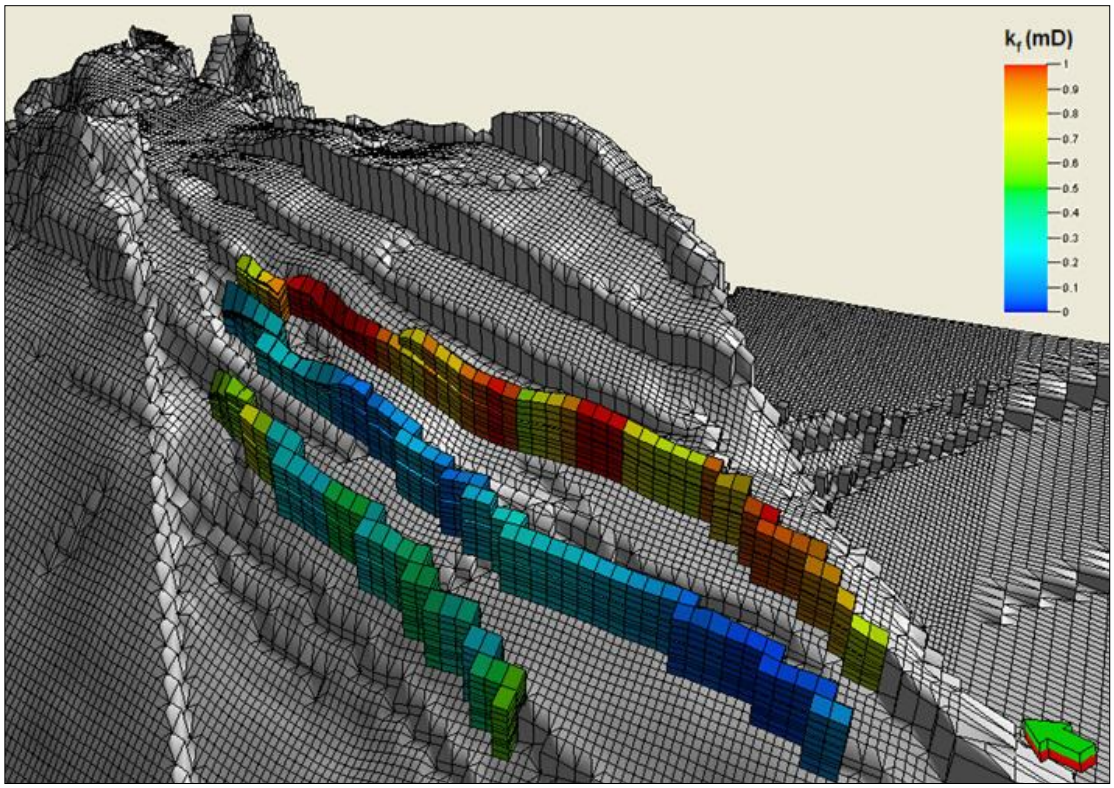

Figure 6.11. *Upscaled representation of the fault permeability estimation derived from the 4D seismic. The updated three faults segments are displayed on a structured surface showing the simulation grid.*

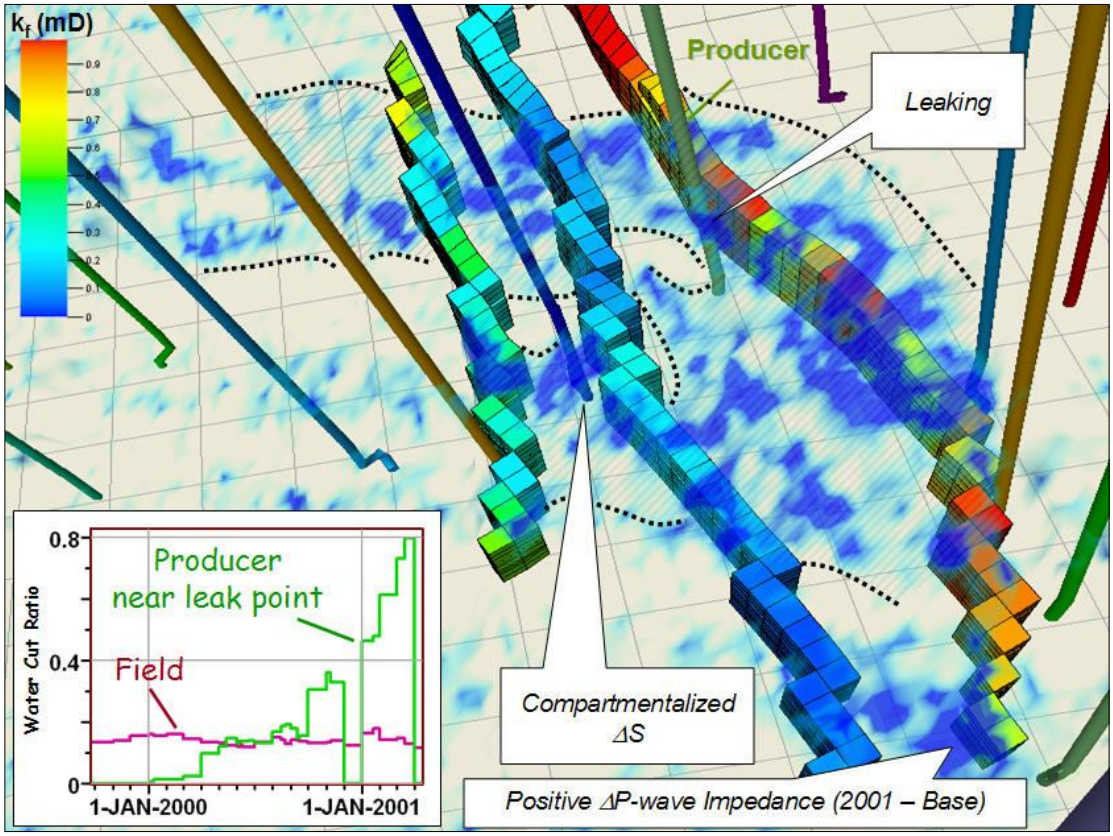

Figure 6.12. *Comparison of the time-lapse seismic signature against the upscaled representation of the 4D derived fault permeability values. All displayed wells are water injectors but the producer that is indicated in the figure. The positive P-wave impedance change has been rendered and displayed in blue. This hardening response has been related to water flooding as discussed in Chapter 3. Fault segments 1, 2 and 3 are displayed from left to right. They separate compartments D, E, F and G respectively.*

Comparison of the time-lapse seismic signature against the upscaled representation of the 4D fault permeability values show agreement as indicated in Figure 6.12. Particularly, the hardening response given by the increase of the water saturation during injection (displayed as blue in the figure) is affected by the fault sealing properties reducing the flow along the reservoir. As shown here, higher permeability values in the top right fault are correlated with anomalies traversing the fault plane. As a consequence, leakages in this fault enhance water flooding leading to a quick increase of the water cut values in the producer well located in the vicinity of this fault. Conversely low fault permeability values seem to constrain the spreading of the signature, hence showing a compartmentalizing 4D effect. This observation helps to explain the rapid water breakthrough for this particular producer. If identified soon before full reservoir flooding, this phenomenon might lead to implications in the

occurrence of by-passed sectors that might remain compartmentalized in between low fault permeabilities.

6.5 Updating the simulation model using the 4D seismic-derived fault transmissibility multipliers

Using the methodology described in Chapter 1, fault transmissibility multipliers are computed. To do so, fault thickness also needs to be assessed. Here, this is calculated using equation (1.14) shown in Chapter 1. Indeed, this linear relationship between fault zone displacement and fault thickness becomes useful when data in the field on fault width is sparse. Fault throws calculated in this way are found to lie between 0.2 m and 1 m (Figure 6.13). This result seems in agreement with values observed in successfully cored faults as measured by means of that analysis indicating a fault rock thickness below 2 m (Knai and Knipe, 1998).

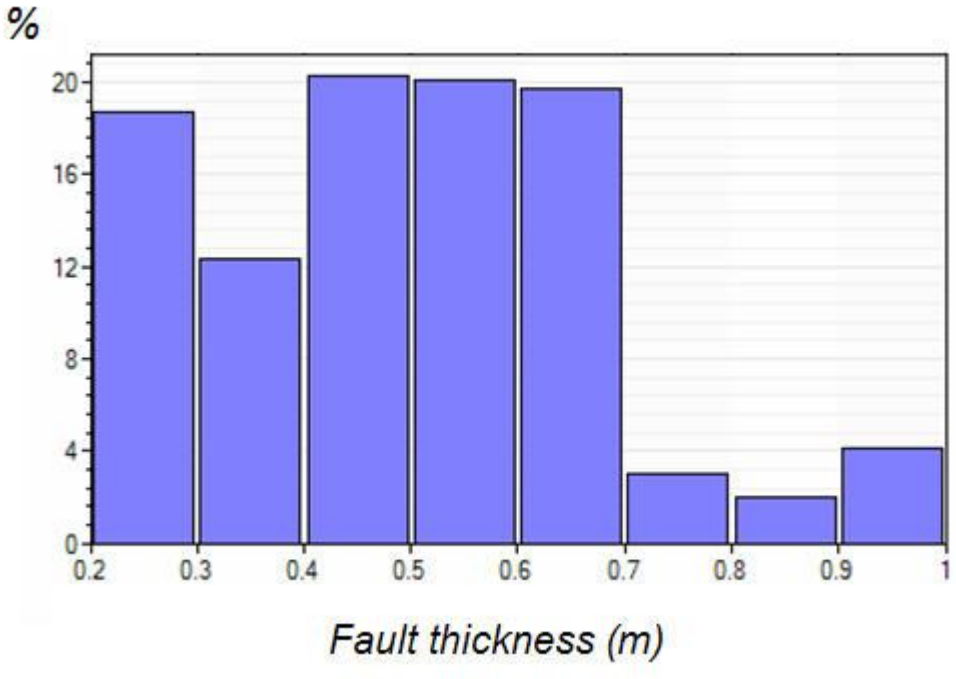

Figure 6.13. *Fault thickness distribution estimated from the fault displacement.*

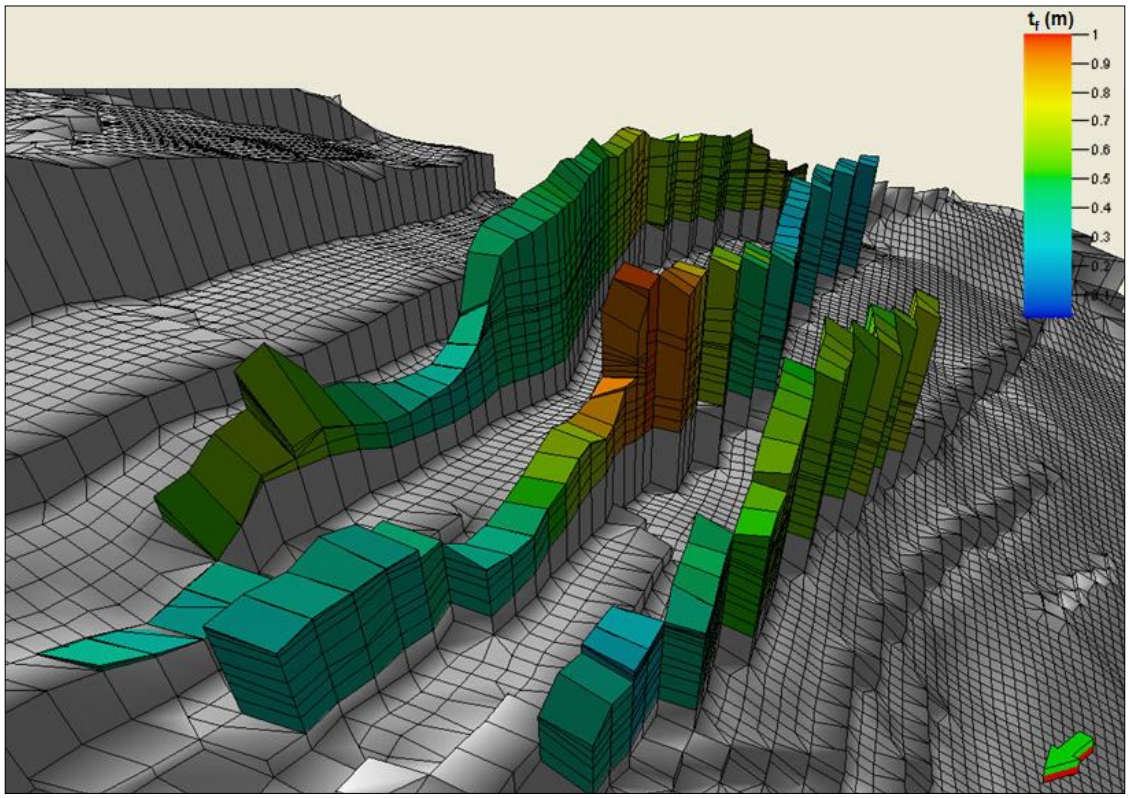

Figure 6.14. *Fault thickness values for each cell included the three fault segments. These estimates are based on the fault displacement via linear approximation. Fault 1, 2 and 3 are shown from right to left. They separate compartments D, E, F and G respectively.*

Fault thickness values are finally distributed according to the simulation grid (Figure 6.14). Subsequently, cell properties and the upscaled representation of the fault thickness and 4D derived - fault permeabilities are used to calculate the new 4D fault multipliers. The derived multipliers are displayed in Figure 6.15. As expected, values lie in between 0 to 1, however, a histogram reveals a skewed distribution toward the low magnitudes as these show higher frequency rate when compared with high transmissibility multipliers (Figure 6.16). Indeed, these low fault transmissibility multipliers suggest the high control of faults on the reservoir compartmentalization as the cell-to-cell transmissibility is to be strongly affected by these magnitudes. Once the fault transmissibility multipliers are applied to the relevant cells of the model, the simulation is re-run.

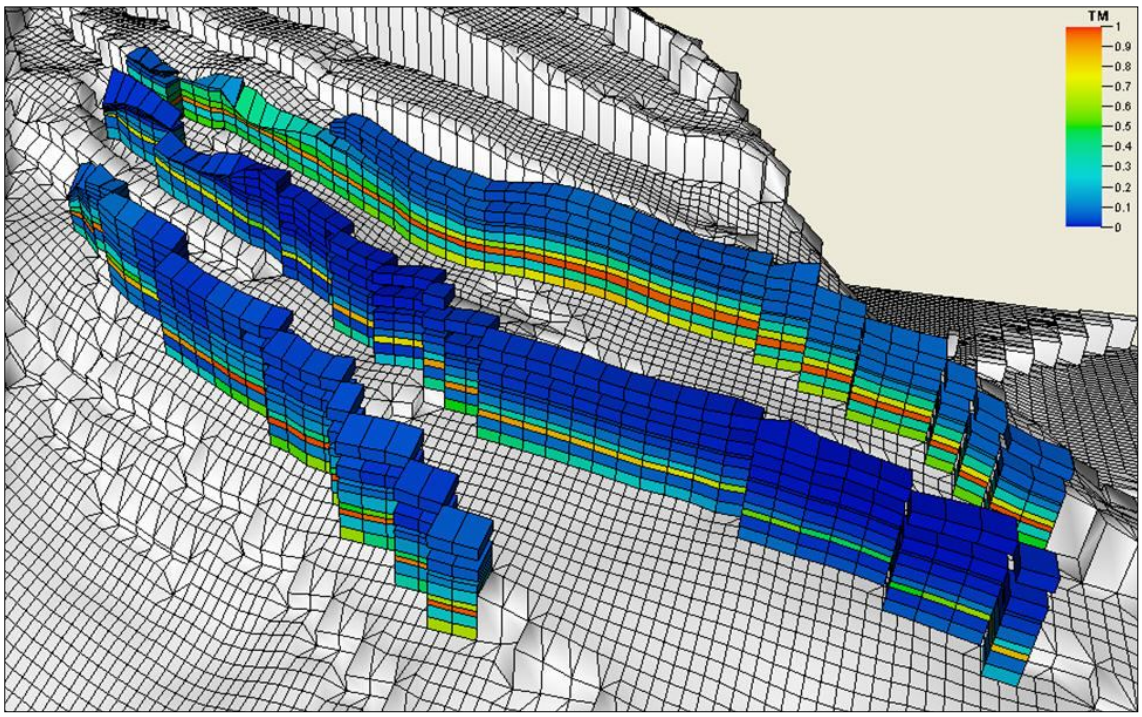

Figure 6.15. *4D fault transmissibility multipliers for the three fault segments analysed in this study. Fault 1, 2 and 3 are shown from left to right. They separate compartments D, E, F and G respectively.*

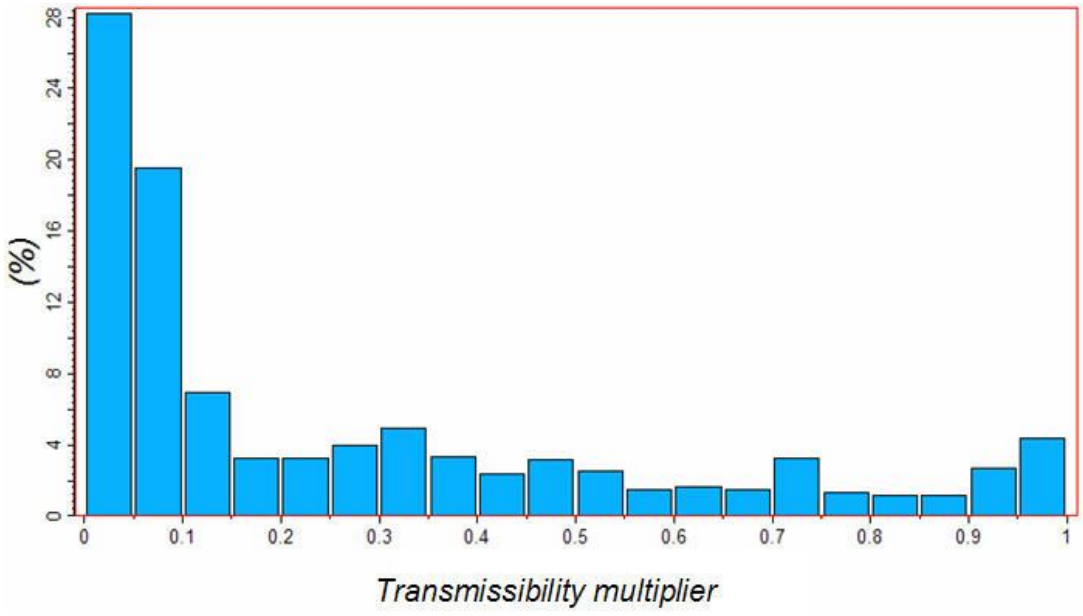

Figure 6.16. *Transmissibility multiplier distribution obtained from the 4D input.*

6.6 Updated simulation results

The least square solution given by the regression analysis in the fault permeability estimation is incorporated into the simulation model via fault transmissibility multipliers and the fluid flow is then simulated. In this section dynamic changes provided by the updated simulation model are now discussed (Figure 6.17). In particular, the pressure and saturation changes derived from the updated model are evaluated and compared with the base case simulation output.

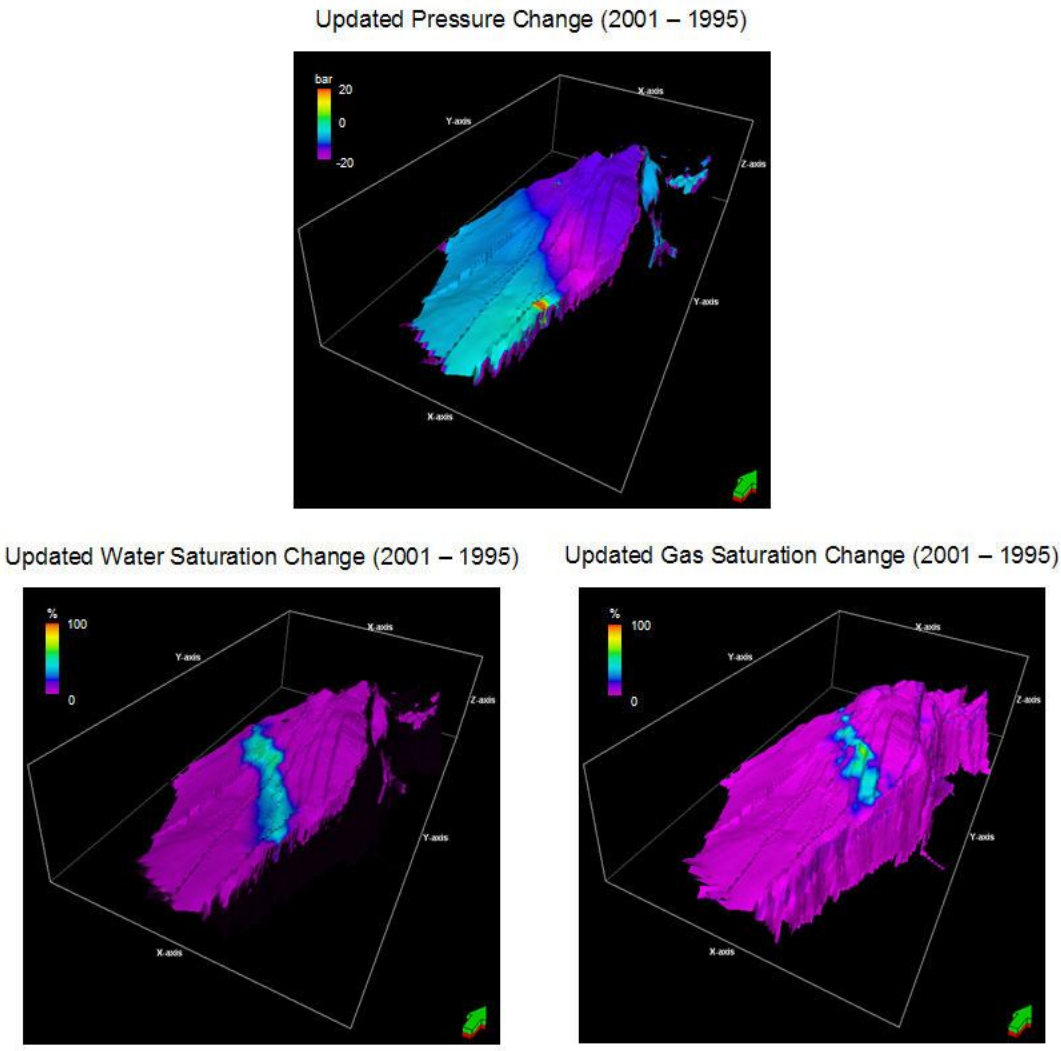

Figure 6.17. *Predictions derived from the updated simulation model which include the 4D input. Pressure (above), water (lower left) and gas saturation (lower right) changes are shown. Differences have been calculated for the 2001-1995 time interval and represent average changes for the Fangst Group.*

In term of the pressure change obtained from the updated simulation model in the time interval 2001-1995, a general decrease in the magnitudes is observed when compared with the base case. However, a cross-plot for the pressure change amongst both models reveals that by introducing the 4D derived fault multipliers most of the differences are found to lie within the range of -5 to 5 bars (Figure 6.18).

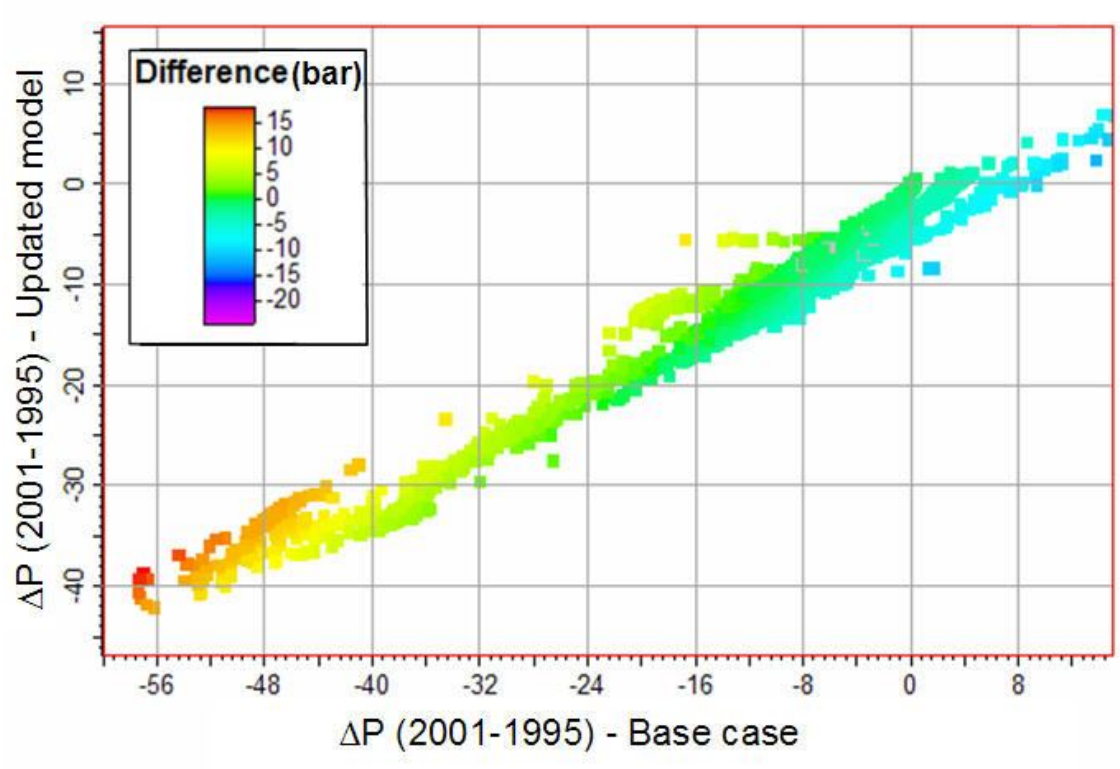

Figure 6.18. *Cross-plot for the pressure change (2001-1995) in the Fangst Group between the base case and the updated model. Points displayed are colour coded according to differences between the updated minus the base case. Most of the differences in pressure change between the models are in between -5 to 5 bar.*

Spatial evaluation of the difference between pressure changes for both models is also shown in Figure 6.19. Here, a general decrease of pressure is exposed for most of the compartments and major differences are mostly located in the compartment E with low pressure changes in the updated model when compared to the base case. Indeed major faults constraining this compartment have been effectively updated in terms of their sealing properties, particularly altering the dynamic changes occurring in the segment E.

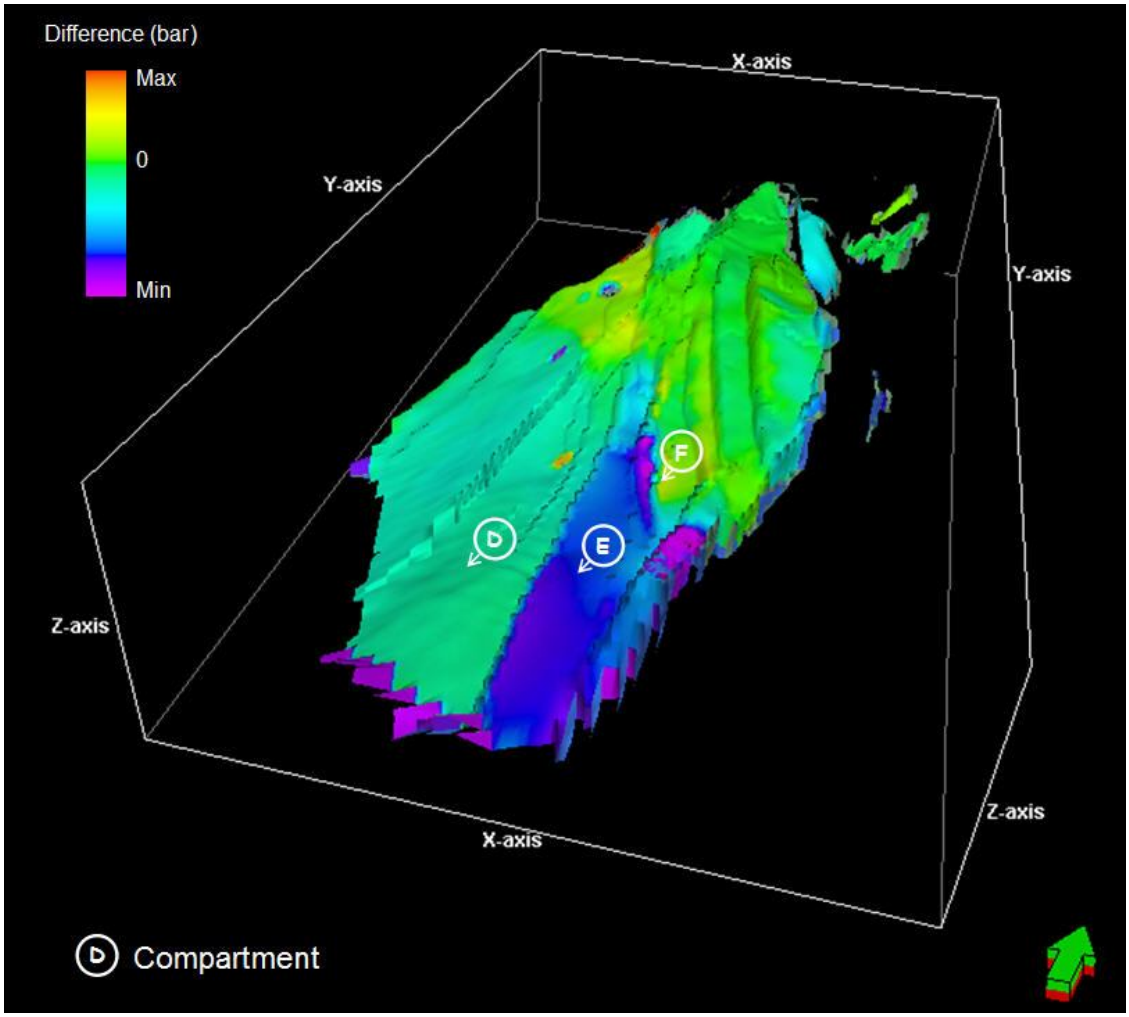

Figure 6.19. *Differences in pressure change (2001-1995) between the updated model and the base case for the Fangst Group. Major differences occur in compartment E as its constraining faults have been altered during the updating.*

In the pressure vector map, comparison between the 2001 pressure derived from the updated and the base case shows that major differences between the two simulations are associated with a change in magnitude as well as in orientation of the pressure vector (Figure 6.20). In the updated model, higher pressure contrast between compartment E and F are detected as indicated by the increase in the vector gradient. This effect is associated with the high sealing capacity of the inter-compartment fault. This observation is in agreement with results shown in Figure 6.12 where the fault segment 2, separating both compartments, divides the 4D signature observed in this sector of the field.

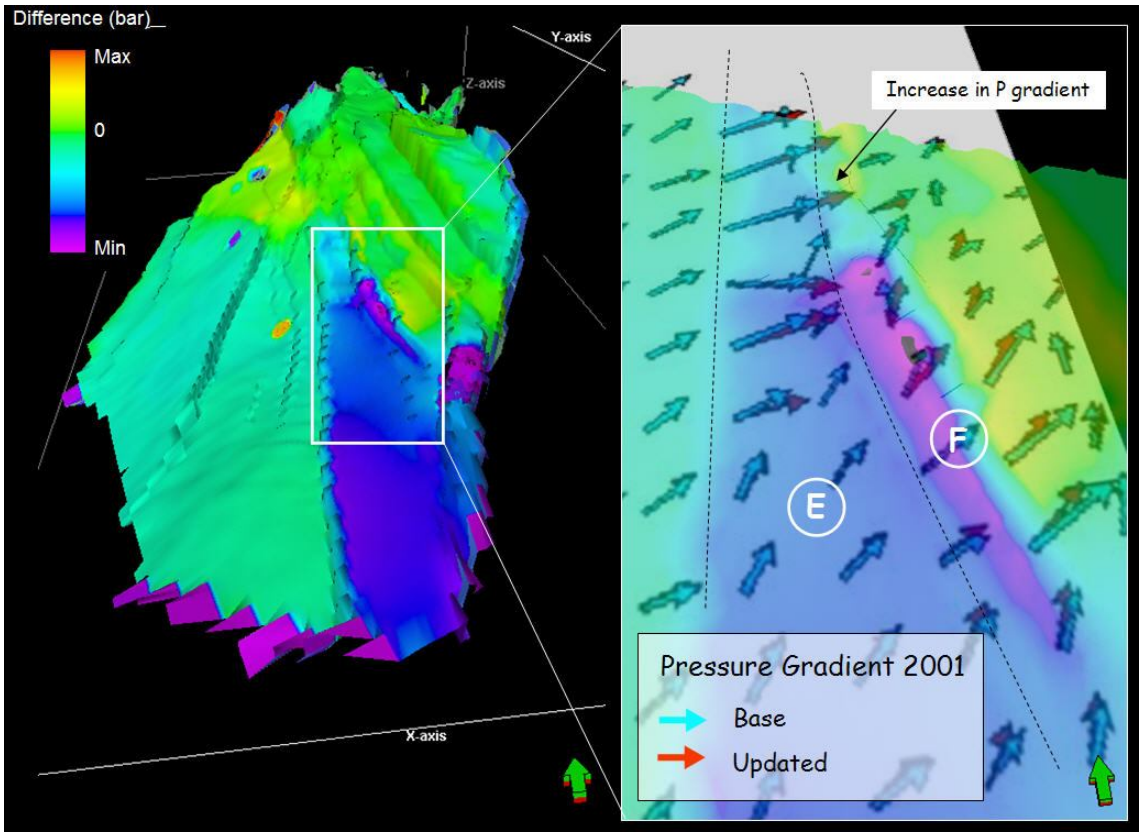

Figure 6.20. *Pressure vector map in a sector of the field. 2001 Pressure gradients derived from the base case and the updated model are shown. In the updated model, higher pressure contrast between compartment E and F are observed as indicated by the increase in the vector gradient shown with red arrows.*

Changes in the 2001 pressure gradient are also analyzed by means of simulated streamlines given between water injectors and producers. Results revealed that the streamlines derived in 2001 for the updated simulation model, enhance the connection between water injection and producer between several compartments. Indeed, Figure 6.21 shows that waterflooding path for the updated model (in red) is more likely to connect producers located in the updip flank of reservoir segments E and G when compared with the base case simulation (in blue). Also, a flow-related breach of the fault separating compartment F and G is evidenced in the updated model, hence changing the connectivity framework between these two blocks. This phenomenon is consistent with the high permeability values introduced in this fault segment (Fault 3) as derived from the 4D estimation.

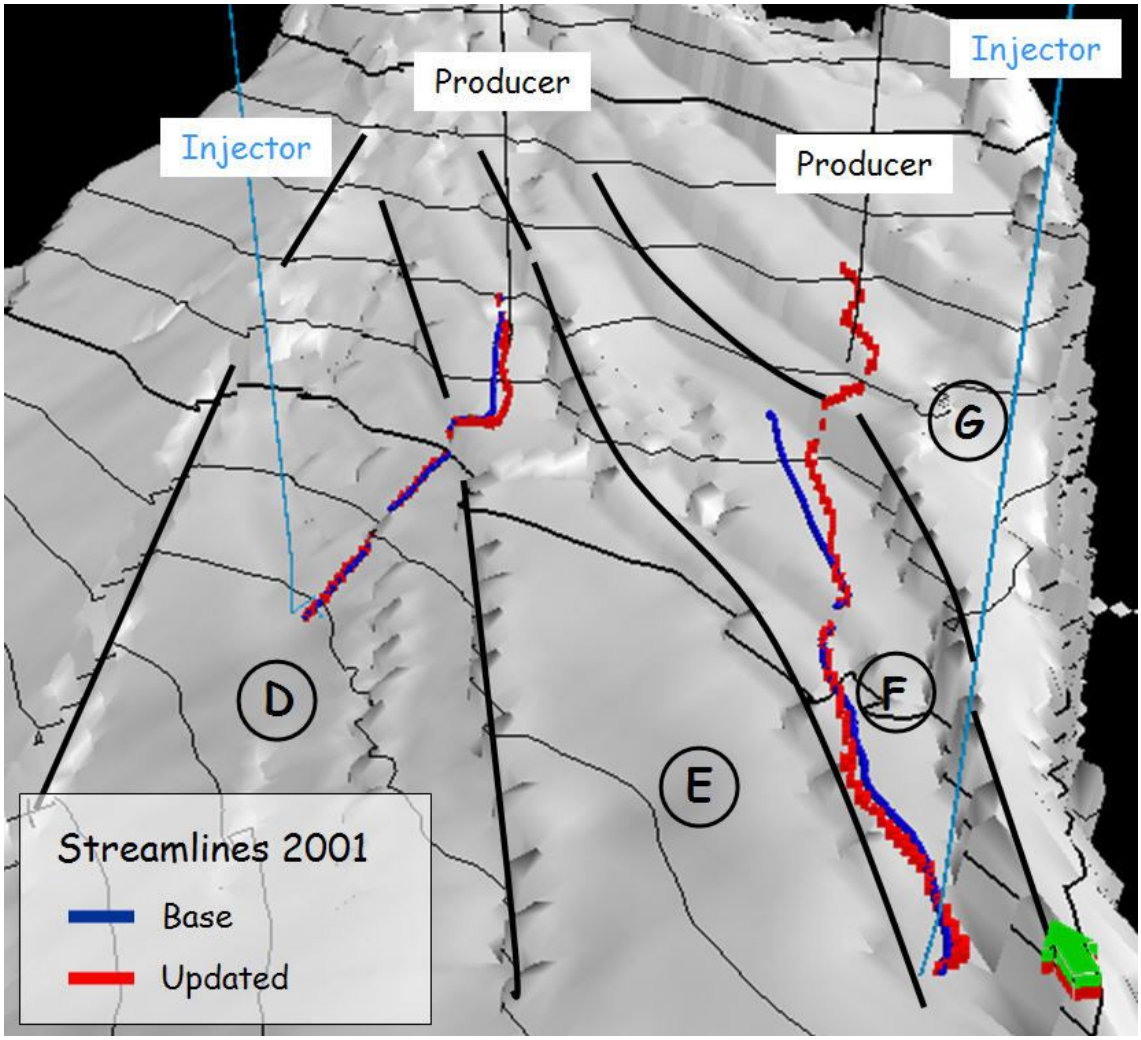

Figure 6.21. *Streamlines derived in 2001 for the base case and updated simulations are shown in blue and red respectively. The waterflooding path for the updated model is more likely to connect producers located in the updip flank of reservoir segments E and G when compared with the base case simulation.*

Also, comparison between simulated pressures of the field for the base case and updated simulation model with down hole pressure measurements taken after 1 hour shut in at different well locations is shown in Figure 6.22. Although measurement sampling in the wells is sometimes irregular, the updated model produces in general a better match to the given history data. Indeed, both models predict an average pressure decrease of 19 bars in 11 years of production; however a lower pressure drop is simulated for the updated model improving the tie with well data.

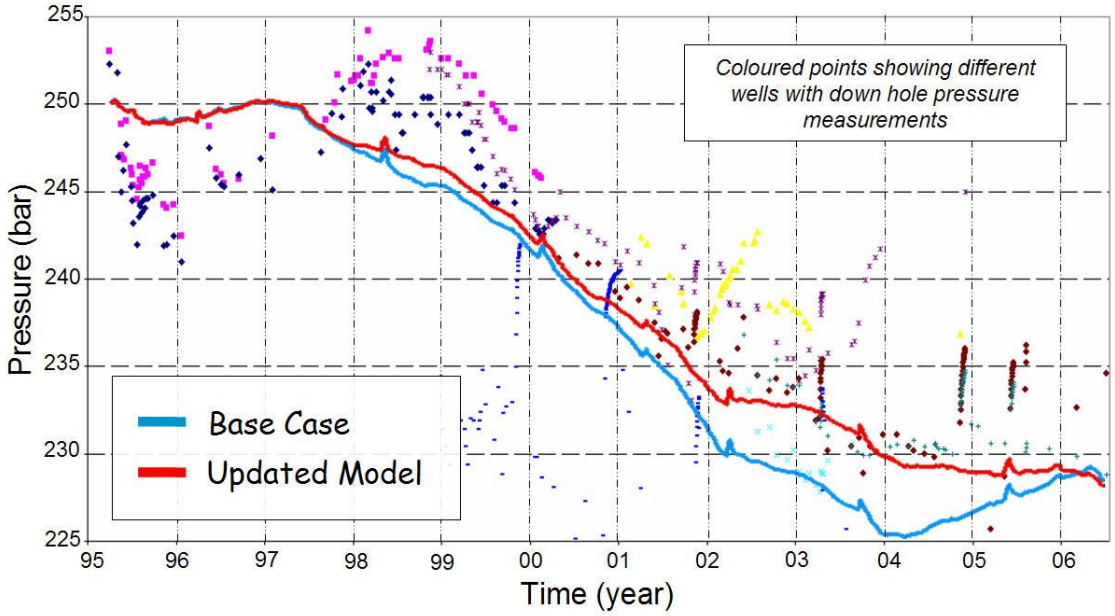

Figure 6.22. *Simulated pressures of the field for the base case (blue) and updated (red) model with down hole pressure measurements taken after 1 hour shut in at different well locations.*

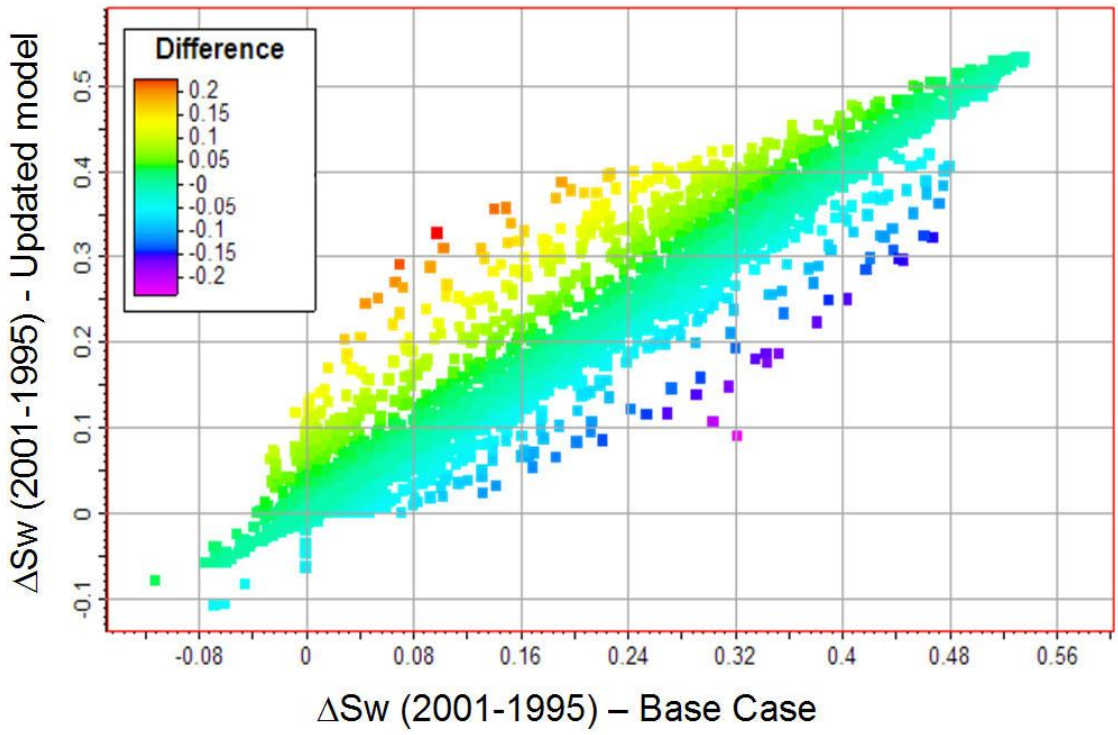

Figure 6.23. *Cross-plot for the water saturation change (2001-1995) in the Fangst Group between the base case and the updated simulations. Points displayed are colour coded according to differences between the updated minus the base case.*

In terms of the water saturation change 2001-1995, simulations for the base case and updated model are also compared by means of a cross-plot (Figure 6.23). Here, differences between the updated and base simulations for the water saturation changes are found to lie within the range of -0.2 to 0.2 (-20% to 20%). The spatial distribution of such differences is displayed in Figure 6.24. Major differences are located in segment F and segment E. Nonetheless, other minor perturbations are taken place in the updip flank of compartments, particularly in segment C for which its fault properties are been kept constant between the two simulation models. This observation suggests inter-dependence between the flow occurring down-flank of the eastern segments related to that occurring in the west. This response highlights the importance of the implications of the fault seal properties on the fluid saturation throughout the field.

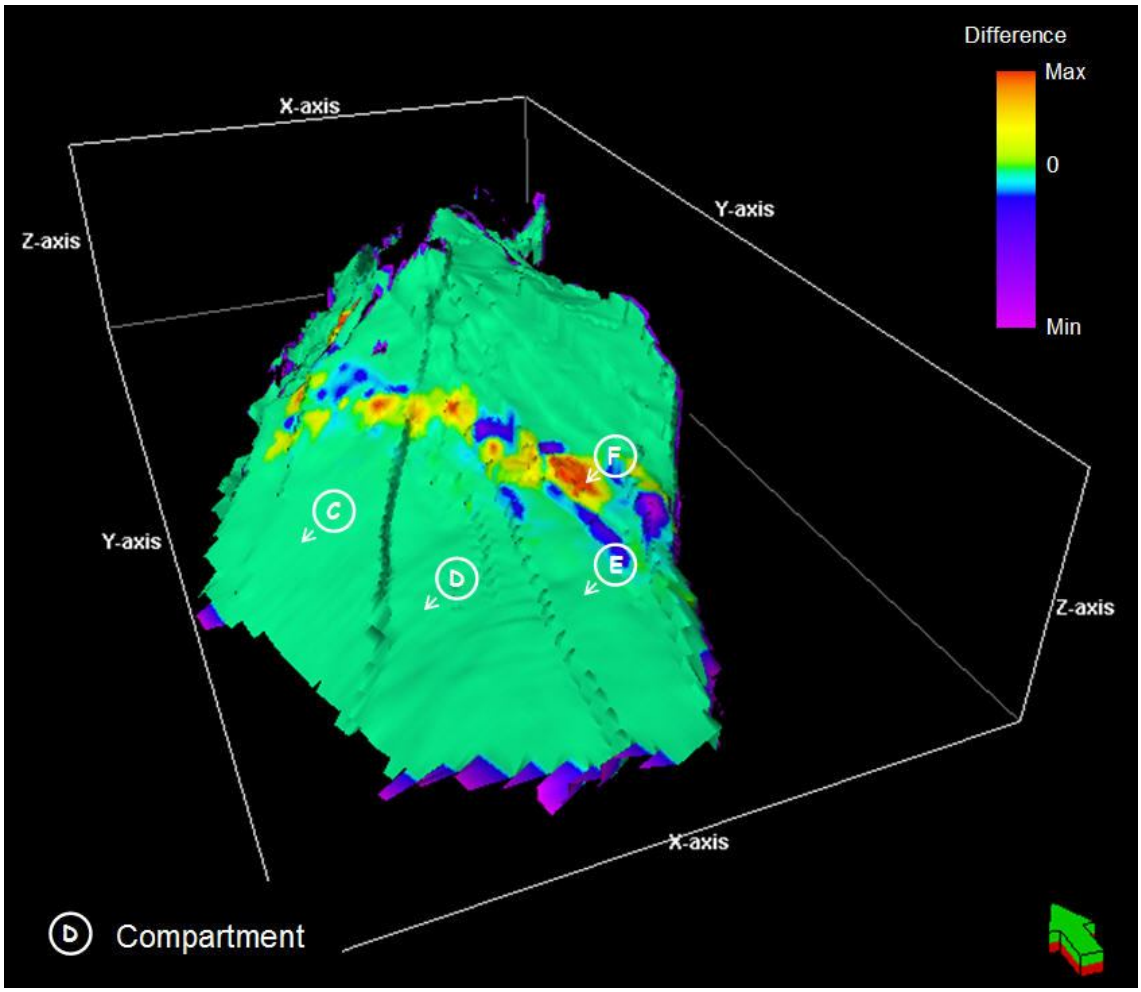

Figure 6.24. *Differences in water saturation change (2001-1995) between the updated and the base case simulations for the Fangst Group.*

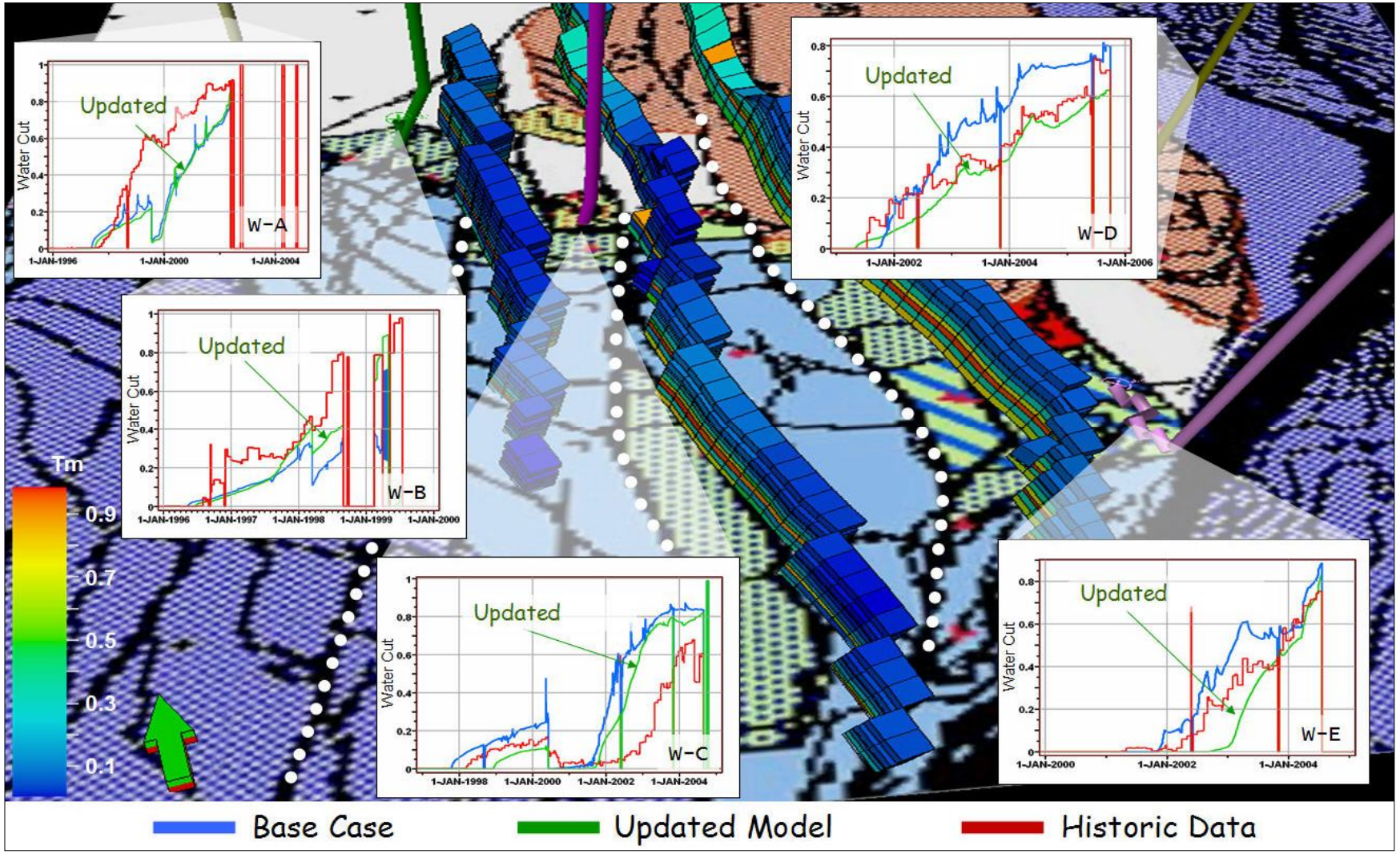

Figure 6.25. *Simulated water cut for the base case and updated simulation model compared to the historical data five well producer (A to E).*

The history match for the simulated water cut derived from the base case and the updated model is also analyzed. Figure 6.25 shows that water cut predictions for five producer wells located in the field. The three updated faults are highlighted with dotted lines in the flooding map and the 4D derived transmissibility multipliers are indicated according to the scale bar shown. When compared to the simulated water cut given by the base case and the updated model in wells located away from the updated sector, no major differences are observed between both models. This is the case for well A (W-A) located in the northwest flank of the field. For wells located in the vicinity of the updated faults, a general decrease of the mismatch with the historical data is observed when the model is updated.

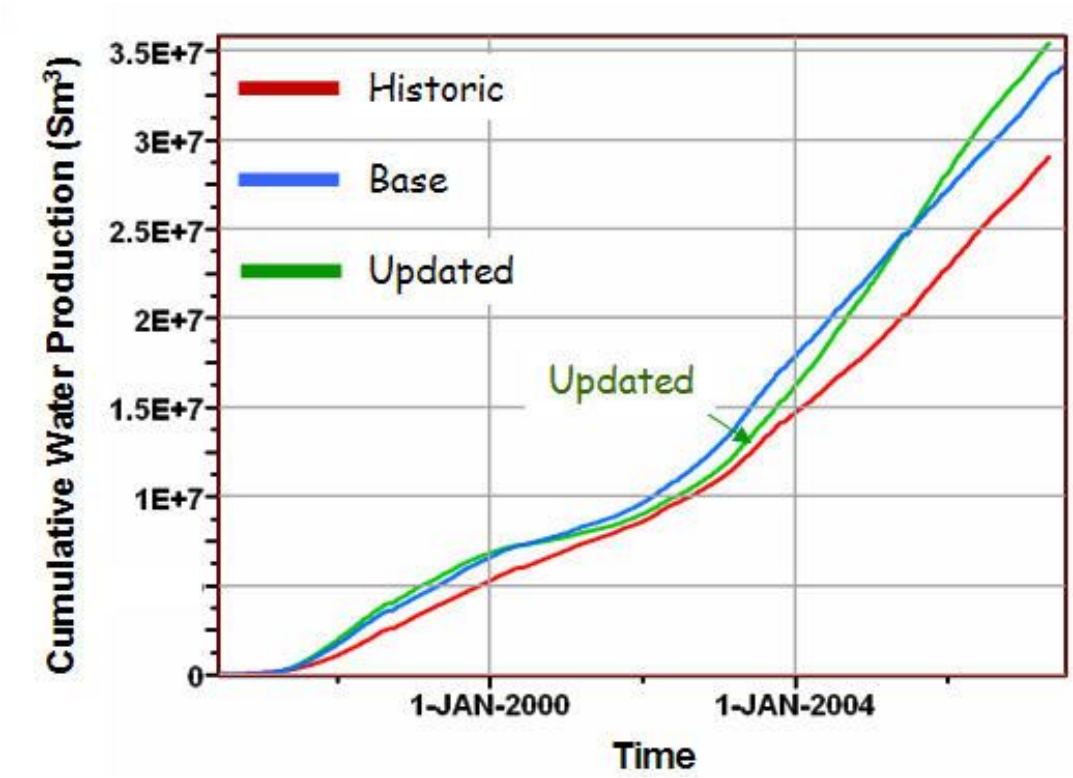

Figure 6.26. *Cumulative water production for the base case and updated simulation compared to the history data.*

Also, a comparison between the simulations and the history of cumulative water production shows improvements and deterioration of the fit at different times (Figure 6.26). Furthermore, when evaluating the spatial match of the simulation output for the base case and the updated model in terms of the water saturation change (2001-1995) with the observed 4D signature in Upper Fangst Group, an enhancement of the fit is observed when the 4D fault properties are introduced into the model (Figure 6.27). Indeed, the updated model increases the simulated water saturation levels within the

reservoir, improving the match in terms of history data and the spatial distribution of the water change as seen in the correlation with the time-lapse seismic signal.

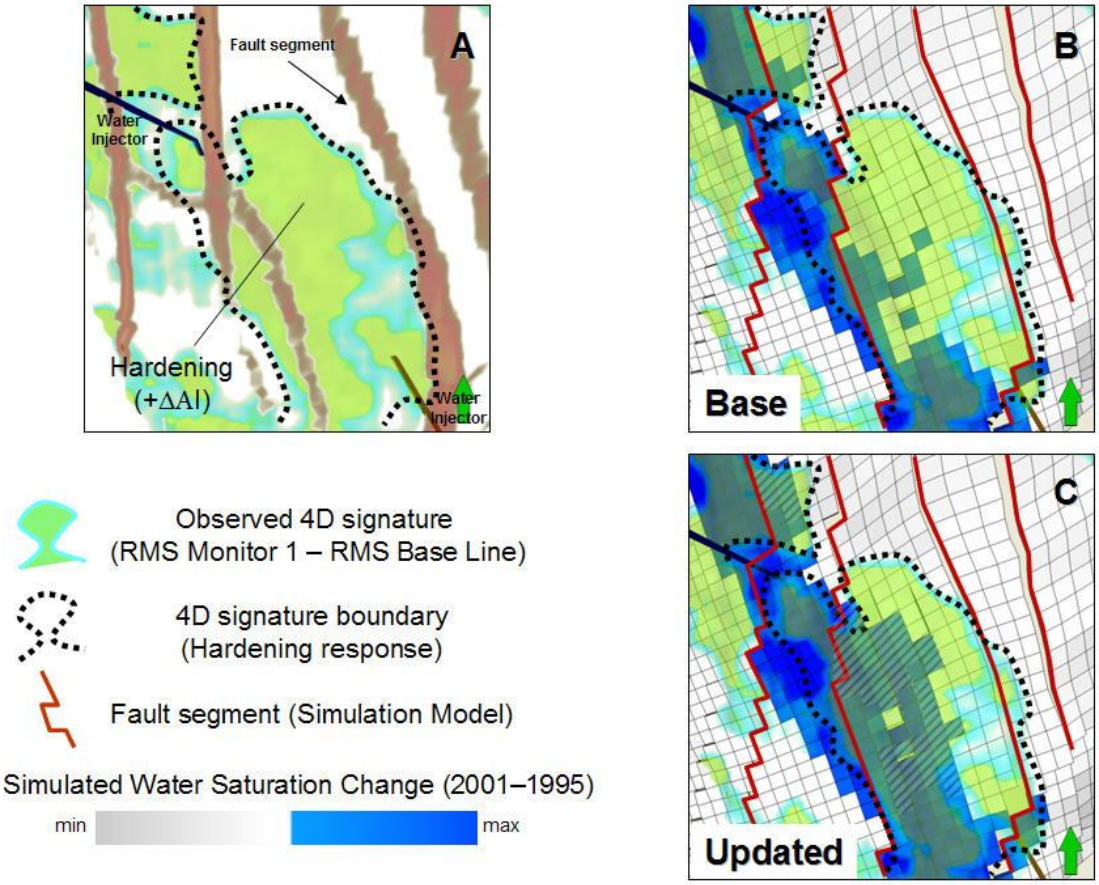

Figure 6.27. *(A) In green colour observed 4D signature (RMS Monitor – RMS Base Line) constrained by fault segments (red). Comparison between the observed 4D signature (green) and the water saturation change (2001-1995) as derived by the simulation without (B) and including the 4D fault multipliers (C). Improvements in C (updated model) are highlighted with a diagonal background.*

Simulated gas saturation changes derived from both models have been also compared. A cross-plot between both models (Figure 6.28) reveals little differences between them with values in between -0.1 to 0.1 (-10 % to 10 %). Such differences are mostly located in compartments E and F as expected, as the fault constraining these segments have been effectively updated. Nonetheless differences are observed in the up-flank side of the compartment C (Figure 6.29). As discussed previously in the evaluation of the water saturation differences, this might indicate inter-dependence between the flow occurring down-flank of the eastern segments and that in the west side of the reservoir.

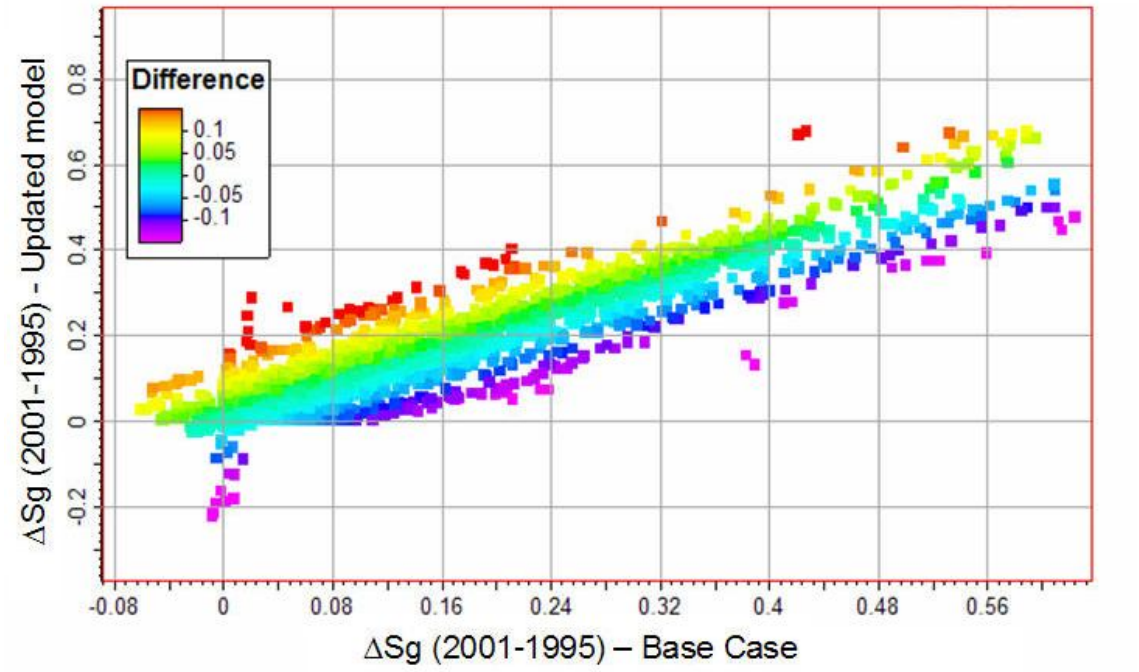

Figure 6.28. *Cross-plot for the gas saturation change (2001-1995) in the Fangst Group between the base case and the updated model. Points displayed are colour coded according to differences between the updated minus the base case.*

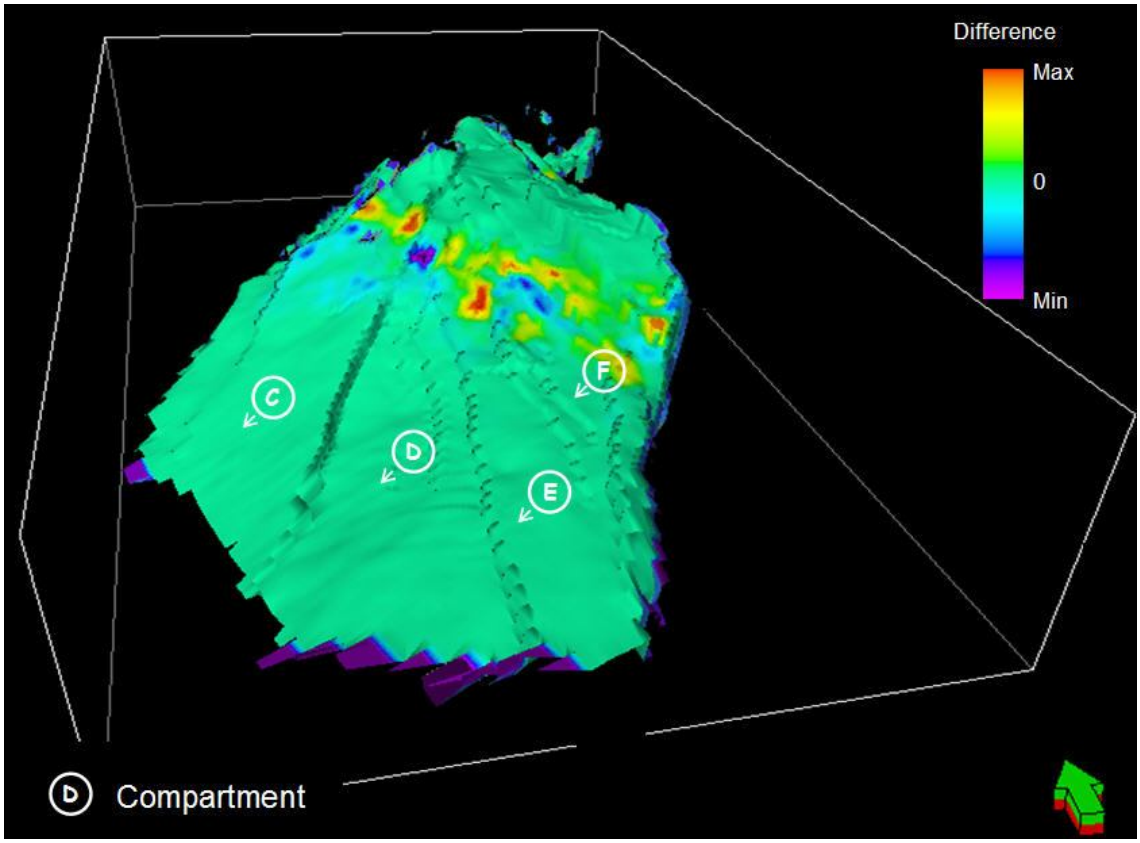

Figure 6.29. *Differences in gas saturation change (2001-1995) between the updated and the base case simulation for the Fangst Group.*

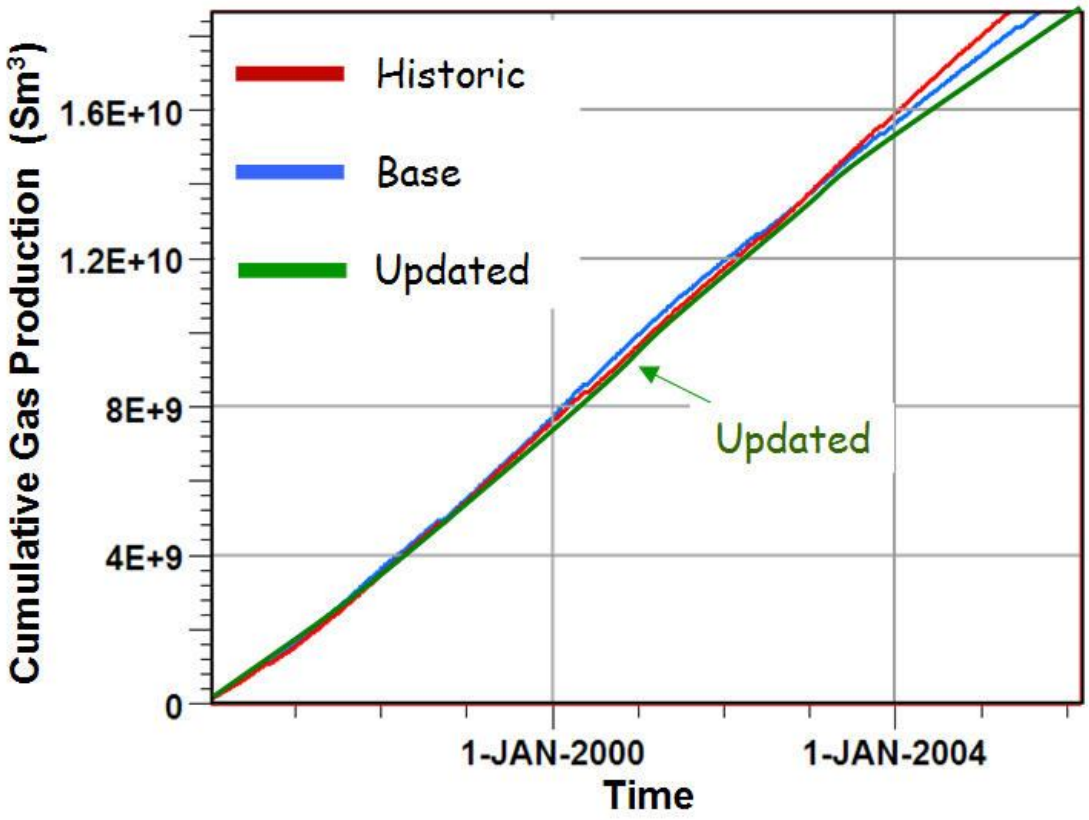

Figure 6.30. *Cumulative gas production for the base case and updated simulations compared to the history data.*

The cumulative gas production for the base case and the updated simulations is displayed in Figure 6.30. Comparison with historic data reveals variations in the fit for both models, nonetheless small improvements in the updated model are observed when comparing up to the year 2002. Soon after this, both models deviate from the historic data, possibly indicating a variation in the connectivity in time. Also, evaluation of the gas saturation change compared to the 4D signature is displayed in Figure 6.31. Similarly to the cumulative gas production, little changes between the base case and the updated model are evidenced as both simulations deliver similar responses. Yet, enhancement is occasionally observed in the updated model as the correlation between the reservoir softening (decrease in P-wave impedance) and the simulation is locally increased.

The cumulative oil production is also evaluated. In general, improvements in the cumulative oil prediction by the updated simulated model are revealed when compared with the historic data (Figure 6.32).

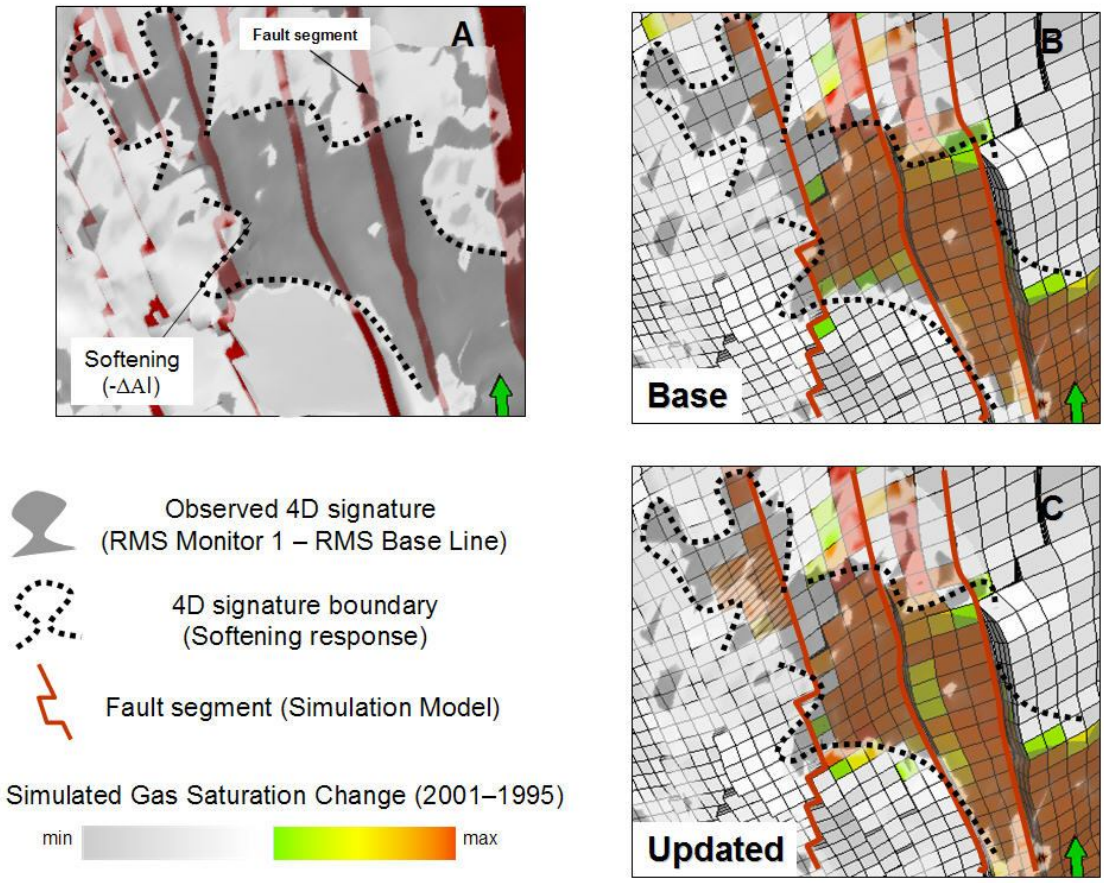

Figure 6.31. *(A) In grey colour observed 4D signature (RMS Monitor – RMS Base Line) constrained by fault segments (red). Comparison between the observed 4D signature (grey) and the gas saturation change (2001-1995) as derived by the simulation without (B) and including the 4D fault multipliers (C). Improvements in C (updated model) are highlighted with a diagonal background.*

The results shown in this section suggest that by including a 4D fault transmissibility multiplier, production data matching might be enhanced. Nevertheless, until now, a least-squares solution given in the regression analysis (for the adjustment between the 4D statistics and the well-derived fault permeability estimates) has been used for the updating of the simulation. Based on this observation, the next section discusses the impact of incorporating the uncertainty window of the 4D estimates by taking into account an automatic history matching workflow.

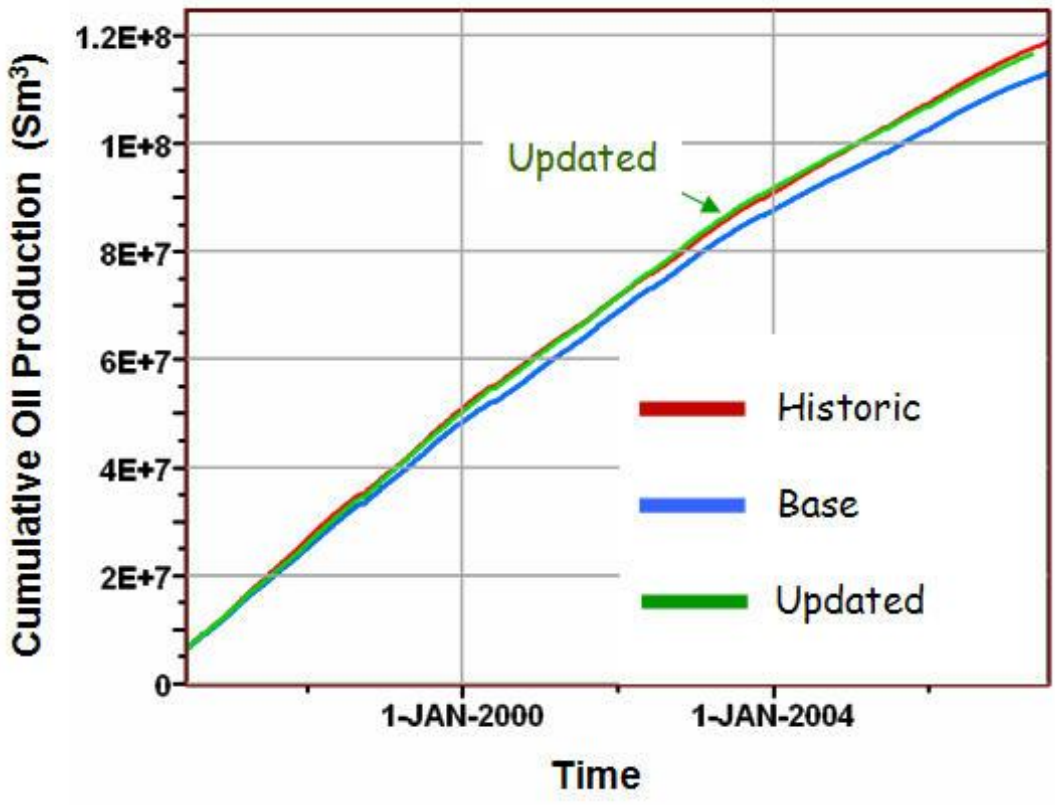

Figure 6.32. *Cumulative oil production for the base case and updated simulations compared to the history data.*

6.7 Automatic history matching incorporating the uncertainty associated with the 4D seismic-derived fault multipliers

In this section we apply an automatic history matching workflow which only takes into account changes in the fault properties in order to improve the fitting with the observed data. In this case we incorporate the new 4D seismic fault multipliers estimated previously using our methodology. This is based on a new integrated history matching which considers the production data as well as the geophysical input (in particular 4D seismic data) and its application has been proven successful also in synthetic models (Villegas et al., 2009). Here, this workflow is applied to the Heidrun field data. In this process, several scenarios for the fault compartmentalization of the reservoir are generated. These scenarios provide a variety of predictions that can be used as input to understand the interaction given by several reservoir parameters, hence allowing the optimizing of future development plans for the reservoir of study. In this work, we

consider a history match process which implements the uncertainty associated with the fault transmissibility estimation. To do so, the fault transmissibility multipliers given by least-squares solution in the regression analysis are used as prior information about the fault seal capacity. Once the impact of fault properties has been evaluated for the prior reservoir model using the black oil simulator, this fault model is iteratively modified based on the 4D seismic results and the history matching of production (Figure 6.33).

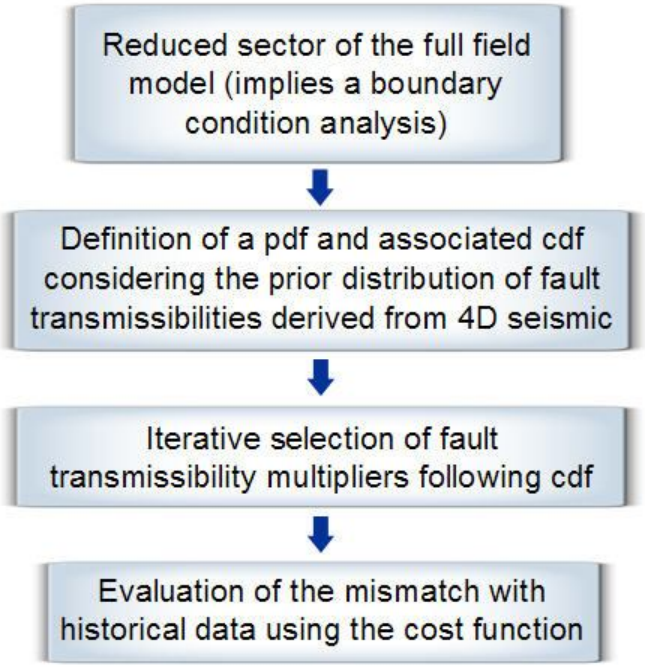

Figure 6.33. *Workflow for the automatic history matching process implemented in this work.*

Considering the uncertainty of the 4D seismic estimation shown in Chapter 5, a Monte-Carlo formulation is employed in the automatic history match approach in which the fault multiplier is randomly selected between a pre-defined minimum and maximum according to a probability density function (pdf). In particular, this pdf is constrained by the minimum and maximum values as well as the least square solution (prior) obtained from the time-lapse seismic results. Hence, the input data includes the fault seal realizations given by the possible fault transmissibility multipliers and the initial simulation model which includes the original transmissibility values and the production data. To evaluate and control the misfits of each simulated realization related to the history data, a cost function J depending on the production rate and pressure is defined.

This part of the workflow has been implemented in a sector of the field constrained by boundary conditions. The sector considers an area where dynamic changes in the reservoir are only associated with variations in the water saturation, and waterflooding has been identified as the main cause of the observed 4D seismic signature. As a consequence, the employed cost function J is only dependent on estimated water rate Q_w and observed water rate Q_{Wobs} at each producer well, and it is defined as,

$$J = \sum_{N} \frac{\left(Q_W - Q_{W_{OBS}}\right)^2}{\sigma_Q^2} \tag{6.1}$$

allowing a measure of the data misfit for a particular simulated scenario. Using this definition it is also possible to compare the accuracy of the simulations including the prior (least square estimation), minimum and maximum fault multiplier realizations as well as the base case.

Scenario	Cost Value (J)
Base Case	5.08×10^4
Maximum	4.25×10^4
Prior	4.00×10^4
Minimum	3.80×10^4

Table 6.1. *Results of the evaluation of the cost function for the base case, prior (least square solution), minimum and maximum fault multiplier scenarios.*

Table 6.1 reveals lower cost function values in the scenarios including the 4D estimation when compared with the base case model. Indeed a 20% decrease of the mismatch is evidenced when including the least square solution. Also, when comparing prior, maximum and minimum realizations, it is shown that minimum fault transmissibility multipliers produce the better fit with history data (misfit reduced in

25% compared to the base case). Now, using 4D seismic estimations given by the minimum, prior and maximum fault multipliers, a triangular pdf is defined to evaluate the performance of a preliminary automatic history matching. This only takes into account fault property changes which are in turn constrained by the pdf. Using the associated cumulative density function (cdf), fault transmissibility values are automatically modified using a random number generator (defined between 0 and 1 as the cdf values) which selects, for different iterations, a fault multiplier scenario included in the defined distribution (Figure 6.34). These scenarios are then simulated and the misfits are evaluated.

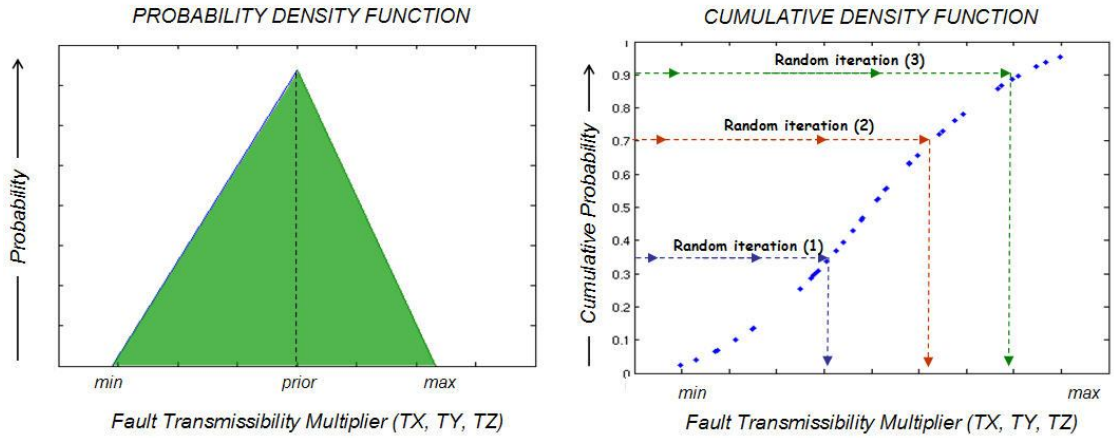

Figure 6.34. *A triangular pdf is defined using the 4D seismic input. The associated cdf allows evaluating different scenarios using a random number generator (defined between 0 and 1 as the cdf values) which selects different fault multipliers in each iteration.*

In the selected sector of the Heidrun field model, fault transmissibility multipliers have been iterated in accordance to the constraints given by the defined pdf. Here the value of the cost function has been moderately reduced to 3.6×10^4. Although this represents a small improvement compared to the cost value revealed when including the minimum 4D-derived multipliers, the automatic iteration offers a new best case for which the misfit reaches the lowest value (approximately 30% less than the base case), hence the lowest mismatch between the simulation output with the historical data.

6.8 Summary

To fully represent fault compartmentalization in reservoir simulation models, current workflows rely on various information which are often sparsely distributed. Fault seal properties are traditionally inserted in the simulation model via geologically-based algorithms, and when available, other techniques such as well-testing or conventional history matching are used to fill gaps of knowledge given by the lack of data. In spite of these efforts, the updating of the sealing properties of the faults in the simulation model is still difficult, as their prediction is in most cases biased by the available data and its integration capability. In order to enhance the fault seal representation in fluid flow simulations, we propose a new workflow that combines a geologically constrained 4D seismic input which is upscaled and introduced into the reservoir model. Here, fault transmissibility multipliers derived from 4D seismic are implemented and they seem to supplement and better resolve the spatial distribution of fault properties as shown by the application to the Heidrun field reservoir. In this real case example, the use of the new integrated workflow reveals that the updating of the field simulation model with such 4D input decreases the mismatch with production data. Also, when performing a preliminary automatic history match workflow guided by the production history, as well as by the 4D seismic estimation and its uncertainty, a more robust basis for the modelling of fluid flow in compartmentalised reservoirs is provided. By evaluating a misfit function, it is found that including such a workflow in the Heidrun field not only reduces the mismatch between simulation and historic data but also increases the spatial correlation with the observed 4D seismic signature.

Chapter 7

Examining the implications of the dynamic fault behaviour in the 4D seismic response

This chapter investigates the phase-dependent compartmentalization created by faults when considering an active production scenario. Here, the study of the dynamic fault sealing potential is addressed using several 4D seismic surveys. Theoretical background on the two phase fault properties is explored. Tests are performed on synthetic examples allowing comparison with the 4D seismic signatures observed in the Heidrun field.

7.1 Introduction

The drainage strategy implemented in the Heidrun field, consist of pressure maintenance by a waterflooding mechanism which is partly assisted by gas injection at the crest on the reservoir. The water drive is controlled by a set of water injectors located in the down-flank side of the field which helps to displace oil towards the producers. Thus, since production started in 1995, the main reservoirs included in the Fangst Group (i.e. Garn and Ile Formations) show a progressive increase of the water saturation as the water oil contact moves updip from its original position. Special emphasis on the surveillance of this process has been made in the southern part of the field as several time-lapse seismic surveys, carried out in this area, have allowed careful tracking of the waterflooding. As discussed in Chapter 3, the fluid substitution taking place (water replacing oil) introduces a seismic effect (P-wave impedance increase) that can be followed throughout the field. Hence, comparison of the 4D seismic signature with the engineering information, has allowed the mapping of the flooding coverage. In general, major reservoir compartments show a clear watering pattern allowing differentiation of the original oil water contact from the new water contact given at a particular production stage. This is the case for segments C to F, where repeated seismic surveys have been used to confirm the flooding extension. However, segment G and H have a different challenge as the water encroachment of these compartments seem to behave differently. Here fluid flow simulations notably differ with historic data, showing more oil potential than those indicated in the prediction (Figure 7.1). Also, comparisons between the time-lapse seismic surveys seem contradictory particularly in these segments; as the new time-lapse data given by the latest seismic difference (2004-1985), did not support the measurements (in terms of the flooded/unflooded areas) from the previous 4D observations (2001-1985) (Furre et al., 2004). As a consequence, the mapping of fluid contacts (i.e. water-oil) in these compartments is difficult to define, and they have been highlighted as uncertain in the flooding maps generated by the operator (Figure 7.2).

Now, as shown in previous chapters of this thesis, faults have proven to control the character of the 4D seismic signature as they affect the fluid and pressure development of the Heidrun field. In this chapter we further explore this concept as we suggest that the findings described in segment G and H could be linked with the dynamic character of the faults bounding the compartments. Here, we take into account the current

understanding of the two phase fault-rock properties to postulate that changes in the phase-dependent behaviour of the fault(s) constraining these segments (i.e. capillary pressure and relative permeability curves), are associated with the complex flooding pattern evidenced. This not only enhances the mismatch between seismic and simulator but also may cause unexpected discrepancies in the 4D signal derived from multiple surveys.

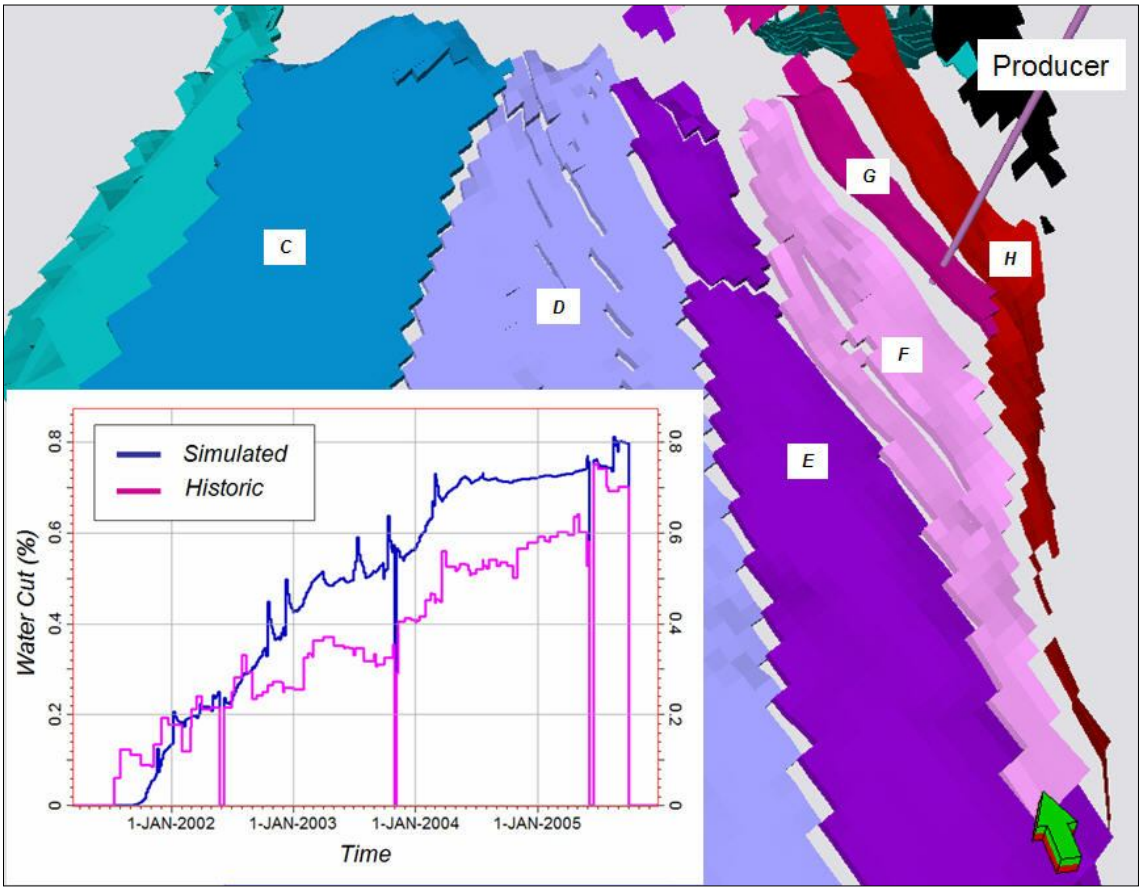

Figure 7.1. *An example of the water cut estimate is shown for an oil producer located in segment G. Simulated (blue) and historic (pink) water cut profiles are indicated in the left hand side corner. Note that observed water cut is generally lower than the simulated values. More oil potential has been indicated and this has been supported by the available time-lapse seismic surveys.*

In this chapter, we use two phase fault-rock principles in a synthetic production scenario (Manzocchi et al., 2002 and Al-Busafi et al., 2005) to evaluate the implications for the 4D signature. Then, based on the observations, a new workflow is employed in which the variance of 4D seismic differences is used as a tool to detect lateral variations of the phase-dependent behaviour of the fault. Tests are performed on a controlled synthetic

model, and weaknesses are also discussed. These are used as an analogue to explain the results of the application to the Heidrun field. The method can be used to assist the detection of such phenomena in a field case which needs to be represented in the simulation model. Finally, this study also highlights the implications of the two phase fault properties into the 4D seismic signature.

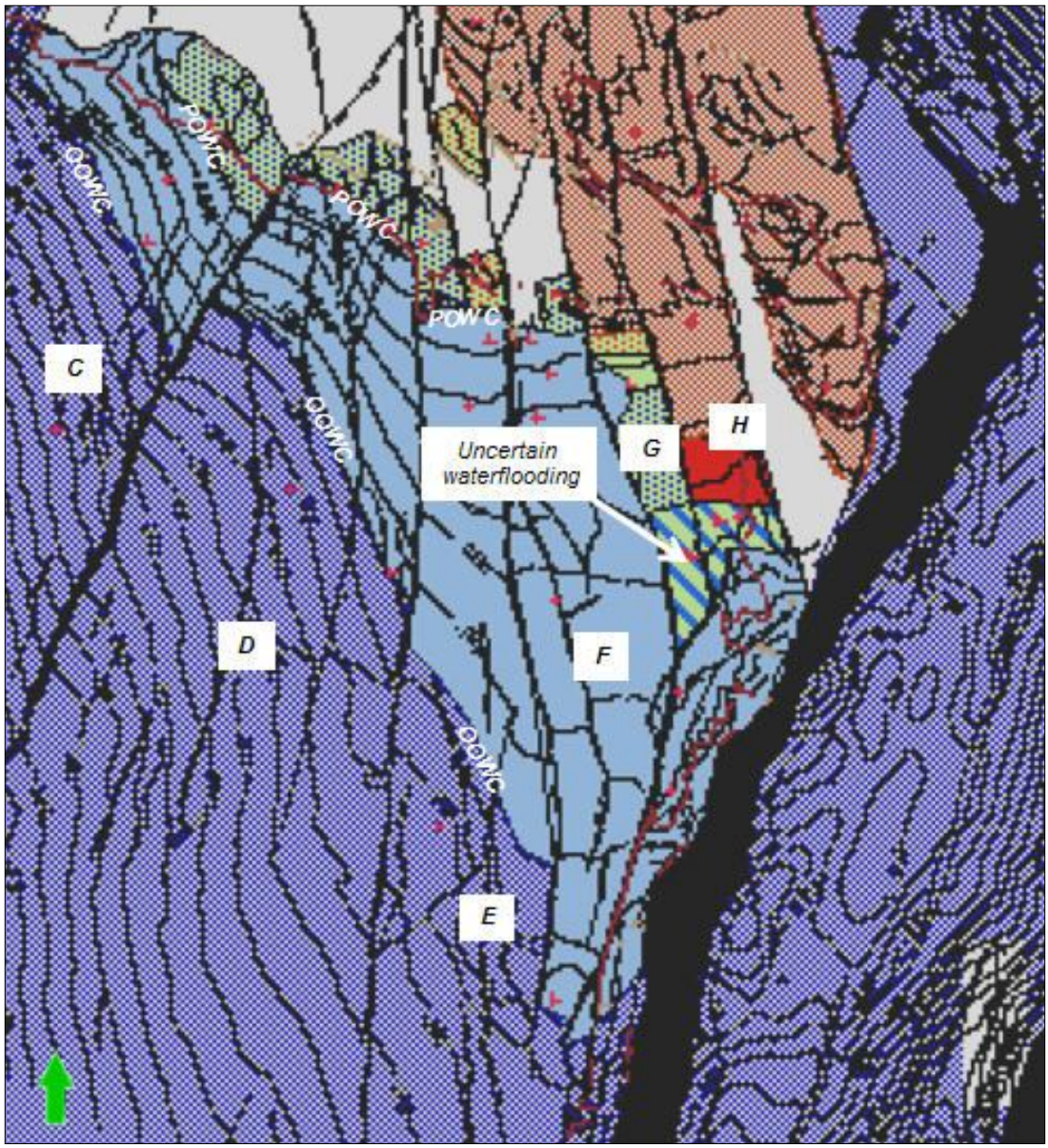

Figure 7.2. *2004 Flooding map for top Fangst Group. Mapping of fluid contacts is segment G and H is uncertain. Indeed 4D seismic suggest more oil than predicted by the simulator (Modified from Furre et al., 2004). OOWC=Original oil water contact, POWC = oil water contact after production (in 2004). Segments C to H are also identified in the map.*

7.2 The two phase fault-rock properties in reservoir flow simulations

Traditionally, fault conceptualizations in production flow simulation models, only consider a single phase behaviour of the fault-rock. Here, permeability and thickness of the fault-rock are used to derive transmissibility multipliers which in turn, are expected to represent the flow across faults (Manzocchi et al., 1999). Although this single phase approximation has been proven useful in the recent past, it fails to fully represent a more complex phenomenon taking place in the fault-rock. In reality, as in unfaulted rock samples, flow should not only be phase specific, but should also change as a function of the amount of water saturation present. Therefore, as in the grid-block representation of the reservoir, capillary pressures and relative permeabilities need to be considered within the fault-rock.

Capillary pressure is defined by the difference between the pore (fluid) pressure of water and hydrocarbon. Here each fluid acts within the interconnected pore space depending on the hydraulic potential. As a consequence, the pore pressure magnitude changes as a function of depth (Zoback, 2007), and this is also referred as the pressure gradient. As the hydrocarbon has a steeper pressure gradient when compared with water, the capillary pressure increases rapidly above the free water level (FWL) where the capillary pressure is zero (Figure 7.3). While the hydrocarbon accumulation grows (hence its saturation), the capillary pressure in the reservoir bed adjacent to the fault increases. Eventually the capillary pressure in the accumulation will match the capillary threshold pressure of the fault allowing migration through the fault. At this point the hydrocarbon connection is enhanced at a flow rate controlled by the relative permeability curves. Figure 7.4 shows a diagram illustrating fault trapping for a hydrocarbon column whose height is sufficient to exceed the capillary threshold pressure of the fault-rock at the top of the hanging-wall compartment. Here, a water injection strategy has been also represented helping to displace the non-wetting phase (hydrocarbons) with the wetting phase (water). The capillary pressure of the reservoir is shown as a function of the hydrocarbon saturation. Relative permeabilities for water and hydrocarbon associated with the fault-rock are also displayed. In position 1, the buoyancy force in the hydrocarbon column is not sufficient to overcome the capillary threshold pressure of the fault. Here, relative permeabilities for hydrocarbons in the fault-rock are equal to zero. When the buoyancy force in the hydrocarbon column is

sufficient to overcome the capillary threshold pressure of the fault-rock (above the dotted line), the fault will have a relative permeability to hydrocarbons higher than zero flowing together with the water phase in the transition zone at a rate governed by both the pressure difference and the relative permeability of the fault-rock (positions 2 and 3). Above this (position 4), a free-water production zone is observed, where only hydrocarbons are considered mobile (i.e. high hydrocarbon relative permeability at residual water saturation).

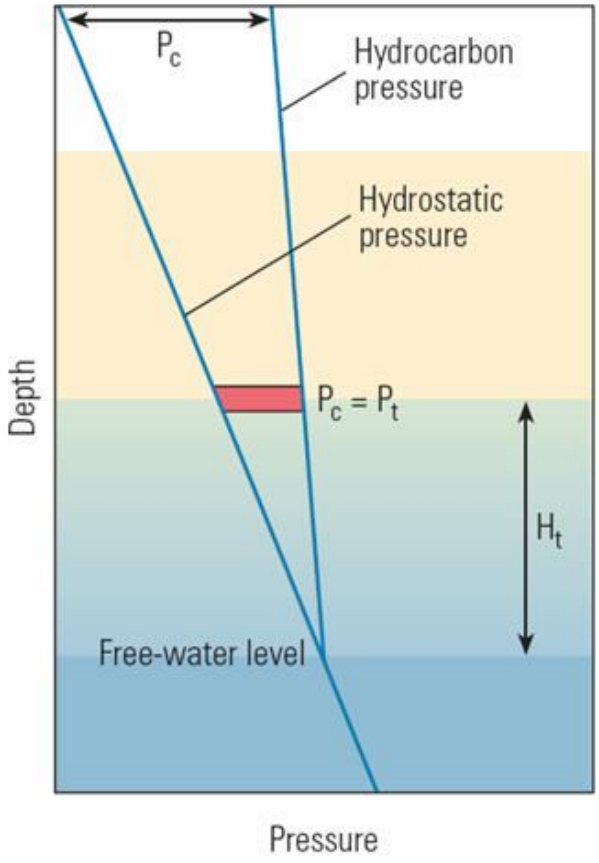

Figure 7.3. *Pressure-depth plot showing capillary pressure (Pc) as the difference between the hydrostatic and hydrocarbon pore (fluid) pressures. Below capillary threshold pressure (Pt) a hydrocarbon column (Ht) is completely trapped. The hydrocarbon flow rate across the seal above Ht is dependent on the relative permeability of the seal. From Cerveny et al., 2005.*

Now, provided water flooding is used as hydrocarbon recovery strategy; capillary pressure in the reservoir decreases as the water saturation is increased. Here, the greater the probability that the capillary threshold pressure of the fault is soon above the

capillary pressure of the reservoir. If, at original hydrocarbon saturation, capillary pressure of the reservoir is above the capillary threshold of the fault, a dynamic two-phase flow takes place within the fault-rock. Along the fluid substitution hydrocarbons are less mobile through the fault until it becomes fully detrimental to this phase. At this point only water is the mobile phase and no dynamic behaviour develops.

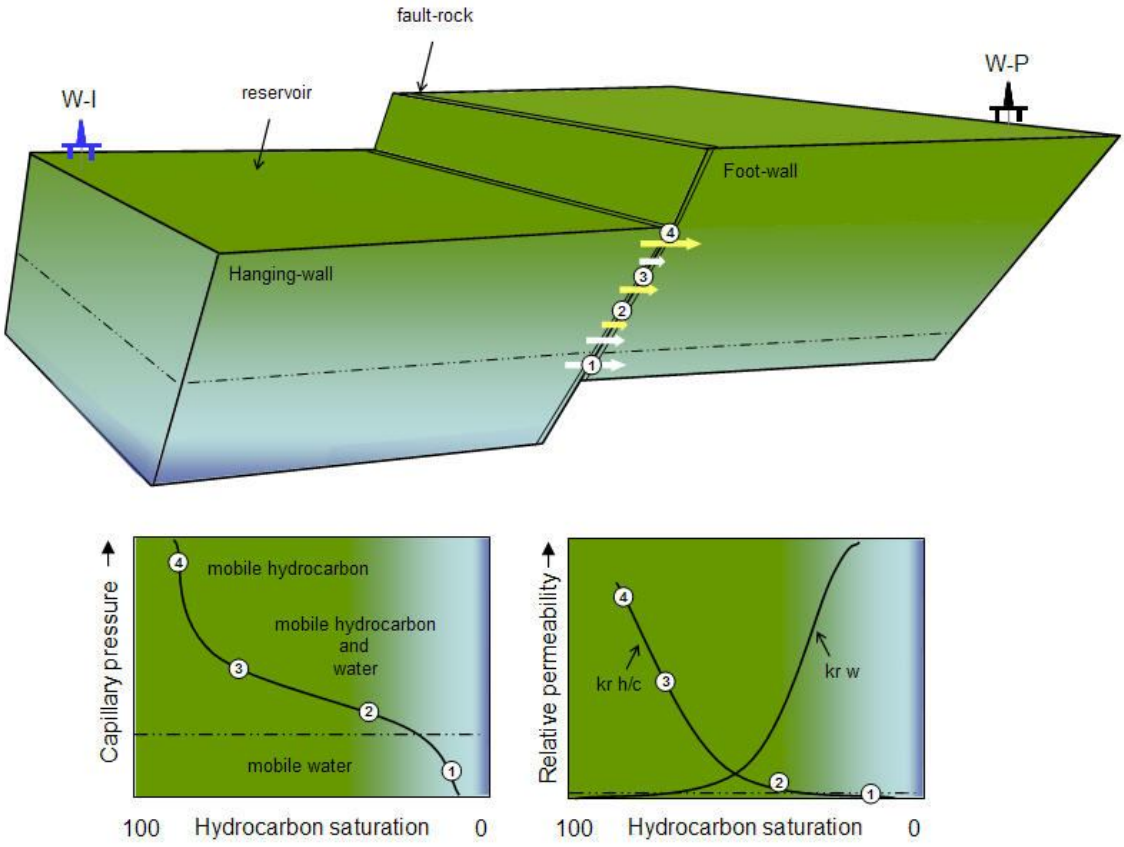

Figure 7.4. *Conceptual model, based on Fisher et al. (2001) for multi-phase flow across a fault in a petroleum reservoir. Hydrocarbons and water are represented as green and blue respectively. The capillary pressure of the reservoir and relative permeability curves of the fault-rock are displayed. A water injector (W-I) helps to displace the oil towards the producer (W-P) located in the next compartment. Fluid flows from the hanging-wall block with higher reservoir pressure towards the foot-wall with lower reservoir pressure. Hydrocarbons are only mobile through the fault when the capillary pressure of the reservoir exceeds the capillary threshold pressure of the fault (above the dotted line). Far from the oil water contact, the greater the chance oil can be mobile through the fault, with flow rates increasing for this phase (yellow arrows), and decreasing for the water phase (white arrows) as the hydrocarbon saturation increases. Waterflooding of the foot-wall block depends on the fault properties.*

To represent the interaction between fluid phases, Manzocchi et al. (2002) propose the following equations. The drainage capillary pressure curve for sediments derived by Ringrose et al. (1993) is employed evenly for the fault-rock:

$$P_c = C \; S_e^{-2/3} \left(\varphi_f / k_f\right)^{0.5} \tag{7.1}$$

where C = 3 is a conversion factor to give capillary pressure in bars, φ_f is fault-rock porosity and k_f is the absolute (single phase) fault-rock permeability in mD. The fault-rock porosity is determined from the fault-rock permeability using the relationship:

$$\varphi_f = 0.05 k_f^{0.25} \tag{7.2}$$

This empirical equation provides a reasonable fit with observed scatter in available publications (e.g. Pittman 1981; Fowles & Burley 1994; Berg & Avery 1995; Evans et al. 1997; Knipe et al. 1997; Fisher & Knipe; 1998).

S_e is the effective wetting phase saturation defined as:

$$S_e = \left(S_w - S_{wc}\right) / \left(S_{wor} - S_{wc}\right) \tag{7.3}$$

where S_w is water saturation, S_{wor} is the water saturation at irreducible oil and S_{wc} is the connate water saturation defined as:

$$S_{wc} = 0.85 - 10^{\left(-0.6\left(-0.5\log\left(k_f\right)\right)\right)} \tag{7.4}$$

Then, by making S_e equal to 1, it is possible to calculate the capillary threshold pressure of the fault-rock. If the reservoir-rock adjacent to the fault shows a capillary pressure below the fault-rock capillary threshold pressure, the fault is impermeable to oil and only water is mobile. However, if the reservoir capillary pressure exceeds the fault-rock capillary threshold pressure, an imbibition process is considered. In this case water and also oil are the mobile phases, and the following capillary pressure curve needs to be considered for the fault-rock:

$$Pc = C\left(1 - S_e^5\right) S_e^{-2/3}\left(\varphi_f / k_f\right)^{0.5} \tag{7.5}$$

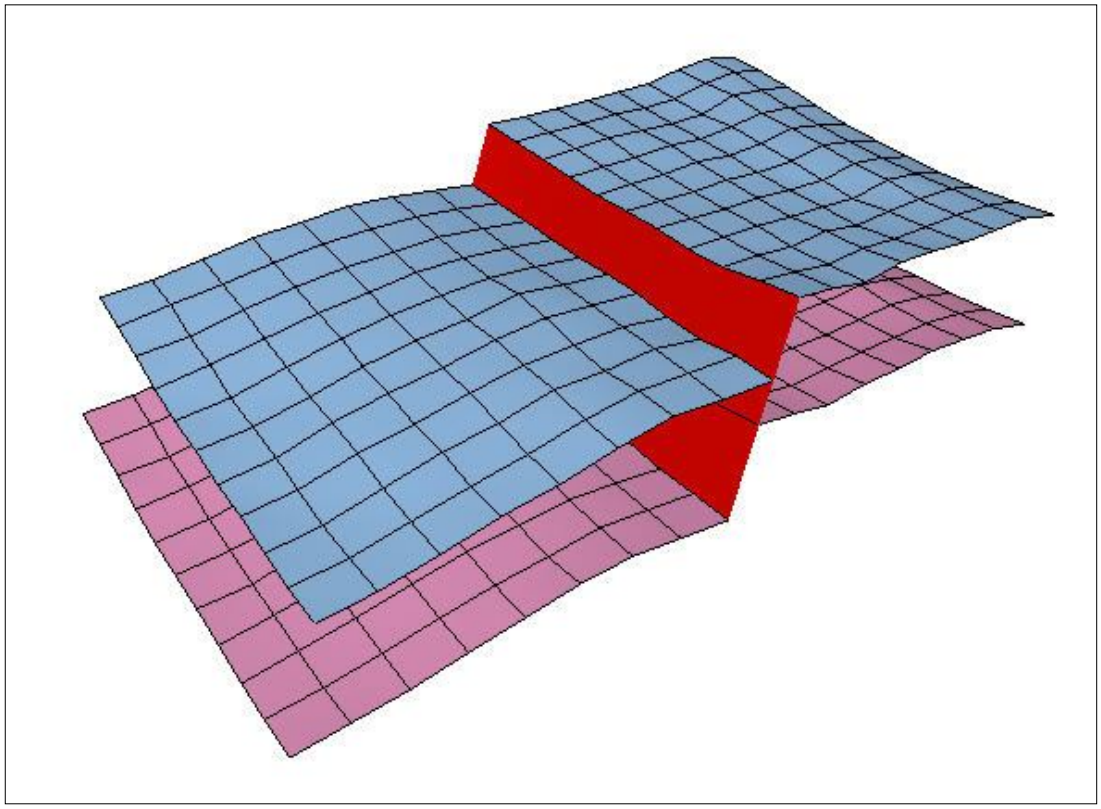

Figure 7.5. *Geometry used for the construction of the synthetic model. Top and base horizons are derived from the interpretation of the Fangst Group in the Heidrun field. The red fault (also identified in 3D seismic) set in juxtaposition both reservoir blocks compartmentalizing this particular sector of the field. Description of the reservoir-rock properties filling this model can be found in Chapter 4.*

This equation is employed when the wetting phase (water) manages to displace the non-wetting phase (oil) as in a water-flooding recovery process. Manzocchi et al. (2002) finally propose water and oil relative permeability curves (k_{rw} and k_{ro} respectively) analogous to those defined by Ringrose et al. (2003) as:

$$k_{rw} = 0.3 S_e^3 \tag{7.6}$$

and

$$k_{ro} = 0.85(1\text{-}S_e)^3 \quad (7.7)$$

Once the prediction is available for the absolute permeability of the fault-rock, these functions can be used to determine complementary two-phase fault-rock properties.

7.3 Implications for compartment waterflooding

The watering capability of the reservoir compartments is strongly dependent on the interaction of capillary pressures of the reservoir and fault rocks. To evaluate this phenomenon, a synthetic model is constructed. Previous studies (e.g. Manzocchi et al., 2002 and Al-Busafi., 2005) also present a synthetic approach which helps to contrast various fault representations. However, in this thesis, a new effort is undertaken to represent the Heidrun reservoir setting (i.e. in Fangst Group) and its waterflooding strategy by incorporating the static and dynamic data derived from a sector of this field into our synthetic model. The reservoir architecture has been derived from the 3D seismic interpretation provided by the operator (Figure 7.5).

The study sector comprises of two reservoir compartments defined by top and base horizon interpretations for the Fangst Group. A fault segment with variable displacement sets in juxtaposition both reservoir blocks. Based on this geometry, the grid dimensions for the synthetic model are given by 16 x 10 cells. Using the available well-log information in the Heidrun field, reservoir-rock properties (i.e. porosity, permeability, and net-to-gross) are propagated throughout the compartments (see Table 4.1 in Chapter 4). To represent the two phase fault-rock properties within the simulation model, a local grid refinement (LGR) is incorporated (Figure 7.6). Its dimensions are constrained by the fault-rock thickness, which is in turn estimated from the fault displacement (Manzocchi et al., 1999). In this study we use a fault rock thickness value of 2 m (with 1 m at each side of the fault plane) and this is equivalent to the observations presented by Knai and Knipe (1998). Indeed, core studies performed in the Heidrun field (described in that work), highlight faults with thickness up to 2 m for throws of 65 m.

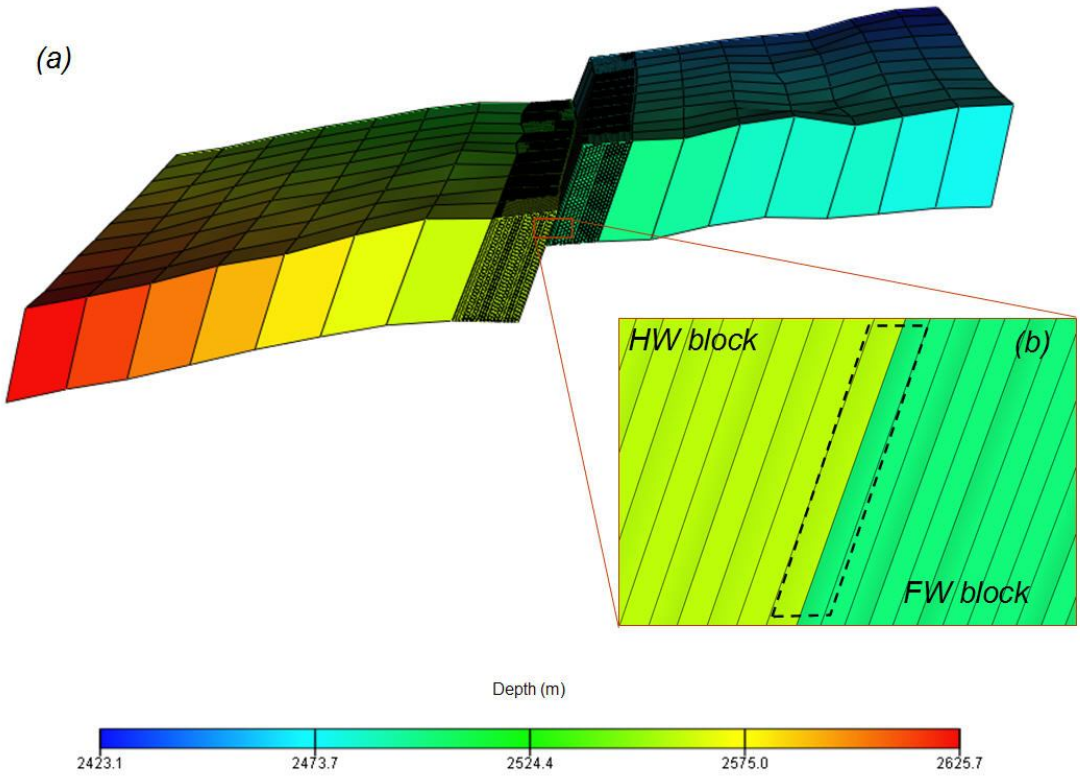

Figure 7.6. *(a) Synthetic model incorporating a local grid refinement (LGR) which helps to represent the fault segment discretely. (b) The two meter fault zone is divided in one meter thickness cells assigned equivalently at each side of the fault segment for hanging-wall (HW) and foot-wall reservoir blocks.*

Two different end-member cases are now evaluated (Figure 7.7). In the first case, the reservoir capillary pressure is below the threshold capillary pressure of the fault. Here, the fault-rock is totally detrimental to hydrocarbon flow; hence the drainage capillary pressure curve is appropriate. This fault is only permeable to water which can form a connected flow path between both compartments. In the second case, the reservoir rock can overcome the fault-rock capillary threshold pressure. In this case the oil and water are mobile in the fault-rock. When waterflooding is considered as part of the hydrocarbon recovery process, this implies a wetting phase (water) displacing the non-wetting phase (oil). Here the imbibition fault-rock capillary pressure curve is appropriate. As a consequence, this fault has a finite relative permeability to oil. In both cases, an absolute fault permeability value of 0.01 mD is used to derive capillary pressure and relative permeability curves according to the equations that are shown above. However, to simulate the situation where the fault allows oil leaking (i.e. second case), the capillary curve values derived for the first case are divided by 100, so the fault

capillary threshold pressure is now lower than before. In all the simulations the same capillary pressure curve is assigned to the reservoir-rock. To assign the properties for the reservoir and fault in the model, we make use of a different saturation number (satnum) which have been associated with spreadsheets including the information for each of the two rock types.

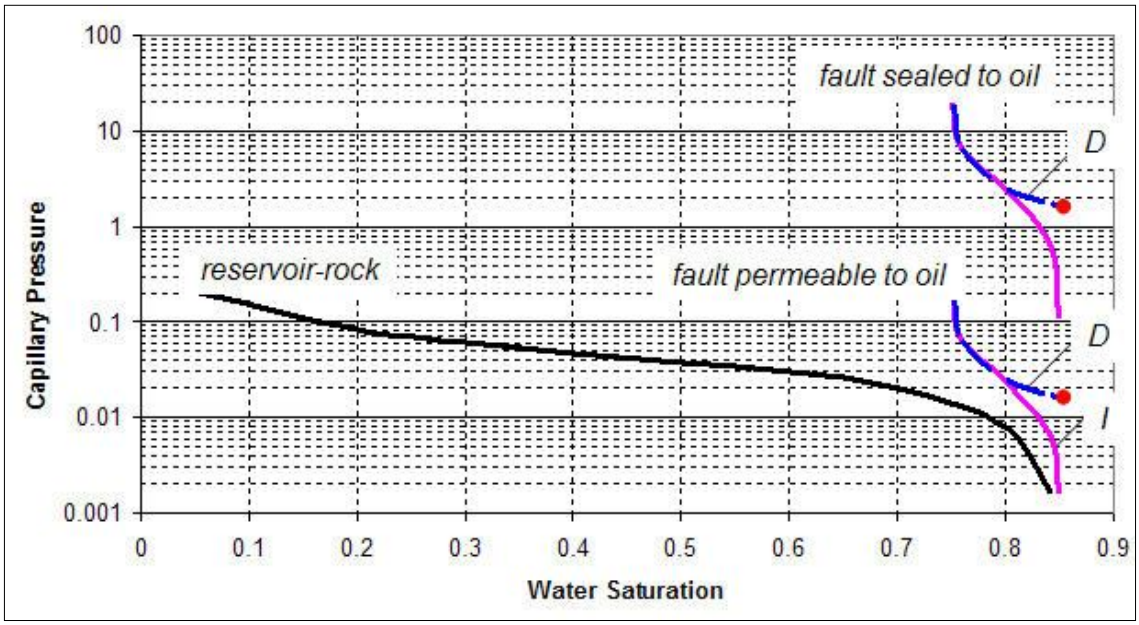

Figure 7.7. *Capillary pressure curves for the reservoir and fault rocks. Drainage (D) and imbibition curves (I) are calculated using equations in Manzocchi et al. (2002) also shown in this chapter. Fault capillary threshold pressure is displayed as a red point. Two end-member cases are analysed using the synthetic model: In the first case the fault capillary threshold pressure is above the reservoir capillary pressure, hence the fault is sealed to oil. In the second case the fault capillary threshold pressure has been decreased. Here, both oil and water are mobile phases in the fault-rock.*

Fluid flow in the synthetic system has been triggered via a water injector and a producer well located at opposite corners of the model. Oil production and water injection is set as 1400 Sm^3/day and the simulation deals with a black oil system where only oil and water phases are taken into account. Also, a control point is included in the footwall compartment of the reservoir, aside from the major fault segment (Figure 7.8). Simulation results for the two cases are displayed in Figure 7.9 and Figure 7.10. Now, using the control point, water saturation is compared between the two end-member cases (Figure 7.11). Indeed modelling shows that changes in the simulated water saturation are observed when the relation between the capillary pressure of the reservoir

and the fault capillary threshold pressure is altered. Only when the capillary trapping of the fault relative to hydrocarbons is weaker (second case), oil flows through the fault forming a connected path between both compartments. Here, relative permeabilities control the fluid mobility in the fault-rock which is distributed between the two different phases. As a consequence, the simulated water saturation profiles, derived from each case, deviate from each other. However, as indicated by the simulations, the water saturation magnitude might not change significantly between both cases, yet the values vary quicker when oil is impermeable to the fault when compared to the case in which this fluid is mobile. Subsequently, variance of each water profile is also different, hence it could be used as a measurement of comparison. In fact, in this synthetic experiment an approximate change of 20% in the water saturation variance has been measured.

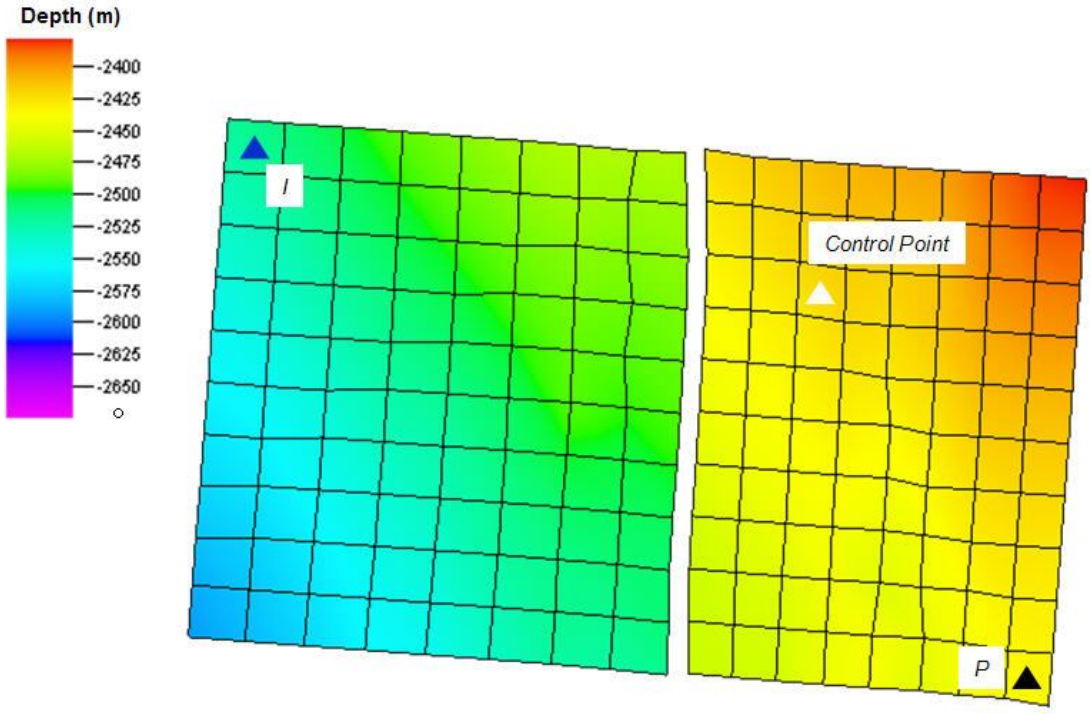

Figure 7.8. *Location of the water injector (I), oil producer (P) and the control located in the footwall compartment of the reservoir.*

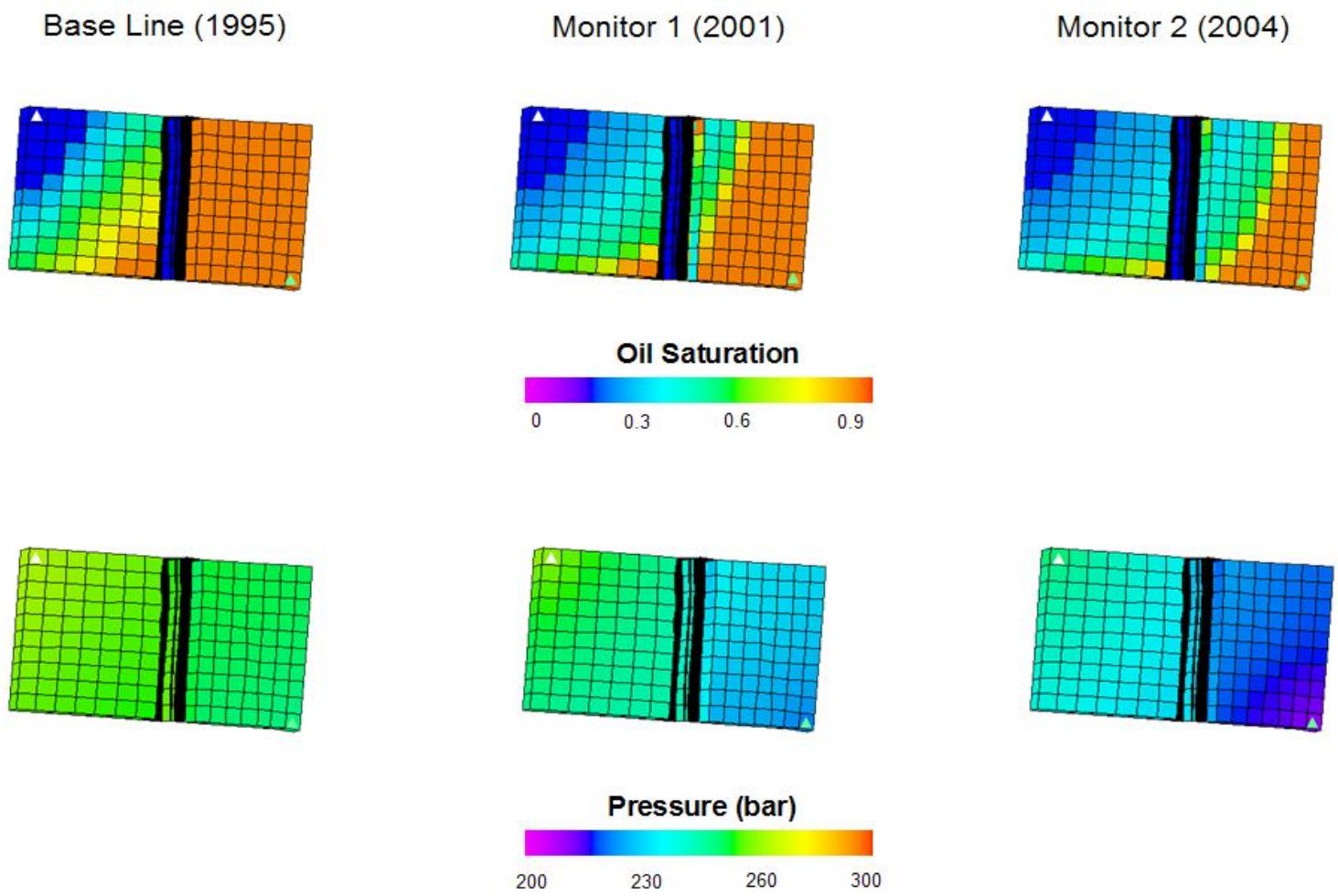

Figure 7.9. *In the first case, the reservoir capillary pressure is below the threshold capillary pressure of the fault. Simulated saturation (above) and pressure (bottom). A water injector (white triangle) and a producer (green triangle) are located in each corner of the model. Here, the water connectivity is enhanced.*

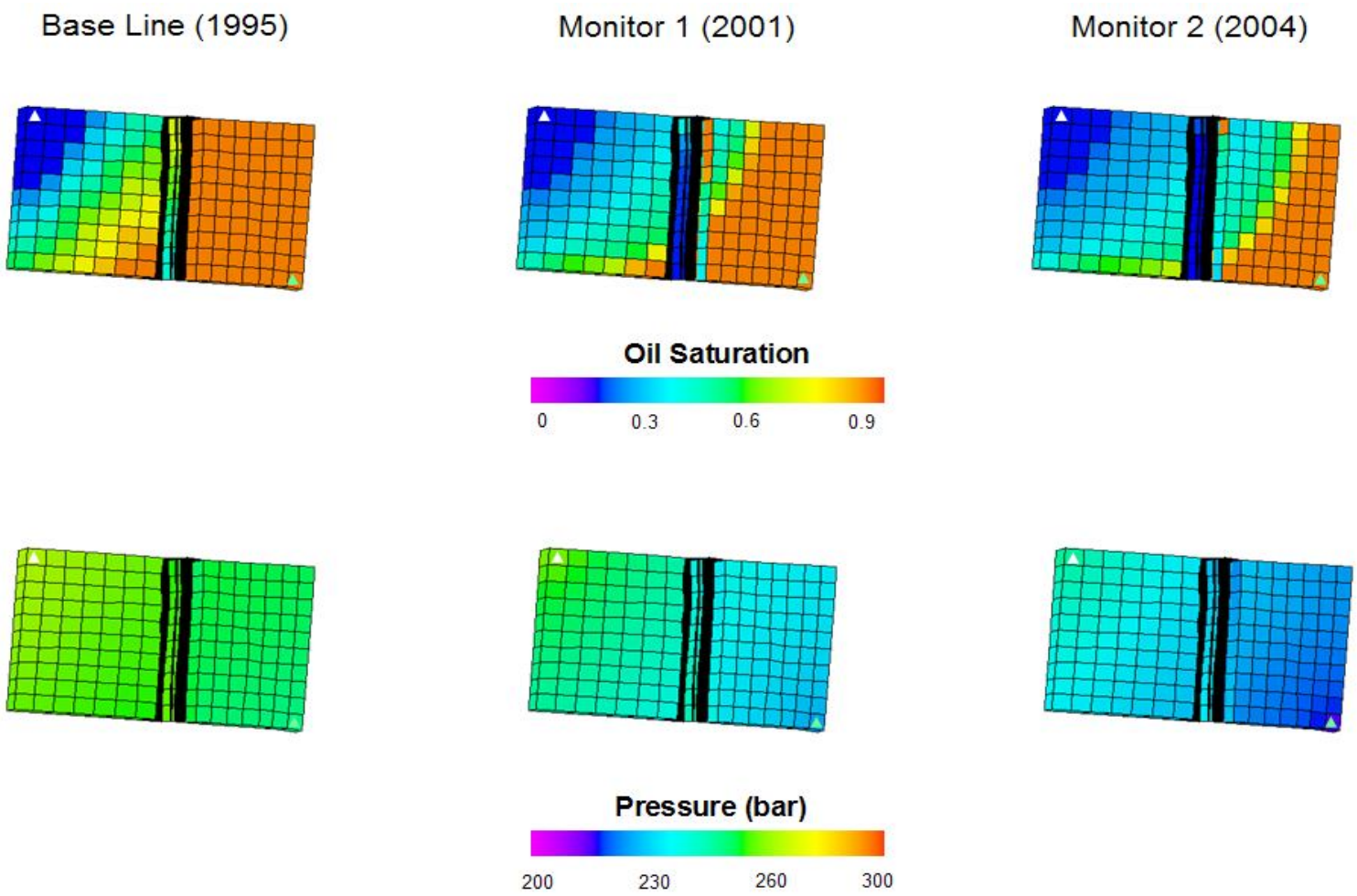

Figure 7.10. *In the second case, the reservoir rock can overcome the fault-rock capillary threshold pressure. Simulated saturation (above) and pressure (bottom). A water injector (white triangle) and a producer (green triangle) are located in each corner of the model. In this case both fluid phases are mobile across the fault-rock.*

This observation can be quickly detected close to the injector where the water changes occur fast and the two different cases differ quickly at the time of the simulation. Hence, if other control points are selected, the simulation time needs to be extended, allowing the progression of the waterfront. Then, if changes in the relation between the capillary pressure of the reservoir and the capillary threshold pressure of the fault are occurring, an anomalous variation of the water changes should appear in the affected zone finally impacting on the waterflooding evolution. However, detection of such behaviour is demanding as multiple flow simulations are used to evaluate the sensitivity associated with modelled parameters (Al-Busafi et al., 2005). These might be time-consuming as a sufficient number of models are run to make a decision. Based on this observation, the next section discusses the application of a workflow which might help to highlight the lateral variations in the dynamic behaviour of the fault using 4D seismic differences when this phenomenon affects the drainage strategy.

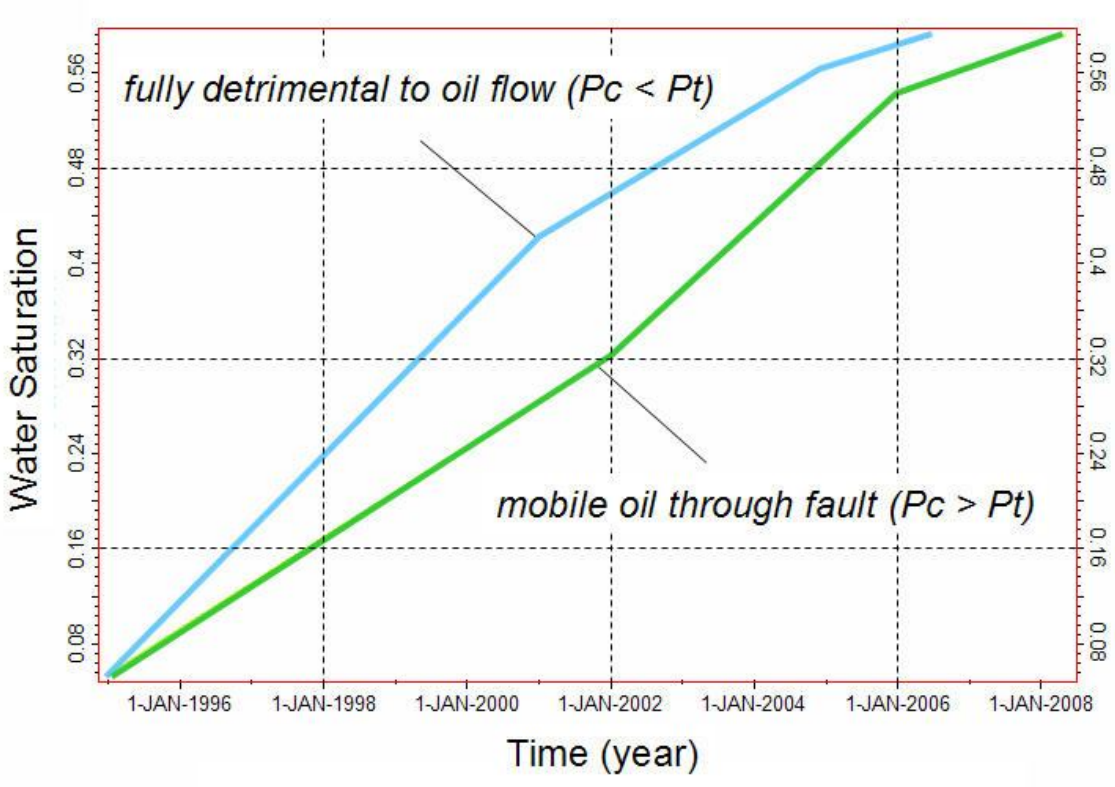

Figure 7.11. *Water saturation profiles for the control point in the two end-member cases. In blue, the reservoir capillary pressure (Pc) is below the threshold capillary pressure of the fault-rock (Pt). In green, the opposite scenario is represented. The profiles deviate from each other as the relations between reservoir and fault rocks changes.*

7.4 Detection of the phase-dependent fault compartmentalisation using 4D seismic

7.4.1 The model

Based on the observations discussed in the previous section, a homogeneous reservoir is considered, consisting of two compartments (separated by a fault) both affected by a strong water drive. A seismic vintage has been acquired at three different time steps (Figure 7.12). In time, the water-oil contact moves further in the updip direction given a waterflooding strategy in the reservoir.

Differences between each monitor and base line seismic surveys highlight the waterflooded area. In particular, saturation changes between the original water-oil contact and the water-oil contact given the first monitor survey is acquired, are measured twice by considering 4D seismic differences. Samples included in this sector are affected by the behaviour of the fault separating the observed compartments. If the relation between the capillary pressure of the reservoir and the fault capillary threshold pressure is laterally altered, a change in the variance (relative to the background magnitude) of the 4D signature is expected in the compartment where its water flooding is dependent on the constraining fault. Here, contrast in the variance of the repeated 4D seismic measurements (monitors minus base) in the waterflooded zone, might help to indicate lateral changes in the relation between the capillary pressures of the reservoir and fault rocks.

7.4.2 Application to a synthetic case

To test such an assumption a new synthetic model is used. The initial conditions given by the reservoir-rock and the fluid are analogous to the previous synthetic examples. However, in this case, the fault segment is divided into two sectors which are equivalent in length (Figure 7.13). A waterflooding scenario is considered. Here a water injector and an oil producer well are located at opposite corners of the model. Now, the further a fault is away from the water oil contact the greater the probability that the fault capillary threshold pressure is exceeded by the reservoir (Manzocchi et al., 2002).

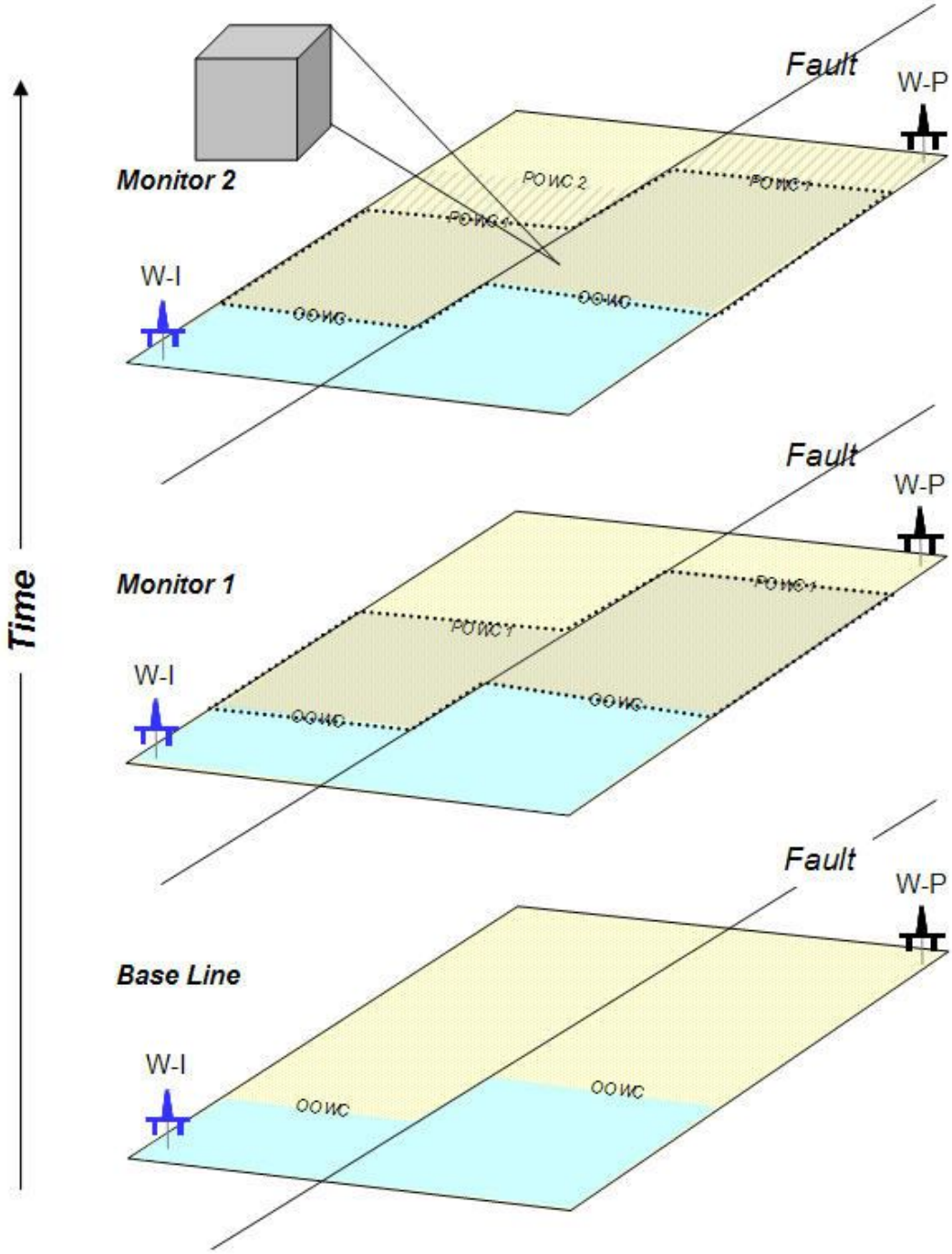

Figure 7.12. *Schematic model used for the proposed workflow. An homogenous reservoir is shown in which a waterflooded strategy is imposed. W-I is a water injector and W-P an oil producer. A base line and two monitor surveys are acquired. Differences between each monitor and the baseline vintages help to measure changes in the waterflooded zone defined between the original oil water contact (OOWC) and the oil water contact (POWC1) when the first monitor is acquired. Thus, time-lapse seismic changes in this area are sampled twice allowing the variance to be measured for such seismic differences. If the relation between the capillary pressure of the reservoir and the fault capillary threshold pressure is altered, a change in the variance of the 4D signature is expected in the right hand side compartment in which the water flooding is dependent on the fault properties.*

Thus, near to the water injection zone, the first half of the fault is represented by a capillary threshold pressure above the reservoir capillary curve, whereas far from the injection zone, the second half considers a low capillary threshold pressure which can be overcome.

As before, production and injection are set as 1400 Sm^3/day and the simulation deals with 9 years of reservoir activity (1995-2004). Three different time steps are selected to evaluate the time-lapse signature: a baseline (1995), and steps given after 6 (2001) and 9 (2004) years of production. These are equivalent to the seismic vintages acquired in the Heidrun field. Saturations and pressures obtained as a result of the simulation are presented in Figure 7.14. The simulation output reveals a progressive watering of the reservoir compartments. Also, as in the Heidrun field, pressure decreases slowly due to the water injection strategy set into place.

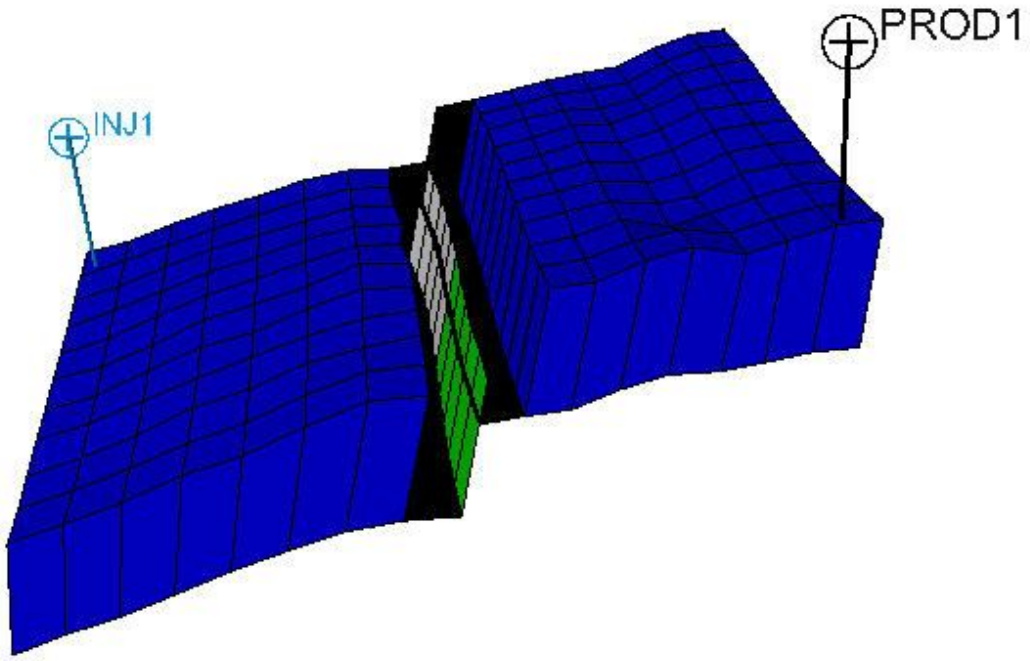

Figure 7.13. *Synthetic model used to test the proposed assumption. In this case the fault segment is divided in two sectors of equal length. In white, the fault-rock is represented by a capillary threshold pressure above the reservoir capillary curve. In green, a low capillary pressure is considered and it can be exceeded by the reservoir capillary pressure. Curves are displayed in Figure 7.7.*

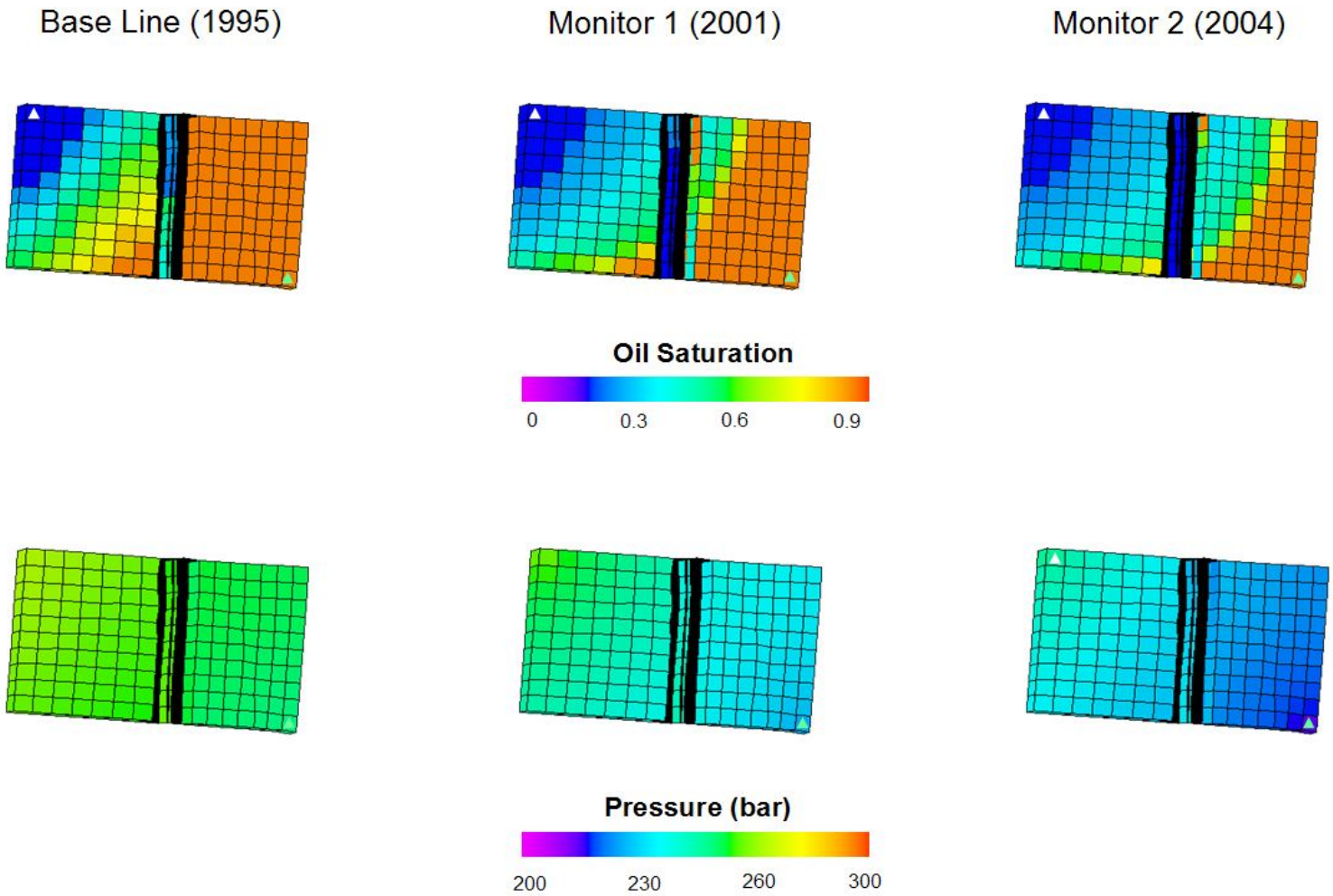

Figure 7.14. *Synthetic model used to test the proposed assumption . Simulated saturation (above) and pressure (bottom). A water injector (white triangle) and a producer (green triangle) are located in each corner of the model.*

Now, saturation (*Cs*) and pressure (*Cp*) coefficients included in the linear approximation for the time-lapse seismic signature (MacBeth, et al., 2006) are used. Previously derived in Chapter 3, these coefficients are inverted from the available well activity of the Fangst Group in the Heidrun field, and as a consequence, they represent an intrinsic property of this particular reservoir. By using them, the engineering domain can be quickly transformed into 4D seismic data maintaining the dynamic character of the reservoir of study. This approach does not make direct use of the petro-elastic modelling, however it is indeed handy when the model is highly complex (e.g. LGR included). Also, as it is linked to the reservoir saturation and pressure in Heidrun, this helps to make educated conclusions.

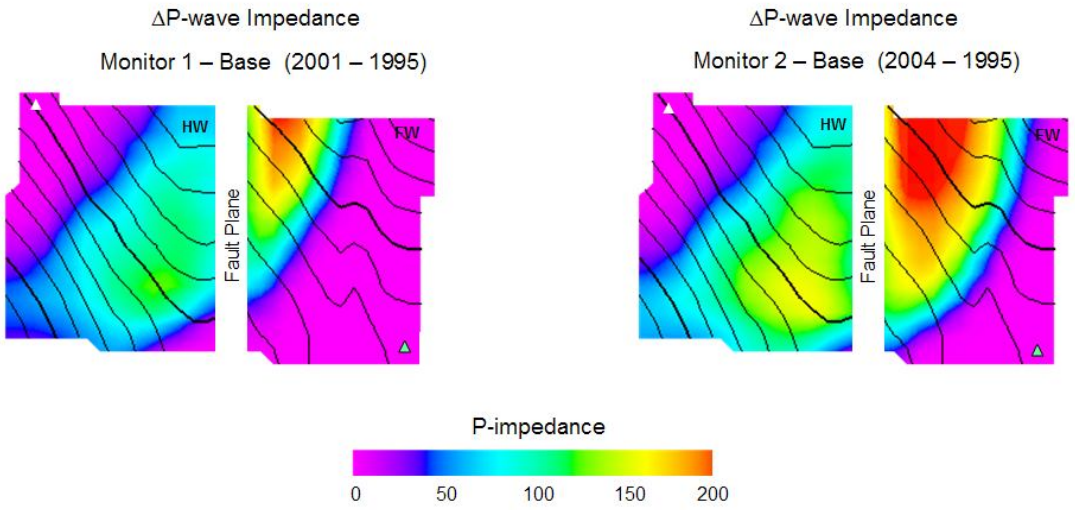

Figure 7.15. *Modelled P-wave impedance change between the base line (1995) and each monitored step (2001 and 2004) given the lateral variations of the capillary threshold pressure of the fault. Hanging-wall and foot-wall are identified in each map as HW and FW. Also the water injector and the oil producer are displayed as white and green triangles respectively.*

In this chapter, saturation and pressure coefficients are used in order to estimate the synthetic P-wave impedance change given the base line (1995) and each monitored step (2001, 2004 and 2006). Results are shown in Figure 7.15. Indeed the water injection scheme is progressively flooding the reservoir, and as a consequence an increase in the P-wave impedance is observed in each map. Now, having estimated this time-lapse signature, we use the variance definition as a detection tool for changes in the phase dependent behaviour associated with the fault.

The following variance (σ^2) formulation is employed:

$$\sigma^2 = \frac{\sum \left(4D_{mon(i)-base} - \overline{4D}\right)^2}{N\text{-}1} \tag{7.8}$$

where, $4D_{mon(i)\text{-}base}$ represents the time-lapse signature between a given monitor and the base line, $\overline{4D}$ is the average time-lapse signal for such difference, and N the number of 4D surveys given by the difference between the monitors and the base line. Application of such definition on the P-wave changes resulting from the synthetic model is shown in Figure 7.16.

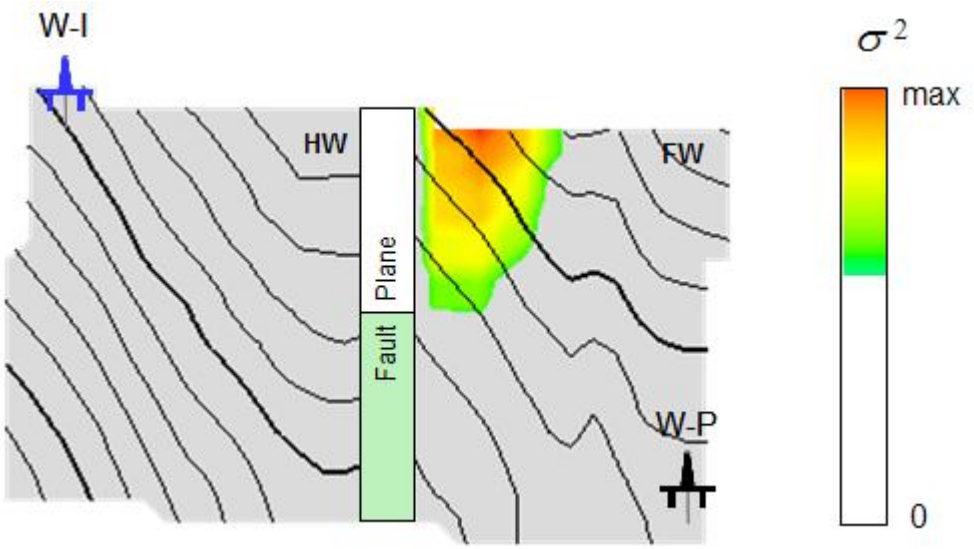

Figure 7.16. *Variance of the 4D signatures given by the differences between each monitor survey and the base line. The two fault sectors (with different capillary threshold pressures) are displayed. In green, a low capillary threshold pressure is represented in the fault-rock and it can be exceeded by the reservoir capillary pressure. In white, the fault-rock has a capillary threshold pressure above the reservoir capillary curve and only water is permeable. Next to this sector water saturation increases quickly in the footwall compared to rest of this compartment. Consequently the variance increases and an anomaly appears in the foot-wall block (FW) in which flooding depends on the fault properties.*

Note that a strong anomaly is differentiated from the background values of the variance. This appears in the foot-wall compartment in which the water flooding character (originating in the hanging-wall block) is strongly dependent on constraining fault. Indeed, when the capillary threshold pressure of the fault is exceeded, the higher the probability hydrocarbons will flow through the fault-rock with higher rates when compared to the water phase. On the other hand, water changes are expected sooner when the capillary pressure of the reservoir cannot exceed the capillary threshold pressure of the fault. In this case only the water phase is mobile with a high rate. Here the variance of the 4D signature seems a useful attribute to detect such phase-dependent control introduced by the fault-rock. As shown in this synthetic test, an anomalous character of the statistical measurement suggests lateral changes in the relation between the capillary pressure of the reservoir and the fault capillary threshold pressure.

If the relation between the capillary pressure of the reservoir and the capillary threshold pressure of the fault remains constant along the fault plane, the fluid transfer given along the fault plane separating reservoir compartments behaves similarly and no isolated anomalies in the 4D seismic variance are expected. Yet, an exception to this observation might occur if strong variations in the transmissibility of the fault are present. This case is analysed in the next section.

7.4.3 Strong variations in the transmissibility of the fault

If strong variations in the transmissibility of the fault are occurring (i.e. strong variations in the net-to-gross and/or fault displacement affecting fault-rock composition) this might introduce lateral disruptions in the waterflooding when this is controlled by the fault. To evaluate such a case, a single phase scenario is considered. Here, fault zone properties are represented as transmissibility multipliers assigned to the grid-cells (10) in contact with one side of the fault segment. These are derived from the shaly fraction of the reservoir and the fault throw as described in Chapter 1. However, in this scenario, fault multipliers assigned to half of the fault segment (5 grid-cells) are now multiplied by 100 to maximize a lateral change in the behaviour of the fault properties (Figure 7.17). Conditions in the fluid flow simulation are identical to the cases shown above. The simulation output is shown in Figure 7.18.

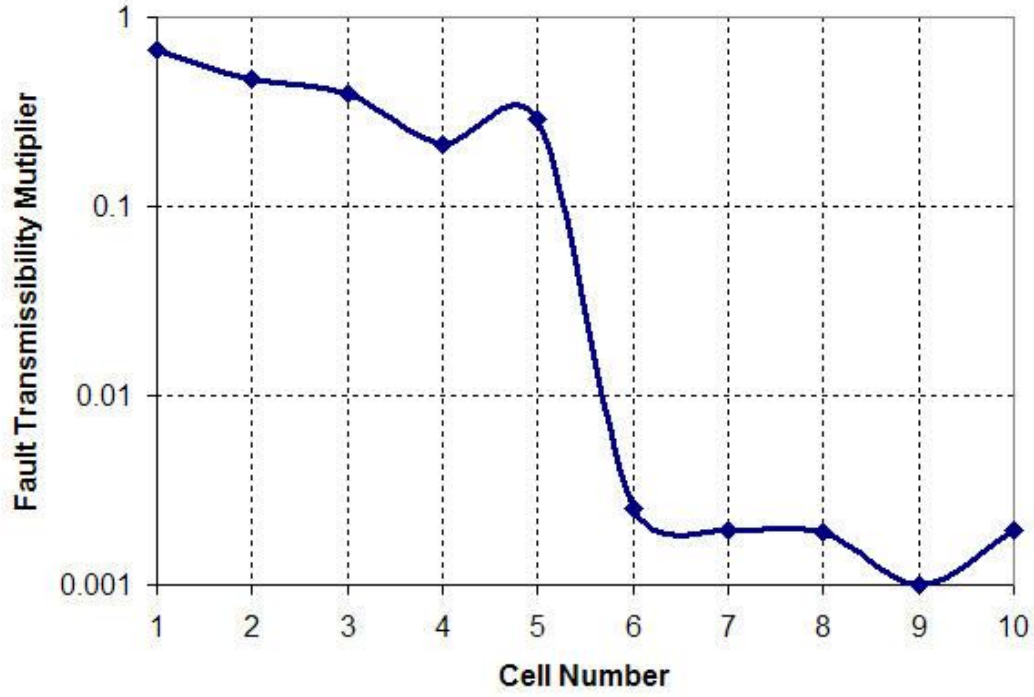

Figure 7.17. *Fault transmissibility multipliers assigned for the fluid flow simulation. In this case, multipliers change in two orders of magnitude to emphasize strong lateral variations of the fault properties.*

As before, saturation (*Cs*) and pressure (*Cp*) coefficients extracted in the Heidrun field are employed to transform the simulation output into a 4D seismic product (Figure 7.18). Results are used to calculate the variance as defined above (Figure 7.20). In this case strong variations in the fault transmissibility multipliers seem to trigger an anomalous signal with high magnitudes of variance. Yet, when using a similar magnitude scale as in the scenario where the fault capillary threshold pressure is altered, this anomaly seems to be particularly patchy and of a less intense character. In spite of these differences, this observation suggests that strong changes in the transmissibility capacity of the fault might lead to a similar behaviour to that observed in the variation of the capillary trapping of the fault. Indeed, in both cases, the variance has been able to capture an anomalous pattern in the watering of the reservoir, but it cannot be used to differentiate the origin of the anomaly unless additional information about the fault properties is available. Hence, if the fault transmissibility is known to be changing significantly along the fault plane, the higher the probability this phenomenon alone can explain the reservoir watering.

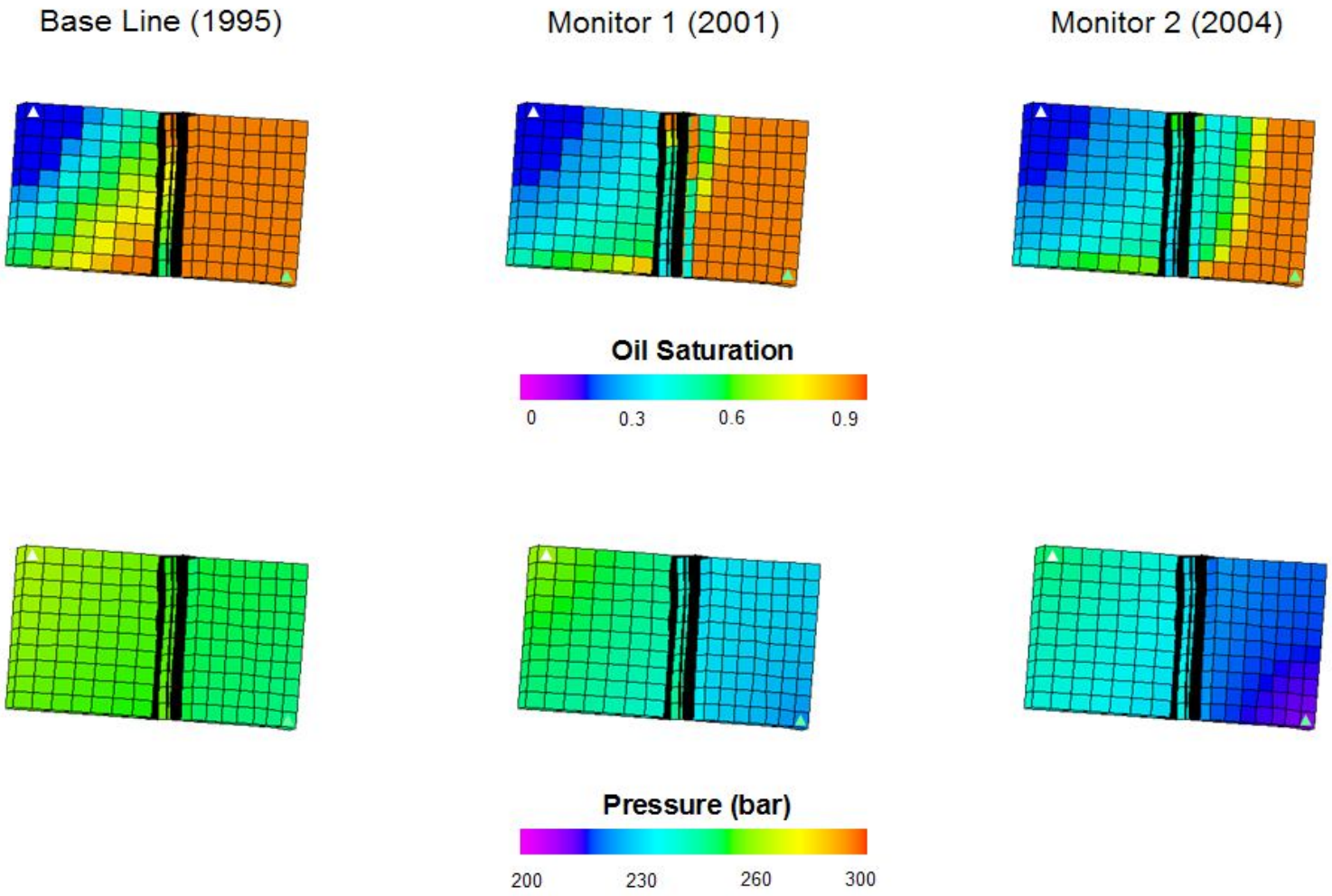

Figure 7.18. *Synthetic model considering strong variations in the fault transmissibility only . Simulated saturation (above) and pressure (bottom). A water injector (white triangle) and a producer (green triangle) are located in each corner of the model.*

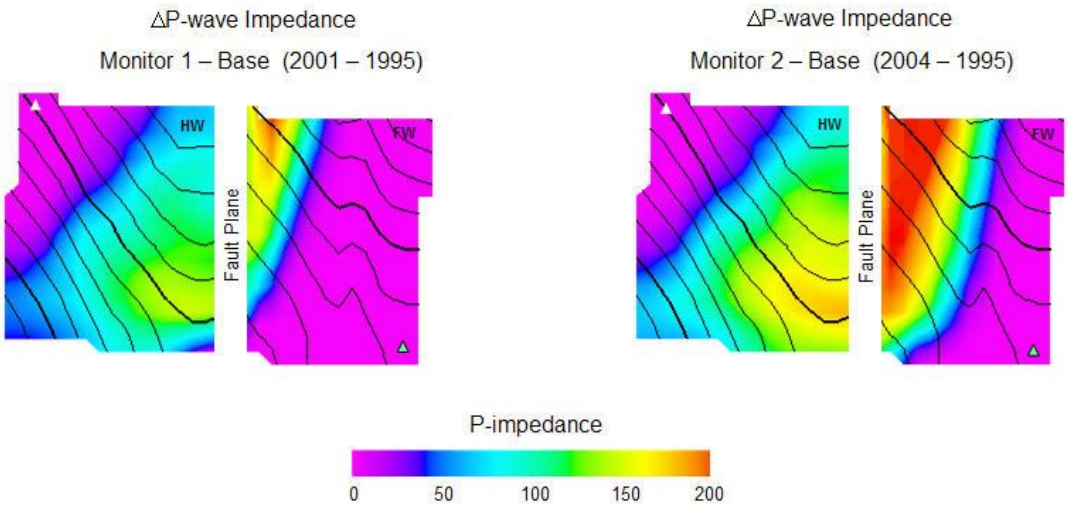

Figure 7.19. *Modelled P-wave impedance change between the base line (1995) and each monitored step (2001 and 2004) given by strong variations of the fault transmissibility multipliers. Hanging-wall and foot-wall are identified in each map as HW and FW. Also the water injector and the oil producer are displayed as white and green triangles respectively.*

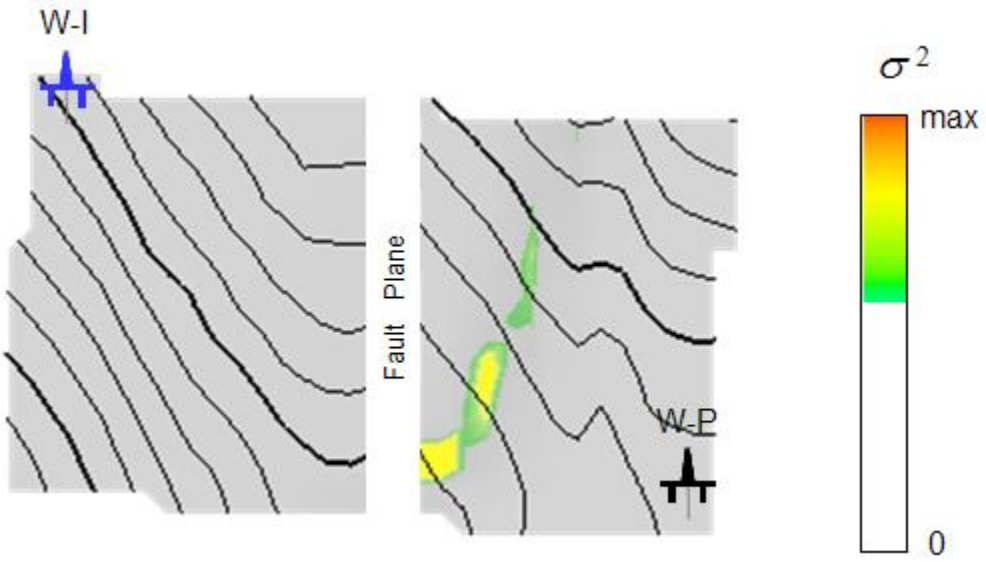

Figure 7.20. *Variance of the 4D signatures given by the differences between each monitor survey and the base line. In this case strong variations in the fault transmissibility multipliers are considered. This triggers an anomaly in the variance magnitudes. Yet when using a similar magnitude scale as in the scenario with variations in the capillary threshold pressure of the fault, the anomaly seems to be patchy and of a less intense character.*

7.5 Application to the Fangst Group, Heidrun field

The Upper Jurassic reservoir in the Heidrun field consists of fairly homogenous shallow marine deposits which are primarily affected by a northeast – southwest trending fault zone. As part of the hydrocarbon recovery plan, an injection strategy has been imposed and waterflooding invades updip from the down side flank of the structure. Even if the petrophysical properties of the reservoir-rock allow too much flow during production (porosities of 35% and permeabilities up to 5000 mD), the fault-rock properties seem to be controlling the fluid flow in this field. In this compartmentalized setting the positioning of new producers and injector wells represent a major challenge as it requires understanding of the drainage pattern, which in some compartments, is of special complexity. This is the case for segments G and H in which 4D seismic data shows more oil potential than that predicted by fluid flow simulations.

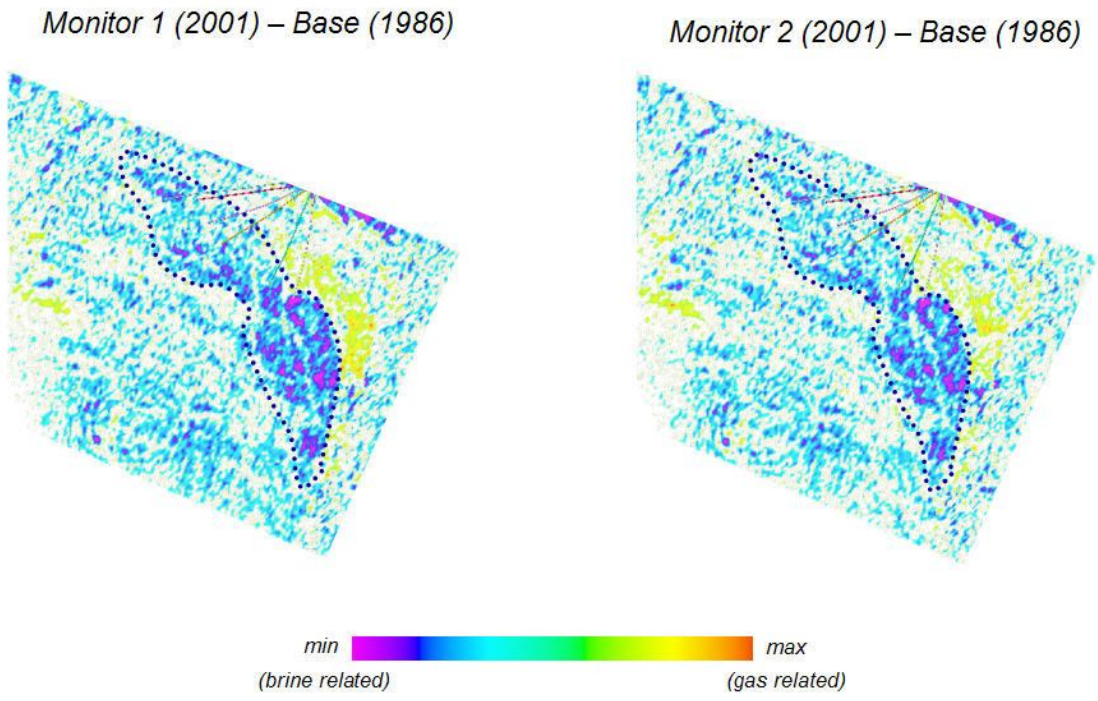

Figure 7.21. *4D signature (at top Fangst Group) given by the RMS amplitude difference between the monitors and the base line seismic surveys. The waterflooded sector given after 6 years of production (surrounded by a dotted line) is sampled twice when performing differences between each monitor and the base line surveys.*

Also, comparisons between the time-lapse seismic surveys seem contradictory particularly in these segments; as the new time-lapse data given by the latest seismic difference (2004-1985), did not support the indications (in terms of the flooded/unflooded areas) from the previous 4D observations (2001-1985) (Furre et al., 2004). A single phase evaluation of the faults affecting the Fangst Group reservoirs has been already addressed in previous chapters. However, a phase-dependent behaviour of the fault-rock might be taking place in this field, thus affecting the drainage. This could raise inconsistencies in the integration of seismic and engineering information if the phenomenon is not taken into account along the interpretation of the 4D signature. Here, detection of phase-dependent phenomenon related to bounding faults might help to explain observed differences in the flooding pattern of the field compartments.

Now, based on the workflow discussed in the previous section, we make use of the available seismic surveys in the Heidrun field (1985, 2001 and 2004) to detect important variations in the flow behaviour. To do so, the base line and the two seismic monitor surveys are employed. *RMS* amplitude differences between the monitor and the base line (2001-1986 and 2004-1986) are extracted in a 16 ms window centred at the top Garn Formation in the Upper Fangst Group (Figure 7.21). Each 4D map reveals the waterflooded sector at the time of the monitor acquisition. However by extracting differences associated with each monitor and the base line, the waterflooded sector when monitor 1 is acquired (after 6 years of production), is sampled twice. These measurements can be then used to extract the variance of the time-lapse signature in this particular sector as shown in equation 6.8. As indicated in Figure 7.22, evaluation of the variance in Top Garn reveals a consistent anomaly with high magnitude which can be differentiated from the background measurement. Association of this result with the flooding map (Figure 7.23) shows that this anomaly is located within some of the waterflooded compartments of the field, particularly in segment G and extending towards segment H. Also, it seems to be linked to the fault segment separating compartments F and G which indeed controls watering of compartments G and H as these are associated upside blocks (hanging-wall) relative to the water injectors located in the downside flank (foot-wall). However, as discussed above in the synthetic examples, to establish the mechanism in which the fault is affecting the waterflooding, additional information is required.

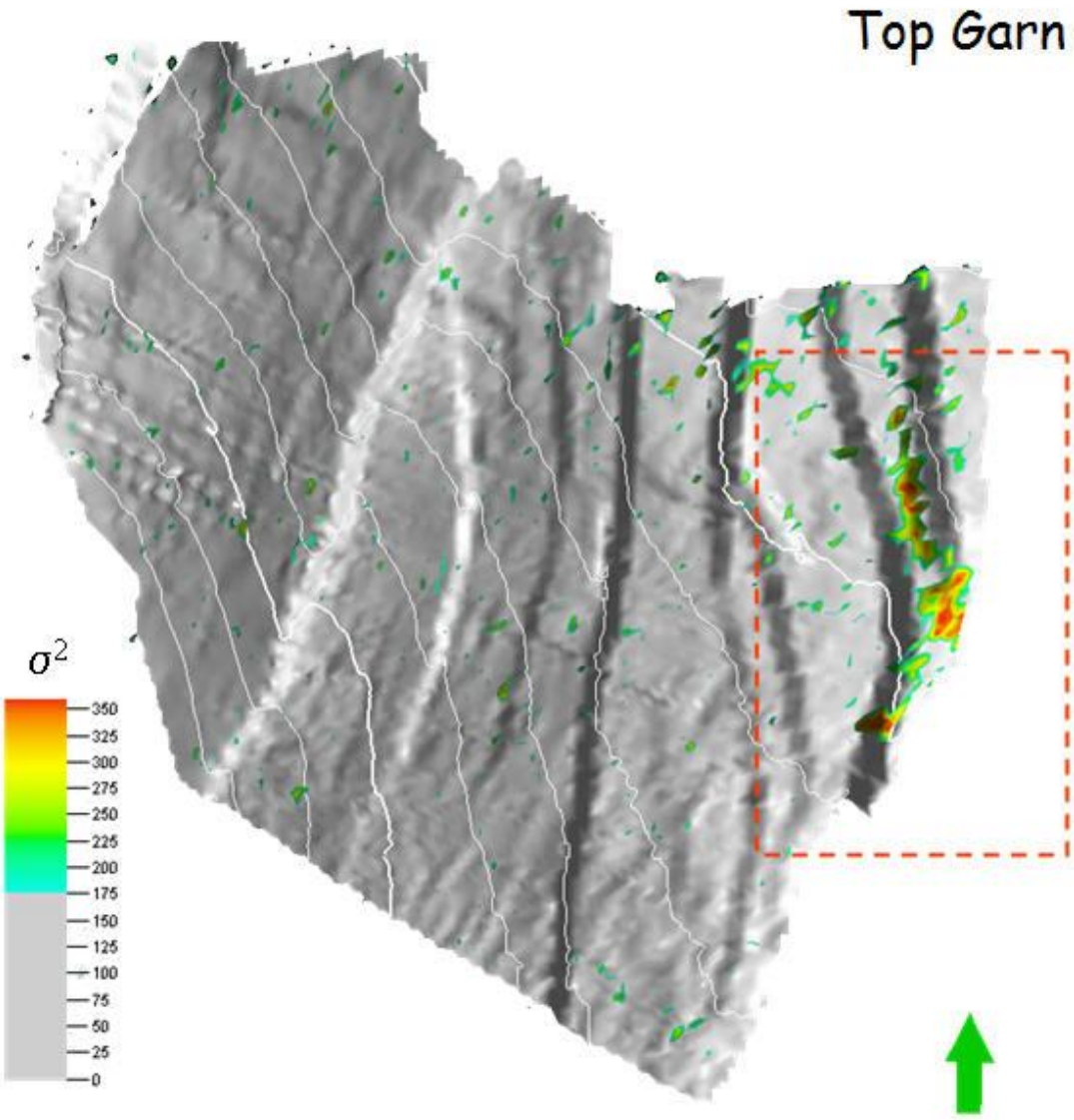

Figure 7.22. *Variance of the time-lapse signature given by the differences between each monitor and the base line surveys. Note (in the red rectangle) that an anomaly is differentiated from the background variance values and it appears in the vicinity of a major fault segment which compartmentalizes the field. Analogous to the model used in the synthetic test, the anomaly suggests a change in the relation between the reservoir capillary pressure and the fault capillary threshold pressure. Here, the fault capillary threshold pressure can be exceeded and oil and water flow rate is strongly dependent on the relative permeability curves of the fault-rock. The phase-dependent effect is strengthened in this area, thus waterflooding behaves differently and the variance of the 4D signature is above the background values.*

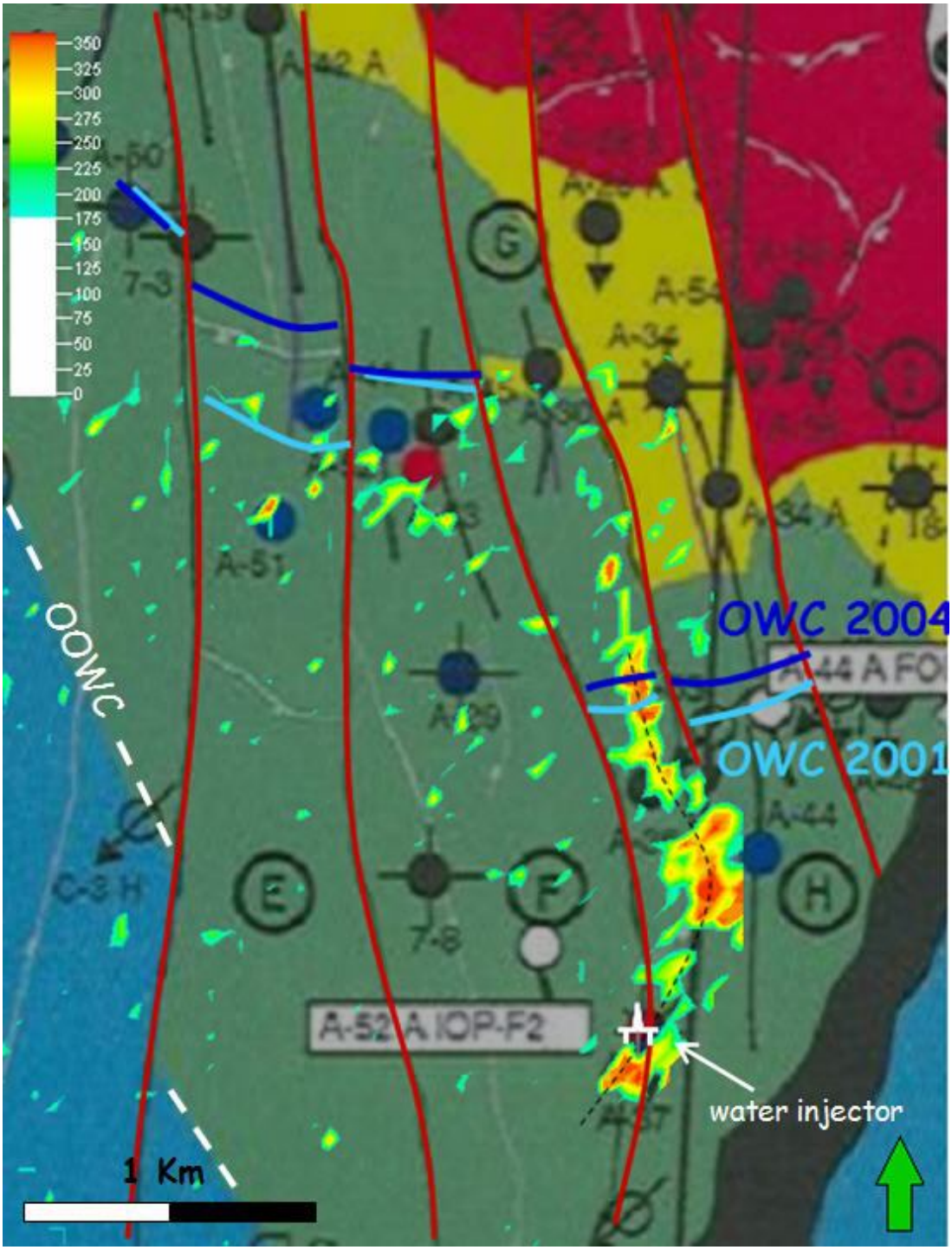

Figure 7.23. *The anomaly in the variance is displayed onto the flooding map. Faults are represented in red. The original oil water contact (OOWC) is shown. Also production oil water contacts (OWC) associated with the acquisition of monitor surveys in 2001 and 2004 are included. Note that the anomaly is located in segment G extending towards segment H. It seems to be related to the fault separating compartments F and G which indeed controls the waterflooding of the area given by the nearby water injectors.*

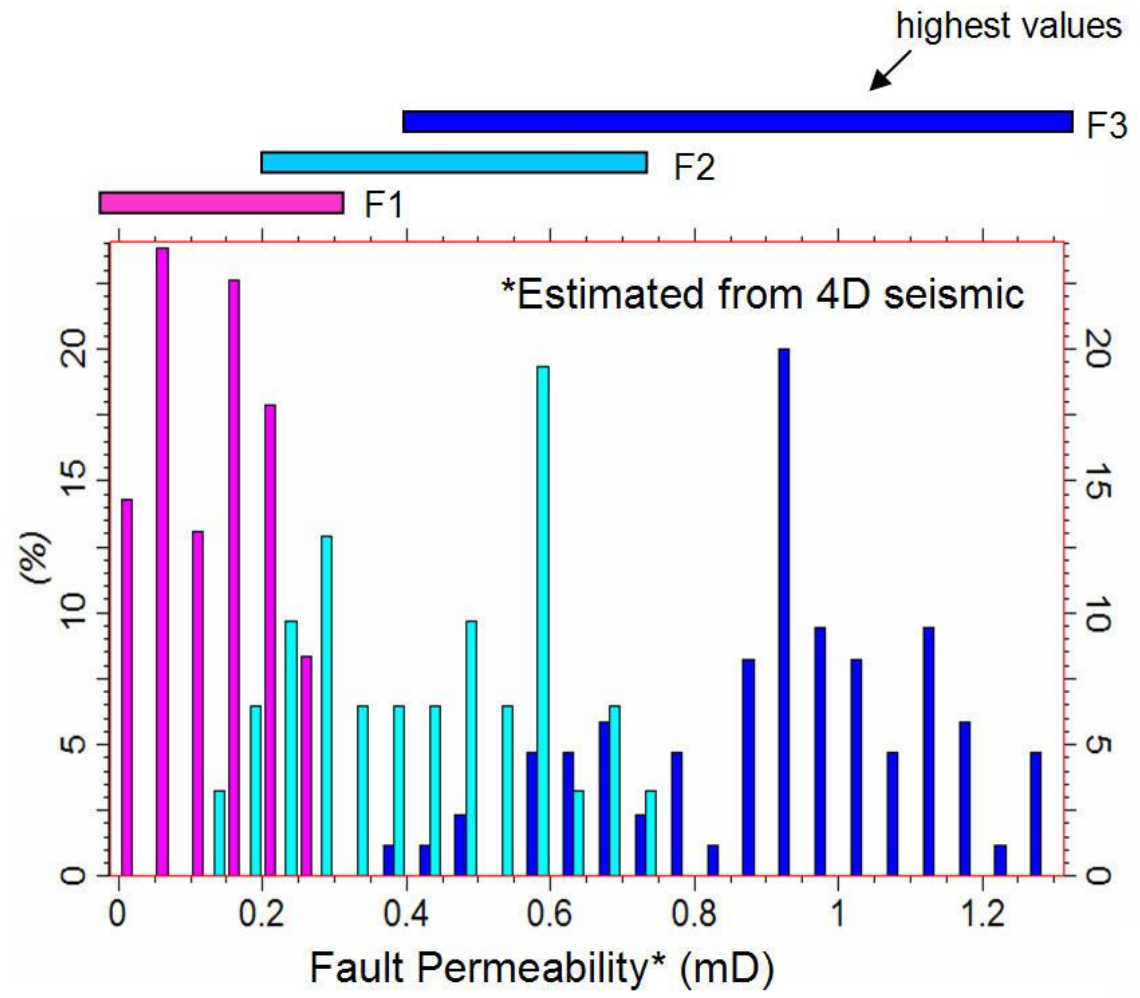

Figure 7.24. *Histogram for the permeability values obtained for the three studied faults in Chapter 5 (estimated from 4D seismic). Permeabilities for the fault separating compartments F and G (F3) are shown in dark blue. This fault shows the highest permeability values when compared to the other faults in the field.*

Here, we calibrate the observations with the results presented in Chapter 5, where fault permeabilities have been estimated for various fault segments in the field. Indeed, as shown in Figure 7.24, the 4D seismic estimation revealed higher permeability values for the fault separating compartments F and G (Fault 3). Yet, no major lateral variations in permeability are evidenced within the same fault segment. This might suggest that the observed anomaly is not likely to be associated with strong changes in the transmissibility. On the other hand, high fault permeabilities help to explain the presence of an enhanced phase effect; as such values imply a lower fault capillary threshold pressure in this fault when compared to others in the field (Figure 7.25). In

this case, the capillary pressure of the reservoir can eventually exceed the capillary threshold pressure of the fault allowing oil transfer between compartments, and this behaviour can contrast with deeper sections of the fault where water is the only permeable phase. In this case, changes in the relation of the reservoir capillary pressure with the fault capillary threshold pressure might perturb the waterflooding, hence affecting the 4D signal and altering its variance triggering the observed anomalies. Also, this phenomenon might also be strengthened in the lower Fangst Group (i.e. Ile Formation) as its measured permeabilities are smaller than the one related with the stratigraphy above (Harris, 1989), thus increasing capillary pressures of the reservoir-rock.

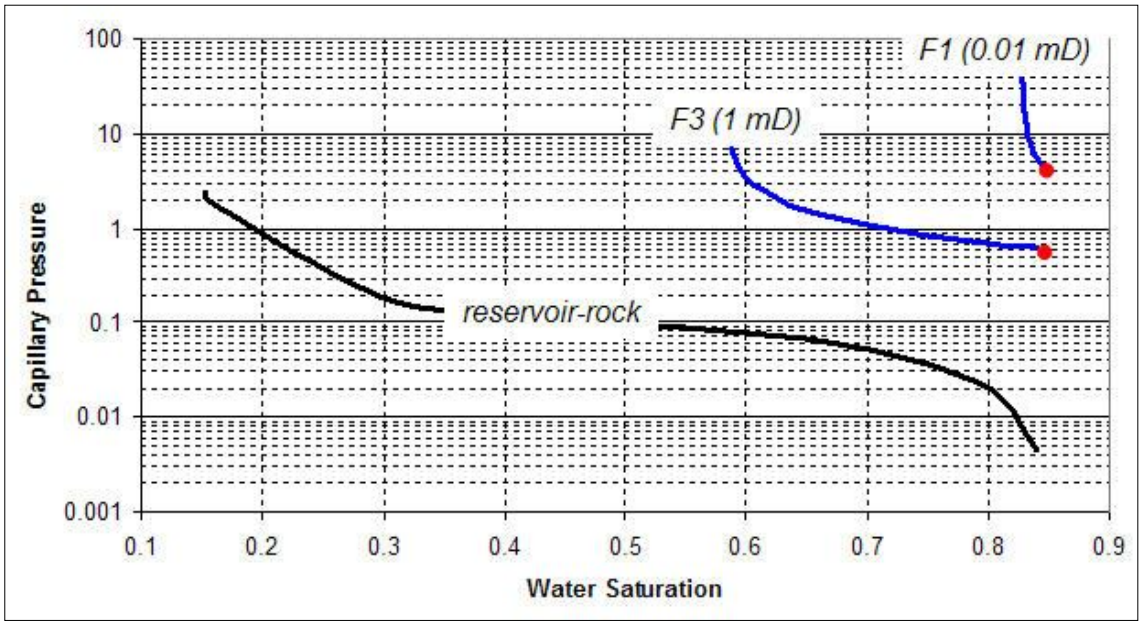

Figure 7.25. *Capillary pressure curves calculated from fault permeability values in the Heidrun field. F1 and F3 represent faults (affecting the Fangst Group) with observed lowest and highest fault permeabilities respectively. Capillary threshold pressure of each fault-rock is indicated with a red circle. Note that an increase in fault permeability introduces a decrease in the capillary threshold pressure of the fault. This is the case for the fault separating compartments F and G (F3) as it shows higher permeabilities compared to other faults. As a consequence, it is more likely to be exceeded by the capillary pressure of the reservoir (shown in black). In this case oil is also a mobile phase with flow dependent on time according to the water saturation which controls the relative permeability curves of the fault-rock.*

Actually, as this fault allows higher oil mobility when compared to others, flushed oil from deeper compartments (i.e. F) can also invade shallower positions in compartments

G and H. Hence, if this phenomenon is not represented in the simulation model, this might trigger major discrepancies in the water saturations estimates given by the simulation model output versus the history data (Manzocchi et al, 2002 and Al-Busafi et al., 2006), as revealed by the uncertainties in the mapping of the flooding segments.

Anomalies in the variance of the 4D signal can be related to strong changes in the fault transmissibility and/or capillary trapping of the fault. In this field case, available data suggests (i.e. estimated fault permeability values) the latter is more likely to be the controlling effect, yet more evidence is needed. Consequently other hypotheses are not discarded. Indeed, along this workflow we have assumed a homogeneous reservoir, where only the variation of the fault properties is responsible for the compartmentalization occurring in the Heidrun field. However, anomalies in the porosity, permeability, net-to-gross relation, sealing capacity of the overburden or geomechanical effects might also impact the local dynamic connectivity, thus in such cases the explanation of observations should be revisited.

In addition, this study emphasizes that by taking into account the relations of the capillary pressure of the reservoir related to the capillary threshold pressure of the faults, the 4D seismic signal can also be explained. This observation is indeed of high importance, particularly when assessing the connectivity of structurally compartmentalized reservoirs as part of the field management activities.

7.6 Additional remarks

Changes in the trapping capacity of faults included in a particular field have been also discussed by Parr and Marsh, 2000. In that case study, the coherency display of the seismic amplitude is evaluated in different seismic vintages, allowing highlighting seismic boundaries which can be used as a measure of the connection between reservoir segments. Here, changes in the seismic boundaries are revealed when comparing two different surveys. The discontinuity detected in 1996 (Figure 7.26a) appears to have healed in 1999 (Figure 7.26b).

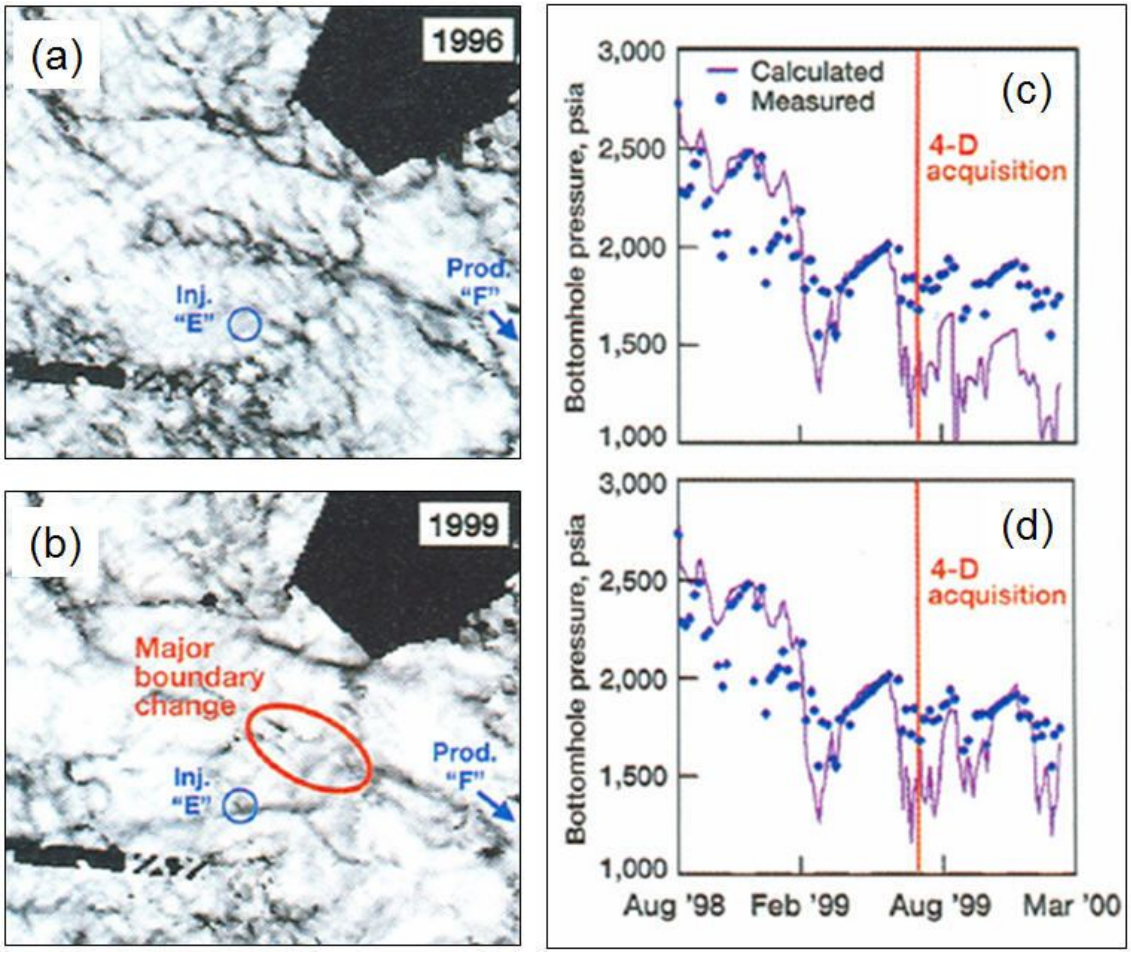

Figure 7.26. *Changes in the coherency of the seismic amplitudes are evidenced when comparing seismic vintages. (a) Initially, Producer F seems unaffected by Injector E as they are located in different compartments according to seismic survey 1996. (b) The 1999 survey suggests the possibility of an alteration of the connectivity (marked in red) as shown by the change in the coherency display. (c) Simulated pressure is difficult to match with production data when reservoir compartments are assumed constantly isolated. (d) On the other hand, good fit can be obtained assuming an enhancement of the connection between the Injector E and Producer F when acquired the 1999 survey. From Parr and Marsh (2000).*

Also in terms of the history matching of the production data, pressure in Producer F is difficult to match in fluid flow simulations if the reservoir compartments are assumed to be constantly isolated as suggested by the 1996 survey (Figure 7.26c). On the other hand, a good fit can be obtained assuming an enhancement of the connection between the Injector E and Producer F when acquired in the 1999 survey (Figure 7.26d). This behaviour could be also analysed by taking into consideration changes in the relation between the capillary pressure of the reservoir and the capillary threshold pressure of the barrier. The presence of an injector well could help to decrease the hydrocarbon saturation (non-wetting phase), hence the capillary pressure of that segment. During this

process, the wetting phase (injected) reaches higher mobility and the connectivity of this phase is enhanced. Consequently boundaries revealed in previous vintages might well disappear in time. Here, the good data quality available in this field case has allowed such an observation. Hence, in this case unlike Heidrun, fine scale changes can be detected and these can be meticulously mapped in space and time.

7.7 Summary

Evaluation of the 4D seismic signature and engineering information in the Heidrun field reveals zones where waterflooding changes are uncertain (Furre et al., 2004). This is the case for segment G and H in which comparisons between multiple 4D measurements are contradictory and fluid flow simulation fails to represent history. In this chapter we make use of the current understanding of the two phase fault-rock properties to postulate a workflow in which the variance of repeated 4D seismic measurements is used to detect anomalous dynamic changes which can be related to alterations in the relations between the capillary pressure of the reservoir and the capillary threshold pressure of the fault-rock. Indeed, tests performed on a controlled synthetic model in which waterflooding is represented; show that the phase–dependent behaviour of the fault might introduce anomalies in the measured statistic. Yet strong variations in the transmissibility of the fault might lead to similar results. Then, if used as a tool to detect perturbations in the connectivity of compartmentalized reservoirs, the variance of the 4D signal should be analysed considering additional information about the reservoir faults. Application to the Heidrun field reveals an anomaly located in compartments with intricate production behaviour. Previously estimated permeabilities for the fault constraining such reservoir segments, suggest that variations in the capillary trapping are more likely to be controlling the waterflooding pattern. The study presented in this chapter, also highlights that the understanding of the variations in relation to the capillary pressure of the reservoir and the fault rocks, might help in the interpretation of the 4D seismic signature in compartmentalized reservoir settings such as in the field examples presented by Parr and Marsh (2000).

Chapter 8

Conclusions and recommendations for future research

In this thesis a new methodology has been proposed to assist in the quantitative evaluation of the permeability associated with reservoir faults. To do this, we make use of the statistics of the 4D seismic to propagate the well centric estimates into regions restricted by data availability. This approach has been successfully applied to the Heidrun field, and has allowed the updating of fault seal behaviour originally held fixed in the reservoir simulation model. Finally new insights into the phase-dependent character of the fault based on 4D seismic have been presented. In this chapter, the results are discussed in a wider context and recommendations for future improvements and applications of this work are suggested.

8.1 Introduction

Historically, we have relied on single disciplinary studies to assess specific elements of the sub-surface. This is the case with the assessment of fault seal capacity, which has been mostly addressed with geologically driven methodologies. Conventional analyses are based predominantly on well information, making spatial evaluation across the field difficult. Nonetheless, results obtained by available well-centric approaches (such as the shale gouge ratio) have been implemented in reservoir simulations, helping to match the observed production. Also, current history matching workflows have been employed allowing uncertainties associated with the fault seal predictions to be assessed. However, given existing challenges, particularly in maximising current hydrocarbon reserves, we are experiencing a demand for the integration of new technologies. This also requires a combination of multiple disciplines by sharing their knowledge in the evaluation of the earth model. Today, monitoring tools such as the 4D seismic method, are serving as platform which allows us to link geosciences and engineering specialities. In the study of dynamic signals (from production data) to tackle reservoir compartmentalization, 4D seismic is now frequently used to detect barriers in an efficient manner, at a qualitative or semi-quantitative stage. Yet, there is room for development in the quantitative side of this evaluation that honours the information content associated with one or more disciplines. In this regard, this thesis has grown the understanding achieved in geological studies into a 4D seismic framework with the objective of creating a more informed determination of the reservoir faults (Figure 8.1).

To do the above, we have taken advantage of the statistics of the 4D signature derived from a 4D attribute map. In particular, we have evaluated two new measurements defined by the amplitude contrast between compartments and the spatial variability of the signature. A polynomial expression has been used to link these empirical measurements to the fault permeability. The coefficients of such a polynomial function are calibrated at the wells in a sector with known geological characteristics. This permits a propagation of the prediction into fault segments with poorer well control. Uncertainties in the 4D seismic prediction have also been considered in a Bayesian framework, allowing the identification of certainty windows for the estimates. These results have been used to update the flow simulation model by adjusting the transmissibility factor between compartments, and have been shown to decrease the mismatch between the simulated forecast and the historical production data. Moreover,

the uncertainty in the 4D seismic predictions has been considered when implementing an automatic history match workflow leading to further improvements. This overall workflow is summarized in Figure 8.2.

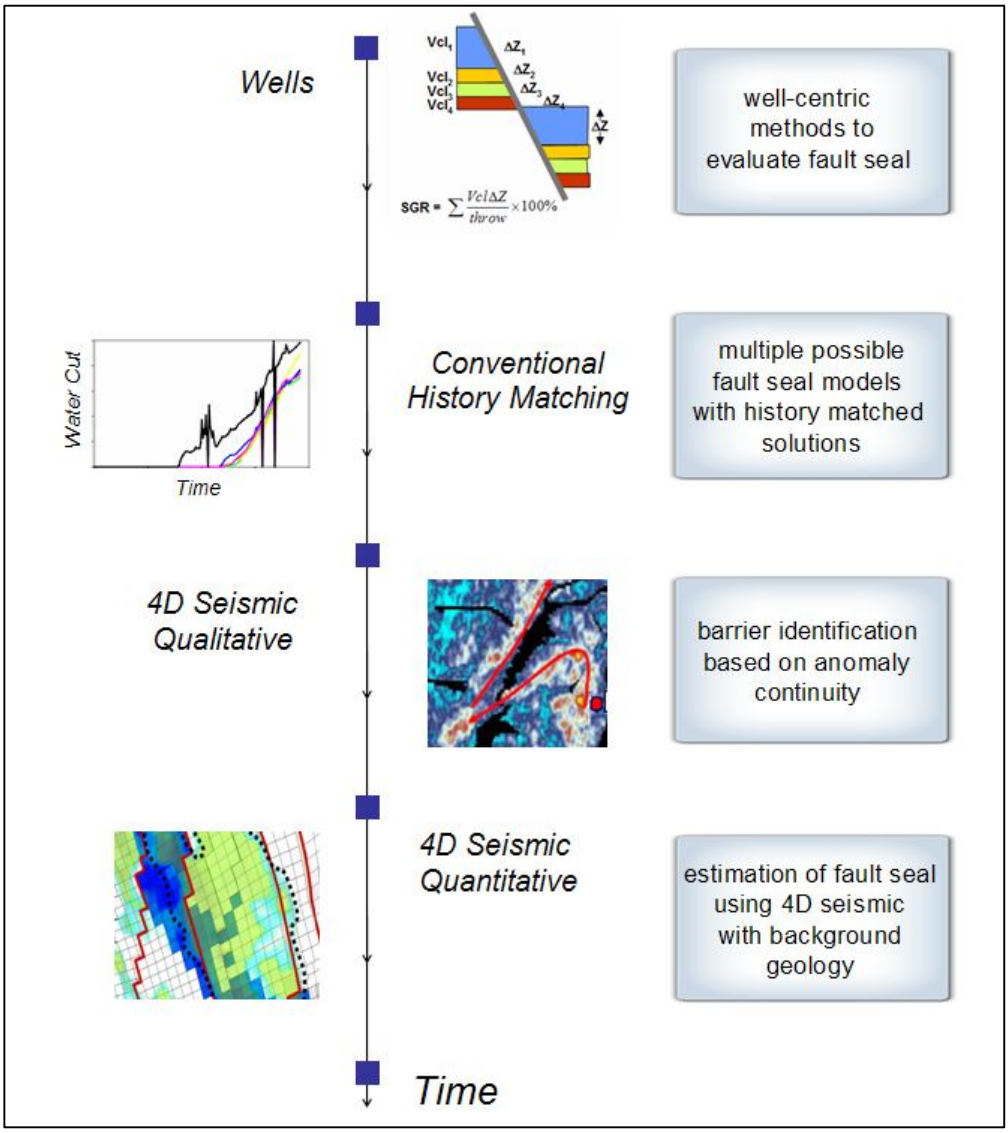

Figure 8.1. *Technology trend in the evaluation of the fault seal capacity.*

The proposed methodology has been tested initially on seismic data derived from a synthetic reservoir model and a production scenario considering a waterflooding strategy. Results obtained in the application of the technique are encouraging enough to investigate its applicability on field data. This observation has motivated the use of such workflow in compartmentalized reservoir settings such as that evidenced in the Heidrun

field. At Heidrun, previous studies had attempted to address the sealing capacity of the faults, however; the availability of well data has limited the evaluation on a field wide basis. This has impacted negatively in the adjustment of faults in the reservoir simulation model, making difficult to match observed and predicted production. In this case, the application of the new approach has proven useful, as it has allowed the characterization of major faults in this field. Our results have been also compared with previous core observations made in fault-rocks studies (Knai and Knipe, 1998), revealing a similarity with the 4D seismic predictions. Results have been used to update of the reservoir model helping to improve the history match.

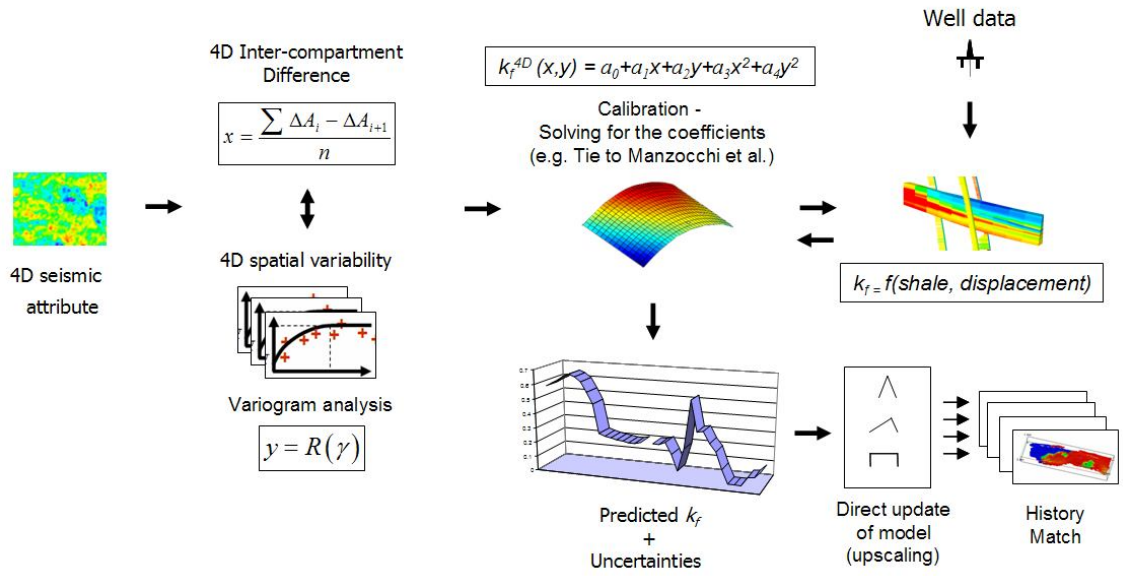

Figure 8.2. *General workflow presented in this thesis. Two statistical measures of the 4D seismic attribute are calibrated with geological fault seal estimates allowing the propagation of the prediction in areas with poor data availability and the updating of the reservoir simulation model.*

Additionally, new insights into the implications of the dynamic fault behaviour in the time-lapse seismic response are presented. Here it is postulated that variations in the relation of the reservoir capillary pressure related to the threshold capillary pressure of the fault-rock might introduce changes in the variance of the 4D signature that contrast with the background values of this statistic. This is investigated at first by evaluating the variance in a synthetic model that considers a production scenario in a compartmentalized reservoir in which a phase dependent phenomenon is introduced into

the fault rock. Also discussed are strong variations in the transmissibility of the fault that might lead to a similar behaviour.

8.2 Conclusions of the thesis

8.2.1 The nature of the time-lapse seismic signal in structurally compartmentalized reservoirs

The time-lapse seismic signature hides the result of a complex interaction between the static properties of the reservoir and the specific perturbation imposed in the field by means of the hydrocarbon recovery process. This phenomenon can be particularly evidenced in the Heidrun field through a relatively clear 4D seismic signal (mainly associated with water flooding) in which its spatial continuity is altered across compartments, revealing the influence of faults on the water flow. This observation is explained by the strong control on the water transfer introduced by the transmissibility capacity of the faults. Certainly, their sealing properties limit the spatial connection of fluid changes, leading to a compartmentalized character of the 4D signature.

In a wider context, we have learnt that favourable reservoir-rock properties might react quickly to the well activity however, in a structural framework, faults are especially important for the 4D seismic signature. These elements of the reservoir seem to constrain pressure and its gradient which affects flow, thus saturation, impacting in the lateral extension, shape and strength of the dynamic perturbation in the compartments, which in turn form the spatial components of the seismic change, whether it is dominated by pressure or saturation variations (Figure 8.3). Qualitatitive interpretation techniques evaluate such observations by mapping the signal and pinpointing isolated anomalies from which barriers can be inferred. However we have based our approach on the measurement of the spatial arrangements of the 4D seismic signature in a regional perspective to derive a quantitative understanding of the reservoir compartmentalization. We believe that in faulted environments, the evaluation of the regionalized features mentioned above, are key to the understanding the compartmentalization, and they represent the reason for the effort in our investigation.

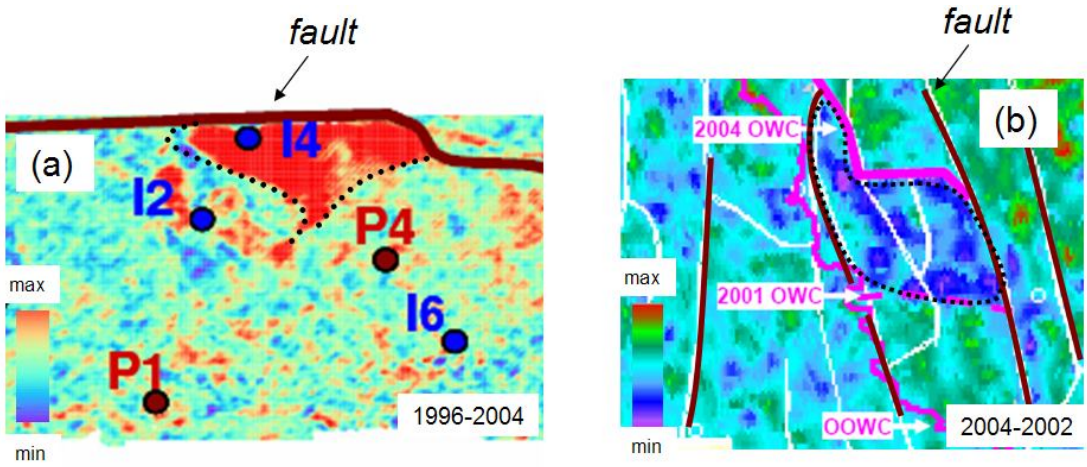

Figure 8.3. *Time-lapse seismic signatures in two different field examples. (a) A pressure-dominated 4D seismic signature in the Schiehallion field (from Edris, 2009). (b) A saturation-dominated 4D seismic signature in the Heidrun field (from Furre et al., 2006). In both cases, the anomaly (identified with the dotted line) seems to be spatially constrained by the structural elements of the field.*

8.2.2 Statistical measurements as a tool for the evaluation of the 4D seismic signature

Throughout this research, we recognize difficulties in connecting the time-lapse seismic response with the sealing capacity of the fault rock directly. With no apparent physical laws describing the link between the acoustic properties of the fault-rock and their implication on dynamic reservoir parameters, the assessment of compartmentalization with 4D seismic represents a difficult task if a deterministic approach is taken. This is because the seismic method might only be used to resolve properties of the host rock and its discontinuities, but it cannot be used to evaluate details in the fault rock. Furthermore, non-repeatable noise around faults, as well as in the compartments, is an important issue that might compromise the quality of the observed 4D seismic data. Thus, evaluations relying on seismic magnitudes alone can bring major uncertainties.

On the other hand, statistics of the 4D seismic could help to highlight valuable information related to dynamic changes. To do so, we have analysed the 4D seismic information in two different ways: primarily as a collection of information that we have

explored with univariate statistical methods and also, as a regionalized variable for which we describe its spatial correlation in one dimension using geostatistical tools. In particular, we have also showed that these measurements are useful to describe disruptions of the dynamic changes. Their strengths relies in that the univariate methods help to describe a collection of information about the 4D variable in a similar way as when investigating a variable sampled in a particular geological layer (e.g. minimum, maximum, or as in our investigation the average and the variance), whereas the variogram capacity allows to measure spatial patterns in geographically distributed data as in mapping analyses, both types of measurement helping in the characterisation of the 4D observations. By linking these measurements with the properties of fault-rocks, we have approximated the complex interaction occurring in reality. Also, this is useful in the presence of noise which can be seen as a disturbance that influences the quality of the dataset, adding samples which are not representative of the studied phenomenon. In this case, the use of statistics might help to alleviate local interference that noise might cause in the regional understanding, basing the analysis on the larger population rather than on a single sample. Consequently, we believe that in order to achieve more from the 4D seismic, statistical approaches can be indeed useful. In our knowledge, this is the first time that the univariate and regionalized character of the 4D seismic are used together to study structurally compartmentalized reservoirs.

8.2.3 Estimation of the fault permeability using 4D seismic

In the application of the proposed workflow used to estimate fault permeability using the 4D seismic signal, we have assumed a fairly homogeneous reservoir structured in several compartments in which the petrophysical properties are favourable (i.e. high permeability, porosity and net-to-gross values) and no major geomechanical effects (e.g. compaction) are taking place due to production. In this case, fluid flow can be strongly affected by the sealing properties of the fault, hence constraining dynamic changes occurring in each compartment. Under these conditions, the Jurassic reservoirs included in the Heidrun field (i.e. Garn and Ile Formations), seem to represent an ideal case scenario for the application of the technique. Indeed, in this example, homogeneous shallow marine sediments possess excellent porosities and permeabilities and the major barriers to fluid flow are given by the fault sealing properties which appear to drive the observed 4D seismic response (Kahar et al., 2006).

An evaluation of the 4D seismic attributes is needed prior to the application of the workflow. The quality of the 4D seismic attribute is associated with its ability to represent the dynamic changes occurring in the reservoir. In this thesis, this has been verified in several ways including a loose association of the 4D seismic anomalies with the well activity (producers or injectors), petro-elastic modelling allowing evaluation of the seismic via stress sensitivity and fluid replacement physics of the rock, and through transformation of the 4D seismic response into pressures and saturation changes which are compared to predictions given in fluid-flow simulations. In the Heidrun field most of the mapped-based attributes deliver a similar response, which in turn seems consistent in particular with fluid movement. Thus, differences of *RMS* (Root Mean Square) seismic amplitudes extracted from the full offset stacks in the Upper Fangst Group, have been proven successful in the identification of the water flooding in previous works and in this thesis, and can therefore be employed as the signature of the dynamic changes occurring in this field. However similar results have been obtained when extracting attributes from partial (near, mid and far) stacks, particularly the near and far offsets. Other computations have been carried out using the three principal attributes given by the instantaneous envelope, phase and frequency, mostly delivering similar results. In all cases, when calculating the 4D seismic change, the difference between attribute maps of each vintage is preferred to the map attribute extracted from the difference cube. The latter introduces a more noisy character which is probably related to irregularities in the co-processing and cross-equalization finally affecting the repeatability. This makes difficult the detection of a coherent 4D signature that can be associated with field production.

In terms of the equation used to relate the 4D seismic products to the fault permeability, a polynomial of second order has proven useful in the application to the Heidrun field. This can be explained by the fairly homogenous and favourable petrophysical properties of the Jurassic reservoir, as these conditions are likely to generate gentle variations in the material incorporated in the gouge of the fault, particularly when fault throws are similar along the fault plane. Yet, this situation could be different if various depositional environments are present in a particular reservoir. Here, variations in the petrophysical properties of the reservoir might be expected, therefore inducing more alterations in the fault-rock properties. In this case, a polynomial of higher order or a different function

might be suggested to allow the representation of the higher variability in the sealing capacity of the fault.

In this thesis, we have used Gamma Ray logs from available wells to estimate the shale gouge ratio. This geological-based predictor has proven to be a consistent measure to characterize the fault seal (Yielding et al., 1997), and it can be transformed into fault permeability which is a useful parameter in the estimation of fault transmissibility multipliers (Manzocchi, et al. 1999). For these reasons, we have decided to employ it as calibration tool. However, we also recognize that these measures can be uncertain (Yielding et al., 2002). As a consequence the more accurate they are taken in a well-controlled sector, the better the quality of the calibration dataset.

Finally, the measurement of the uncertainty associated with the fault permeability prediction from the 4D seismic plays an important role within the workflow. Its quantification can be implemented as a tool which can help to highlight ambiguities in the sealing behaviour of the fault.

8.2.4 Implications of the dynamic fault behaviour in the 4D seismic signature

New insights into the implications of the two-phase fault properties on the 4D seismic are discussed in this thesis. Tests using synthetic models that consider a waterflooding strategy have shown that an adjustment of the relation between the reservoir capillary pressure and the capillary threshold pressure of the fault-rock can alter the variance of the time-lapse seismic signature. Yet, such observations have also been made when strong changes in the single-phase transmissibility of the fault are considered. Indeed, in the phase dependent fault seal case, water is highly permeable given the capillary threshold pressure of the fault. However, further up in reservoir this threshold might be exceeded leading to a reduction in water flow that contrasts with the behaviour occurring further below (Figure 8.4a). Likewise, a fault with high transmissibilities in areas affected by waterflooding helps to improve the water transfer, which in turn would contrast with the effects of a sudden decrease of the fault transmissibility, particularly if this occurs away from the water source (Figure 8.4b). Therefore, in both cases, the waterflooding is locally enhanced in the vicinity of a particular segment of the fault. Here, the variance of the 4D seismic signal captures anomalous high magnitudes, as the

water saturation change might vary quickly when compared to the surroundings of the fault segment detrimental to water flow.

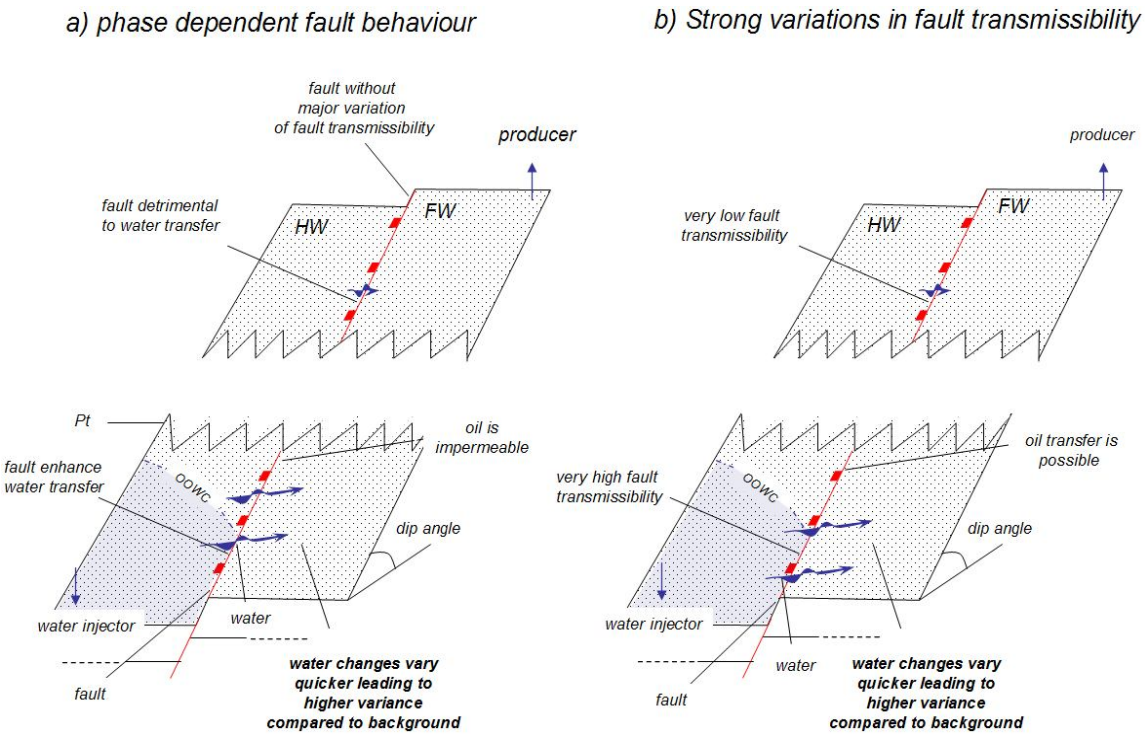

Figure 8.4. *Comparison between a phase dependent fault behaviour and a case where fault transmissibility vary significantly along the fault plane. In the diagrams, a water injector is located in the hanging-wall compartment (HW) and the watering of the foot-wall compartment (FW) is controlled by the fault properties. The original water oil contact is also displayed (OOWC) and the waterflooding strategy continues until the both reservoir compartments are flooded. In the phase dependent fault case (left) water transfer is enhanced below the capillary threshold pressure of the fault (Pt) whereas high fault transmissibility close to the water injection also leads to a similar behaviour (right). Consequently, in both cases, water saturation varies quicker in the deeper flank of the reservoir, leading to a higher variance of the 4D signature compared to the background measures.*

Due to this physical behaviour, the variance lacks uniqueness when trying to identify the cause of anomalies. However, such drawback could be addressed by incorporating additional information of the fault. If so, this statistic could be used to identify a fault seal control dependent on individual fluid phases. Hence, the smaller the variation of the fault transmissibilities along the fault plane, the higher the probability that a phase-

dependent phenomenon is responsible for the existence of anomalies in the variance of the 4D seismic signature.

Additional understanding of flow behaviour through faults might be useful in highly compartmentalized field cases, particularly when aiming to reduce differences between the fluid flow simulator predictions and the historical production data. In reality, the single phase approximation of the fault-rock might be not enough to fully represent the observed behaviour. Even if based on the correct predictions of the fault-rock permeability and thickness, fault multipliers which only take into account one phase, might be too open to the flow of oil and too restrictive to the flow of water (Manzocchi et al., 2002). This seems to be the situation for the Jurassic reservoirs in the Heidrun field in which some compartments show an anomalous water encroachment when compared to the rest of the field. Here, we have found difficult to fully explain the compartment watering with the single-phase approximation offered by the fault transmissibility multipliers. In this real example, observations and forecasts are particularly hard to conceal, thus increasing the complications in the mapping of the fluid contacts.

In this thesis, the variance of the 4D seismic signature is used in conjunction with the fault permeability values to suggest that the trapping mechanism in a fault constraining the eastern compartments of Heidrun field might be dependent on the individual fluid phases, therefore helping to explain fluid uncertainties observed in that sector. Yet, we recognize that more data might be required to gain more insight on the issue. Also, other hypotheses are not discarded. Indeed our application of the variance as tool of detection assumes a homogeneous reservoir, where mainly fault properties constrain fluid flow, like evidenced in the Heidrun field. On the other hand, if anomalies in the porosity, permeability, net-to-gross relation, sealing capacity of the overburden/underburden and/or geomechanical effects are occurring, this would also impact on the dynamic connectivity, and the explanation of those observations should be revisited.

.

8.3 Recommendations for future work

At the time this study has been carried out, an important effort has been addressed in the development of the techniques presented. In this regard, further research is recommended to enhance the approach taken here and expand their application by considering other real study cases. Here, some other topics of investigation are suggested.

8.3.1 Implementation of the geological model

Here the integration of the static geological model might be useful when evaluating the fault permeability estimation obtained with the time-lapse seismic approach. Indeed, information on the geological model includes a fine definition of the reservoir-rock which can feed the material incorporated in the gouge of the fault. Therefore, as the fault seal can change with fine variations of the lithology, we might be able to explore local sensitivities in the 4D seismic predictions.

8.3.2 Combined structural and stratigraphic compartmentalization

Until now, the workflow is based on the assumption that in a deformed and fairly homogenous reservoir, resistance to flow is mainly controlled by the fault-rocks. However, as more heterogeneities are included in the reservoir, this can introduce a different component of compartmentalization which is mostly stratigraphic rather than structural (Bentley, 2008). In this case, application of the proposed workflow to estimate fault permeability using the 4D seismic, might lead to unsatisfactory results as the signature is not only a product of the flow interaction with the faults. Hence, the challenge lies in the separation of the structural from the stratigraphic constraint from the 4D signature in a manner that allows characterizing each component of the compartmentalization so they can be individually represented in the simulation models.

8.3.3 Vertical fault heterogeneity

Until now the technique employed to estimate fault permeability using the 4D seismic, is based on the use of seismic attribute maps. This allows the study of lateral variation of the fault properties particularly when this dominates the fluid flow as in thick compartmentalized reservoirs such as the Heidrun field. However, cases where a notable vertical variation of the reservoir properties occurs (e.g. in net-to-gross) can introduce important vertical changes in the material incorporated in the fault-rock. This implies the need to extend the estimation of the fault properties in three dimensions. One way to tackle this can be by means of the extraction of multiple 4D seismic attribute maps following the reservoir layering. To achieve this, several issues should be addressed first. In this regard, the ability to separate a coherent seismic signature for each flow unit should be evaluated. Here, the seismic resolution plays an important role. Also, inversion of P-wave impedance changes might be useful to enhance the extraction of the dynamic changes consistent with the reservoir layering (Figure 8.5). Some of these issues are currently dealt by other research projects in the ETLP (Edinburgh Time Lapse Project) group at Heriot-Watt University (He, 2009).

8.3.4 Limits and uncertainties

In the estimation of fault permeability it is important to understand its limits. From the geological point of view, compartments with very small sizes might find the extraction of the 4D seismic measurements difficult. Moreover, the presence of isolated shale units can bring in a local stratigraphic component into the compartmentalization that needs to be separated from the fault seal evaluation. In terms of the 4D seismic, this can as well introduce some interference in the reservoir signal, complicating the assessment. In addition, 4D seismic noise (e.g. related to lack of 4D repeatability) might impact importantly. This is a major subject of study and it is currently tackled by the ETLP group (Huang, 2009). Furthermore, when using well data information to constrain 4D seismic, it is important to establish an accurate velocity model, otherwise spatial misplacement of information becomes an important risk in the interpretations. Also, in the detection of the dynamic fault behaviour using the 4D seismic response, the number of seismic vintages might limit the robustness of the variance estimation.

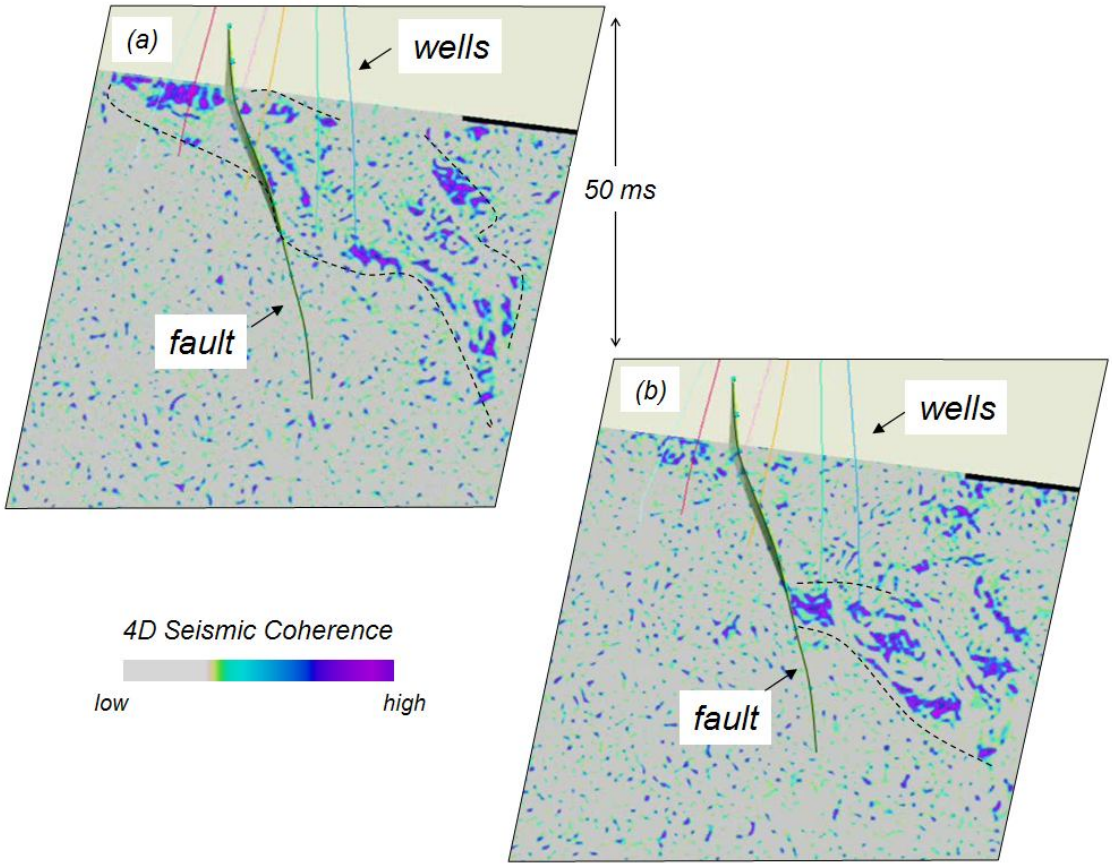

Figure 8.5. *Coherence of the P-wave impedance changes in the Fangst Group. The attribute is extracted in two different horizontal sections separated by 50 milliseconds. (a) Above, the apparent continuity of the 4D seismic signal seems to indicate a leaking fault. Below (b) the opposite case is evidenced. Here the 4D P-wave impedance data has allowed detecting variations of the fault behaviour in the vertical domain.*

8.3.5 Integration with other information

In this thesis, the 4D seismic measurements have proven useful, allowing the evaluation of the inter-compartment connectivity in a real field case. However, we recognize that other tools, particularly those which measure dynamic signals are highly valuable and they might be integrated in the assessment when possible. This is the case for the well test information in which its contribution has been tackled by other part of the research in the ETLP group (Shams et al., 2007). Also unconventional techniques such as, time-lapse geochemistry signals might help to add some insights in the compartmentalization

analysis. These are based on fluid samples collected in a pre-production stage and over the years of field development. Integration of this information with the 4D seismic appears to be useful in a compositionally graded field in the Gulf of Mexico. Here, a combined time-lapse approach illustrates the complex drainage pattern which justifies differences observed in the compositional characteristics of the fluids present in the reservoir compartments (Chuparova et al., 2008). However in spite of these efforts more analytical approaches are needed. To do so, further research might need to aim at the challenges in the integration capacity of different data types, especially to achieve quantitative multi-disciplinary workflows.

8.3.6 Final remarks

As part of the future lying ahead of us, the use 4D seismic, as means of evaluation of reservoir compartmentalization, is becoming a strong trend within company portfolios. Indeed, this tool allows detection of dynamic barriers as part of qualitative analysis. However, in a time for which there is a need to improve earth models to enhance the life of the field, workflows for the quantification of the sub-surface are certainly important. Incorporation of our technique can assist in setting up meaningful prior information related to the fault seal capacity that can be recognized as acceptable by the 4D seismic and the geological background. This can reduce uncertainties associated with the non-uniqueness included in multiple history matched solutions. Additional field applications can bring more insights, providing stimulus for new improvements in the use of multi-disciplinary data. Also, we believe that three-dimensional assessment of the compartmentalization will play an increasing role. Here, integration of 4D seismic with other information might be uneasy due to different investigation scales. Also, in doing so, we would need to tackle challenges associated with the software requirements and computing capabilities as each data type has different spatial arrangements. Nevertheless, rewards associated can be tremendously significant, and this should motivate further developments.

Appendix A

Variogram Analysis

A.1 Introduction

In the study of the time-lapse seismic signature observed in 4D seismic attribute maps; this thesis employs the variogram in order to evaluate the spatial variability or continuity of the extracted 4D seismic signal. This statistical tool is of particular importance when the data samples to be analyzed depend on location, and as a consequence the variable is defined as regionalized. This is a key concept within geostatistics which has been developed by Matheron (1965) to treat problems that arise when using univariate or bivariate statistics to estimate the variation of a variable in space. Here, the variogram can help to express the rate of change of the regionalized variable along a specific location. Indeed, its continuity depends on the size, shape, orientation and spatial arrangements of the observed samples. In this thesis, we suggest the use of variograms to extract additional information about the spatial character of the dynamic changes occurring during field development. In particular, when such changes are controlled by the fault trapping capacity, variograms can be used to characterize the effect the barriers can have on the 4D seismic signature. Fundamentals of the variogram analysis are described in this appendix.

A.2 Variogram analysis

A.2.1 Calculation

The variogram describes quantitatively the variation of referenced observations as a function of the separation distance. When this is calculated from the sampled data, the result is referred as the experimental or sample variogram and its classical definition is given by,

$$\gamma_h = \frac{1}{2N_h}\sum_{i=1}^{N_h}\left(z_i - z_{i+h}\right)^2 \qquad \text{(A.1)}$$

where z_i is the observed value at location i, z_{i+h} is the observed value at another point within a distance of h and N_h is the number of pairs within the lag interval h (Figure A.1).

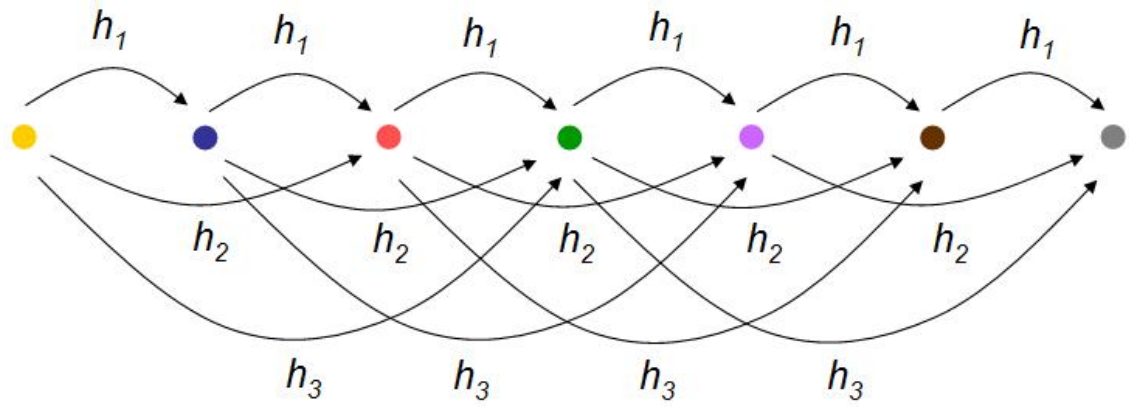

Figure A.1. *Classification of the separation distances in a unidirectional case with equally spaced observations. The lag interval is h_1 and h_2, h_3, etc., are multiples of the lag interval (from Trauth, 2005).*

Once the experimental variogram is determined results can be plotted as a function of the lag interval.

A.2.2 Interpretation

To interpret the variogram three major features are examined. These are known as the Sill, the Range and the Nugget effect. These are briefly described below:

- *The Sill*: this measurement indicates the variogram value in which a plateau is reached. This normally occurs as the separation distance increases. When this is the case, the studied phenomenon is known to be stationary. This indicates that the mean and variance of the samples are not dependent on location. If the variogram increases infinitely, the phenomenon is referred as non stationary.
- *The Range*: this measurement indicates the distance the variogram takes to reach the sill. It is also referred to as the correlation length.
- *The Nugget*: When sampling errors or short scale variability is present, data might be dissimilar at short distances. Here the variogram is above zero at distance equal to zero, creating a discontinuity or vertical jump at the origin of the variogram known as nugget effect.

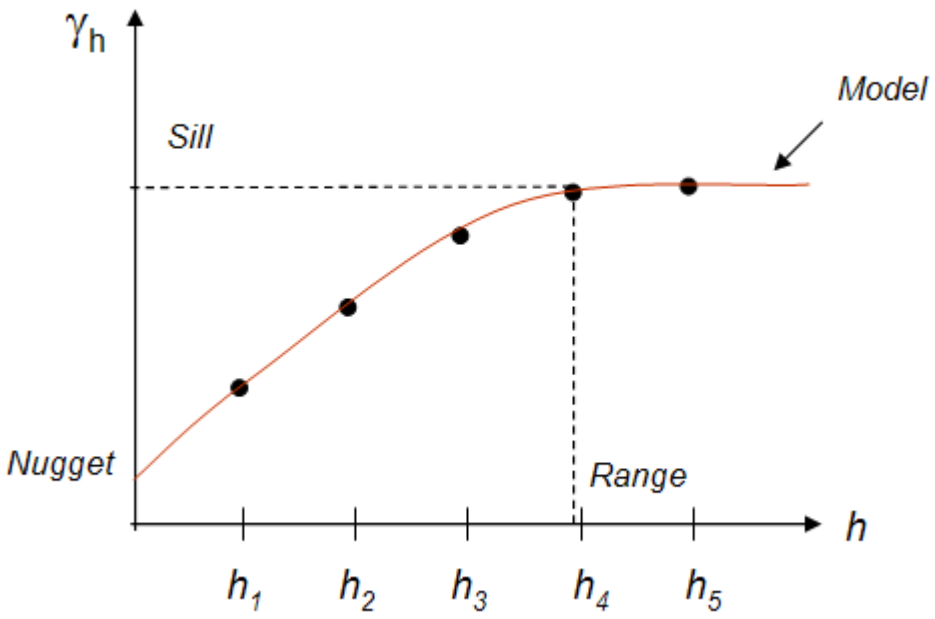

Figure A.2. *Plot of the experimental variogram against distance h. In order to estimate major features a model (displayed in red) is used.*

To estimate these features, an interpretation process is undertaken in which a model is fitted to the experimental variogram (Figure A.2). Fundamentals on variogram modeling are discussed in the next section.

A.2.3 Variogram modelling

To represent the experimental variogram, this is approximated using a variogram model. The objective of such process is to capture the general trend observed, allowing the estimation of the features described above. Models commonly used are spherical, exponential and gaussian.

A.2.3.1 Spherical model

This model is defined by,

$$\gamma_h = \begin{cases} s\left(\frac{3}{2}\frac{h}{a} - \frac{1}{2}\frac{h^3}{a^3}\right) & if \quad h \leq a \\ s \quad if \quad h > a \end{cases} \tag{A.2}$$

where s is the sill, a is the range and h is the lag interval. Figure A.3 show the graphic representation of this variogram model. This model shows a linear behavior at shorter distances with a sharp transition to a flat sill. Also, it is in common use.

A.2.3.2 Exponential model

The exponential model is defined by,

$$\gamma_h = s\left(1 - exp\left(-3 \cdot \frac{h}{a}\right)\right) \tag{A.3}$$

where s is the sill, a the range and h is the lag interval.

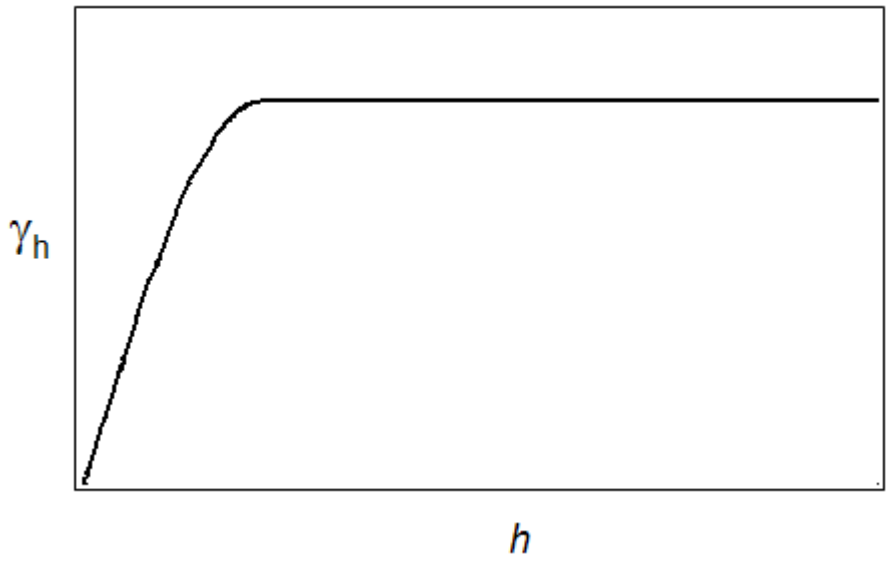

Figure A.3. *Spherical model.*

This variogram model is displayed in Figure A.4. This model also shows a linear behaviour, however much steeper than in the spherical model. Also, it is characterized by an asymptotic approach to the sill at longer distances.

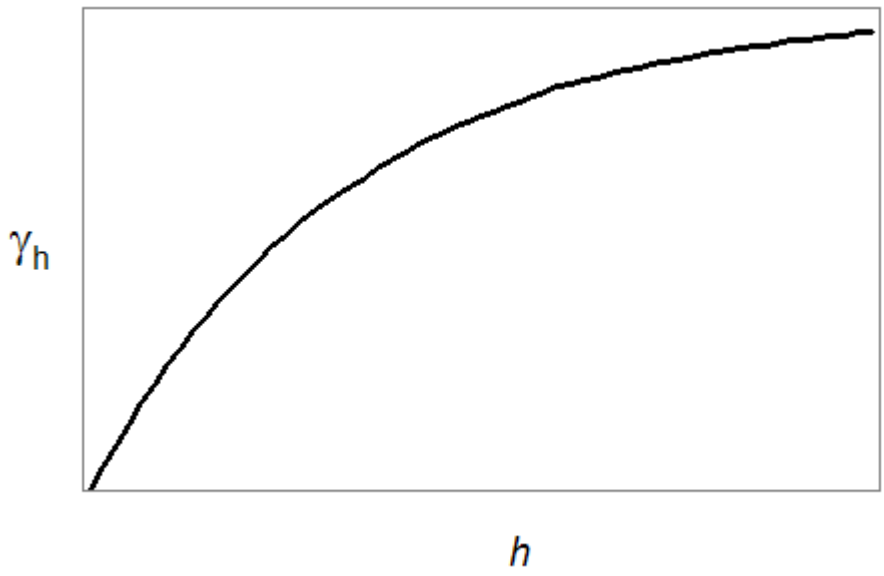

Figure A.3. *Exponential model.*

A.2.3.3 Gaussian model

The Gaussian model is defined by,

$$\gamma_h = s\left(1 - exp\left(-\frac{h^2}{a^2}\right)\right) \tag{A.4}$$

where s is the sill, a the range and h is the lag interval. However at distances close to zero,

$$1 - exp\left(-\frac{h^2}{a^2}\right) \approx \frac{h^2}{a^2} \tag{A.5}$$

as a consequence this variogram shows a parabolic behaviour near the origin. This model is often used when the observed phenomena shows a high degree of continuity at short distances. Also a transition to an exponential behaviour appears at longer distances (Figure A.4).

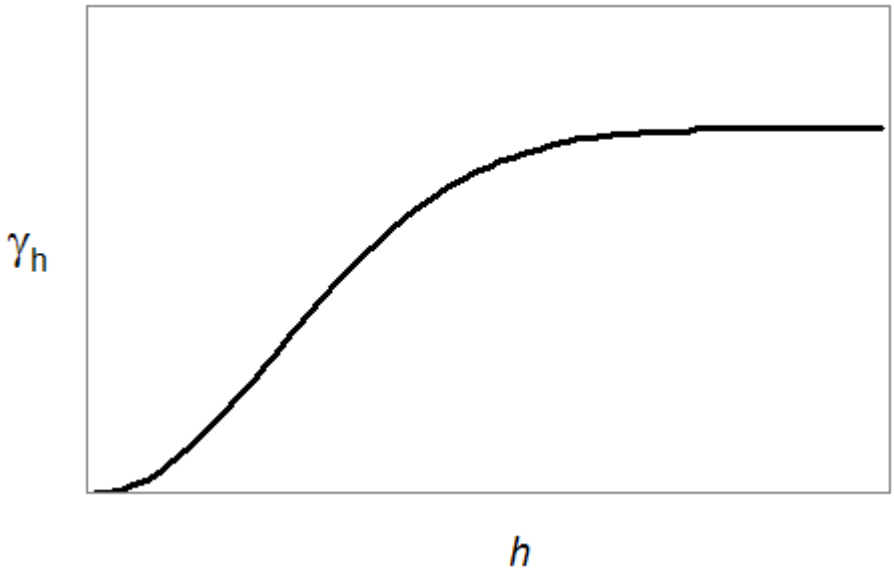

Figure A.4. *Gaussian model.*

A.3 Example

Figure A.5 shows equally spaced measurements (each 100 feet) for two different well locations. According to the magnitudes of the observed properties, it has been possible to separate the reservoir from the non reservoir rock. However, by taking into account univariate statistics it is difficult to characterize the sample variability (Figure A.6). Here experimental variograms are calculated for each particular case (Figure A.7).

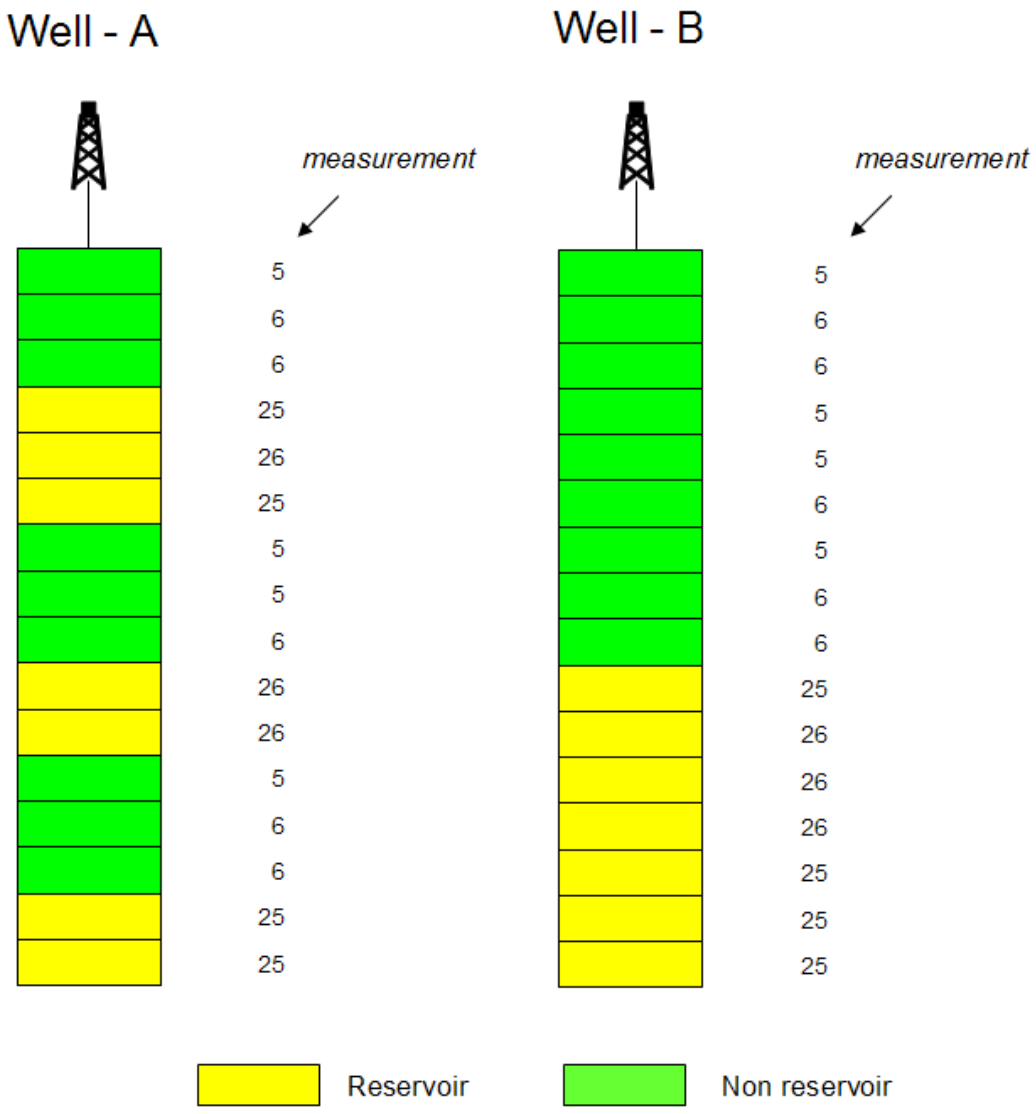

Figure A.5. *Measurements in two different well locations. Magnitudes shown in the property measured have allowed the separation of the reservoir (yellow) from the non reservoir rock (green).*

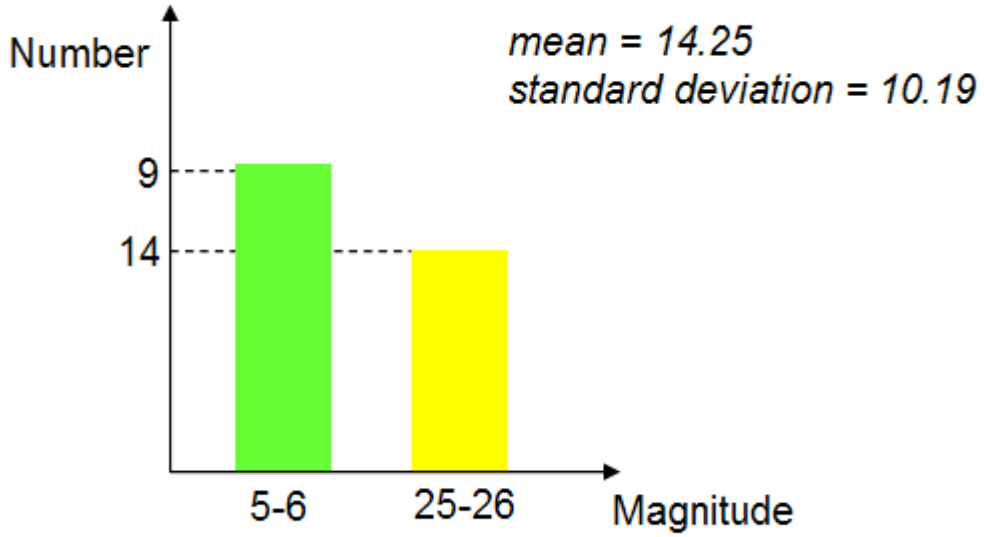

Figure A.6. *By taking into account univariate statistics it is difficult to differentiate the behaviour shown in both wells. The histogram is identical for both datasets as wells as their mean and standard deviation.*

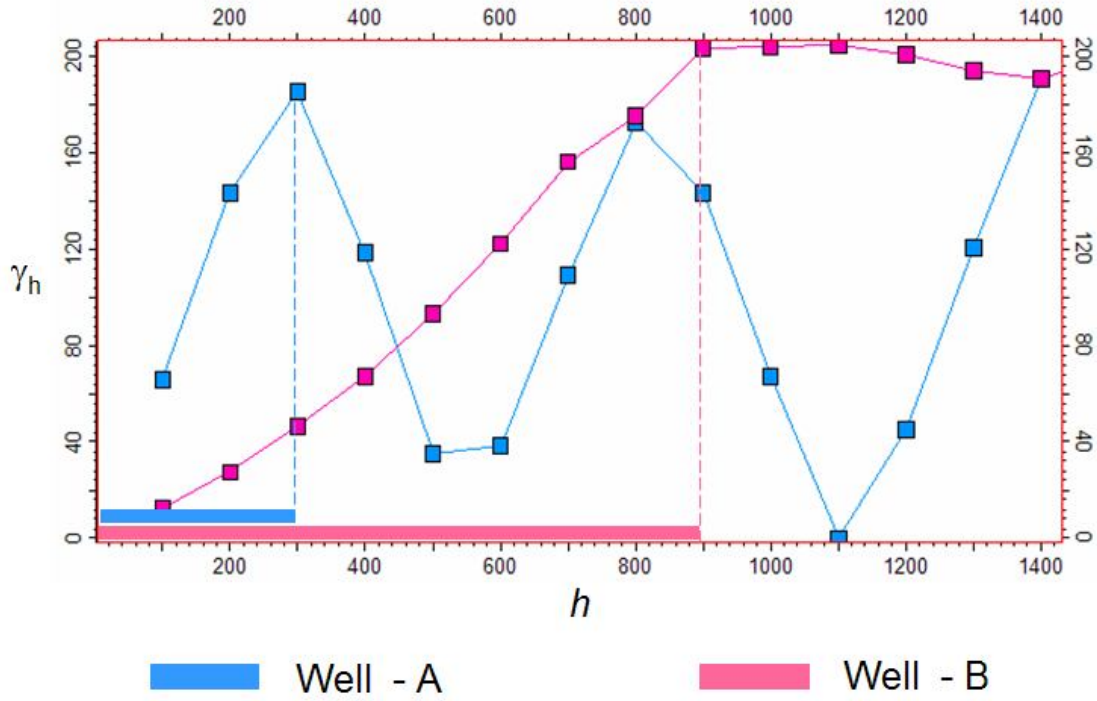

Figure A.7. *Experimental variograms calculated for each well. Note that Well – A achieves a lower correlation length (displayed in blue) than in well B (displayed in pink).*

Once the experimental variograms have been calculated for each well, a variogram model is selected to estimate the variogram features. Here a Gaussian model has been selected.

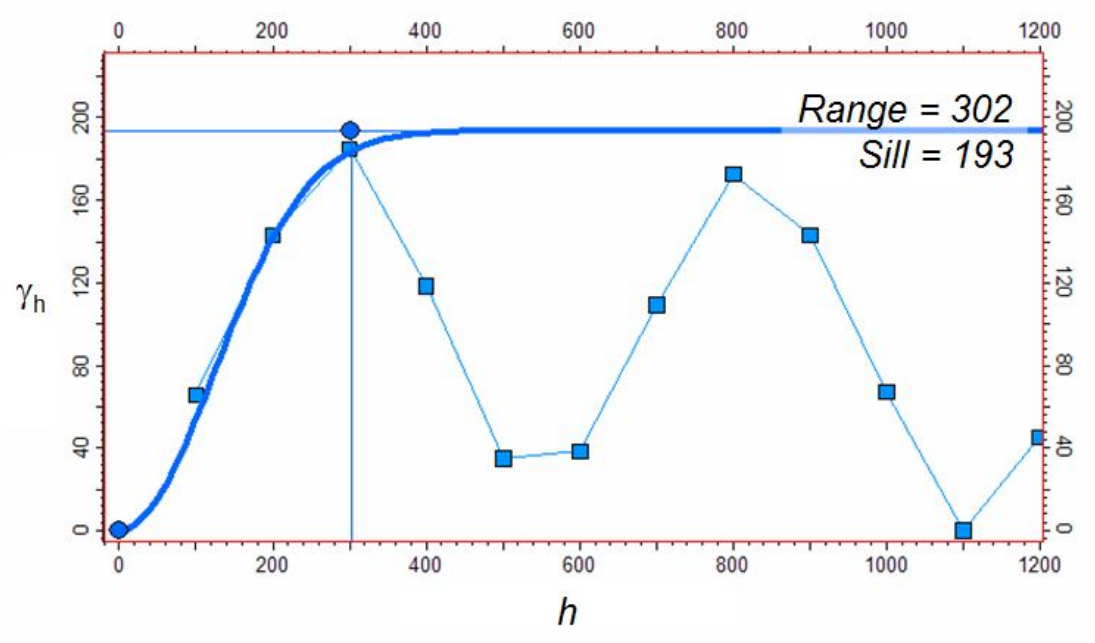

Figure A.8. *Variogram modelling for the Well – A.*

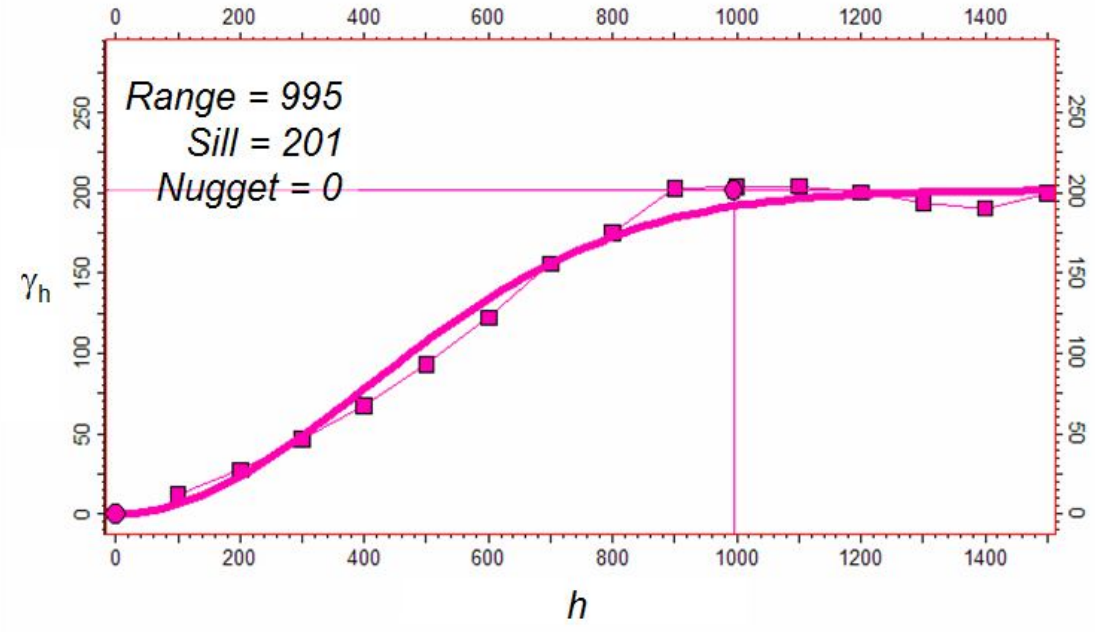

Figure A.9. *Variogram modelling for the Well – B.*

By estimating the variogram features in the modelling process it has been possible to quantify the correlation lengths (ranges) for each well (Figure A.8 and A.9). In this example, a lower range value is evidenced in Well – A (Range = 302) when compared with the Well – B (Range = 995). Hence, by characterizing the spatial variability it is possible to detect differences in the distribution of measurements identified in each well, an observation which is difficult to achieve considering univariate statistics. Similarly, this dissertation has made use of this geostatistical tool to capture continuity of the 4D seismic signatures. Our aim in this procedure is to detect differences in the 4D seismic map grid, particularly when this is analysed as a collection of 1D data sets sampling in different locations with preferred direction (like wells), observed dynamic changes in the reservoir. This is because the variogram analysis represents a useful tool when evaluating the variation of a property as a function of the space.

References

Al-Busafi, B., Fisher, Q. J. and Harris, S. D. (2005). The importance of incorporating the multi-phase flow properties of fault rocks into production simulation models. Marine and Petroleum Geology 22, 365 – 374.

Al-Hinai, S.M.S., Fisher, Q. J., Grattoni, C.A. (2008). Impact of Fault Rocks on Reservoir Characterisation - Multi-phase Flow Properties for Production Simulation Models. 70th European Association of Geoscientists and Engineers Conference and Exhibition, Rome, Italy. Expanded abstract.

Al-Maskeri, Y., and MacBeth, C. (2004). Quantitative assessment of fault connectivity across a fault using 4D seismic, 66th European Association of Geoscientists and Engineers Conference and Exhibition, Paris, France. Expanded abstract.

Al-Maskeri, Y. and MacBeth, C., (2005). Location and evaluation of flow barriers using 4D seismic, 75th Society of Exploration Geophysicists Annual Conference, Houston. Expanded abstract.

Al-Maskeri, Y. (2005). Quantitative 4D Seismic for the Analysis of Reservoir Heterogeneity and Connectivity. Ph.D. Thesis. Institute of Petroleum Engineering. Heriot-Watt University.

Anderson, R., Boulanger, A., He, W., Xu, L., Flemings, P., Burkhart, T., and Hoover, A. (1997). 4D time-lapse seismic monitoring in the South Timbalier 295 Field, Gulf of Mexico. In Society of Exploration Geophysicists International Exposition and Annual Meeting, Dallas, Texas.

Antonellini, M., and A. Aydin. (1994). Effect of faulting on fluid flow on porous sandstones: petrophysical properties. American Association of Petroleum Geologists Bulletin, 78, 355–377.

Allan U.S. (1988). Model for Hydrocarbon Migration and Entrapment within Faulted Structures. American Association of Petroleum Geologists Bulletin 73, 803-811.

Aster, R. C., Borchers, B. and Thurber, C. H. (2005). Parameter estimation and inverse problems. International Geophysics Series 90. Elsevier.

Avseth, P., T. Mukerji and G. Mavko (2005). Quantitative Seismic Interpretation. Applying rock physics tools to reduce interpretation risk. Cambridge University Press.

Baquero, M., Acosta, J., Kassabji, E., Zamora, J., Sousa, J.C., Rodríguez, J., Grobas., J., Melo, L. and Schneider, F. (2009). Polyphaase development of the Falcon Basin in northwestern Venezuela: implications for oil generation. From: James, K. H., Lorente, M. A. and Pindell, J. L. (eds) The Origin and Evolution of the Caribbean Plate. Geological Society, London, Special Publications, 328, 587–612.

Barkved, O., Buer, K., Halleland, K. B., Kjelstadli, R., Kleppan, T. and Kristiansen, T. (2003). 4D Seismic Response of Primary Production and Waste Injection at the Valhall Field, 65th Meeting of the European Association of Geoscientist and Engineers.

Batzle, M. and Wang, Z. (1992). Seismic properties of pore fluids, Geophysics, 57, 396-1408.

Bayes, T. (1763). An essay towards solving a problem in the Doctrine of Chances. By the late Rev. Mr. Bayes, F.R.S. communicated by Mr. Price, in a letter to John Canton, A.M.F.R.S.. Philosophical Transactions, 53, 370–418.

Benguigui A. and MacBeth C. (2009). Updating the Simulation Model using 4D-derived fault transmissibility multipliers: An Application to the Heidrun Field. 71th Meeting of the European Association of Geoscientist and Engineers. Expanded Abstracts.

Benguigui A. and MacBeth C. (2008). Quantitative Evaluation of Reservoir Fault Communication using 4D Seismic: An Application to the Heidrun Field. 70th Meeting of the European Association of Geoscientist and Engineers. Expanded Abstracts.

Bentley, M. R., and Barry, J. J. (1991). Representation of fault sealing in a reservoir simulation: Cormorant Block IV, UK North Sea. Society of Petroleum Engineers reprint no. 22667, 119–126.

Bentley, M. (2008). Reservoir compartments: beyond fault seal. International Conference on reservoir compartmentalization. The Geological Society. London. Abstract.

Berg, R. R., (1975). Capillary pressure in stratigraphic traps. American Association of Petroleum Geologists Bulletin, 59, 939–956.

Bouvier, J. D., C. H. Kaars-Sijpesteijn, D. F. Kluesner, C. C. Onyejekwe, and Van der Pal, R. C. (1989). Three-dimensional seismic interpretation and fault sealing investigations, Nun River field, Nigeria. American Association of Petroleum Geologists Bulletin, 73, 1397–1414.

Bretan P., Yielding G. and Jones H. (2003). Using Calibrated Shale Gouge Ratio to Estimate Hydrocarbon Column Heights. American Association of Petroleum Geologists Bulletin 87, 397-413.

Brevik, I (1997) The effect of pore pressure and brine saturation on seismic properties in the Heidrun Fangst reservoir Unit, F&U-LoU 97S241041.

Brown A. (2003). Capillary Effects on Fault-Fill Sealing. American Association of Petroleum Geologists Bulletin 87, 381-395.

Caers, J. (2005). Petrolem Geostatistics. Society of Petroleum Engineers.

Calvert, R. (2005). Insights and methods for 4D reservoir monitoring and characterization. EAGE/SEG Distinguished instructor short course, No. 8.

Cerveny, K., Davies, R., Dudley, G., Fox, R., Kaufman, P., Knipe, R. and Kantz, B. (2005). Reducing Uncertainty with Fault-Seal Analysis. Oilfield Review, 38-51.

Childs, C., Walsh, J.J and Watterson, J. (1997). Complexity in fault zones and implications for fault seal prediction. In Møller-Pedersen, P. and Koestler, A.G. (eds.) Hydrocarbon Seals: Importance for Exploration and Production. Special publication of the Norwegina Petroleum Society, 7, 1-72.

Chopra, S. and Marfurt, K. J. (2007). Seismic attributes for Prospect Identification and reservoir characterization. Editorial of the Society of Exploration Geophysicists.

Chuparova, E., Kratochvil, T., Westrich, C., Guillory, J., Bikun, J., Kleingeld, A. and Kornacki, A. (2008). Integration of time-lapse fluid geochemistry, well logging and seismic to monitor reservoir connectivity. International Conference on reservoir compartmentalization. The Geological Society. London. Abstract.

Corbett, P. (2009). Petroleum Geoengineering: Integration of static and dynamic models. Distinguished Instructor Short Course. Society of Exploration Geophysicists.

Davis, J. (1986). Statistics and Data Analysis in Geology. John Wiley and Sons, Toronto, Canada.

Dragsten K. (1994). Drainage strategy for the Heidrun Field. Statoil Report.

Dubrule, O. (2003). Geostatistics for seismic data integration in earth models. Distinguished Instructor Short Course. Society of Exploration Geophysicists.

Edris, N. (2009). Identification of an appropriate data assimilation approach in seismic history matching and its effect on prediction uncertainty. PhD thesis. Institute of Petroleum Egineering. Heriot-Watt University.

Eiken, O., Aronsen, H., Furre, A. K., Klefstad, L., Nordby, L. H., Osdal, B. and Skaar, M. (2003). Seismic Monitoring of the Heidrun, Norne and Midgard Fields Using Steerable Streamers. 65th Conference of the European Association of Geoscientists and Engineers.

El Ouair, Y., Buland, A., Osdal, B. and Furre, A.-K. (2005) Improving drainage interpretation using a new Bayesian time-lapse inversion. 67th Conference of the European Association of Geoscientists and Engineers.

Fisher Q.J. and Knipe R.J. (1998). Fault Sealing Processes in Siliciclastic Sediments. In Jones G., Fisher Q.J. and Knipe R.J. (eds.). Faulting, Fault Sealing and Fluid Flow in Hydrocarbon Reservoirs. Geological Society Special Publication 147. 117-134.

Floricich, M., MacBeth, C., and Staples, R. (2005). An engineering-driven approach for separating pressure and saturation using 4D seismic: Application to a Jurassic reservoir in the UK North Sea. In SEG International Exposition and Annual Meeting, Houston, Texas.

Floricich, M., MacBeth, C., Stammeijer, J., Staples, R., Evans, A. and Dijksman, N. (2006) A new technique for pressure-saturation separation from time-lapse seismic: Schiehallion case survey, Conference of the European Association of Geoscientists and Engineers. Expanded abstracts.

Floricich, M. (2006). An engineering-consistent approach for pressure and saturation estimation from time-lapse seismic data. PhD thesis. Institute of Petroleum Egineering. Heriot-Watt University.

Foxford, K. A., Walsh, J. J., Watterson, J., Garden, I.R., Guscott, S. C., and Burley S. D. (1998). Structure and content of the Moab fault zone, Utah, USA and its implications for fault seal prediction. In Jones, G., Fisher, Q. J., and Knipe R.J., (eds.). Faulting, Fault Sealing and Fluid Flow in Hydrocarbon Reservoirs. Geological Society Special Publication, 147, 87 – 103.

Fowles, J., and S.D. Burley, 1994. Textural and permeability characteristics of faulted, high porosity sandstones. Marine Petroleum and Geology, 11, 608-623.

Fulljames, J. R., L. J. J. Zijerveld, R. C. M. W. Franssen, G. M. Ingram, and Richard, P.D. (1996), Fault seal processes, in Norwegian Petroleum Society, (eds.), Hydrocarbon seals — importance for exploration and production. Conference
Abstracts. Oslo, Norwegian Petroleum Society.

Furre, A. K., Munkvold, F. R. and Nordby, L. H. (2003). Improving Reservoir Understanding Using Time-Lapse Seismic at the Heidrun Field, 65th Meeting of the European Association of Geoscientists and Engineers.

Furre, A. K., Nordby, L. H. and Bakken, E. (2004). Heidrun time-lapse interpretation project 2004. Statoil report HNO HD PTEK 0124.

Furre, A-K., Bakken, E., and Nordby, L. H. (2005). Heidrun Time-Lapse 2001-2004 – Further Improvement of Reservoir Understanding: 67th Meeting, EAGE, Expanded Abstracts.

Furre, A. K., Bakken, E., Kløv, T. and Nordby, L.H. (2006). Heidrun 2001-2004 time-lapse seismic project: integrating geophysics and reservoir engineering. Fisrt Break, 24, 33-39.

Gassmann, F. (1951). ber die Elastizitt poroser Medien. Vierteljahrsschrift der Naturforschenden Gesellschaft in Zrich, 96, 1–23.

Gibson, R. (1988). Physical character and fluid-flow properties of sandstone derived fault gouge. In Coward, M.P., Johnson, H. and Daltaban, T. Structural Geology in Reservoir Characterization. Geological Society Special Publication, 127, 83-97.

Han, D. and Batzle, M. L.. (2004) Gassmann's equation and fluid-saturation effects on seismic velocities. Geophysics, 69, 2, pp. 398-405.

Hanssen, T. H., E. Bakken, and Nordby, L. H. (2004). Time-lapse seismic and real options: new measures are required to show value of creation: Search and Discovery Article 40117.

Harris, N. (1989). Reservoir Geology of Fangst Group (Middle Jurassic) Heidrun Field, Offshore Mid Norway AAPG Bulletin 73, 1415-1435.

Harris, D., Yielding, G., Levine, P., Maxwell, M. and Rose, P., (2002). Quantifying the effect of faults on flow of hydrocarbon through reservoirs: a fault seal analysis case study from the Strathspey field, North Sea. Field Rehabilitation II abstracts, Geological Society.

He, W., Guerin, G., Anderson, R., and Mello, U. (1998). Time dependent reservoir characterization of the LF sand in the South Eugene Island 330 Field, Gulf of Mexico. The Leading Edge, 17, 1434–1438.

He, W. (2009). 4D seismic inversion: improved workflow and preliminary tests on 4D seismic data. 20th Technical Meeting of the Edinburgh Time Lapse Project.

Hesthammer, J., and Fossen, F. (2000). Uncertainties associated with fault sealing analysis. Petroleum Geoscience. 6, 37-45.

Heum, O. R. (1996). A fluid dynamic classification of hydrocarbon entrapment. Petroleum Geoscience, v. 2, p. 145–158.

Huang Y. and MacBeth C. (2009). Direct correlation of 4D seismic and well activity for dynamic reservoir interpretation. Conference of the Society of Exploration Geophysicists. Houston, USA. Expanded abstract.

Hull, J. (1988). Thickness-Displacement relationships for deformation zones. Journal of Structural Geology , 10, 431 – 435.

Irving, A., Breton, P., & Guillon. (2007). Reservoir fault properties estimated using seismic shale gouge ratio. Geological Society Conference, London.

Jack, I. (1998). Time-Lapse seismic in reservoir management. Distinguished Instructor Short Course. Society of Exploration Geophysicists.

Jev, B. I., C. H. Kaars-Sijpesteijn, M. P. A. M. Peters, N. L. Watts and Wilkie, J. T. (1993). Akaso field, Nigeria: Use of integrated 3-D seismic, fault-slicing, clay smearing and RFT pressure data on fault trapping and dynamic leakage. American Association of Petroleum Geologists Bulletin, 77, 1389–1404.

Jones R.M and Hillis RR. (2003). An Integrated Quantitative Approach to Assessing Fault-Seal Risk. American Association of Petroleum Geologists Bulletin 87, 507-524.

Jørstad, A., Furre, A-K. and Al-Najjar, N. F. (2000) Heidrun IOR Pilot Reservoir Monitoring Project. Statoil Summary report, HD-PETEK-U 00060.

Kahar, Y., Anno, P. D. and L. G. Haram (2006). Fluid flow phenomena from 4D interpretation, Heidrun Field, Norwegian North Sea. Extended Abstract International Exposition and Seventy-Sixth Annual Meeting. New Orleans.

Knai T.A and Knipe R.J. (1998). The Impact of Faults on Fluid Flow in the Heidrun Field. In Jones G., Fisher Q.J. and Knipe R.J (eds.). Faulting, Fault Sealing and Fluid Flow in Hydrocarbon Reservoirs. Geological Society Special Publication 147, 269-282.

Knipe, R.J. (1989). Deformation mechanisms – Recognition from natural tectonites. Journal of Structural Geology, 11, 127-146.

Knipe, R. J. (1992). Faulting processes and fault seal, in R. M. Larsen, H. Brekke, B. T. Larsen, and E. Talleras, (eds.), Structural and tectonic modelling and its application to petroleum geology. Elsevier, 325–342.

Knipe, R. (1993). The influence of fault zone processes and diagenesis on fluid flow, in A.D. Horbury (eds.). Diagenesis and basin development. American Association of Petroleum Geologists Studies in Geology 36, 135 – 154.

Knipe R.J. (1997). Juxtaposition and Seal Diagrams to Help Analyze Fault Seals in Hydrocarbon Reservoirs. American Association of Petroleum Geologists Bulletin 81. 187-195.

Knott, S. D. (1993). Fault seal analysis in the North Sea: American Association of Petroleum Geologists Bulletin, 77, 778–792.

Koenig, R.H. (1986). Oil discovery in 507/7; an initial look at the Heidrun field, in A.M. Spencer, E. Holter, C.J. Campbell, S.h. Hanslein, P. H. H. Nelson, E. Nysetter, and E.G. Ormaasen. (eds.). Habitat of hydrocarbons on the Norwegian continental shelf. 307-311.

Koster, K., Gabriels, P., Hartung, M., Verbeek, J., Deinum, G., and Staples, R. (2000) Time-Lapse Seismic Surveys in the North Sea and Their Business Impact. The Leading Edge, 286-293.

Kragh, E. and Christie, P. (2002). Seismic repeatability, normalized rms and predictability. The Leading Edge, 20, 640–647.

Legrand, N. (2007). Assessing the impact of dynamic fault behaviour on history matching. M.Sc. Project Report. Institute of Petroleum Engineering. Heriot-Watt University.

Lehner, F. K., and Pilaar, W. F. (1996). On a mechanism of clay smear emplacement in synsedimentary normal faults, in Norwegian Petroleum Society, (eds.)., Hydrocarbon seals — importance for exploration and production. Conference abstracts. Norwegian Petroleum Society. Oslo, Norway.

Lindsay, N. G., F. C. Murphy, J. J. Walsh, and Watterson, J. (1993). Outcrop studies of shale smear on fault surfaces: International Association of Sedimentologists Special Publication 15, 113–123.

MacBeth, C. (2004). A classification for the pressure-sensitivity properties of a sandstone rock frame. Geophysics, 69, 497–510.

MacBeth, C., Soldo, J., and Floricich, M. (2004). Going quantitative with 4D seismic. In SEG International Exposition and Annual Meeting, Denver, Colorado.

MacBeth, C., Stephen, K., and McInally, A. (2005). The 4D signature of OWC movement due to natural production in a stacked turbidite reservoir. Geophysical Prospecting, 53, 183–203.

MacBeth, C. and Al-Maskeri, Y. (2006). Extraction of permeability from time-lapse seismic data. Geophysical prospecting, 54, 333–349.

MacBeth, C., Floricich, M. and Soldo J. (2006) Going Quantitative with 4D Seismic Analysis. Geophysical Prospecting , 303-317.

MacBeth, C. (2007). An introduction to quantitative 4D seismic interpretation for dynamic reservoir description. EAGE Education Days.

MacBeth, C., Stephen, K. and Gardiner, A. (2008). The impact of sub-seismic shale layers on the reservoir's stress sensitivity. Conference of the Society of Exploration Geophysicists. Expanded Abstract.

Manzocchi, T., Walsh, J.J., Nell, P. and Yielding, G. (1999). Fault transmissibility multipliers for flow simulation models. Petroleum Geoscience, 5, 53-63.

Manzocchi, T., Heath, A.E., Walsh, J.J., and Childs, C. (2002). The representation of two phase fault-rock properties in flow simulation models. Petroleum Geoscience, 8, 119-132.

Marsh, M. (2004). 4D in reservoir management - Successes and Challenges. IOR Views e-Newsletter, 8.

Marsh, M., Whitcombe, D., Raikes, S., Parr, R., and Nash, T. (2003). BP's increasing systematic use of time-lapse strategy. Petroleum Geoscience, 9, 7–13.

Matheron, G. (1965). Les variables régionalisées et leur estimation. Une application de la théorie des functions aléatoires aux sciences de la nature. Masson, Paris, France.

Mavko, G., Mukerji, T. and Dvorkin, J. (1998). The rock physics handbook. Tools for seismic analysis in porous media. Cambridge University Press.

Mitra, S. (1988). Effect of deformation mechanism on reservoir potential in central Appalachian over-thrust belt. American Association of Petroleum Geologists bulletin, 72, 536-554.

Møller-Pedersen, P., and Koestler, A.G. (1997). Hydrocarbon seals: Importance for Exploration and Production. Norwegian Petroleum Society Special Publication 7.

Naruk, S.J. , Dula, W.F., Busch, J.P., Couzens-Schultz , B.A., Garmezy, L., Griffiths H., Gunst A.M., Hedlund, C.A., McAllister, E., Onyeagoro, U.O., Ozumba, B.M. and Younes, A. (2002). Common Characterstics of Proven Sealing and Leaking Faults. American Association of Petroleum Geologists Hedberg Research Conference. Barossa Valley, South Australia.

Nordby, L. H. and Furre, A.-K. (2002): Heidrun time-lapse seismic project 2002, Statoil report UPN HNO HD PTEK 0049.

Onyeagoro, K., Naruk, S., Eikmans, D., Van der Vlugt, F., Jolley, S., Zijlstra, E., De Keijzer, M., Kristensen, M., Reemst, P., and King, R. (2009). New Fault Permeability and Capillary Entry Pressure Relations for Production History Matching of Matured Fields. American Association of Petroleum Geologists Abstract. Annual Convention and Exhibition, Denver, Colorado.

Pardo-Igúzquiza, E. (1999). VARFIT: a fortran-77 program for fitting variogram models by weighted least squares. Computers & Geosciences 25, 251-261.

Parr, R.S. and Marsh, M. (2000). Development of 4-D reservoir management West of Shetland: World Oil, 221 No. 9.

Reid, B.E., Høyland, L.A., Olsen, S.R. and Petterson, O. (1996). The Heidrun Field – Challenges in Reservoir Development and Production. Offshore Technology Conference, OTC 8084 Houston.

Robertson, E.C. (1983). Relationship of fault displacement to gouge and breccia thicknesses. Institute of Mining Engineering, 35, 1426 – 1432.

Shams, A., MacBeth, C., and Barens, L. (2007). Local connectivity analysis in a deep water complex turbidite using seismic time lapse and well interference test. Devex. Aberdeen, UK. Abstract.

Smith, T., Sondergled, C., and Rai, C. (2003). Gassmann fluid substitution: A tutorial. Geophysics, 68, 430–440.

Schlumberger. (2004) Simulation software manuals.

Schowalter, T. T. (1979). Mechanics of secondary hydrocarbon migration and entrapment. American Association of Petroleum Geologists Bulletin, 63, 723–760.

Sonneland, L., Signer, C., Veir, H., Saeter, T. and Schlaf, J.,(2000). Detecting low barriers with 4-D seismic, 70th Annual International. Meeting. Society of Exploration. Geophysicists., Expanded abstract, 1477-1480.

Sperrevik, S., Gillespie, P. A., Fisher, J.P., Halvorsen, T. and Knipe, R. Empirical estimation of fault properties. In Hydrocarbon Seal Quantification. Edited by A.G Koestler and R. Hunsdale. NPF Publication 11, pp 109-125. Published by Elsevier.

Staples, R., Hague, P., Weisenborn, T., Ashton, P. and Michalek, B. (2005). 4D seismic for oil-rim monitoring, Geophysical Prospecting, 53, 243-251.

Stephen, K. and MacBeth, C. (2006). Seismic history matching in the Schiehallion UKCS Field. First Break, 24, 43–49.

Sverdrup, E., Helgesen, J. and Vold, J. (2003). Sealing properties of faults and their influence on water-alternating-gas (WAG) injection efficiency in the Snorre Field, northern North Sea, American Association of Petroleum Geologists Bulletin, 87, 1437 – 1458.

Trauth, M. (2005). Matlab Recipes for Earth Sciences. Springer.

Villegas, R., MacBeth, C. and Benguigui, A. (2009). History matching of reservoirs by modifying fault properties using 4D seismic results: a synthetic study. Conference on Faults and Top Seals of the European Association of Geoscientists and Engineers. Montpellier, France. Expanded Abstract.

Walsh, J.J., Watterson, J., Heath, A. E. and Child, C. (1988). Representation and scaling of faults in fluid flow models. Petroleum Geoscience, 4, 241 – 251.

Yielding, G., Freeman, B., and Needham, D.T. (1997). Quantitative fault seal prediction. American Association of Petroleum Geologists Bulletin 81, 897-917.

Yielding G, Øverland JA and Byberg G. (1999). Characterization of Fault Zones for Reservoir Modeling: An example from the Gullfaks Field, Northern North Sea. American Association of Petroleum Geologists Bulletin 83, 925-951.

Yielding, G.. (2002). Shale Gouge Ratio – Calibration by geohistory. In Kosetler, A.G. and Hunsdale, R. (eds.). Hydrocarbon seal quantification. Norwegian Petroleum Society Special Publication 11, 1-15.

Zoback, M. (2007). Reservoir Geomechanics. Cambridge University Press.

Zoeppritz, K. (1919). Erdbebenwellen VIIB, On the reflection and propagation of seismic waves. Göttinger Nachrichten, I, 66-84.